



HAL
open science

Multiscale investigation of thermal and hydric behavior of buildings : integration of artificial intelligence in building energy simulation

Mohamed Ali Hamdaoui

► **To cite this version:**

Mohamed Ali Hamdaoui. Multiscale investigation of thermal and hydric behavior of buildings : integration of artificial intelligence in building energy simulation. Fluids mechanics [physics.class-ph]. Normandie Université, 2023. English. NNT : 2023NORMC228 . tel-04349897

HAL Id: tel-04349897

<https://theses.hal.science/tel-04349897>

Submitted on 18 Dec 2023

HAL is a multi-disciplinary open access archive for the deposit and dissemination of scientific research documents, whether they are published or not. The documents may come from teaching and research institutions in France or abroad, or from public or private research centers.

L'archive ouverte pluridisciplinaire **HAL**, est destinée au dépôt et à la diffusion de documents scientifiques de niveau recherche, publiés ou non, émanant des établissements d'enseignement et de recherche français ou étrangers, des laboratoires publics ou privés.



Normandie Université



UNIVERSITÉ
CAEN
NORMANDIE

THÈSE

Pour obtenir le diplôme de doctorat

Spécialité **MECANIQUE DES FLUIDES, ENERGETIQUE, THERMIQUE, COMBUSTION,
ACOUSTIQUE**

Préparée au sein de l'Université de Caen Normandie

**Multiscale investigation of thermal and hydric behavior of
buildings - Integration of artificial intelligence in building energy
simulation**

Présentée et soutenue par
MOHAMED ALI HAMDAOUI

Thèse soutenue le 20/09/2023
devant le jury composé de

MME FLORENCE COLLET	Professeur des universités, UNIVERSITE RENNES 1	Rapporteur du jury
M. ZOHIR YOUNSI	Maître de conférences HDR, Ecole des hautes études d'ingénieur (HEI) Junia	Rapporteur du jury
MME ALEXANDRA BOURDOT	Maître de conférences, École normale supérieure Paris-Saclay	Membre du jury
M. MOHAMED BOUTOUIL	Directeur de recherche, Builders Ecole d'ingénieurs Caen	Président du jury
M. NASSIM SEBAIBI	Maître de conférences HDR, Builders Ecole d'ingénieurs Caen	Directeur de thèse

Thèse dirigée par **NASSIM SEBAIBI (Ecole d'ingénieurs - Builders For Society)**



Abstract

A novel approach to the building sector, including new construction and rehabilitation, is necessary in light of the global energy context. This transition has been pushed by a number of variables, including the rise in global population and rising consumer demands. Additionally, as the building industry's environmental effect has come into greater focus, it is more important than ever to limit greenhouse gas emissions. As a significant contributor to carbon dioxide emissions, the construction industry must drastically alter its strategy to cut energy use. Any innovative approach must be both technically effective and ecologically acceptable. In this situation, simulating the heat and cooling needs of the building is a helpful tool for designing, planning, and improving its energy efficiency.

The goal of this thesis is to conduct an experimental and numerical investigation of the hygrothermal behavior of buildings. Experimentation will be used to construct and evaluate a thermo-hydric simulation model. The model will then be used in numerical simulations with a variety of programs. Finally, some suggestions for enhancing the building's performance will be given. In this instance, some of the building materials employed in the PhD project for energy simulation of buildings is gathered from both new and old research. The PhD project focused on the creation of eco-friendly sustainable materials and a novel coupling methodology to forecast thermo-hydric behavior at the scale of whole building. The materials choices have been selected through an analytical method in order to validate their energy performance at the wall scale. The solutions are advancing toward the incorporation of hygroscopic materials, followed by full-scale numerical modeling. In terms of improving thermal comfort, indoor air quality, energy consumption, and indoor humidity management, hygroscopic envelopes appear to be a potential path in the face of building energy challenges and environmental effect constraints. The fundamental problem, however, is the lack of precise and trustworthy simulation techniques that can calculate the hygrothermal performance of building envelopes. The transient thermo-hydric behavior of this type of envelope at the building-scale reference values are currently unavailable. In order to ascertain the accuracy of thermal and hydric calculation tools, the current effort has this objective. The physics of moisture transport in hygroscopic materials (capable of fixing moisture) is complicated, which makes it challenging to calculate coupled heat and mass fluxes. The hygrothermal behavior in hygroscopic envelopes was therefore studied using experimental and newly computational methods. Experimental and numerical modeling of hygrothermal behavior of hygroscopic envelopes were therefore carried out with a multi-scale perspective. Construction materials' mechanical, hydric, and thermal characteristics have been characterized in the experimental section. During this experimental campaign, the effects of the building material's thermal and hydric states on its hygrothermal property values were examined.

In another work, several experimental published data, at wall scale, were used to study the hygrothermal response of different building envelope configurations and validate the linearized sorption curve due to the hysteresis effect. The results of the confrontation revealed that the numerical solution and experimental measurements agreed well. This indicates that the suggested model can recreate the majority of the features observed in the physical system under study.

In the next section, we created a technique for combining artificial intelligence with building energy modeling tools to estimate the evolution behavior of thermal and hydric dynamics at the entire building scale. The new computing methodology was confronted with many experimental data for different building locations, size and climate.

The findings in the context of this PhD project have demonstrated the need of rigorous modeling of coupled heat, air and mass transfer through the walls and whole building scale investigation on the thermo-hydric behavior prediction of indoor air quality (temperature and humidity), besides going further on the evaluation of the building's energy loads.

Summary

In light of the energy needs of buildings and their possible environmental implications, it appears that low carbon materials, especially hygroscopic envelopes, are an effective way to improve thermal comfort, indoor air quality, energy consumption, and indoor humidity control. An energy model should be developed to assess the savings that would be realized with a retrofit or new constructions. in order to convince the stakeholders in the building industry of the many advantages of employing hygroscopic envelopes. The dynamic hygrothermal response of such a sort of enclosure is still without any reference values. In order to verify the aforementioned energy model, the primary goal of this PhD thesis is to establish a set of suitable numerical and experimental settings. The advantages of using hygroscopic envelopes in real-world applications in terms of energy savings and less environmental effect will then be determined based on the model's outputs. Numerous numerical models will be created and improved in order to achieve these goals since they serve as the project's main foundations. Modeling coupled heat and mass transfers is challenging because of the complicated physics of how water moves through hygroscopic materials which may well hold humidity. To accurately anticipate in the future the thermo-hydric behavior of hygroscopic media, such as the building envelopes, a multi-scale analysis has been conducted using experimental and numerical approaches.

As a result, the initial scale characterization concentrated on the examination of a unique low-carbon material and a new, more straightforward methodology at both the wall and building scales. The novel suggested materials and approach produce encouraging outcomes. Enough to conduct a full-scale pilot test of the modeling and simulation tool and can apply it to actual building challenges in the long term. In fact, the new modeling and simulation method made it possible to severely reduce the amount of time needed for calculation to get accurate results while simultaneously increasing precision at both the building and the wall scale. This dissertation investigated a number of ways to enhance current building design processes. For developing new materials and investigate modeling and simulation methods at different sizes, several studies were carried out. A novel linearization method has enabled the characterization and simplification of the parameters related to heat and mass exchanges. The main characteristics of the thermo-hydric performance of materials are acquired by this method using a small number of variables based on dependable physical understanding. Additionally, this method enables the simplification of large-scale models while yet preserving excellent forecast accuracy and reliability.

The most important factors affecting HAM transfer were the subject of an independent investigation at the wall scale. With a reduction in the amount of calculation time needed to maintain an acceptable level of computation efficiency. More trustworthy numerical results at the wall scale have been obtained by applying a linearized sorption curve to the hysteresis effect.

Additionally, it was shown that the new approach's predictability and numerical precision needed to be improved by including the impacts of linearity on the hysteresis effect on the overall model capacity. Moreover, in regard to building physics, internal surfaces are considered to be sensitive to thermal and hydric boundary conditions fluctuations, whereas external surfaces are supposed to be responsive to solar radiation, rain, and mixed forced and natural convection processes due to the ambient air temperature, wind, and ventilation systems. Quantifying the effects of internal and external influences on building energy consumption and performance, consequently, presents considerable issues. A quantitative knowledge of the underlying energy behavior of a structure and its inhabitants may be developed and put into practice to overcome these difficulties. Within that part of the study, we suggest developing a thorough virtual building simulator that can model how energy usage changes depending on the environment, both indoors and outdoors.

An experimental effort from the thesis of Bouasria [1] on a compact building concept has been produced in the lab to examine the hygrothermal behavior of earth and straw bio-based constructions. In order to identify the differences in the hygrothermal conditions within the building, a series of tests were carried out to measure the external temperature and humidity conditions associated with various inside locations in the building. The experimental results were utilized to create a numerical model that could replicate variations in interior relative humidity and temperature. Our project operates within the context of the continuity of the work as well as the validation of the results of the dynamic co-simulation between artificial intelligence and dynamic thermal simulation (AI-BES). This model was used to simulate the heat and moisture exchange between the indoor and outdoor environments at the size of the entire building, converting the conventional thermal results into hygrothermal data while keeping the physical aspect of the model. The approach for numerical building modeling will be able to simulate the thermal/hydric behavior of various interior and outside conditions. With the help of this depiction, urban architecture can be altered in line with regional characteristics and climatic situations. Building designers and planners will be able to make better decisions thanks to more precise modeling of internal and exterior environments within urban architecture, which will improve overall energy efficiency and reduce environmental footprints. This technique will make it easier to adapt and upgrade both new and old buildings, which will be crucial in limiting climate change and enhancing indoor comfort for populations throughout the globe.

Synthèse en français

Introduction

Remettre en perspective l'ensemble de l'enveloppe d'un bâtiment dès la phase de conception est nécessaire pour améliorer les performances. Il s'agit avant tout d'améliorer l'efficacité énergétique, le confort thermique et le respect de l'environnement. Les transferts thermiques dynamiques ou hydrique entre l'intérieur et l'extérieur sont influencés par l'enveloppe. Dans tous les cas, le choix des matériaux utilisés pour construire l'enveloppe est crucial. Les concepteurs peuvent utiliser des outils de simulation pour examiner comment les différents matériaux affecteront l'efficacité d'un bâtiment et comment déterminer les spécifications optimales pour chaque composant de l'enveloppe, comme l'isolation, les fenêtres et d'autres éléments.

Chaque saison de l'année est affectée par l'adoption de modèles globaux d'urbanisme et d'architecture qui utilisent des matériaux et des concepts préconçus. Bien que l'utilisation intensive d'équipements thermo-mécaniques pour le contrôle de la température soit bénéfique, elle entraîne également une consommation excessive d'énergies indésirables qui a un effet néfaste sur l'environnement. La simulation énergétique permet d'analyser le comportement énergétique d'un bâtiment et de formuler des jugements pertinents pour l'application des solutions d'économie des énergies. Le monde du bâtiment est l'une des industries les plus importantes en termes de consommation d'énergie, étant donné la gigantesque utilisation mondiale d'énergie associée à des émissions de CO₂ de l'ordre des milliards de tonnes. Il est donc essentiel de faire un effort sincère et urgent pour réduire les dépenses énergétiques. Le développement d'outils de simulation améliorés pour les systèmes énergétiques des bâtiments contribue de manière significative à la réduction de la consommation d'énergie, à la diminution des émissions de carbone et à la protection de l'environnement.

Les bâtiments font partie des industries qui émettent le plus de gaz à effet de serre, ce qui, au tournant du siècle, a suscité de vives inquiétudes tant pour l'environnement que pour l'économie mondiale. Dès qu'un véritable objectif politique a été atteint en ce qui concerne les réglementations régissant l'utilisation prudente de l'énergie, ce secteur a été rapidement propulsé sur le devant de la scène. Par la suite, un certain nombre de mesures ont été mises en place par l'introduction de diverses règles énergétiques ultérieures, qui ne cessent d'être révisées afin d'atteindre la neutralité carbone dans les différentes industries utilisant de l'énergie polluante ainsi qu'une réduction de la consommation d'électricité. Cet effort sera principalement axé sur le développement d'une approche permettant de simuler la quantité d'énergie utilisée par les bâtiments dans des zones climatiques différentes dans ce contexte. Néanmoins, la mise en œuvre

de ces règles énergétiques dans les nouvelles constructions ou lors de la rénovation de structures existantes peut entraîner la création d'espaces clos inhabitables avec des murs hermétiques et un renouvellement minimal de l'air intérieur. Il a été établi qu'il est possible d'utiliser la ventilation naturelle avec des fenêtres intelligentes qui s'ouvrent en fonction de la température intérieure afin de préserver la chaleur en hiver et d'éviter la surchauffe en été.

De ce fait, les échanges de transferts d'humidité sous diverses formes deviennent plus importants que les échanges de chaleur, au point qu'il est impossible de les ignorer sans engendrer d'importantes inexactitudes dans les calculs numériques. De plus, la présence d'humidité excessive est générée et amplifiée par une perméabilité insuffisante des structures. Il est donc essentiel de tenir compte de ces facteurs lors de l'analyse et de la conception des enveloppes des bâtiments afin de renforcer l'efficacité des simulations énergétiques. Dans cette situation, l'inclusion d'un modèle hygrothermique dans les simulations énergétiques des bâtiments permet d'identifier les variables clés qui affectent les performances de ces systèmes. En outre, l'utilisation de matériaux à faible impact, tels que les éco-matériaux, les matériaux bio-sourcés, et les matériaux recyclés, est limitée, en particulier par le manque total de bases de données sur leurs caractéristiques fondamentales et de détails sur leur comportement à long terme. Outre ce manque d'information, le domaine de la conception des bâtiments manque de compétences en matière de techniques de conception durable. Il est nécessaire de disposer de techniques fiables et précises, en particulier pour évaluer les performances et le cycle de vie des matériaux, ainsi que l'effet de la consommation d'énergie sur la qualité de l'environnement intérieur d'un bâtiment.

Dans ce contexte, l'humidité est l'un des principaux facteurs contribuant à la détérioration des structures. La communauté scientifique, qui sert de décideur international, s'est concentrée sur ce sujet afin de mieux comprendre les processus liés aux transferts hygrothermiques à de nombreuses échelles, y compris les atmosphères des espaces habités, les matériaux poreux et les enveloppes des bâtiments. Afin de surmonter ces problèmes énergétiques et environnementaux. Les communautés écologiques de la planète ont un double objectif : réduire les émissions de gaz à effet de serre jusqu'à la neutralité, et réduire autant que possible la consommation d'énergie dans les bâtiments. L'optimisation des caractéristiques du bâtiment, en premier lieu les enveloppes, est une stratégie clé pour atteindre ces objectifs.

Les façades du bâtiment sont les éléments d'interaction avec le monde extérieur. Ils sont chargés de transférer la masse, l'énergie, et la chaleur à l'intérieur et à l'extérieur de la structure. Comme ce sujet dépend du comportement du bâtiment, de son environnement et des conditions météorologiques, l'étude de la performance énergétique des bâtiments devient de plus en plus multidisciplinaire. Cependant, pour atteindre les performances énergétiques nécessaires, les techniques de construction ont évolué pour répondre à ces besoins.

Les bâtiments deviennent plus imperméables, et l'isolation des murs est renforcée. Cette évolution entraîne des problèmes liés à l'humidité, tels que la formation de moisissures, la détérioration de la qualité de l'air et la condensation à l'intérieur des façades. Par conséquent, l'utilisation d'enveloppes de bâtiment hautement isolées et étanches est concevable uniquement à l'aide de simulations fiables permettant de comprendre, de prévoir et d'évaluer leurs effets. La capacité des algorithmes prédictifs à estimer le comportement d'un bâtiment à l'intérieur est utilisée pour estimer sa performance. Par conséquent, une mauvaise application virtuelle des scénarios réels réduit la durabilité et la performance énergétique des structures. Par conséquent, il est désormais plus difficile de concevoir les systèmes énergétiques de climatisation pour maintenir un niveau optimal de confort climatique. Il est donc important de tenir compte de la façon dont l'humidité se diffuse dans les enveloppes, ce qui permettra d'accroître l'efficacité énergétique du bâtiment tout en maintenant les niveaux de confort nécessaires.

À la suite de ces faits, il semblerait que l'utilisation de matériaux hygroscopiques dans les enveloppes des bâtiments soit une stratégie créative et prometteuse pour améliorer la performance thermique, la qualité de l'air intérieur, la consommation d'énergie, et notamment le contrôle du confort thermo-hydrrique dans les bâtiments. Un matériau est qualifié d'hygroscopique s'il peut absorber l'humidité. Les matériaux étudiés sont des produits à faible taux d'émission de carbone. En tant que base pour de futurs bâtiments durables, nous prenons également en compte les ressources locales. Par conséquent, notre objectif est d'évaluer les qualités des matériaux hygroscopiques qui sont suggérés pour les économies d'énergie et les solutions écologiques ainsi que pour leurs performances améliorées dans les applications architecturales telles que les murs, les toits et les sols.

Contexte général

Ce contexte encourage la recherche scientifique à réexaminer les performances des matériaux de construction qui forment l'enveloppe du bâtiment en termes de bilan énergétique et d'effets sur l'environnement (épuisement des ressources naturelles, consommation d'énergie, émissions polluantes...). Cette recherche donne un aperçu de l'état actuel de l'efficacité énergétique de diverses structures de construction. Elle propose certaines normes qui peuvent être utilisées pour évaluer et examiner les capacités des nouveaux matériaux de construction à l'aide d'un certain nombre de mesures. Elle donne également un aperçu général des méthodologies et des approches actuellement utilisées pour évaluer les effets des performances des bâtiments et déterminer leur potentiel d'efficacité énergétique.

En outre, il présente l'idée d'enveloppes " écologiques " ou " durables " dans le contexte des bâtiments à haute performance énergétique, ainsi que les normes précises employées pour déterminer le niveau de rendement de ces enveloppes. En outre, il examine les difficultés et les

problèmes pertinents qui doivent être pris en compte lors de la conception d'enveloppes de bâtiments durables sur le plan environnemental et efficaces sur le plan énergétique. Dans cette situation, les matériaux de construction biosourcés qui intègrent des produits de déchets naturels constituent un substitut intéressant aux techniques de construction conventionnelles. De nombreuses recherches scientifiques ont été menées sur ce matériau dans le but d'analyser ses propriétés fondamentales (capacités thermiques, hydriques et mécaniques), ainsi que leur caractérisation à l'échelle des bâtiments. Cependant, la modélisation complète de la diffusion de la chaleur et de la masse à travers le bâtiment afin de mieux concevoir les systèmes énergétiques n'en est encore qu'à ses débuts. Pour obtenir des résultats précis pour la conception de structures réelles, il est essentiel de créer des modèles numériques qui tiennent compte de tous les facteurs liés à la fois aux caractéristiques des matériaux et à la conception des enveloppes hygrothermiques des bâtiments.

Principaux objectifs de la thèse

Les objectifs de ces recherches encouragent l'étude et la création de solutions de construction respectueuses de l'environnement et efficaces sur le plan énergétique. Les labels offrent la possibilité de comprendre comment les bâtiments sont liés les uns aux autres et à l'environnement en général et d'un point de vue systémique. En outre, ils servent de base à la création de buts et d'objectifs en matière d'efficacité énergétique, ainsi que de points de référence pour le suivi de leur progression. D'autre part, la plupart des logiciels de calcul actuels n'intègrent pas les mécanismes hygrothermiques physiques. Or, le confort en hiver et en été est fortement influencé par l'humidité de matériaux poreux. C'est pourquoi cette étude tente d'utiliser une approche numérique et expérimentale pour comprendre le comportement thermo-hydrique des enveloppes hygroscopiques. Pour ce faire, une recherche en laboratoire sera menée sur le transfert de chaleur et de masse à l'intérieur d'une cellule d'essai micro-météorologique ventilée à zone unique, dans un environnement climatique réel. Afin d'évaluer un outil numérique créé pour prédire la réponse thermo-hydrique des enveloppes hygroscopiques. Cette étude prend en compte les impacts de l'humidité sur le confort thermique et la consommation d'énergie dans la perspective des bâtiments.

Elle sera d'un grand intérêt pour les chercheurs qui étudient le comportement des enveloppes hygroscopiques dans différents climats, ainsi que pour les utilisations potentielles de cette idée dans les futurs bâtiments à haute performance destinés à répondre à des réglementations environnementales et énergétiques strictes. L'objectif est de déterminer le fait que le transfert de masse et les échanges convectifs par changement de phase à la surface de ces interfaces génèrent des libérations ou des absorptions de chaleur latente, qui peuvent contribuer soit à un refroidissement naturel en été, soit à une déperdition de chaleur supplémentaire pendant la

période de chauffage. Les résultats de l'étude serviront de référence pour les professionnels et les architectes qui travaillent dans le domaine de la construction propre et durable et qui cherchent à maximiser les performances de l'enveloppe en été et en hiver.

Les objectifs de recherche actuels répondent à la nécessité d'une modélisation totale du transport couplé de chaleur et de masse à l'échelle du bâtiment et de l'enveloppe. C'est dans ce contexte qu'est née l'initiative "Whole Building Heat, Air, and Moisture Response" (réponse à la chaleur, à l'air et à l'humidité de l'ensemble du bâtiment). L'objectif est de fournir un outil numérique complet pour la conception, la modélisation et l'étude expérimentale/numérique du comportement hygrothermique de l'enveloppe hygroscopique des bâtiments réels. Afin de convertir la simulation thermique classique en données hygrothermiques, l'objectif est d'évaluer son potentiel en combinant la simulation énergétique des bâtiments avec l'intelligence artificielle (Deep Learning). En conséquence, les quatre chapitres ci-dessous regroupent les principaux efforts réalisés dans le cadre du projet de doctorat.

Synthèse du manuscrit

Chapitre 1.

Le premier chapitre présente une analyse de référence des phénomènes physiques qui interviennent dans les échanges de chaleur, d'air et d'humidité à l'intérieur des bâtiments. Afin d'accroître leur capacité et leur précision, il a fallu créer de nouveaux modèles et améliorer ceux qui existaient déjà. La nécessité d'incorporer ces modèles dans la conception architecturale est également abordée dans ce chapitre, ainsi que les problèmes liés à leur utilisation pratique.

Ce chapitre comprend également des informations bibliographiques sur les propriétés des milieux poreux, de nombreux processus physiques impliquant des transferts couplés de masse et de chaleur, et leur modélisation, ainsi que les principales méthodes utilisées dans la modélisation hygrothermique des bâtiments. Le chapitre fournit un examen approfondi des principaux mécanismes qui transportent la chaleur et la masse entre les environnements intérieurs et extérieurs des bâtiments, ainsi que des informations sur la façon de modéliser ces processus analytiquement ou numériquement. Par conséquent, une analyse exploratoire de la littérature est conduite pour fournir une vue d'ensemble des stratégies les plus récentes afin de découvrir ces approches de simulation. Des études sélectionnées qui entrent dans des détails considérables sont examinées en profondeur. Il s'agit notamment de modèles physiques, qui se concentrent sur la résolution numérique du comportement hygrothermique simulé des bâtiments, et de modèles axés sur les données, qui utilisent des approches d'intelligence artificielle pour créer un modèle prédictif. Les avantages du modèle proposé en termes de performance et de précision sont ensuite mis en évidence par le biais de diverses comparaisons et analyses.

Les modèles physiques sont divisés en deux groupes pour être évalués à l'aide de la méthode CFD et de la méthode nodale dans un premier temps. Ces deux groupes contiennent une variété de modèles, mais chacun d'entre eux utilise et applique un module particulier d'une manière spécifique. En fonction de l'utilisation prévue du modèle, il peut en résulter une variété de réponses. Les modèles logiques, quant à eux, utilisent principalement des modèles de réseaux neuronaux artificiels. Ils sont basés sur des données recueillies par le biais d'expériences ou de valeurs numériques ou mesurées. Par conséquent, aucune paramétrisation préalable n'est nécessaire. L'étude souligne la nécessité d'une approche normalisée de la modélisation hygrothermique à l'aide d'enveloppes hygroscopiques. Le choix de l'outil ou du modèle le plus approprié est facilité car il offre une meilleure compréhension de la simulation hygrothermique. En outre, les études citées apportent une contribution significative au développement des recherches actuelles et futures dans l'évaluation de la performance énergétique des bâtiments.

Chapitre 2.

Le deuxième chapitre portera sur la description des phénomènes de transfert. Selon les méthodes actuelles, les équations seront fondées sur les équations de conservation de l'énergie et de la masse. Les différentes formes de transfert sont explorées, en mettant l'accent sur les simplifications possibles ainsi que sur les techniques de résolution analytique et numérique des équations différentielles. Les résultats seront utilisés pour calculer les effets combinés des processus de transfert de masse et de chaleur, ainsi que pour évaluer les effets de ces différents facteurs sur les performances thermiques et hydriques totales du système. En outre, le choix approprié des conditions aux limites permettra d'évoquer efficacement tous les types de transport de chaleur et de masse. Les modèles phénoménologiques actuels des échanges combinés de chaleur, d'air et d'humidité dans les murs des bâtiments sont également suggérés. Le modèle étudié est basé sur des facteurs de transfert (température pour le transfert de chaleur, humidité ou pression de vapeur d'eau pour le transfert d'humidité, et pression totale pour le mouvement de l'air) qui sont indépendants de la nature des matériaux. En particulier, plusieurs stratégies seront suivies pour explorer les moyens de reproduire les phénomènes montrés dans les observations expérimentales réelles et de résoudre les équations gouvernantes par le calcul.

Ces solutions permettent aux murs multicouches de conserver une continuité au niveau des interfaces entre les couches et d'aborder leur modélisation en évitant des exigences compliquées en matière de limites au moment des contacts entre les couches. Les principaux avantages de ce modèle sont sa simplicité et son adaptabilité, qui permettent d'envisager différents types d'interfaces et une conception préliminaire du bâtiment qui tient compte de toutes les combinaisons possibles des nombreux aspects susceptibles d'influer sur les performances en termes d'efficacité énergétique.

Chapitre 3.

Le troisième chapitre décrit un effort de caractérisation des propriétés microstructurales (porosité), thermo-physiques (conductivité thermique et chaleur spécifique) et hydriques (isothermes d'adsorption et de désorption, rétention d'eau et perméabilité à la vapeur d'eau) des matériaux de construction. Cette caractérisation a permis de comprendre les paramètres qui influencent les performances des enveloppes des bâtiments. Ce travail s'est principalement concentré sur l'étude de la relation entre l'humidité et les caractéristiques hydriques, telles que les courbes isothermes de sorption et de désorption, ainsi que sur la relation entre l'état thermique du matériau et les valeurs des propriétés thermo-physiques, en particulier la conductivité thermique et la chaleur spécifique. Les matériaux testés dans le cadre de la recherche sont constitués de terre et de paille. La performance énergétique des structures murales constituées de ces matériaux peut être mesurée et simulée à l'aide d'une approche éprouvée qui a été créée dans le but de mener cette étude. Ensuite, une analyse numérique a été réalisée pour étudier la performance énergétique des nouveaux murs. En outre, les bases de données ont été élargies pour inclure des informations sur les caractéristiques hygrothermiques des matériaux de construction. Les résultats de l'étude ont permis de suggérer des combinaisons créatives de matériaux afin de réduire la quantité d'énergie consommée par les bâtiments utilisant le mur développé.

De la même manière, en incluant la linéarisation de la courbe de sorption causée par l'influence de l'hystérésis, les méthodologies de modélisation des échanges thermiques et hydriques au niveau des murs ont été améliorées. L'application de cette technique de linéarisation innovante la plus récente a permis d'obtenir des résultats numériques plus précis à l'échelle des parois. Les résultats de cette étude et ceux qui ont déjà été rapportés dans la littérature ont été comparés et il a été déterminé qu'il n'y a pas de différences significatives entre eux.

Chapitre 4.

Le quatrième chapitre est consacré au développement d'une stratégie de co-simulation pour garantir une modélisation hygrothermique précise et complète du bâtiment. La co-simulation en question implique deux modèles, le premier est une simulation thermique dynamique du bâtiment lancé sur un logiciel BES connu, et le second est un modèle d'intelligence artificielle (Deep Learning) développé à l'aide d'un logiciel open-source. Cette intelligence artificielle a été entraînée à l'aide de données provenant des résultats numériques de la simulation dynamique du bâtiment. L'efficacité de ce modèle a été évaluée en termes de temps de calcul et de précision dans la reproduction des résultats de la modélisation conformément aux résultats expérimentaux actuellement disponibles dans la littérature scientifique sur l'impact de la température, de l'humidité et du rayonnement solaire sur la qualité de l'air intérieur.

Par conséquent, de nombreuses validations par rapport aux données numériques et expérimentales issues du travail de thèse de Bouasria en 2022 [1] ont été présentées afin de démontrer le bon fonctionnement de la technique de co-simulation AI-BES. Elle comprend également une comparaison numérique des simulations de co-simulation avec celles des expériences. Au laboratoire Builders-ing, les mesures ont été effectuées sur un banc expérimental créé à cet effet. Ensuite, une étude de cas a été menée pour examiner l'influence de l'intégration de l'intelligence artificielle sur la transformation des sorties de la simulation thermique dynamique traditionnelle en données hygrothermiques. Afin d'anticiper le comportement hygrothermique des structures (enveloppe et environnement d'habitation) ainsi que les besoins énergétiques, il est nécessaire de prendre en considération les transferts couplés de chaleur et de masse dans la paroi tout en conservant les aspects physiques (géométrie, thermique, hydrique, etc.).

Afin de répondre efficacement aux besoins des utilisateurs et d'offrir une interprétation claire des résultats, ce chapitre a examiné comment comprendre et respecter les objectifs et les contraintes de cette technique. La technique de co-simulation numérique des bâtiments permettra également d'identifier le comportement hygrothermique de différents scénarios intérieurs et extérieurs. Cette technique sera très utile aux décideurs pour réduire les dépenses énergétiques et augmenter le confort des occupants des bâtiments tout en diminuant la consommation d'énergie et les émissions de CO₂ qui contribuent aux déséquilibres globaux de la planète.

LISTS OF SYMBOLS AND ACRONYMS

A_i	Actual measured/experimental data	(-)
A	Apparent solar-radiation constant	(-)
B	Atmospheric extinction coefficient	(-)
b_j	Bias weight at layer level j	(-)
c	Energy constant for the specific heat of sorption	(-)
C	Volumetric heat capacity	($\text{J m}^{-3} \text{K}^{-1}$)
c_0	Entropic adjustment factors	(-)
c_g	Adsorption constant of GAB model	(-)
c_p	Specific heat of dry material	($\text{J kg}^{-1} \text{K}^{-1}$)
C_v	Molar concentration of vapor	(mol m^{-3})
d	Pore diameter	(m)
D_b	Bound water diffusivity	($\text{m}^2 \text{min}^{-1}$)
D_{BC}	Diffusion coefficient	($\text{m}^2 \text{s}^{-1}$)
D_c	Molecular diffusion coefficient proportional to the mean free path	($\text{m}^2 \text{s}^{-1}$)
D_K	Knüdsen diffusion coefficient proportional to the pores size	($\text{m}^2 \text{s}^{-1}$)
D_K	Knudsen diffusion	($\text{cm}^2 \text{s}^{-1}$)
D_m	Moisture diffusion coefficient of the porous media	($\text{m}^2 \text{s}^{-1}$)
D_T	Moisture diffusion coefficient related to the temperature gradient	($\text{m}^2 \text{s}^{-1} \text{K}^{-1}$)
$D_{T,liq}$	Liquid diffusion coefficient related to the temperature gradient	($\text{m}^2 \text{s}^{-1} \text{K}^{-1}$)
$D_{T,vap}$	Vapor diffusion coefficient related to the temperature gradient	($\text{kg m}^{-1} \text{s}^{-1} \text{K}^{-1}$)
$D_{T,vap}$	Vapor diffusion coefficient related to the temperature gradient	($\text{m}^2 \text{s}^{-1} \text{K}^{-1}$)
D_v	Water vapor diffusivity	($\text{m}^2 \text{min}^{-1}$)
D_w	Moisture water diffusion coefficient	($\text{kg m}^{-1} \text{s}^{-1} \text{K}^{-1}$)
D_w	Moisture water diffusion coefficient	($\text{m}^2 \text{s}^{-1}$)
D_θ	Moisture diffusion coefficient related to the moisture gradient	($\text{m}^2 \text{s}^{-1}$)
$D_{\theta,liq}$	Liquid diffusion coefficient related to the moisture gradient	($\text{m}^2 \text{s}^{-1}$)
$D_{\theta,vap}$	Vapor diffusion coefficient related to the moisture gradient	($\text{m}^2 \text{s}^{-1}$)
D_ϕ	Liquid conduction coefficient	($\text{kg m}^{-1} \text{s}^{-1}$)

E	Phase conversion number	(-)
E_b	Beam normal irradiance	(W m ⁻²)
E_d	Diffuse horizontal irradiance	(W m ⁻²)
E_o	Extraterritorial solar radiation	(W m ⁻²)
E_{sc}	Solar constant	(W m ⁻²)
E_t	Total clear-sky irradiance	(W m ⁻²)
$E_{t,b}$	Beam element	(W m ⁻²)
$E_{t,d}$	Diffuse element	(W m ⁻²)
$E_{t,r}$	Ground-reflected element	(W m ⁻²)
f	Dimensionless diffusivity tensor	(-)
G	Flow rate of water vapor	(kg s ⁻¹)
h	Capillary pressure	(m)
H	Hour angle	(-)
H_0	Molar sorption enthalpies of the monolayer	(J mol ⁻¹)
H_b	Enthalpy of bound water	(J kg ⁻¹)
$h_{c,ext}$	Convective heat exchange coefficient of the exterior surface	(W m ⁻² K ⁻¹)
$h_{c,int}$	Convective heat exchange coefficient of the interior surface	(W m ⁻² K ⁻¹)
h_m	Mass convective exchange coefficient	(m s ⁻¹)
$h_{r,int}$	Radiative heat exchange coefficient of the interior surface	(W m ⁻² K ⁻¹)
H_s	Enthalpy of water solid phase	(J kg ⁻¹)
h_v	Evaporation enthalpy of water	(J kg ⁻¹)
H_w	Enthalpy of water liquid phase	(J kg ⁻¹)
j_l	Volume flow density of moisture liquid diffusion	(m ³ m ⁻² s ⁻¹)
j_v	Mass flow density of moisture vapor diffusion	(kg m ² s ⁻¹)
j_w	Flow density of water content	(m ³ m ⁻² s ⁻¹)
k_0	Entropic adjustment factors	(-)
K_A	Partition coefficient	(-)
K_b	Boltzmann constant	(kg m ² s ⁻² K ⁻¹) (J K ⁻¹)
K_g	Adsorption constant of GAB model	(-)
K_h	Hydraulic conductivity	(m s ⁻¹)

K_p	Permeability	(m ²)
K_w	Liquid water permeability	(kg m ⁻¹ s ⁻¹ Pa ⁻¹)
L	Characteristic length	(m)
L	Latitude of the station	(-)
L	Total lumianace	(W m ⁻² sr ⁻¹)
L_v	Latent heat of evaporation	(J kg ⁻¹)
m_a	Mass of air particle	(kg)
m_B	Mass diffusion rate	(Kg s ⁻¹)
m_{rain}	Mass flux for rain	(kg m ⁻² s ⁻¹)
m_w	Mass flux for liquid water	(kg m ⁻² s ⁻¹)
N_{Ax}	Molar flux density	(mol m ⁻² s ⁻¹)
N_c	Rate of moisture molecular diffusion	(mol m ⁻² s ⁻¹)
N_K	Rate of moisture diffusion (Knüdsen effusion)	(mol m ⁻² s ⁻¹)
P	Pressure	(Pa)
p_0	Constant atmospheric air pressure	(Pa)
$P_{A\infty}$	Partial vapor pressure of fluid	(Pa)
p_c	Suction pressure	(Pa)
P_i	Predicted network output	(-)
p_l	Liquid pressure	(Pa)
p_{sat}, p_{vap}	Water vapor saturation pressure	(Pa)
q	Heat flux density	(W m ⁻²)
Q	Heat flux	(W)
Q_{air}	Energy load of air	(kg kg ⁻¹)
Q_{air}	Energy load of air	(W)
Q_{br}	Thema bridges load	(W)
Q_{rad}	Solar radiation	(W)
$Q_{rad,int}$	Internal source radiation	(W m ⁻²)
$Q_{rad,sky}$	Radiative heat transfer term	(W m ⁻²)
Q_v	Air flow rate of renewal air	(m ³ h ⁻¹)
R	Ideal gas constant	(J mol ⁻¹ K ⁻¹)

$RH_{blowing}$	Supply air relative humididty	(%)
S_{ϕ}	Source term	(W m ⁻³)
T	Temperature	(K) or (°C)
$T_{blowing}$	Supply air temperature	(K) or (°C)
T_{in}	Indoor air temperature	(K) or (°C)
T_{out}	Outdoor air temeprature	(K) or (°C)
T_{sky}	Sky temperature	(K) or (°C)
$T_{surrounding}$	Average surface temperature of all surfaces in an area	(K)
u	Relative moisture concentration	(kg kg ⁻¹)
U	Global heat transfer coefficient	(W m ⁻² K ⁻¹)
u_a	Absorption moisture content corresponding to current RH-Value	(kg kg ⁻¹)
u_{ads}	Main curves of the adsorption	(kg kg ⁻¹)
u_d	Desorption moisture content corresponding to current RH-Value	(kg kg ⁻¹)
u_{des}	Main curves of the desorption	(kg kg ⁻¹)
u_j	Linear combiner output due the input signals	
u_r	Residual moisture contents of the scanning curve	(kg kg ⁻¹)
u_s	Saturated moisture contents of the scanning curve	(kg kg ⁻¹)
V	Velocity vector	(m s ⁻¹)
v_j	Induced local field	(-)
V_w	Liquid phase velocity	(m min ⁻¹)
W	Moisture content	(m ³ m ⁻³)
W_{air}	Mean specific volume of air	(m ³ kg _{da} ⁻¹)
w	Water vapor Permeance	(kg m ⁻² s ⁻¹ Pa ⁻¹)
$w_{i,j}$	Synaptic weights of the neuron	(-)
W_r	Total of all radiative heat sources in the volume area	(W)
W_v	Vapor mass fraction	(-)
X	Mass moisture content	(Kg Kg ⁻¹)
X_0	Monolayer moisture content	(m ³ m ⁻³)
x_n	Input signal	(-)
z	Water vapor resistance.	(m ² s Pa kg ⁻¹)

Greek

α	Thermal diffusion coefficient	$(\text{m}^2 \text{s}^{-1})$
β_v	Convective mass transfer coefficient	$(\text{kg m}^{-2} \text{s}^{-1} \text{Pa}^{-1})$
Γ_ϕ	Diffusion coefficient for the standard physical parameter	$(\text{m}^2 \text{s}^{-1})$
δ	Thermogradient coefficient	(1 K^{-1})
δ_p	Water vapor permeability	$(\text{kg m}^{-1} \text{s}^{-1} \text{Pa}^{-1})$
ε_b	Volume fraction of liquid	$(-)$
ε_s	Volume fraction of solid	$(-)$
ε_v	Volume fraction of vapor	$(-)$
θ_d	Water content on the boundary drying curve at suction	$(\text{m}^3 \text{m}^{-3})$
θ_r	Residual moisture content	$(\text{m}^3 \text{m}^{-3})$
μ	Water vapor resistance factor	$(-)$
δ	Water vapor permeability	$(\text{kg m}^{-1} \text{s}^{-1} \text{Pa}^{-1})$
σ	Coefficient of solubility	$(-)$
Σ	Tilted angle	(degree)
ρ_g	Ground reflectance	$(-)$
δ	Solar declination	$(-)$
τ_b	Beam optical depths	$(-)$
τ_d	Diffuse optical depths	$(-)$
θ_z	Zenith angle	$(-)$
Ω	Solid angle	(sr)
Ψ	Coefficient of linear thermal loss	$\text{W m}^{-1} \text{K}^{-1}$
θ_s	Saturated moisture content	$(\text{m}^3 \text{m}^{-3})$
θ_u	Water content at the meeting point of the two boundary curves	$(\text{m}^3 \text{m}^{-3})$
θ_w	Water content on the boundary wetting curve at suction	$(\text{M}^3 \text{m}^{-3})$
λ	Thermal conductivity	$(\text{W m}^{-1} \text{K}^{-1})$
μ	Dynamic viscosity of liquid	(Pa s)
ξ_a	Absorption moisture capacity at the current relative humidity	(kg kg^{-1})
ξ_d	Desorption moisture at the current at the current relative humidity	(kg kg^{-1})
ξ_{hys}	Moisture capacity at hysteresis	(kg kg^{-1})

ρ	Density	(kg m ⁻³)
ρ_s	Density of water solid phase	(kg m ⁻³)
ρ_v	Density of water vapor phase	(kg m ⁻³)
ρ_w	Density of water liquid phase	(kg m ⁻³)
τ_{rm}	Moisture propagation in a capillary porous media	(s)
φ	Relative humidity	(-)
$\varphi(x)$	Activation function	(-)
ϕ	Standard physical parameter	(-)

Abbreviations

<i>AC</i>	Air-Conditioning	(-)
<i>AI</i>	Artificial intelligence	(-)
<i>ALC</i>	Algae lightened clay	(-)
<i>ANN</i>	Artificial Neural Network	(-)
<i>ASC</i>	Algae Structural Cob	(-)
<i>BES</i>	Building Energy Simulation	(-)
<i>Bi</i>	Biot number	(-)
<i>CFD</i>	Computational Fluid Dynamics	(-)
<i>CGW</i>	Coffee Ground Wastes	(-)
<i>CLC</i>	Coffee Lightning Clay	(-)
<i>CNN</i>	Convolutional Neural Network	(-)
<i>CTF</i>	Conduction transfer functions	(-)
<i>ECM</i>	Effective Capacitance Moisture	(-)
<i>EMPD</i>	Effective Moisture Penetration Depth	(-)
<i>EU</i>	European Union	(-)
<i>GAB</i>	Guggenheim-Anderson-de Boer	(-)
<i>HAM</i>	Heat, Air and Moisture	(-)
<i>HVAC</i>	Heating, Ventilation and Air-Conditioning	(-)
<i>LSTM</i>	Long Short-Term Memory	(-)
<i>Nu</i>	<i>Nusselt Number</i>	(-)
<i>PDE</i>	Partial Differential Equations	(-)

<i>Pe</i>	Peclet number	(-)
<i>Pr</i>	Prandlt number	(-)
<i>R²</i>	Coefficient of determination	(-)
<i>Re</i>	Reynolds number	(-)
<i>RH</i>	Relative Humidity	(-)
<i>RMSE</i>	Root mean square error	(-)
<i>RNN</i>	Recurrent Neural Network	(-)
<i>Sc</i>	Schmidt number	(-)
<i>SC</i>	Structural Cob	(-)
<i>Sh</i>	Sherwood number	(-)
<i>SSE</i>	Sum of Square Error	(-)
<i>SSR</i>	Sum of Squares Regression	(-)
<i>SST</i>	Sum of Squares Total	(-)

TABLE OF CONTENTS

GENERAL INTRODUCTION.....	1
GENERAL CONTEXT.....	3
MAIN OBJECTIVE OF THE THESIS	3
SYNTHESIS OF THE MANUSCRIPT	4
CHAPTER 1.....	4
CHAPTER 2.....	5
CHAPTER 3.....	6
CHAPTER 4.....	7
1. STATE OF THE ART ON THE THERMO-HYDRIC BEHAVIOR OF BUILDINGS AND THEIR ENERGY PERFORMANCE.....	8
1.1 INTRODUCTION.....	10
1.2 BACKGROUND OF BUILDING ENERGY BEHAVIOR AND PERFORMANCE	10
1.3 AIM OF THE CHAPTER	14
1.4 MAIN METHODOLOGY FOR BUILDING ENERGY SIMULATION	15
1.5 UNDERSTANDING OF HYGROTHERMAL TRANSFERS IN BUILDINGS	16
1.5.1 Characteristic of hygroscopic low carbon material.....	16
1.5.2 Heat and moisture transfer in hygroscopic material.....	18
1.5.2.1 Moisture transports in porous media.....	18
1.5.2.1.1 Vapor phase.....	19
1.5.2.1.2 Liquid phase.....	20
1.5.2.2 Thermal diffusion in porous media.....	20
1.5.2.3 Different methods for Heat, Air and Moisture (HAM) modeling	21
1.5.2.4 Mathematical models of coupled heat and moisture transfer in porous media	22
1.6 PHYSICAL MODELING.....	22
1.6.1 Nodal approach.....	23
1.6.1.1 Strength of the nodal approach	25
1.6.1.2 Weakness of the nodal approach	26
1.6.1.3 Simplified models for simulating surface moisture adsorption and desorption	26
1.6.1.3.1 Effective Moisture Penetration Depth (EMPD) model	26
1.6.1.3.2 Effective Capacitance Moisture (ECM) model.....	27
1.6.2 Computational Fluid Dynamics (CFD) approach.....	27
1.6.2.1 Strength of the CFD approach	31

1.6.2.2	Weakness of the CFD approach	34
1.6.3	Co-simulation of hygrothermal behavior modeling.....	34
1.6.4	Inputs for hygrothermal simulation tools	36
1.6.4.1	Geometry	36
1.6.4.2	Mesh generating	36
1.6.4.3	Materials properties	38
1.6.4.4	Sorption isotherm	38
1.6.4.4.1	Brunauer, Emmett, and Teller (BET) Model.....	39
1.6.4.4.2	Guggenheim-Anderson-de Boer (GAB) model	40
1.6.4.4.3	Van Genuchten model	40
1.6.4.5	Hysteresis effect.....	41
1.6.4.5.1	Mualem II model	42
1.6.4.5.2	Pedersen Model.....	43
1.6.4.5.3	Huang's hysteresis model	43
1.6.4.6	Boundary and initial conditions	43
1.6.4.6.1	Exterior environment	44
1.6.4.6.2	Interior environment	44
1.6.4.6.3	Outside Surface Heat Balance.....	44
1.6.4.6.4	Vapor and capillary balance on outdoor wall surface	45
1.6.4.6.5	Inside Surface Heat Balance.....	45
1.6.4.6.6	Vapor balance on indoor wall surface	46
1.6.4.6.7	Discussion on the physical models.....	46
1.7	STATISTICAL METHODS USING DEEP LEARNING.....	49
1.7.1	Deep Learning modeling	49
1.7.2	Artificial Neural Networks principles.....	49
1.7.3	Artificial Neural Networks architectures.....	50
1.7.3.1	Weights	50
1.7.3.2	Bias	50
1.7.3.3	Activation function $\varphi(x)$	51
1.7.4	Learning methods in Artificial Intelligence	52
1.7.4.1	Statistical comparison and error-correction	53
1.7.5	Deep Learning approach for building energy simulation.....	54
1.7.5.1	Strength and weakness of the deep learning approach.....	55
1.8	EXISTING DATA FOR VALIDATION	56
1.8.1	Analytical validation	56
1.8.2	Numerical-Numerical Validation.....	56
1.8.3	Experimental Validation.....	56

1.9	CONCLUSION OF THE CHAPTER	57
2.	BASIC NOTIONS OF HEAT AND MASS TRANSFER	60
2.1	INTRODUCTION TO THE CHAPTER.....	62
2.2	PARTIAL DIFFERENTIAL EQUATIONS TO FINITE DIFFERENCE EQUATIONS	62
2.2.1	Classification of partial differential equations.....	63
2.2.2	Boundary condition types	64
2.2.3	Heat and mass transport equations	65
2.3	MODES OF HEAT TRANSFER.....	66
2.3.1	Conductive transfer	66
2.3.1.1	One-dimensional stationary conduction, Fourier law.....	66
2.3.1.2	Analytical resolution of the one-dimensional unsteady conduction.....	67
2.3.1.2.1	Infinite plane wall with Dirichlet boundary condition.....	67
2.3.1.2.1.1	Separation of variables method	67
2.3.1.2.1.2	Laplace transformation method.....	70
2.3.1.2.2	Infinite plane wall with Neumann boundary condition	72
2.3.1.3	Numerical resolution of the one-dimensional unsteady conduction	74
2.3.1.3.1	Partial differential equations for heat transfer.....	75
2.3.1.3.2	Explicit scheme	76
2.3.1.3.3	Implicit scheme	78
2.3.1.3.4	Crank and Nicolson scheme	79
2.3.2	Convective transfer.....	80
2.3.2.1	Method of dimensionless analysis, Buckingham π theorem	81
2.3.2.2	Determination of convective exchange coefficient for a plane wall.....	84
2.3.3	Radiative transfer	86
2.3.3.1	Radiative properties of real bodies	86
2.3.3.2	Solar radiation	90
2.3.3.2.1	ASHRAE Clear sky equations for solar radiation.....	90
2.3.3.2.2	Clear-Sky Solar Radiation	91
2.3.3.2.3	Calculation of Clear-Sky Solar Irradiance Incident on receiving surface.....	94
2.4	MODES OF MASS TRANSFER	96
2.4.1	Mass diffusion	96
2.4.1.1	Fick's Law	96
2.4.1.2	Diffusion coefficient	98
2.4.1.3	Diffusion of fluids through porous media.....	99
2.4.1.4	One-dimensional stationary mass diffusion	100
2.4.1.5	One-dimensional unsteady mass diffusion.....	103

2.4.2	Mass convection	108
2.4.2.1	Dimensional analysis applied to convective mass transfer.....	108
2.5	DEVELOPED COUPLED HEAT AND MASS TRANSFER MODELS.....	109
2.5.1	Common models of coupled heat and mass transfer.....	110
2.5.1.1	Philip and De Vries model.....	110
2.5.1.2	Luikov Model.....	110
2.5.1.3	Whitaker model	111
2.5.1.4	Künzel model.....	111
2.5.1.5	Mendes model	112
2.6	CONCLUSION OF THE CHAPTER	113
3.	CHARACTERIZATION OF A NOVEL GEO-BASED MATERIAL FOR MULTILAYERED WALL AND HIGHLIGHTING OF SORPTION CURVE LINEARIZATION ON THE COUPLED HEAT AND MASS TRANSFER.....	114
3.1	INTRODUCTION TO THE CHAPTER.....	115
3.2	AIM OF THE CHAPTER	117
3.3	EXPERIMENTAL SETUP AND MATERIAL ELABORATION	117
3.3.1	Characterization techniques	118
3.3.2	Natural fiber.....	118
3.3.3	Structural earth.....	119
3.3.4	Lightened earth	120
3.3.5	Soils preparation.....	120
3.3.6	Material properties measurement	121
3.3.6.1	Water vapor permeability, porosity and vapor resistance factor	121
3.3.6.2	Thermal conductivity, heat capacity and dry density.....	122
3.3.6.3	Sorption isotherm curves.....	122
3.4	MECHANICAL AND HYGROTHERMAL PROPERTIES	123
3.4.1	Hygrothermal properties of the structural part (Structural Cob. SC)	123
3.4.2	Hygrothermal properties of the insulating part (Coffee Lightened Clay. CLC).....	124
3.4.3	Material compression strength	128
3.5	NUMERICAL SIMULATION OF HYGROTHERMAL BEHAVIOR	130
3.5.1	Geometry, boundary conditions and mesh generating.....	130
3.5.2	Mathematical modeling and sorption linearization due to hysteresis effect	133
3.5.3	Model validation of linearization effect on sorption curve with experimental data	138
3.5.3.1	Scenario 1. Temperature variation with constant humidity	139
3.5.3.2	Scenario 2. Humidity variation with constant temperature.....	141
3.5.4	Hygrothermal performance evaluation of CLC and SC wall	143

3.5.4.1	Scenario 1. Temperature variation with constant humidity	144
3.5.4.2	Scenario 2. Humidity variation with isotherm condition.....	145
3.5.4.3	Heat flow transfer through the CLC+SC wall for isotherm and isohydric scenario	147
3.6	CONCLUSION OF THE CHAPTER AND DISCUSSION	149
3.6.1	Summary of main results.....	149
3.6.2	Discussion on model limitations and perspectives.....	150
4.	A NOVEL METHODOLOGY FOR INTEGRATING ARTIFICIAL INTELLIGENCE INTO BUILDING ENERGY SIMULATION TO INVESTIGATE HYGROTHERMAL BEHAVIOR AT THE BUILDING SCALE.....	151
4.1	SUMMARY OF THE CHAPTER.....	153
4.2	INTRODUCTION TO THE CHAPTER.....	153
4.3	STUDY METHODOLOGY	156
4.4	LAB-SCALED BUILDING EARTHEN PROTOTYPE	158
4.4.1	Understanding difference between thermal and hygrothermal transfers in buildings	161
4.4.2	Basic notions of nodal approach for whole building energy simulation (BES)	162
4.4.2.1	Computing and simulation strategy of thermal method	163
4.4.2.2	Thermal simulation parameters definition	163
4.4.2.2.1	Conduction through the walls	163
4.4.2.2.2	Outside and inside surface heat balance	166
4.4.2.2.3	Sky and solar calculations.....	167
4.4.2.2.4	Shading calculations	167
4.4.2.2.5	Infiltration/ventilation.....	168
4.4.2.2.6	Zone gain heat loads	169
4.4.2.2.7	HVAC sizing simulation	169
4.4.3	Fundamentals of coupled heat and mass transfer	169
4.4.4	Deep learning modeling	170
4.4.5	Coupling method between physical models and deep learning.....	174
4.5	RESULTS AND DISCUSSIONS OF DEVELOPED APPROACH	177
4.5.1	Sensitivity analysis.....	178
4.5.2	Outputs of the standard building energy simulation (BES).....	179
4.5.3	Thermal physical model coupled with ANN (deep learning) to transform outputs into hygrothermal Data	181
4.5.4	Coupled thermal physical model with LSTM (deep learning) to transform outputs into hygrothermal Data	182
4.6	ENERGY PERFORMANCE OF STUDIED EARTHEN CONSTRUCTION BUILDING.....	184
4.6.1	Needs for air conditioning.....	184

4.6.2	Basic method for estimating the cooling loads	185
4.6.3	Ideal Air-Conditioner system pre-sizing (basic simplified method)	192
4.6.4	Energy performance of our building based on the outputs of different dynamic simulation approaches.....	194
4.7	APPLICATION OF THE NOVEL CO-SIMULATION TECHNIQUE TO A REAL BUILDING ...	199
4.7.1	Pre-processing and DATA gathering	199
4.7.2	Monitoring and analysis of building behavior	202
4.7.2.1	Instrumentation and locations	202
4.7.2.2	Energy use and internal loads.....	203
4.7.2.3	Experimental measurement data.....	205
4.7.3	Outputs of the fundamental building energy simulation (BES).....	206
4.7.4	Transformed hygrothermal data resulting from the combination of ANN model and standard BES	208
4.7.5	Transformed hygrothermal data resulting from the combination of LSTM model and standard BES	209
4.7.6	Energy performance of earthen constructed buildings based on the outputs of different dynamic simulation approaches	211
4.8	CONCLUSION OF THE CHAPTER AND DISCUSSION	215
4.8.1	Summary of main results	215
4.8.2	Discussion on building energy modeling and Deep Learning co-simulation ...	216
GENERAL CONCLUSION AND PERSPECTIVES.....		218
REFLECTION AND PERSPECTIVES ON BUILDING ENERGY SIMULATION OF HYGROTHERMAL BEHAVIOR.....		219
OPTIMIZATION OF ENERGY PERFORMANCE FOR BUILDING WITH LOW CARBON ENVELOPES		219
BENEFITS OF THE IMPLEMENTATION OF AI WITH THE BASIC PHYSICAL MODELS OF BES		220
LIMITATIONS OF IMPLEMENTATION OF AI WITH THE BASIC PHYSICAL MODELS OF BES		221
BIBLIOGRAPHY.....		222
APPENDIX		236
ACKNOWLEDGEMENT.....		237

LIST OF FIGURES

Figure 1.1 Final energy consumption by sector and use in Europe.....	11
Figure 1.2 Schematic overview of hygrothermal simulation approaches [138]	15
Figure 1.3 Different form of physical interaction between the building envelope and the heat, air and moisture [138].....	21
Figure 1.4 Detailed schematic description of the Nodal approach for hygrothermal simulation [138]	24
Figure 1.5 Detailed schematic description of the CFD approach for hygrothermal simulation [138]	29
Figure 1.6 Co-simulation simplified flowchart [138].....	37
Figure 1.7 Humidity sorption isotherm as a function of relative humidity [138]	39
Figure 1.8 Schematic representation of the intermediate variations of the hysteresis phenomenon of the sorption curves [138].....	41
Figure 1.9 Feed-Forward of Artificial Neural Network architect with a nonlinear model of a neuron [138]	51
Figure 1.10 Different activation functions of a neuron [138]	52
Figure 1.11 Different learning method of ANN [138]	53
Figure 2.1 Heat conduction in a plane wall [118]	66
Figure 2.2 Heat conduction through a multilayer wall.....	67
Figure 2.3 Infinite wall with constant surface temperature	68
Figure 2.4 Infinite wall with convective exchange on the surfaces	72
Figure 2.5 Schematic of a laminar flow	80
Figure 2.6 Schematic of a turbulent flow.....	81
Figure 2.7 Free convection at a plain vertical wall	86
Figure 2.8 Radiative behavior of a surface [120]	87
Figure 2.9 Hemispheric space [120]	88
Figure 2.10 Solar angles for vertical and horizontal surfaces [124]	94
Figure 2.11 Mass diffusion of gases [125]	96
Figure 2.12 Diffusion in a porous medium: (a) molecular diffusion, (b) straight pores, (c) tortuous pores with branching, (d) Knüdsen diffusion [126].....	99
Figure 2.13 Mass diffusion through a wall.....	100
Figure 2.14 Effect of the mass Biot number on the concentration distribution [127]	102

Figure 2.15 Analogy of electrical circuits for mass transfer with number of.....	102
Figure 2.16 Mass transfer in a plane wall	104
Figure 2.17 Semi-infinite domain of a plane wall	107
Figure 3.1 Sorption curve of Structural Cob (SC with 0 % of coffee ground wastes) [165] ..	123
Figure 3.2 (a) Thermal conductivity, (b) Porosity, (c) Density, and specific heat (d) of Coffee Lightened Clay for various amounts of CGW in CLC [165]	125
Figure 3.3 Moisture sorption isotherm curve of Coffee Lightened Clay (CLC with different portions of coffee ground wastes) [165]	126
Figure 3.4 Water vapor resistance factor of CLC samples upon CGW additions [165]	127
Figure 3.5 Permeability of CLC samples upon CGW additions [165]	127
Figure 3.6 Coffee lightened clay and Structural cob samples used for mechanical ($\varnothing 11$ cm \times 22 cm) and thermal (30 \times 30 \times 4 cm) tests [165].....	128
Figure 3.7 CLC (a) and SC (b) compression strength tests as a function of deformation [165]	129
Figure 3.8 Scheme of geometry and boundary conditions for numerical simulation [165]	131
Figure 3.9 Outdoor and indoor climatic boundary conditions for the isothermal (RH=50 %) and isohydric (T=23°C) scenario, Alioua et al [17] (Refitted from original) [165]	132
Figure 3.10 1D wall meshing along the X axis [165]	133
Figure 3.11 Water vapor sorption hysteresis phenomena behavior of Promis et al. [141]	135
Figure 3.12 Water vapor sorption hysteresis phenomena behavior of Lelievre et al [142]	135
Figure 3.13 Water vapor sorption hysteresis phenomena behavior of Maaroufi et al. [100] ..	136
Figure 3.14 Moisture sorption isotherm linearized of Date Palm Concrete (DPC) (Refitted and modified from original [17]) [165]	138
Figure 3.15 Conceptual study plan [165]	139
Figure 3.16 Numerical and experimental temperature variations at various depths within the DPC wall by taken into account the linearization of hysteresis effect [165]	140
Figure 3.17 Numerical and experimental humidity variations at various depths within the DPC wall by taken into account the linearization of hysteresis effect [165].....	142
Figure 3.18 Schematics of the multilayer wall composed of SC+CLC and the measured points [165]	143
Figure 3.19 Numerical investigation of temperature variations at various depths within the SC+CLC multilayered wall by considered the linearization of hysteresis effect [165]	144
Figure 3.20 Numerical investigation of humidity variations at various depths within the SC+CLC multilayered wall using linearization of the RH hysteresis cycle [165]	146

Figure 3.21 Moisture behavior of the interface between CLC and SC walls [165]	146
Figure 3.22 Quantitative analysis of the energy performance of multilayered wall (SC+CLC) for isotherm (a) and isohydric (b) scenarios [165].....	147
Figure 4.1 Schematic overview of hygrothermal simulation approaches.....	157
Figure 4.2 Sorption curve of the simulated materials for the structural (a) and insulating (b) wall parts [1]	159
Figure 4.3 Basic structure of lab-scale building and location of measurement points inside and outside at different positions [1]	160
Figure 4.4 Shade profile during the whole day taking into account the actual conditions in relation to the building site	168
Figure 4.5 Different forms of physical interaction between the building envelope and the heat, air and moisture [138].....	170
Figure 4.6 Simplified representation of an ANN model [138]	171
Figure 4.7 The structure of Recurrent Neural Network with hidden neurons.....	172
Figure 4.8 Single-layer LSTM network unrolled for many timesteps	173
Figure 4.9 Co-simulation between BES (Building Energy Simulation) and AI (Artificial Intelligence).....	174
Figure 4.10 Flowchart for coupling thermal physical models with deep learning	175
Figure 4.11 Boundary conditions of the simulated building	176
Figure 4.12 Lab-scale building location at the Builders engineer school	176
Figure 4.13 Indoor and outdoor real climate conditions of the building recorded in Caen town of the Normandy region (June 2022).....	177
Figure 4.14 Influence of ANN architect on RMSE of outputs.....	179
Figure 4.15 Numerical and experimental thermal simulation results of BES (TRNSYS) for temperature and relative humidity variations of inside air zone.....	180
Figure 4.16 Results of numerical and experimental hygrothermal modeling using coupled BES and ANN for temperature and relative humidity variations of inside air zone (Earthen construction building).....	182
Figure 4.17 Results of numerical and experimental hygrothermal modeling using coupled BES and LSTM for temperature and relative humidity variations of inside air zone (Earthen construction building)	183
Figure 4.18 Schematic of an ideal air conditioning system simplified for our case study	194
Figure 4.19 Hourly energy needs for cooling and dehumidification (06 - 13 June 2022).....	197
Figure 4.20 Daily energy needs for cooling and dehumidification (06 - 13 June 2022).....	198

Figure 4.21 Basic structure of a real earth building and orientation of the spaces from different sights [199] (GPS - DMS 35°28'24.3"N 5°09'49.7"E DD 35.4734028 , 5.1638)	200
Figure 4.22 Shade profile during the whole day taking into account the actual conditions in relation to the building site [199] (Latitude 35.4734028 Longitude 5.1638 Time Zone UTC+01:00 Altitude 451m Month of July)	201
Figure 4.23 Boundary conditions of the simulated building [199]	202
Figure 4.24 Measuring points of the building under investigation [199].....	202
Figure 4.25 Climatic environment of building location [199].....	205
Figure 4.26 Indoor and outdoor real climate conditions of the building recorded in Ouled Ammar region of Algeria (July 2010) [199]	206
Figure 4.27 Numerical and experimental thermal simulation results of TRNSYS for temperature and relative humidity variations of the inside air zone	207
Figure 4.28 Results of numerical and experimental hygrothermal modeling using coupled BES and ANN for temperature and relative humidity variations of the inside air zone (Earthen construction building) [199]	208
Figure 4.29 Results of numerical and experimental hygrothermal modeling using coupled BES and LSTM for temperature and relative humidity variations of the inside air zone (Earthen construction building) [199]	210
Figure 4.30 Schematic of an ideal air conditioning system simplified for our case study	212
Figure 4.31 Hourly energy needs for cooling (22 July – 28 July 2010)	213
Figure 4.32 Daily energy needs for cooling (22 – 28 July 2010)	214

LIST OF TABLES

Table 1.1 Various bio-based materials used in low-carbon buildings [138].....	17
Table 1.2 Summary of building hygrothermal simulation studies based on the Nodal approach [138]	25
Table 1.3 Summary of the commonly used software for hygrothermal simulation at building scale [138]	26
Table 1.4 Summary of the commonly used CFD software for hygrothermal simulation [138]	31
Table 1.5 Summary of building hygrothermal simulation studies based on the CFD approach [138]	32
Table 1.6 Summary of co-simulation studies on hygrothermal behavior of buildings [138]	35
Table 1.7 Main difference between CFD and Nodal approach [138].....	47
Table 1.8 Synthesis of parameters and application models for hygrothermal behavior simulation of porous media [138]	48
Table 1.9 Summary of building hygrothermal simulation studies based on the ANN approach [138]	55
Table 2.1 Approximate Extraterritorial Solar Radiation data for 21st day of Each Month	90
Table 2.2 Constants for ASHRAE equations for the 21st day of each month.....	92
Table 2.3 Different world time zones	95
Table 2.4 Summary of dimensionless numbers.....	109
Table 3.1 Physicochemical properties of coffee ground wastes [165].....	117
Table 3.2 Biochemical composition of coffee ground wastes [165].....	118
Table 3.3 Physical properties of reed and wheat straw fibers [1]	119
Table 3.4 Chemical composition of structural soil [1].....	119
Table 3.5 Chemical composition and mechanical properties of lightened earth [1].....	120
Table 3.6 Mixture proportion of the developed structural and insulating wall parts made of coffee ground wastes [165].....	121
Table 3.7 Hygrothermal properties of Structural Cob (SC 0 %) [165].....	124
Table 3.8 Hygrothermal properties of Date Palm Concrete (DPC)	137
Table 3.9 Model comparison and validation for scenario 1 [165].....	141
Table 3.10 Model comparison and validation for scenario 2 [165].....	143
Table 4.1 Mixture proportion of the developed structural and insulating wall parts made of Algae [1].....	158

Table 4.2 Hygrothermal properties on dry materials of the structural and insulation walls [1]	159
Table 4.3 Sensors technical data	161
Table 4.4 Difference between thermal and hygrothermal simulation	161
Table 4.5 RMSE between the simulated and experimental values of temperature and relative humidity for different simulation approaches	184
Table 4.6 Convective exchange coefficient considered for different situations [194]	186
Table 4.7 Thermal load by transmission through walls and windows	187
Table 4.8 Solar radiation factor “F” [195]	187
Table 4.9 Absorption coefficient for walls, roofs and windows “ α ” [195]	188
Table 4.10 Deduction factor for protected windows “ d_f ” [195]	188
Table 4.11 Hours of maximum cooling requirements in spaces with different orientations ([195] doc. AirWell)	189
Table 4.12 Solar radiation for latitude 50 of Caen city ([195] doc. AirWell)	190
Table 4.13 Thermal load from solar radiation on walls and windows	191
Table 4.14 Thermal load due to air renewal	192
Table 4.15 Thermal load due to thermal bridges	192
Table 4.16 Indoor hygrothermal comfort setpoint conditions	193
Table 4.17 Air-conditioning air blowing characteristics	193
Table 4.18 Mean Relative Error of daily energy needs (06 – 13 June 2022)	198
Table 4.19 Thermal properties on dry materials of the Ouled Ammar earth-building structural walls	199
Table 4.20 Properties of construction types of the earthen building at Ouled Ammar region	199
Table 4.21 Experimental measurements of building behavior and temperature and relative humidity data acquisition [199]	203
Table 4.22 HVAC systems used for air conditioning [199]	203
Table 4.23 Various equipment located inside the studied zone of the building [199]	204
Table 4.24 Studied zone lighting scenario [199]	204
Table 4.25 Studied zone living scenario [199]	204
Table 4.26 Windows opening and closing schedule - summer period [199]	205
Table 4.27 RMSE between the simulated and experimental values of temperature and relative humidity for different simulation approaches	211
Table 4.28 Mean Relative Error of daily energy needs for cooling (22 – 28 July 2010)	214

General introduction

Rethinking a building's complete envelope from the design phase is necessary to improve performance. It entails improvements in energy efficiency, thermal comfort, and environmental ethics beyond all else. Thermal or hydric dynamic movements between the internal and external surroundings are controlled by the envelope. In every way, the choice of materials used to construct the enclosure is crucial. Design professionals may use simulation tools to examine how various materials will affect a building's efficiency and how to determine the optimal specifications for each envelope component, such as insulation, windows, and other parts.

Every season of the year is impacted by the adoption of global urban planning and architectural models that employ pre-established materials and concepts. Although the intense use of thermo-mechanical equipment for temperature control is beneficial, it also results in excessive consumption of fossil energies, that has an adverse effect on the environment. Energy simulation enables the analysis of a building's energy system and the formulation of pertinent judgments for the application of energy-saving solutions. The building industry is among the most significant industries in terms of energy utilization, given the massive global energy consumption associated with CO₂ emissions of about billions of tons. Therefore, it is essential to make a sincere and urgent effort to cut energy spending. The development of improved computational tools for the simulation of building energy systems contributes significantly to decreasing energy consumption, lowering carbon emissions, and safeguarding the environment.

Buildings are among the industries that release the greatest greenhouse gases, and as of the turn of the millennium, this has raised serious worries for both the environment and the global economy. Once a genuine political objective had been fulfilled regarding the regulations that govern the prudent use of energy, this sector was swiftly thrust to the fore of the stage. Following that, a number of steps were put into place through the introduction of various subsequent energy rules, which never stop being revised in order to attain carbon neutrality in the different industries using pollutant energy as well as a reduction in power usage. This effort will be primarily focused on developing a method for simulating how much energy is used by buildings in a different region in this setting. Nevertheless, implementing these thermal rules in new constructions or during the renovation of existing structures may result in uninhabitable enclosed spaces with tightly sealed walls and minimal indoor air renewal. It has been established that it is feasible to use natural ventilation with smart windows that open in accordance with the interior temperature in order to preserve heat in the winter and prevent overheating in the summer. Because of this, the interchange of humidity transfers in various forms becomes more substantial than the exchange of heat, to the point that it is impossible to ignore them without incurring major inaccuracies in the numerical calculations.

Additionally, the presence of excessive moisture is generated and amplified by insufficient permeability in structures. Therefore, it is essential to take these factors into account while analyzing and designing the building envelopes in order to increase the effectiveness of energy simulations. In this situation, the inclusion of a hygrothermal model in building energy simulations enables the identification of the key variables affecting these systems' performance. Additionally, the use of low-impact materials, such as eco-materials, bio-sourced materials, and recycled materials is constrained, in particular by the total lack of databases on their fundamental characteristics and details on their long-term behavior. Aside from this information gap, the building design field lacks skills in sustainable design techniques. There is a need for trustworthy and accurate techniques, in particular, to evaluate the performance and life cycle evaluation of materials as well as the effect of building energy usage on a building's interior environmental quality.

In this situation, humidity is one of the main factors contributing to the deterioration of structures. The scientific community, which serves as an international decision-maker, has concentrated on this topic to better understand the processes connected with hygrothermal transfers at many scales, including the atmospheres of inhabited spaces, porous materials, and building envelopes. In order to overcome these energy and environmental problems. The eco-friendly communities of the planet have a dual goal: to reduce GHG emissions to the horizon until neutrality is attained, and to cut energy usage in buildings as much as feasible. The optimization of the building's features, especially the envelopes, is a key strategy for achieving these goals. The building's exterior serves as its initial point of interaction with the outer world. It is in charge of transferring mass, energy, and heat into and out of the structure. Particularly considering that building energy standards demand that generate more energy than they need. As this topic depends on the behavior of the building, its surroundings and the weather, the study of energy performance of buildings is becoming more and more interdisciplinary. However, in order to attain the necessary energy performance, the building systems have evolved in response to these needs. Buildings are becoming more impermeable, and the insulation of the walls is being strengthened. In turn, this leads to problems associated with humidity, such as the growth of mold, deterioration of the air quality, and condensation inside the facades. Therefore, the usage of highly insulated and sealed building envelopes is only conceivable with reliable simulations to comprehend, forecast, and assess their effects. The ability of the predictive algorithms to estimate how a building would behave inside is employed to estimate its performance. As a result, poor virtual application of real scenarios reduces the durability and energy performance of structures. As a result, it is now more challenging to design the energy systems of air conditioning to maintain the optimal level of climatic comfort. Hence, it is important to consider how humidity moves through the envelopes, by doing this, it will be feasible to increase the building's energy efficiency

while maintaining the necessary levels of comfort.

In light of these facts, it would appear that the use of hygroscopic materials in building envelopes is a creative and promising strategy for enhancing thermal performance, indoor air quality, energy consumption, and notably control of thermo-hydric comfort within structures. A material is classified as hygroscopic if it can absorb moisture. The materials studied are low carbon products. As a foundation for upcoming sustainable buildings, we also take into account local resources. Therefore, our goal is to evaluate the qualities of hygroscopic materials that are suggested for energy-saving and eco-friendly solutions as well as for improved performances in architectural applications such as walls, roofs, and floors.

General context

This context prompts the scientific community to reconsider the performance of the building material that forms the construction envelope in terms of energy balance and environmental effects (depletion of natural resources, energy consumption, polluting emissions, etc.). This research provides an overview of the state-of-the-art energy efficiency of various building structures. It suggests certain standards that may be used to assess and examine the capabilities of new construction materials using a number of measures. It also gives a general review of the methodologies and approaches that are now in use to evaluate the performance effects of the buildings and determine their potential for energy efficiency. Moreover, it presents the idea of "green" or "sustainable" envelopes in the context of energy-efficient buildings, as well as the precise standards that are employed to determine the performance level of these envelopes. Furthermore, it discusses the relevant difficulties and problems that must be taken into account when constructing environmentally sustainable and energy-efficient building envelope designs. In this situation, bio-based building materials that incorporate a natural waste product present an intriguing substitute for conventional building techniques. Numerous scientific investigations have been conducted on this material with the goal of analyzing its inherent properties (thermal, hydric, and mechanical capabilities), as well as its characterization at the scale of buildings. However, comprehensive modeling of heat and mass transmission within a building to better design energy systems is still in its early stages. To get accurate results for the design of actual structures, it is crucial to create numerical models that account for all factors linked to both the material characteristics and the design of building envelopes.

Main objective of the thesis

The objectives of these investigations encourage the study and creation of environmentally friendly construction solutions that are energy efficient. The labels offer a chance to comprehend

how buildings relate to one another and to the environment generally and from a systems perspective. Additionally, they serve as a foundation for the creation of energy efficiency goals and objectives, as well as benchmarks for monitoring their advancement.

On the other hand, most computation algorithms nowadays do not include physical hydrodynamic mechanisms. However, comfort in winter and summer is significantly influenced by the humidity in these materials. This is why the study attempts to use a numerical and experimental approach to understanding how hygroscopic envelopes behave in terms of thermo-hydric behavior. This will be accomplished by lab-based research based on heat and mass transport within a ventilated single-zone micrometeorological test cell in a true climatic environment. In order to evaluate a numerical tool created to predict the thermo-hydric response of hygroscopic envelopes, this study takes into account the impacts of humidity on thermal comfort and energy consumption from the perspective of buildings.

It will be of great interest to researchers investigating the behavior of hygroscopic enclosures in various climates, as well as prospective uses of the idea in future high-performance buildings intended to fulfill stringent environmental regulations. The goal is to determine if mass transfer and convective exchanges through phase change on the surface of these envelopes produce releases or absorptions of latent heat, which can contribute to either natural cooling in the summer or extra heat contribution during the heating period. The study's findings will act as a standard for professionals and architects working in the field of clean and sustainable building who seek to maximize the performance of the enclosure in the summer and winter. The present research goals address the requirement for total modeling of coupled heat and mass transport at the building and envelope scales. The "Whole Building Heat, Air, and Moisture Response" initiative came into being in this setting. The objective is to provide a comprehensive numerical tool for the design, modeling, and experimental investigation of the hygrothermal behavior of the hygroscopic envelope for real buildings. In order to convert the typical thermal simulation into hygrothermal data, the objective is to assess its potential by combining building energy simulation with Deep Learning. As a result, the four chapters below group the primary efforts completed for the PhD project.

Synthesis of the manuscript

Chapter 1.

The first chapter provides a state-of-the-art analysis of the physical processes involved in heat, air, and moisture movement in buildings. In order to increase their capacity and boost their accuracy, this involved both the creation of new models and improvements to already-existing

ones. The necessity of incorporating these models into architectural design is also discussed in this chapter, along with problems associated with their practical use. This chapter also includes some bibliographic information on the properties of porous media, numerous physical processes involving coupled transfers of mass and heat, and their modeling, as well as the key methods used in hygrothermal modeling of structures.

The chapter provides a thorough review of the primary mechanisms that transport heat and mass between interior and outdoor environments in buildings, along with information on how to model these processes analytically or numerically. Therefore, an exploratory review of the literature is conducted to provide an overview of the most recent stated strategies in order to explore these simulation approaches. Selected studies that go into considerable detail are extensively examined.

These include physical models, which concentrate on solving the modeled hygrothermal behavior of buildings numerically, and data-driven models, which use machine learning approaches to create a predictive model. The benefits of the suggested model in terms of performance and accuracy are then highlighted through a variety of comparisons and analyses.

The physical models are divided into two groups for assessment using CFD and Nodal methods in first step. These two groupings contain a variety of models, but each of them uses and applies a particular model in a specific way. Depending on the model's intended usage, this can result in a variety of results. Statistical models, on the other hand, mostly employ neural network models. They are based on data gathered through experiments/numerical or measured values. Therefore, no prior parametrization is required. The study emphasizes the requirement for a standardized hygrothermal modeling approach using hygroscopic envelopes. The choice of the most appropriate tool or model is made easier since it offers a better comprehension of hygrothermal simulation. In addition, the studies cited provide a significant contribution to the development of current and future investigations in the evaluation of the energy performance of buildings.

Chapter 2.

The second chapter will cover a description of the transfer phenomena. According to the current methods, the equations will be founded on the energy and mass conservation equations.

The various forms of transportation are explored, emphasizing any potential simplifications as well as the techniques for solving the differential equations analytically and numerically. The findings will be used to calculate the combined efficiencies of the mass and heat transfer processes as well as to assess the effects of these various factors on the system's total thermal and hydric performances. Additionally, stating the appropriate choice of boundary conditions will effectively evoke all kinds of heat and mass transport.

The current phenomenological models of combined heat, air, and moisture exchanges in building walls are also suggested. The investigated model is based on driving factors for transfer (temperature for heat transfer, humidity or water vapor pressure for moisture transfer, and total pressure for air movement) that are independent of the composition of the materials. In particular, several strategies will be followed to explore the most current and planned methods capable of duplicating the phenomena shown in actual experimental observations and solving the governing equations computationally. This solution enables multilayer walls to maintain continuity at the level of the interfaces between layers and to approach their modeling by avoiding complicated boundary requirements at the level of the contacts between layers. The key benefits of this model are its simplicity and adaptability, which enable consideration of various interface types and preliminary building design that takes into account all conceivable combinations of the many aspects that might affect performance in terms of energy efficiency.

Chapter 3.

The third chapter describes an effort to characterize the microstructural (porosity), thermo-physical (thermal conductivity and specific heat), and hydic (isotherms of adsorption and desorption, water retention, and permeability to water vapor) features of building materials. This characterization enabled an understanding of the parameters that influence the performance of building envelope frameworks. The major focus of this work was on the investigation of the relationship between humidity and hydic characteristics, such as the sorption and desorption isotherm curves, as well as the relationship between the material's thermal state and the values of thermo-physical properties, in particular the thermal conductivity and the specific heat. The research's test materials are made of earth and straw.

The energy performance of wall structures made of these materials can be measured and simulated using an attempted approach that was created for the purpose of conducting this study. Following that, a numerical analysis was conducted to investigate the energy performance of the novel walls. In addition, databases were expanded to include information on the hygrothermal characteristics of building materials. Utilizing the study's findings, creative material combinations were suggested in an effort to reduce the amount of energy used by buildings employing the developed wall. In a similar manner, by including the linearization of the sorption curve caused by the influence of hysteresis, the methodologies for modeling the thermal and hydic exchanges at the walls were improved. Applying this most recent innovative linearization technique has led to more accurate numerical outputs at the wall scale. The results of this study and those that have already been reported in the literature have been compared, and it has been determined that there are no significant differences between them.

Chapter 4.

The fourth chapter is assigned to the development of a co-simulation strategy to guarantee accurate and comprehensive building hygrothermal modeling. The co-simulation in consideration involves two models, the first is a dynamic thermal simulation of the building launched on known BES software, and the second is Deep Learning models developed using open-source artificial intelligence software. This Artificial Intelligence was trained using data from the building's dynamic simulation outputs. The effectiveness of this model has been assessed in terms of computational time and precision in reproducing the modeling outcomes in accordance with the experimental findings that are currently available in the scientific literature on the impact of temperature, humidity, and solar radiation on the quality of indoor air. Therefore, many validations against numerical and experimental data from the thesis work of Bouasria in 2022 [1] have been presented in order to demonstrate the correct operation of the AI-BES co-simulation technique. It also includes a numerical comparison of the co-outcome's simulations with those of the experiments. At the Builders-ing laboratory, the measurements were made on an experimental bench created for these purposes. Following that, a case study was conducted to examine the influence of artificial intelligence integration on the transformation of the outputs of traditional dynamic thermal simulation into hygrothermal data.

In order to anticipate the hygrothermal behavior of structures (envelope and habitation environment) as well as the energy needs, it is necessary to take into consideration the coupled heat and mass transfers in the wall while maintaining the physical aspects (geometry, thermal, hydric, etc.). In order to effectively serve the needs of the users and offer a clear interpretation of the results, this chapter discussed how to understand and respect the goals and constraints of this technique. The numerical building co-simulation technique will also be able to identify the hygrothermal behavior of different interior and outdoor scenarios. In order to lower energy expenses and increase the comfort of building occupants while lowering energy consumption and CO₂ emissions that contribute to global warming, this technique will be very helpful for decision-makers.

Chapter 1.

State of the art on the thermo-hydric behavior of buildings and their energy performance

Contents

1.1	INTRODUCTION	10
1.2	BACKGROUND OF BUILDING ENERGY BEHAVIOR AND PERFORMANCE	10
1.3	AIM OF THE CHAPTER	14
1.4	MAIN METHODOLOGY FOR BUILDING ENERGY SIMULATION	15
1.5	UNDERSTANDING OF HYGROTHERMAL TRANSFERS IN BUILDINGS	16
1.5.1	Characteristic of hygroscopic low carbon material	16
1.5.2	Heat and moisture transfer in hygroscopic material.....	18
1.5.2.1	Moisture transports in porous media	18
1.5.2.1.1	Vapor phase	19
1.5.2.1.2	Liquid phase	20
1.5.2.2	Thermal diffusion in porous media	20
1.5.2.3	Different methods for Heat, Air and Moisture (HAM) modeling	21
1.5.2.4	Mathematical models of coupled heat and moisture transfer in porous media.....	22
1.6	PHYSICAL MODELING	22
1.6.1	Nodal approach.....	23
1.6.1.1	Strength of the nodal approach.....	25
1.6.1.2	Weakness of the nodal approach	26
1.6.1.3	Simplified models for simulating surface moisture adsorption and desorption	26
1.6.1.3.1	Effective Moisture Penetration Depth (EMPD) model.....	26
1.6.1.3.2	Effective Capacitance Moisture (ECM) model.....	27
1.6.2	Computational Fluid Dynamics (CFD) approach	27
1.6.2.1	Strength of the CFD approach	31
1.6.2.2	Weakness of the CFD approach	34
1.6.3	Co-simulation of hygrothermal behavior modeling	34
1.6.4	Inputs for hygrothermal simulation tools.....	36
1.6.4.1	Geometry	36
1.6.4.2	Mesh generating	36
1.6.4.3	Materials properties	38
1.6.4.4	Sorption isotherm	38
1.6.4.4.1	Brunauer, Emmett, and Teller (BET) Model	39
1.6.4.4.2	Guggenheim-Anderson-de Boer (GAB) model	40
1.6.4.4.3	Van Genuchten model	40

1.6.4.5	Hysteresis effect	41
1.6.4.5.1	Mualem II model	42
1.6.4.5.2	Pedersen Model	43
1.6.4.5.3	Huang's hysteresis model	43
1.6.4.6	Boundary and initial conditions	43
1.6.4.6.1	Exterior environment	44
1.6.4.6.2	Interior environment	44
1.6.4.6.3	Outside Surface Heat Balance	44
1.6.4.6.4	Vapor and capillary balance on outdoor wall surface	45
1.6.4.6.5	Inside Surface Heat Balance	45
1.6.4.6.6	Vapor balance on indoor wall surface	46
1.6.4.6.7	Discussion on the physical models	46
1.7	STATISTICAL METHODS USING DEEP LEARNING	49
1.7.1	Deep Learning modeling	49
1.7.2	Artificial Neural Networks principles	49
1.7.3	Artificial Neural Networks architectures	50
1.7.3.1	Weights	50
1.7.3.2	Bias	50
1.7.3.3	Activation function $\varphi(x)$	51
1.7.4	Learning methods in Artificial Intelligence	52
1.7.4.1	Statistical comparison and error-correction	53
1.7.5	Deep Learning approach for building energy simulation	54
1.7.5.1	Strength and weakness of the deep learning approach	55
1.8	EXISTING DATA FOR VALIDATION	56
1.8.1	Analytical validation	56
1.8.2	Numerical-Numerical Validation	56
1.8.3	Experimental Validation	56
1.9	CONCLUSION OF THE CHAPTER	57

1.1 Introduction

Simulating the hygrothermal performance of hygroscopic building materials presents real issues in terms of regulations, labeling, and decision-making. There are presently no reference models for the thermo-hydric behavior of a whole structure. To present a general overview of the most current approaches described, an exploratory literature review is conducted regarding various simulation methodologies. In the literature on hygrothermal performance simulations, there are many theoretical techniques that we emphasize. Very thorough research is selected and carefully examined. The authors fully explain the most recent level of understanding of the modeling of hygrothermal phenomena. These include physical models, which concentrate on solving the modeled hygrothermal behavior of buildings numerically, and data-driven models, which use machine learning to create a prediction model. Both approaches are the subject of the study. We end with a discussion of the limitations of the two techniques, as highlighted in our literature research.

In light of this, each approach has benefits and drawbacks, depending on the application. The proper technique will be determined based on the application. In a sense, the classification of the physical models into two categories for review is done with CFD and Nodal methods. The category includes algorithms that make an effort to formulate a physical model and/or come up with a numerical solution based on various characterizations of hygrothermal behavior, including models based on heat and mass transport theories or empirical models based on engineering fundamentals. On the other hand, the primary model used for statistical models is deep learning. Using computer algorithms, machine learning models can detect complicated patterns in data. They entail the creation, testing, and assessment of mathematical models whose parameters are refined through training to forecast a desired value or reaction. This is performed with the objective of directly modeling the targeted system from its observable reactions.

The study focuses on the requirement for a consistent method of hygrothermal modeling using hygroscopic envelopes. It makes it simpler to choose the optimal method or model since it provides a clearer understanding of the hygrothermal simulation. This research also highlights how infrequently data-driven methodologies are utilized to forecast the hygrothermal activity of hygroscopic enclosures. This study indicates future research gaps that need to be solved in order to support data-driven building performance design.

1.2 Background of building energy behavior and performance

Research is heavily focused on reducing the usage of fossil energies, particularly in the building industry. In 2017, worldwide energy consumption in the building sector contributed 21% [2] of total annual final consumption, ranked after the industry and transportation sectors.

Furthermore, 9 % [2] of the energy required for ultimate consumption worldwide was lost and never utilized. Buildings have become more energy-intensive as a result, which has increased electricity output and, therefore, CO₂ emissions during the previous few decades.

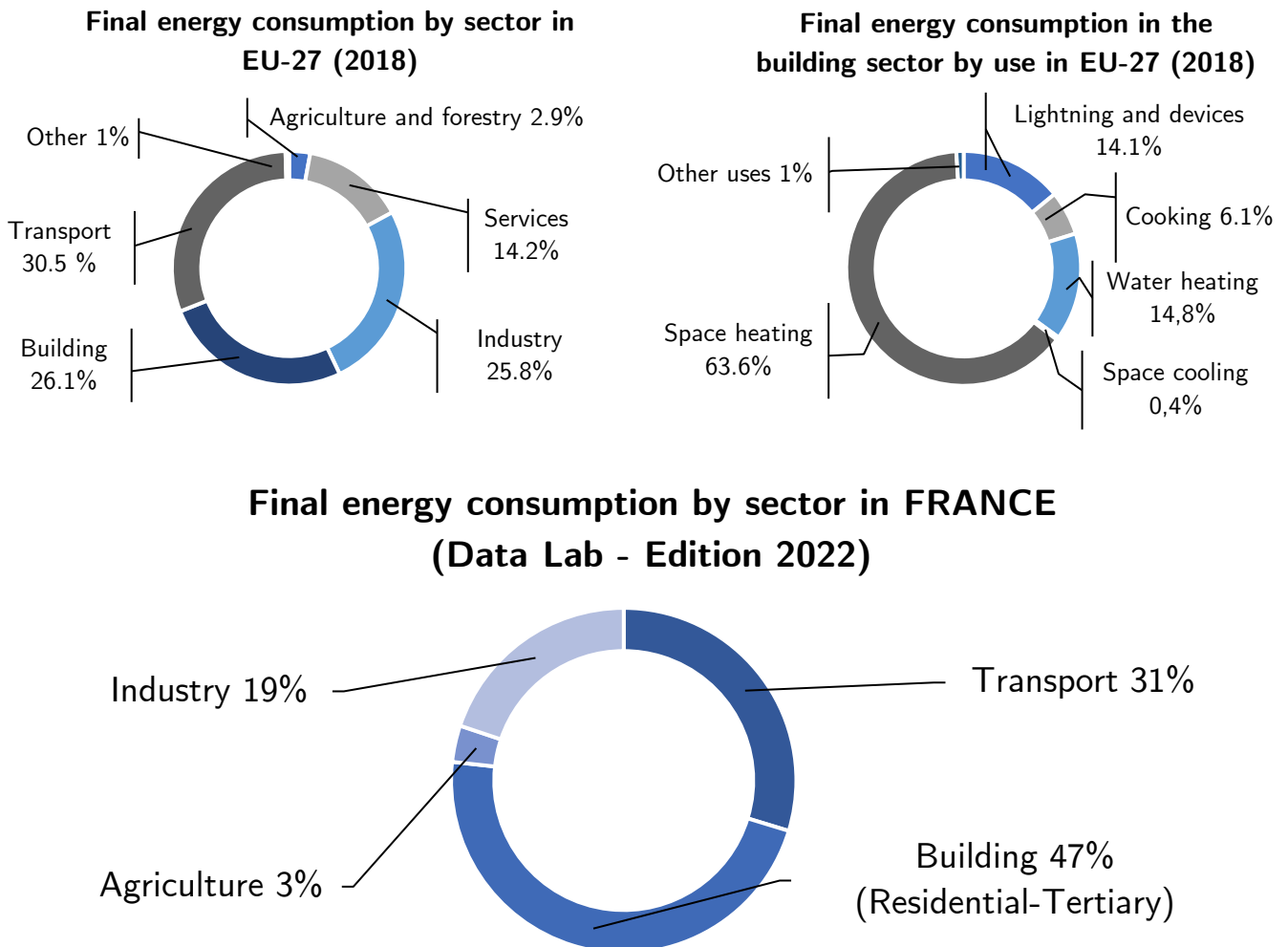


Figure 1.1 Final energy consumption by sector and use in Europe (Eurostat EU-27, 2018) and in France (Data Lab - Edition 2022)

www.statistiques.developpement-durable.gouv.fr

Global climate policy has started to drastically alter over the past three decades, particularly after the United Nations' release of Our Common Future [3], often referred to as the Brundtland Report, in 1987. The last one emphasizes a sustainable development approach that safeguards the ecology and climate while also integrating global environmental and development issues into the official concerns of all nations throughout the world. As a result, the United Nations Framework Convention on Climatic Changes (UNFCCC) [4] was established in 1992 to address the key issues threatening both the global climate and economic development, particularly in fields involving buildings that require a significant amount of energy.

Thus, several efforts have been undertaken at the national and international levels, even in Europe, to maintain ecosystem sustainability and balance in order to make them durable and effective. Nevertheless, a number of international conventions and protocols' nomenclatures have been developed to classify these initiatives, such as the Montréal and Kyoto Protocols, which were established in 1987 [5] and 1997 [6], respectively, and the Paris Agreement, which went into effect in 2016 [7]. One of their objectives is to maintain greenhouse gas emissions at a level that ensures biodiversity and enables the ecosystem to react to climatic changes in a typical way. There are now a number of new trends being implemented to lower high greenhouse gas emissions and decrease energy usage, particularly in the building sector, which consumes up to 26.1 % of the energy used in the European Union, making it the second-largest energy user [8]. To be more specific, as shown in **Figure 1.1**, the residential building sector's total energy consumption accounts for space heating only at a percentage of roughly 63.6 % [9].

Therefore, two major trends have emerged recently to counter both increases in energy consumption and greenhouse gas emissions. Improving the insulating material performance of the building envelope to lower energy consumption and developing new low carbon materials to limit carbon dioxide footprints. Alternative materials can be used to accompany and accomplish such motivations. Alternative materials include rammed earth and straw, which are frequently referred to as porous materials, as well as aerated concrete [10], [11], hemp concrete [12]–[16], and bio-based material [17], [18]. The fundamental benefit of such porous materials is their reduced heat conductivity when compared to denser concrete, which is directly related to the utilization of natural fibers and the presence of air. However, porousness typically coincides with a decline in mechanical strength, therefore it is important to strike a proper compromise between mechanical and thermal aspects. Due to their larger porosity and tortuosity when this mechanical-thermal equilibrium is achieved, buildings have the ability to trap moisture and possibly release it depending on the weather and outside circumstances. These later actions must be taken into consideration since they may also have an impact on the calculations and simulations of the total energy requirements of the building [19].

Considering rules and labeling as well as decision-making, the dynamic energy modeling of this form of building construction is a critical concern (implementation, materials choice, architectural design, retrofit, etc.). As of right now, there is no reference modeling available for this envelope type's transient hygrothermal behavior.

Additionally, there is currently no model that accounts for the manner in which coupled heat and mass transfer occurrences affect this type of building construction's overall energy performance. The need for modeling techniques to estimate coupled heat and moisture fluxes of building materials and envelopes has increased during the past several decades [20].

It would also be highly beneficial to assess the hygrothermal capabilities of more environmentally friendly hygroscopic materials, as well as the influence of various climatic conditions on suitable low-carbon structures. Two of the numerous numerical simulation techniques used in the building projects to determine the energy balance requirements are building energy simulation (BES) and computational fluid dynamics (CFD). The BES technique uses a single mass model to estimate physical parameters at a single node. Since the contour of those parameters are homogeneous throughout the region, it is possible to undertake a long-term unsteady analysis. The BES technique can be paired with the CFD approach, which, on the other hand, concentrates on numerically meshing the whole building volume into individual fragments or volumes. This leads to a high processing workload, especially for transient state simulations. Therefore, it takes a lot of work to estimate potential future enhancements in the building industry utilizing various models and methodologies.

These need for energy calculations that integrate effective computing techniques into building modeling tools while accounting for oddities such the coupled heat and moisture transport through the envelope. As a result, according to the usage scenarios, scientists and engineers employ a broad variety of simulation approaches [21]–[25]. For the purpose of enhancing and assessing energy performance, an accurate hygrothermal model is required. Actually, there are two distinct categories of models.

- Physical models that are based on energy balance equations and physical information about the system. Software supporting energy simulation, such as TRNSYS, EnergyPlus, WUFI, and COMSOL Multiphysics, is frequently used to determine them.
- Statistical models devoid of physics-based concepts, using mainly observed input/output data and statistical estimation techniques, notably Artificial Intelligence (AI).

Each method, however, has benefits and disadvantages of its own. A comparison study between these several models was developed by Benzaama et al. [26]. Their findings are.

- For physical models like TRNSYS tools. (i) these models frequently need a significant amount of setup and processing time. (ii) include several inputs into the model's definition, such as the set of building wall properties. In certain experiments, recovering this input is challenging, if not impossible.
- Thermal performance estimates based on readily available data, preferably big datasets, using genetic and machine learning approaches are required for statistical models as ANN or LSTM.

It is challenging to comprehend the physical phenomena that these models represent after computations, because the hygrothermal behavior varies in relation to meteorological factors, occupant behavior, and set-point temperature and humidity.

1.3 Aim of the chapter

Many modeling methods that analyze the energy dynamics of buildings [27], [28], do not account for moisture migration through the walls. Understanding that heat and moisture transmission can occur simultaneously and related [29], [30]. The behavior of walls as well as the temperature and humidity of the interior air can be directly impacted by thermal and moisture gradients. To the researcher's best knowledge, there are a lack of a published evaluation of the hygrothermal models used for bio-based materials, and the simulation models for buildings described in the literature are too basic to be utilized for a thorough investigation of thermal comfort.

In order to replicate the actual hygrothermal behavior of bio-based buildings for various climates, taking into consideration the residents and the HVAC (Heating, Ventilation, and Air-Conditioning) systems, these fundamental obstacles need to be overcome. This research seeks to discuss the existing approach for modelling the hygrothermal behavior of structures made of bio-based materials. The main goals of this investigation are.

- To explore investigations on hygroscopic envelopes' hygrothermal performance.
- To describe the method for combining heat and mass transfer and to explain their relationship.
- To explore any methodological differences that could account for unexpected results from various hygrothermal models.
- To demonstrate the effectiveness of hygroscopic envelopes studied by hygrothermal simulations in the literature.
- To outline the mathematical and physical models that were employed in the hygrothermal simulation.
- To compile a list of the computer programs that can model heat and moisture transport inside a building.
- To show how to include mass transfer into tools for dynamic thermal modeling.

The goal of the current research is to demonstrate this knowledge gap and the hygrothermal models applied up to this point at various scales. Therefore, the physical techniques utilized to simulate the hygrothermal behavior of the enclosures will be discussed. This will be accomplished by illustrating their applicability and viability using these models for various enclosure configuration choices.

The next subsection provides an explanation of the computational methods. In order to replicate temperature and humidity profiles at various building sizes and different periods, we will then go through some of the machine learning approaches that are frequently used to construct a prediction model from relevant data.

1.4 Main methodology for building energy simulation

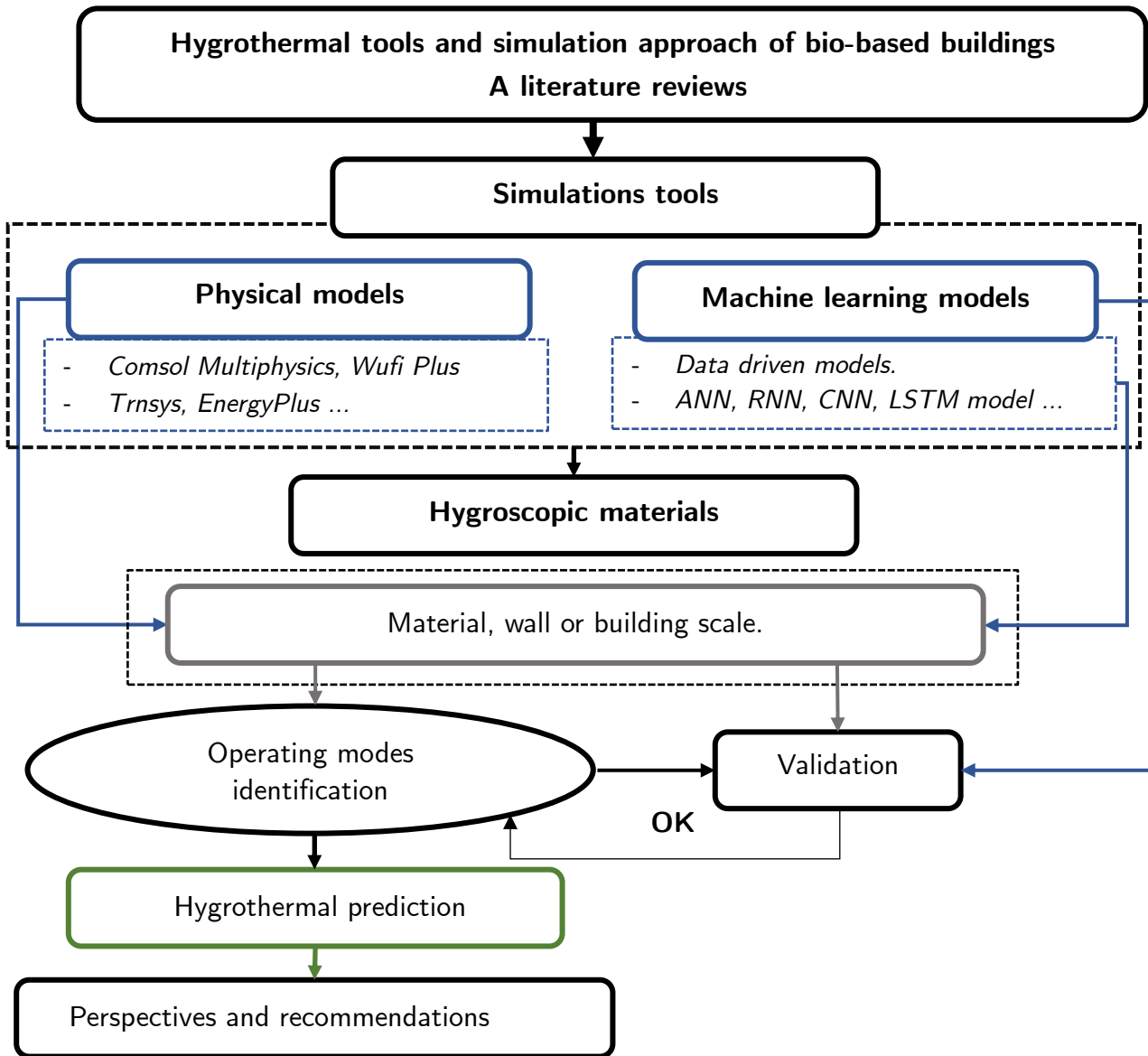


Figure 1.2 Schematic overview of hygrothermal simulation approaches [138]

After reviewing the pertinent existing literature, we generated a conceptual framework that integrates and describes our study process. As mentioned in more level of detail in the subsequent subsections, we split our working strategy into three primary stages (Figure 1.2), each of which is made up of a number of procedures.

- Stage one - Understanding the hygrothermal transfer in buildings, with an emphasis on the hygroscopic materials utilized in the literature and the underlying physical principles.
- Stage two - Outlining each method's benefits and drawbacks while presenting the physical models that were employed in the literature.
- Stage three - An explanation of Deep learning models and how they are used to construct studies of hygrothermal behavior.

1.5 Understanding of hygrothermal transfers in buildings

Nonlinear dynamics are highly attached to the heat and moisture transports in permeable building materials and envelopes. It is challenging to develop precise models for coupled heat and moisture movement in hygroscopic materials [31]. Therefore, it is essential to comprehend the building materials that facilitate heat and moisture transmissions, as well as the general principles and fundamental underlying processes, before delving further into the coupling of the two behaviors.

1.5.1 Characteristic of hygroscopic low carbon material

Low-carbon construction materials are produced using bio-based or straw/rammed earth components. They can be thought of as mixtures of sizable amounts of dense-carbon ingredients and waste from industry [32], which significantly help with carbon storage and environmental sustainability. Governments and public institutions promote their usage in newly constructed and renovated infrastructures and buildings. Thus, a special class of building materials has been created for the construction industry that uses natural fibers to generate massive porous structure and, in consequence, greatly reduce heat conductivity [33]. Bio-based materials can include, among others, wood, rape, straw, hemp, flax stems, cork, and rice husk [34]. On the other hand, straw and rammed earth materials are made from raw soil or dried stones, which are natural resources. These materials are used in the building sector for framing, insulation, supporting composite constructions, and binders. They are available in a number of forms, including panels, beams, bricks, rolls, bulk, and vegetative concrete blocks. Eventually, they are also blended with industrial materials. According to their resource type and functionalization, examples of hygroscopic materials from earlier studies can be categorized (**Table 1.1**).

For hundreds of years, raw/rammed earth components have been employed to construct buildings [35]. Their ability to effectively address rehabilitative requirements, improve energy efficiency, and increase interior comfort are just a few benefits of using them. For a variety of construction styles, raw earth may be utilized as a filler material such as cob, straw earth, and woodchip earth, as well as a building material as bauge and smashed earth brick [36]. Additionally, they can be utilized as a coating for a foundation. According to their thermal dephasing and buffering capabilities, bio-based/raw-earth materials have been widely employed in building construction because they behave well in case of thermal insulation and hygrometric comfort.

They are often categorized as hygroscopic materials [37] and as permeable mediums because of their accessibility to water liquid and vapor diffusion. These materials can, however, regain moisture, which can change their physical characteristics, notably their mechanical, thermal, and hydric parameters. For instance, moisture absorption decreases the thermal resistance of insulating elements, which causes a rise in heating energy demand [38], [39].

Table 1.1 Various bio-based materials used in low-carbon buildings [138]

Study	Building components	Wall Thickness (mm)	Material type	Type of use
Zhang et al. [40]	Magnesium phosphate cement (MPC) and corn stalk (CS)	30 – 35	Bio-composites	Structural Wall
Reuge et al. [41]	Lime-hemp render / panel made of hemp shiv and an organic binder / hemp flax and cotton / compressed straw / clay-hemp plaster	340	Bio-composites	Insulation Wall
Bagarić et al. [42]	Recycled aggregate concrete / Glass wool thermal insulation	420	Low carbon	Structural & insulation wall
Dong et al. [43]	Exterior coating / Wood fiberboard / Oriented Strand board Panel	80 – 177	Bio-based	Structural wall
Alioua et al. [17]	Date palm concrete (DPC)	150	Bio-composites	Structural wall
Tadeu et al. [44]	ICB (insulation cork board) / OSB (Oriented strand board) / Mortar/ concrete	78 – 255	Bio-composites	Structural & insulation wall
Moujalled et al. [15]	Hemp concrete / Lime-sand plaster	330	Bio-composites	Structural wall
Colinart et al. [14]	Hemp concrete coated with lime-based plasters	76	Bio-composites	Structural wall
Hou et al. [45]	Hollow concrete filled with compressed straw bricks	260	Bio-composites	Structural wall

Therefore, it is essential to prevent the formation of undesirable uncontrollable mechanisms that might influence the materials. Choosing the appropriate use and approach to restoration and intervention requires studying the deterioration pathologies [46], [47].

The physic-chemical content of materials (microstructural characteristics) and their exposure to environmental processes are both considered to be internal and external reasons for material deterioration. Commonly, freeze-thaw cycles and their corresponding gradients, moisture, temperature, pollutants, and contaminants are the major factors in building material damage [48]. One of the primary external variables that contribute to building damage is rising damp [49], which includes major degradation processes, particularly in historical buildings [50], [51], through humidity and air pollution impacts on limestone degradation in ancient buildings [52], [53]. Another important aspect of deterioration events is the climate, additionally, it has an impact on how often freeze-thaw cycles occur and creates a mechanical stress that weakens building stone surfaces, causing the building surface to deteriorate [54]. Understanding material degradation characteristics, such as moisture buffering, is crucial if one wants to accurately estimate the hygrothermal performance of a structure and avoid using the wrong energy balance modeling, which includes combined heat and moisture transfer at all building dimensions.

1.5.2 Heat and moisture transfer in hygroscopic material

1.5.2.1 Moisture transports in porous media

Water transfers are referred to as moisture in both the liquid and vapor forms. Each phase's (liquid and vapor) motion is caused by a different set of mechanics, which together regulate the humidity distribution in hygroscopic material [55]. Any one of these mechanisms will have a different impact on the quantity of water that is fixed inside or on the surface of a material depending on the structure's qualities, including its porosity, the constitution of its pores, the state of its pore system, and the environment it is subjected to. The transfer processes between these two forms of water vary [56]. The most important moisture binding mechanisms are either the surface adsorption of pre-existing moisture in the surrounding air or capillary condensation inside the materials [24]. Adsorption and capillary condensation can both happen at the same time in a certain hygroscopic environment and porous medium.

As the relative humidity begins to increase in comparison to the initial state of the porous material at a constant temperature value (isothermal condition), for instance, we can observe that the material starts to accumulate weight and adsorb the water that is present in the air [57]. This can be explained by the effect of intermolecular Van der Waals forces on the water molecules, which leads to the phenomena previously mentioned [58].

Often, the optimum water content that can be attained is significantly less than the total water content that can be obtained with full saturation. According to the Langmuir hypothesis, mono-molecular adsorption takes place at low relative humidity margins, often less than 20 %, and results in the retention of a single layer of water molecules on the surfaces of the pores [59]. Multi-molecular adsorption, which is described as the fixing of many layers on the initial layer (BET theory), happens when the relative humidity is over 50 % [60].

Multi-molecular layers that build within the pores may have the ability to merge for minuscule appropriate pore diameters and relative humidity levels more than 50 %. At this point, a capillary splits the liquid phase from the gaseous form to create a liquid bridge. In the pores of the hygroscopic substance, capillary condensation occurs when the relative humidity is less than 100 % and the equilibrium between a liquid phase and a vapor phase is reached. For this reason, the vapor and liquid phases are described as follows.

1.5.2.1.1 Vapor phase

The chance of water molecule collisions in the interior surfaces of the hygroscopic material is higher in big holes than in tiny pores, which is interesting to notice when considering moisture transfer under the phase vapor [61]–[63]. This occurs since shock against other molecules is considerably less than shock against solid objects. In this case, the mean free path of the water vapor molecule indicates the actual displacement traveled by the water pathetically small substance between two molecular collisions [64]. Based on pore size and molecule density, two scenarios may be formed.

First, vapor transmission in pores with a size bigger than that of the mean free path can be described using molecular diffusion. The second phenomenon is known as the Knüdsen effusion [65], which is the passage of vapor via pores whose radius is lower than the mean free path. When the pore size is greater than the mean free path, Fick's law (1855) may be used to explain the molecular diffusion phenomenon. According to the ideal gas and constant total pressure hypothesis.

$$N_c = -D_c \nabla C_v \quad 1.1$$

D_c is the molecular diffusion coefficient related to the mean free path, C_v is the molar concentration of vapor, and N_c is the rate of molecular moisture diffusion.

The Knüdsen effusion phenomenon happens at pores with a dimension smaller than the mean free path for the same reasons as molecular diffusion. As a result, the contacts between molecules diminish, and collisions impact their movement. In this instance, the pore radius determines the diffusion coefficient instead of the mean free direction.

$$N_K = -D_K \nabla C_v \quad \text{and} \quad D_K = \frac{d}{3} \sqrt{\frac{8K_b T}{\pi m_a}} \quad 1.2$$

In this equation, N_K stands for the rate of moisture diffusion, D_K for the Knüdsen diffusion coefficient proportional to the size of the pores, C_v for the molar concentration of vapor, d for the pore diameter, K_b for the Boltzmann constant, T for the gas's absolute temperature, and m_a for the mass of the air particle.

1.5.2.1.2 Liquid phase

Moisture transfer by the liquid phase [16], [30], [44], is operated either by the forces due to capillary pressure gradients during the adsorption or desorption processes, or by gravity forces [24]. However, it is often transported in the decreased pressure direction. Therefore, by neglecting the gravity forces, the Darcy's law can describe the liquid flux density.

$$j_l = -\frac{k_p}{\mu} \nabla P_l \quad 1.3$$

Where j_l is the volume flow density of moisture liquid diffusion, K_p is the permeability, μ is the dynamic viscosity of liquid and p_l is the liquid pressure.

With $P_c = P_l - P_0$, and according to the law of Laplace, where P_c is the suction pressure and P_0 is the atmospheric air pressure, the equation above can be written as a function of moisture water content,

$$j_w = -D_w \nabla W \quad 1.4$$

Where j_w is the flow density of water content, D_w is the moisture water diffusion coefficient and W is the moisture water content.

1.5.2.2 Thermal diffusion in porous media

Heat transfer can be described as a change in the enthalpy of a material caused by a change in temperature. This variation is often due to a number of reasons. First, the heat flux density gradient is directly proportional to the temperature gradient, as defined by Fourier's law, and to the conductivity of the material. Second, the heat flux gradient can also be transported by the moisture flux, defined as a source term in the general heat equation [31]. When working with continuous media, this phenomenon is often neglected.

But it can be considered when working with porous media by including it as a source term when dealing with hygroscopic materials that are permeable to moisture adsorption. As a result, the heat transfer equation is as follows.

$$\rho c_p \frac{\partial T}{\partial t} = \nabla(\lambda \nabla T) + \nabla(L_v \nabla j_v) \tag{1.5}$$

Where ρ is the density of material, c_p is the specific heat of the dry material, λ is the thermal conductivity of material, L_v is the latent heat of evaporation and j_v is the mass flow density of moisture vapor diffusion. In the general form of the heat transport equation for porous media, only the energy of the vapor phase change is considered, with liquid diffusion being neglected.

1.5.2.3 Different methods for Heat, Air and Moisture (HAM) modeling

Energy and mass conservation transport equations can be used to explain heat and mass transfers through building envelopes. Heat flux by conduction, convection, and radiation are quantified in energy balance equations [66]. In mass balance calculations, vapor diffusion, moisture convection, and liquid transfer are all taken into account as methods for transporting moisture, although air-moisture convection can also be entrained by mechanical forced or natural airflows [67].

Any analysis of the hygrothermal balance of a building's whole envelope must bear in mind the interrelationship of these phenomena, known as the Heat, Air, and Moisture transfer phenomenon (HAM) [68]. The interactions between the different elements of the building's interior environment and envelope are shown physically in **Figure 1.3**.

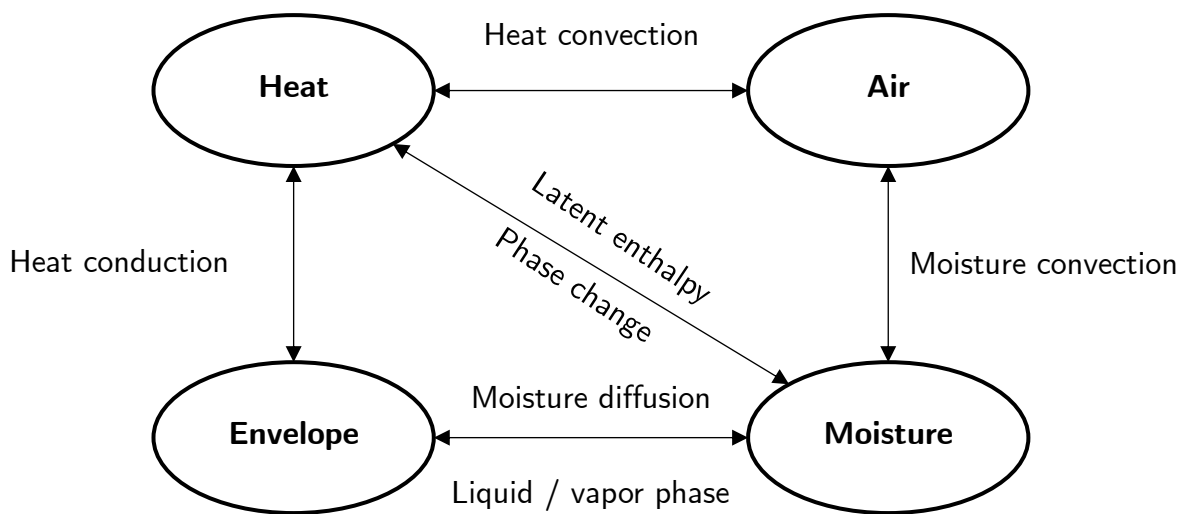


Figure 1.3 Different form of physical interaction between the building envelope and the heat, air and moisture [138]

In the literature, there are several computer-based techniques for estimating building hygrothermal behavior. Concerning the fundamental mathematical and physical explanations, these models present in significant amounts of sophistication. The degrees in which the model takes into account the following parameters determines how complicated the model is, physical model regime (steady-state, quasi-static, or dynamic), knowledge and accessibility of many details, such as material qualities, temperature, building size, and climate conditions.

Dimensions of heat and moisture transports (1D, 2D, or 3D). All of the hygrothermal modeling tools that will be covered in the next sections of this study rely on various techniques, including physical and mathematical computational approaches. To numerically solve the physical issue, they can employ the finite difference, finite volume, or finite element methods. The study also includes the statistical approach known as the Artificial Intelligence (AI) approach, which is based on deep learning techniques.

1.5.2.4 Mathematical models of coupled heat and moisture transfer in porous media

Models for heat and moisture transport are developed using the laws of mass and energy conservation. The driving forces for moisture flow are shared by all hygrothermal theories for porous building walls and materials.

Current hygrothermal models incorporate a variety of moisture-related driving factors, including moisture content, capillary pressure, partial water vapor pressure, relative humidity, and air moisture content. The most popular models of coupled heat and mass transfer are displayed in the section (2.5.1) at the page (110).

1.6 Physical modeling

Current simulation methods for estimating the energy behavior of buildings are based on physical theories that do not adequately account for all real settings and circumstances. Few building simulation tools explicitly describe the envelope [24], [69], and state whether or not the entire hygrothermal load from the interior and outside has been taken into account. This is because the bulk of the existing simulation software considers this factor to be less important.

While it is challenging to take into account the entire heat, air, and moisture equilibrium model in order to illustrate the interrelationship between all scales, particularly within the inside of the building, its enclosure, and the external climate conditions, where the interior relative humidity is mostly kept manifesting freely and without supervision. However, it's crucial to understand that the air pressure gradients between the building's interior and outside lead to air circulation, which has a significant impact on how the structure responds in terms of heat, air, and moisture transmission.

As a result, moisture buffering significantly affects indoor water vapor pressure variations as compared to outside [70]. The performance of the building envelope as well as energy consumption may be significantly impacted by rain absorption and moisture formation inside the envelope [29]. If the indoor relative humidity is not adequately controlled, it can have an important impact on the intended quality of the interior environment and increase the risk of poor air quality.

1.6.1 Nodal approach

The nodal method is founded on the idea that every construction zone is a single volume that can be described as a group of physical variables in a homogeneous state. The basic representations of a node are a room, floor, or hallway, but it is possible for it to also represent something more sophisticated, such as internal load, which includes heat generated by occupants, equipment, or HVAC systems. As a result, each zone has its own unique set of physical characteristics, such as pressure, humidity, and temperature. The heat and moisture balance equations may be solved using a matrix computing technique for each node of the entire building volume.

The most popular Building Energy Simulation (BES) software, including TRNSYS and EnergyPlus, uses the nodal technique, a one-dimensional method. Adsorption of rain and moisture buildup inside the building walls can severely influence both energy use and envelope performance. **Table 1.2** provides an overview of prior research that used the nodal approach, and **Figure 1.4** provides a detailed description of the nodal approach computing technique for hygrothermal modeling.

In their study, Coelho et al. [35] included all the complicated geometry, involving windows and doors, and categorized them according to their orientation. They determined that the best match was reached by the weather file of temperature and water-vapor pressure gathered from the monitoring campaign and the employment of weather files from the same city did not produce the best outcomes. The WUFI Plus program they used to generate their numerical calculations was strongly validated by experiments.

Additionally, Moujalled et al. [15] study concentrated on a numerical evaluation of a building's hygrothermal performance at two scales: wall and envelope. Finding more accurate thermal and hydric performance of hemp lime concrete beneath realistic environmental conditions was their main goal. They were able to get a strong validation of the numerical results in comparison to experiments through deploying the WUFI Pro program as a simulation tool.

In order to investigate moisture-safe attic construction for extremely cold regions, Wang et al. [71] adopted a nodal technique for their hygrothermal simulations. They demonstrate that the hygrothermal conditions of the unventilated attic chamber are significantly influenced by the interior moisture load levels. Therefore, the moisture-safe conditions in an unventilated attic can be maintained when the interior moisture level is maintained regularly, and the ceiling air leakage penetration rate is maintained below 20 %. They carried out their simulation using WUFI Plus, and the numerical results were effectively verified using experimental data in their study.

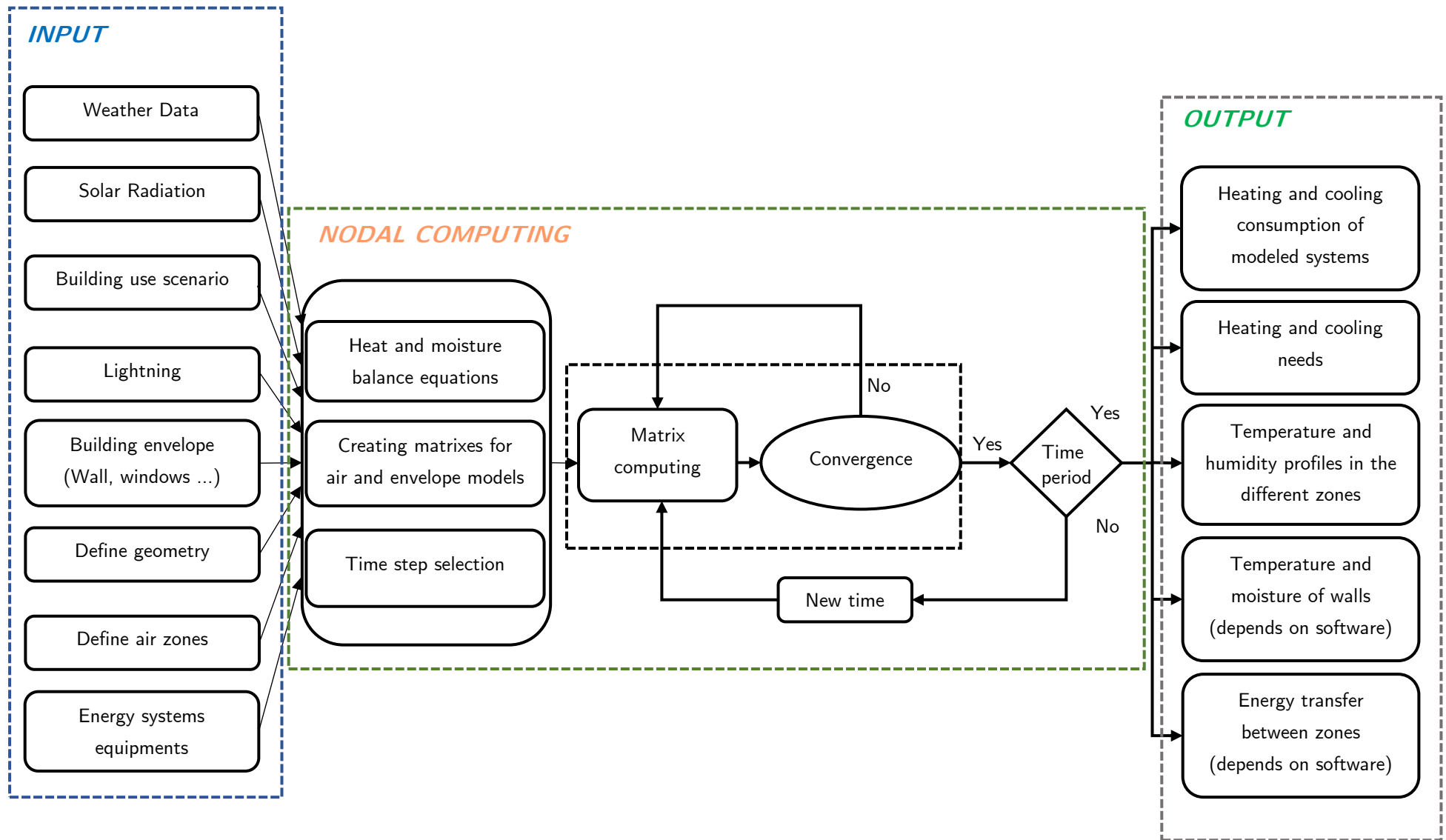


Figure 1.4 Detailed schematic description of the Nodal approach for hygrothermal simulation [138]

Table 1.2 Summary of building hygrothermal simulation studies based on the Nodal approach [138]

Study	Nodal Approach	Building scale		Software and models
		Wall	Envelope	
Coelho et al. [35]	✓	x	✓	Wufi Plus. Coupled heat and moisture transfer of Künzel Model. All complex geometry (Windows, doors) were regrouped based on the orientation.
Moujalled et al. [15]	✓	✓	✓	Wufi Pro 5.1 & Matlab. 1D simulation at the wall scale with a coupled heat and moisture transfer inside building walls / Thermography analysis for thermal leaks.
Wang et al. [71]	✓	x	✓	Wufi Plus. Attic zonal model/ Indoor zonal model / Zonal modeling of the HAM building behavior.

1.6.1.1 Strength of the nodal approach

These simulations use zone-to-zone continuity equations as their foundation. In addition to being technically simpler to resolve than finite volume/element modeling, they are also easier to utilize because no detailed meshing is needed. They require less computations, thus their processing time is faster. They permit the measurement of air flows between zones, air heat balance, humidity, and temperature, as well as fluctuations in each. According to the literature, nodal whole-building energy/hygrothermal simulations are most frequently performed using the four software programs listed in **Table 1.3**.

They all explain the dynamic changing of interior relative humidity and temperature as a consequence of varying outer weather and hygrothermal loads, as well as the impact of moisture buffering by internal condition charges. They are utilized to offer physical solutions to a range of issues and applications. Large-scale modeling of temperature oscillations and energy requirements in precise areas are the major usage for building energy simulation software notably TRNSYS and EnergyPlus [72]. Therefore, moisture interchange models at the wall scale are implemented in such programs using a simplified model that ignores the full coupling of heat and moisture movement mechanisms inside the building envelope [73], [74].

Currently, there are alternative software programs, such as SPARK and WUFI Plus [69], [75], which are developed from fundamental theoretical models of coupled heat and moisture transfer at both wall and building scales, that provide whole building heat air and moisture (HAM) simulation.

Table 1.3 Summary of the commonly used software for hygrothermal simulation at building scale [138]

Software	Availability	Model type	HAM model	Numerical scheme	Scale
TRNSYS [27]	Commercial	1D	Simplified (EMPD)	Dynamic	Envelope
EnergyPlus [76]	Open Source	1D	Full model Simplified (EMPD)	Dynamic	Envelope
WUFI Plus [75]	Commercial	1D	Full model	Dynamic	Envelope Wall
SPARK	Open Source	1D	Full model	Dynamic	Envelope

These two last mentioned techniques have the ability to properly define heat transfer and moisture diffusion inside the layers of the building walls, allowing for an exact description of the exchange of water vapor between the room air and the defined walls.

1.6.1.2 Weakness of the nodal approach

For various applications, it's important to have a complete comprehension of the local air quality and envelope design in order to evaluate the local thermal comfort standards and the range of hydric comfort. This approach is not applicable to a 1D simplified heat and moisture model for the air volume. When a specific area is required for heat and moisture exchanges in the air or even at the wall scale, computational fluid dynamics (CFD) can assist in obtaining an accurate prediction. Below is a list of certain limits:

- The nodal method clearly fails to account for some physical development, including changes in temperature, pressure, and velocity scalars inside a space.
- It is challenging to conduct a thorough investigation of the air quality and thermal comfort inside a zone.
- Their interior atmosphere's response to loads, such as heat loss from as solar patch, is not taken into account [77].
- A Temperature profile based on the length or width of the space is difficult.
- Applying the nodal technique to a large room volume (such as a hall) is complicated.

1.6.1.3 Simplified models for simulating surface moisture adsorption and desorption

1.6.1.3.1 Effective Moisture Penetration Depth (EMPD) model

The EMPD model uses a compacted combined solution to describe the adsorption and desorption of surface moisture [78]. The sorption-active layer or humidity buffer is the thin layer that faces

the inner or outer surface and interacts with the air. This implies that walls, particularly those that are exposed to the environment, are undervalued for water vapor adsorption and desorption between the interior and the outside [12], [63]. The thin layer accumulates and releases moisture into the surrounding air when subjected to periodic air humidity variations. Although that layer's temperature and vapor pressure variations should be linear, which is not always the case. As a result, the effective moisture penetration depth (EMPD) and frequency of ordinary vapor pressure changes at the wall surface, both affect how thick the sorption-active layer is.

The effective penetration depth for moisture transmission in porous construction materials for daily changes is typically in the range of millimeters. Only fluctuations in moisture with a single cycle, such daily variations, may be accurately specified and represented since moisture adsorption in this model is expressed by a single active sorption layer. The EMPD approach was further improved in the TRNSYS [73] and EnergyPlus [74] algorithms to solve this limitation by defining the moisture buffering as convective mass exchange with the surface layer of the walls and mass diffusion at a deep layer of a few millimeters. Employing this resolution approach, short-term exchanges between the air and the surface buffer and mid-term transfers using the deeper buffer can be predicted.

1.6.1.3.2 Effective Capacitance Moisture (ECM) model

The earlier EMPD technique is further optimized by assuming that the temperature and humidity characteristics in the moisture-buffering layer are identical to those in the room air. As a consequence, a single moisture capacity for the total room volume is created by combining the moisture capabilities of the room air, walls, and furniture [79]. This simplest approach is employed by certain building energy modeling tools as a successful capacitance moisture model.

1.6.2 Computational Fluid Dynamics (CFD) approach

A nodal method assumes that the air is uniform, but HAM models based on the well-mixed air assumptions may produce inaccurate data in scenarios where low-air circulation zones exist, such as in the area of heating systems.

For example, compared to covered partitions, wall assemblies with effective ventilation might have larger surface convective transfer coefficients and differing transfer potentials [80]. As a result, just a piece of the wall seems to be engaged for calculation in the HAM transfer strategy, with the majority appearing to be essentially unreactive. For such a scenario, models based on precise conservation equations for mass, momentum, and energy in the air and fine spatial discretization of an air volume are needed.

A very precise research requires the modeling of room air using the Computational Fluid Dynamics

(CFD) method, which enables the calculation of the scalar fields of temperature and vapor pressure in a specific volume with great accuracy. Typically, several thousand to several million control volumes are used to mesh an entire designated volume. For each control volume, the conservation equations can be computed employing finite element or finite volume techniques. One of the fundamentals of software that uses the CFD technique (Large Eddy Simulation (LES) or Direct Numerical Simulation (DNS)) is the solution of the Navier-Stokes's equation. Additionally, it can resolve the conservative energy equation for solid domains and air volumes as well as the mass conservation equation for various species. Hence, all the governing conservation equations can be written as follows.

$$\frac{\partial \phi}{\partial t} + \vec{V}_\phi \nabla \phi = \Gamma_\phi \nabla^2 \phi + S_\phi \quad 1.6$$

Where numerous physical characteristics, such as temperature or species concentration, are represented by the symbol ϕ . The standard physical parameter's diffusion coefficient and source term are Γ_ϕ and S_ϕ , respectively, and ϕ 's velocity vector is represented by V .

There are different possibilities, including ANSYS FLUENT, COMSOL Multiphysics, OpenFoam, and other CFD software. They provide a wide range of numerical solution techniques that are not necessarily restricted to modeling building energy. With a thorough simulation plan technique, they may be used with any system. A detailed explanation of the CFD approach technique for computing hygrothermal behaviors is shown in **Figure 1.5**, and some studies on the application of CFD software for examining hygrothermal transfer at various scales are listed in **Table 1.5**.

The finite difference approach was used by Simo-Tagne et al. [81] to model the coupled one-dimensional heat and moisture transmission of a wood and concrete wall. The numerical results for both material walls showed a great concordance with the experimental data gathered from the literature. They also demonstrate that lighter wood types are appropriate for improved building interior insulation.

The COMSOL Multiphysics program served as the primary simulation tool for Alioua et al. [17] reduced one-dimensional numerical model. The hygrothermal behavior of the Künzel and Mendes models applied to Date Palm Concrete (DPC) materials was described using their own mathematical equations. The authors demonstrate how the hysteresis effect can be employed in models to enhance moisture transfer estimation through the DPC wall, and they successfully align the outputs of their numerical simulations with the outcomes of their investigations. In the same setting, Huang et al. [18] used COMSOL Multiphysics to explore the intricate behavior of coupled heat and moisture flows at the wall scale of bamboo laminated panels. In order to incorporate modeling software inputs with material characteristics, they conducted an experimental analysis of the wall's hygrothermal output in a climate chamber.

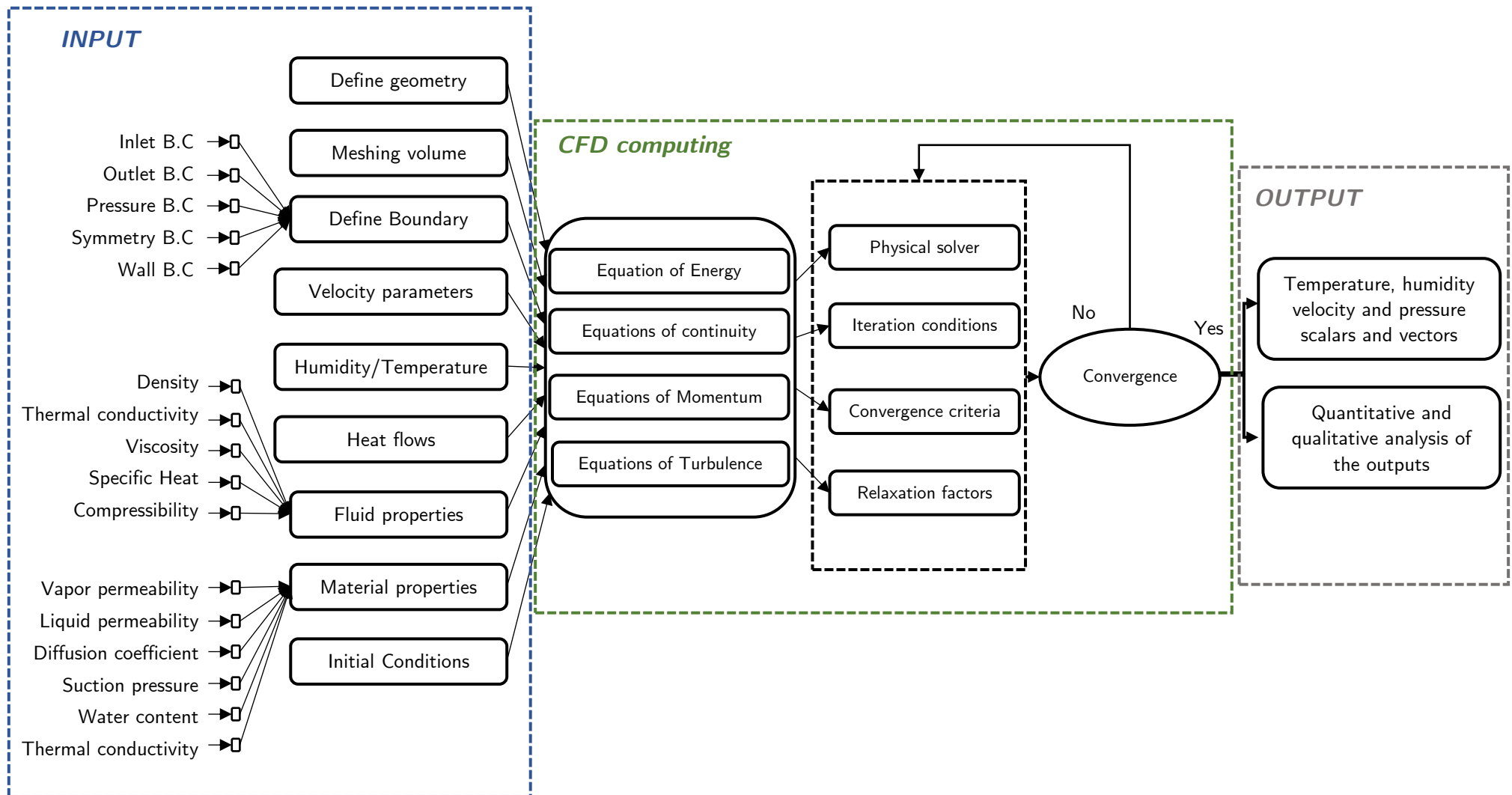


Figure 1.5 Detailed schematic description of the CFD approach for hygrothermal simulation [138]

They were able to demonstrate that the water vapor diffusion resistance parameter has the most impact on relative humidity simulation performance, but thermal conductivity predominates at steady state when it comes to temperature gradient. The relative humidity variation between the simulation and experimental data is more significant than the temperature variation. They also claim that when it comes to affecting the results of temperature simulations, density is the parameter that is most sensitive in the transient phase.

Moreover, Seng et al. [13] demonstrated in their model that whenever the relative humidity is under 95 %, the moisture diffusion coupled with the heat gradient seems to be the main driving potential of moisture transport. According to their study, the moisture distribution in hemp concrete is largely driven by liquid transfer at these saturation settings, but in the other situation of a relative humidity exceeding 95 %, the enthalpy effect caused by the phase transition of water becomes as great as the one of heat transfer through conduction.

Promis et al. [16] also applied the COMSOL Multiphysics program for the 3D modeling of the coupled heat and moisture transfers for a wall made of hemp concrete and rape straw concrete. They utilize the climatic conditions data from the literature as their weather inputs. They successfully validate the computational simulation results through experiments and demonstrate that the hysteresis pattern is approximately linear between 50 % and 75 % relative humidity.

In multilayer walls created from hollow concrete loaded with compressed straw bricks, Hou et al. [45] calculated 1D coupled heat and moisture exchanges using HMCT1.0 software. Their CFD technique is based on FORTRAN and Visual Basic mixed-language programming. So, in order to examine material qualities, they rely on a climate chamber with controlled conditions, which enables them to demonstrate that the temperature gradient has significantly affected the diffusion of moisture within the wall. There was good agreement between simulations and experiments.

Simulink/Matlab software is used by Labat et al. [61] to model the coupled heat and moisture movements. The main process taken into account in this investigation was vapor diffusion, with liquid transfer in the porous medium being excluded. Their numerical study demonstrates that the latent heat effect had the most significant influence on the heat flux balance at the building size due to vapor diffusion.

For the simulation of heat and moisture exchange, several studies, including Van Belleghem et al. [62], employed the FLUENT program. The authors simulate heat and moisture flows in the air as well as in the porous material by using computer simulation. The authors demonstrate that the biggest factor affecting temperature changes is the convective heat transfer coefficient. Additionally, because diffusive mass transfer is greater than convective mass transfer, the change from laminar to turbulent flow type has no impact on relative humidity within the porous material.

Additionally, the anticipated relative humidity during the desorption process rises when the hysteresis model is used. Additionally, they note that the simulated temperature and relative humidity were not significantly affected by the heat capacity and thermal conductivity of the porous material.

1.6.2.1 Strength of the CFD approach

For its ability to provide a detailed analysis of the various fluxes that occur inside and outside. The CFD technique is popular because it can offer a thorough study of the numerous fluxes that happen inside and outside of structures. It is therefore a great option for examining the precise fluctuations of the desired physical properties on a microscale. In addition, the volume is divided into tiny, controlled volumes using uniform or irregular meshing, particularly close to wall-type boundaries to account for the high gradients of many physical attributes. The equations of mass conservation, momentum, energy, and the fluid dynamics state equation are only a few of the key concepts that are combined in this approach.

Depending on the issue at hand, it could also incorporate turbulence models. It is also feasible to couple the CFD program with other software interfaces, as with Matlab, to take things even further. Compared to the nodal technique, the CFD approach takes longer to produce a solution, but it offers more information, including precise airflow scalars and vectors in the zones as well as air temperature and humidity fields at every location in the defined area.

Table 1.4 Summary of the commonly used CFD software for hygrothermal simulation [138]

Software	Availability	Model type (simplified)	Numerical scheme	Scale	Access to code source
COMSOL Multiphysics [82]	Commercial	Heat and moisture model	Steady/ Unsteady	Wall/ Envelope	Unable
OpenFoam [83]	Open Source	Heat model	Steady/ Unsteady	Wall/ Envelope	Able
ANSYS Fluent [84]	Commercial	Heat model	Steady/ Unsteady	Wall/ Envelope	Unable
StarCCM+ [85]	Commercial	Heat model	Steady/ Unsteady	Wall/ Envelope	Unable

In order to simulate the required phenomena, one of the relevant hygrothermal models (one of those indicated in the sub-section (2.5.1) can be modeled using the OpenFoam [83] CFD program, which gives users access to the source code of the physical models. However, this necessitates a robust understanding of the C++ programming language.

Table 1.5 Summary of building hygrothermal simulation studies based on the CFD approach [138]

Study	CFD Approach	Building scale			Softwares & features
		Material	Wall	Envelope	
Zhang et al. [40]	✓	✓	×	×	MATLAB. GAB model was considered to fit sorption isotherm curves.
Reuge et al. [41]	✓	×	✓	×	Home-made 1D Cartesian tools for simulation (TMC and TMCKIN). Use of VAN GENUCHTEN model to define the isotherms of adsorption. Thermal conductivities are described by the self-consistent scheme.
Bagaric et al. [42]	✓	×	✓	×	WUFI Pro. Transient numerical simulation. Simulations of the energy performance of building according to EN ISO 52016-1:2017.
Dong et al. [43]	✓	×	✓	×	COMSOL Multiphysics & Fortran coding. Hygrothermal behavior is mathematically defined with Künzle and Liu model. 1D simulation approach through a porous multilayer wall.
Simo-Tagne et al. [81]	✓	×	✓	×	FORTTRAN 90 Coupled one-dimensional heat and moisture transfer model. Gauss-Seidel relaxation iteration method is used.
Alioua et al. [17]	✓	×	✓	×	COMSOL Multiphysics. Dynamic coupled heat and moisture transfers. Hysteresis model is considered. A mesh of 50 layers represents a good compromise. Periodic variation of the ambient conditions.
Promis et al. [16]	✓	×	✓	×	COMSOL Multiphysics. Hygrothermal models with the moisture hysteresis effect. Simplify the numerical model (1D approach) GAB model for hysteresis modeling // Mass transfer only.

Kang et al. [86]	✓	×	✓	×	Wufi Pro 5.3. 1D simulation at the wall scale. Coupled heat and moisture transfer at the wall scale.
Huang et al. [18]	✓	×	✓	×	COMSOL Multiphysics. Dynamic coupled heat and moisture transfer. Simplify the numerical model (1D approach).
Seng et al. [13]	✓	✓	×	×	Programming approach. Implementing the Partial Differential Equations (PDE) in module of FEM package. Complete coupled heat and moisture transfer.
Hou et al. [45]	✓	×	✓	×	HMCT1.0 software. Mixed-language programming of FORTRAN and VB. Coupled heat and moisture transfer for multilayered wall.
Labat et al. [61]	✓	×	✓	×	Simulink/Matlab software. Vapor diffusion is the only mechanism taken into account. The liquid transport in porous media was neglected.
Lelievre et al. [57]	✓	✓	✓	×	COMSOL Multiphysics. Coupled heat and moisture equations model.
Van Belleghem et al. [62]	✓	✓	×	×	CFD Fluent. Heat and moisture transfers in the air, porous material and at the interface is modeled in its full complexity. CFD-HAM coupled models (Solid & fluid domains). Relative humidity is the driving potential.
Qin et al. [87]	✓	×	✓	×	Programming approach. A good agreement is established between the numerical results and the measures values with easy method to determine the material physical properties.

1.6.2.2 Weakness of the CFD approach

In certain situations of research, a thorough and detailed 2D or 3D simulation of the building with a very fine mesh is necessary, exposing one of the most significant limitations of the CFD technique, its considerable calculation time. In practice, as the mesh size drops, the computation time grows. The evolution of the CFD technique is also constrained by the complexity of the model implementation. Its application is highly challenging without prior understanding of fluid dynamics, characteristics, and the solution sets.

Additionally, current CFD tools like ANSYS Fluent [84], OpenFoam [83], and StarCCM+ [85] do not take coupled heat and mass transfer at the building's wall scale into account. Nevertheless, COMSOL Multiphysics software [88] has included this ability to model heat and moisture transport in building materials and at the wall scale (**Table 1.4**).

1.6.3 Co-simulation of hygrothermal behavior modeling

The synchronization of time steps is the major concern that arises during the numerical performance of the simulations. The yearly computation of the full-scale characteristic of the room's air for each designated zone takes a few seconds when applying the nodal technique. However, it stills depending on the processing capabilities of the CPU, where the building envelope can take hours or even days to produce the appropriate results. In this situation, employing a coupling softwares technique may be problematic for too long of computation durations. Zhai et al. [89] description of such "co-simulation" techniques often refers to static or dynamic coupling.

The static coupling is the one- or two-step data transfer between the Energy Simulation program and the CFD software. Actually, one of the programs computes the answer first, after which the input data is transferred to the second program, which then completes the calculation process through a series of feedback loops. The dynamic coupling strategy, on the other hand, simulates a continuous data exchange for each computation time step. The three types of coupling for this method are one-time-step dynamic, quasi-dynamic, and completely dynamic [89]. The flowchart for the streamlined co-simulation technique is shown in **Figure 1.6**, and various studies on the co-simulation of hygrothermal building behavior are shown in **Table 1.6**.

The hygrothermal behavior of a wall with varied heat and moisture convective coefficients was investigated by Berger et al. [10] using MATLAB, and the whole-building hygrothermal simulation was performed using the Domus Software. In this work, the authors are able to reduce the order model for the full hygrothermal simulation and couple the two software packages. This opens the door to the potential of decreasing equation order in subsequent research, which demonstrated that a time step of about 6 minutes is ideal for co-simulation. On the other hand, Zhang et al.

[90] employed a co-simulation between the 1D HAM model in porous medium and the 3D CFD STREAM V8 program.

Table 1.6 Summary of co-simulation studies on hygrothermal behavior of buildings [138]

Study	Building scale			Coupled softwares	CFD	Nodal	Multilayered wall
	Material	Wall	Envelope				
Berger et al. [10]	x	✓	✓	Matlab (Wall) Domus (Building)	✓	✓	x
Zhang et al. [90]	x	✓	✓	CFD STREAM V8	✓	✓	✓
Steeman et al. [63]	x	✓	✓	TRNSYS & HAM tool	✓	✓	✓
Li et al. [91]	x	✓	x	COSMOL & MATLAB	✓	✓	✓
Steeman et al. [92]	x	✓	x	FLUENT HAM model	Heat in solid / HAM in fluid / EPD model	✓	x

In order to simplify the simulation of the coupled hydrothermal model, the authors regarded the relative humidity to be the primary driving force and the vapor diffusion to be the only mechanism engaging in moisture transfer. One of the software programs used for dynamic thermal modeling of buildings is TRNSYS. Except for a few works like those of Steeman et al. [63], hygrothermal transfer has not yet been included into software. The coupling heat, air, and moisture transport (HAM) in porous materials was employed by the authors in the implicit time discretization scheme of the Building Energy Simulation program TRNSYS.

In the simulation of actual building applications, the proposed coupled model is adaptable and capable of simulating multilayered walls with varied boundary conditions. They use analytical solutions and various experimental benchmarks to confirm that their co-simulation is operating correctly. Additionally, a number of researchers including Li et al. [91], [93] have tested the COMSOL and MATLAB combination. They employ COMSOL to solve the heat and moisture partial differential equations in their study, which can run in parallel with MATLAB through a graphical user interface. In their co-simulation, the gradient of the moisture content serves as the driving potential, and the Darcy-Boussinesq approximation is used to approximate natural air convection. Their HAM-BE models are validated using experimental data as well as other numerical benchmarks. In earlier investigations, Steeman et al. [92] integrated the HAM with the FLUENT program to incorporate the coupled heat and moisture governing formulas of the porous material. The relative humidity was employed as the main driving potential for moisture diffusion, and the second upwind scheme was applied for the convective terms.

The outcomes of computational simulations were better in line with the benchmark data when a hysteresis model was employed. Finally, their simulations demonstrated how well the microclimate vitrine protects against changes in relative humidity.

1.6.4 Inputs for hygrothermal simulation tools

The input parameters for each of these techniques include geometrical information, meshing size, hygrothermal physical factors, meteorological information, equipment loads, and comfort scenarios. On the other hand, these characteristics are almost usually presented in a more or less challenging way. In addition to the estimation inaccuracy of the various parameters, simplification assumptions also introduce uncertainty. Therefore, various hypotheses with consequences on model effectiveness must be made in order to decrease the complexity of the hygrothermal dynamical development that occurs in buildings. It is quite difficult to comprehend the level of precision of the model because of all these challenges. As a result, it appears difficult to combine the phenomena of heat and moisture transfer inside a permeable structure into a broad overview without adding too many complicated technical details. The basic variables that affect simulations are investigated for in the sections that follow.

1.6.4.1 Geometry

The enclosure geometry has to be adequately characterized before doing any hygrothermal analyses using CFD or Nodal methods. Alternatively, modeling the geometry can be done without a graphical interface when using a computation software like FORTRAN [43], [81], [87]. For the CFD or Nodal technique, the enclosure geometry must, nevertheless, give macro building data, enclosure assembly information, and micro-details.

1.6.4.2 Mesh generating

Only the CFD technique requires the meshing procedure, which is crucial for the accuracy of the simulations. Since each zone or building volume is given to a single global mesh, the nodal method does not involve any meshing. The mesh pre-processing phase in any numerical research is the process of splitting the examined zone into distinct elementary volumes. In regions where velocity, temperature, or pressure gradients are the most prominent, meshes should be small and adaptable to the physical phenomenon. It is advised to execute iterative mesh size adjustment tests to explore these regions' sensitivity with regard to the output of the final numerical outcomes if they cannot be predicted, as was already performed by Alioua et al. [17]. The simulation softwares offer certain techniques to mesh the boundary layer close to the wall in the case of wall heat and moisture transfer studies so that the coefficients and physical phenomena at this location can be estimated more effectively and exactly.

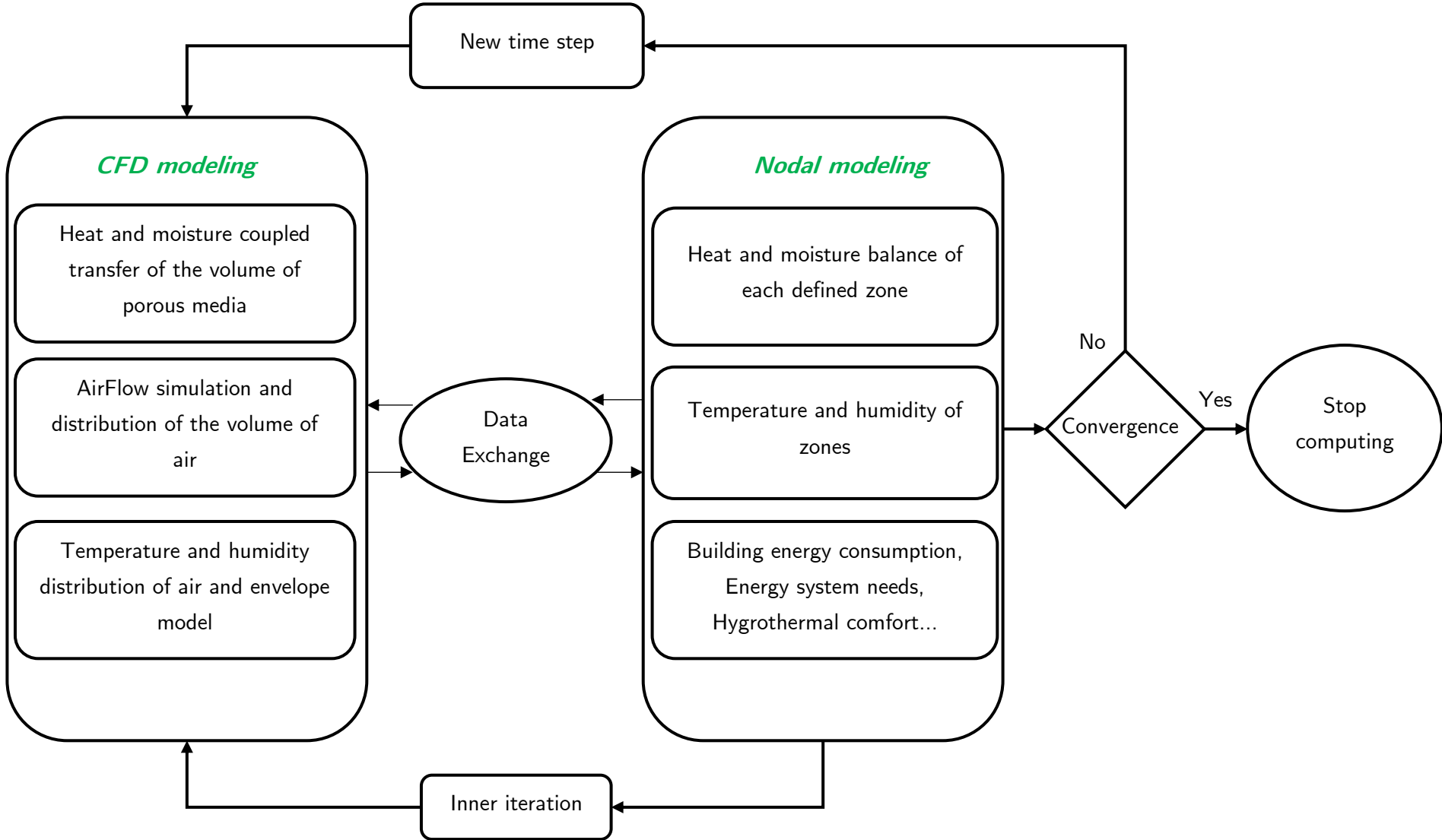


Figure 1.6 Co-simulation simplified flowchart [138]

In the majority of numerical modeling, and notably for the CFD technique, a sensitivity analysis of the mesh is required. To do this, simulations with more meshes must be run more often. It is advised to adjust the mesh until the outputs are independent of mesh sizes if the simulation results are mesh-dependent. As a result, the outcomes are no longer influenced by the grid resolution. We need to be aware that if the mesh size is too wide, any local occurrences, such as air recirculation, flow blockage, hot spots, etc., will not be captured. It is important to note that Alioua et al. [17] utilized 100 meshing layers for a wall thickness of 15 cm, whereas Skerget et al. [94] used 200 layers for a 1D discretization mesh with a wall thickness equal to 36.5 cm. Steeman et al. [63] based their work on a mesh thickness that ranges from 3 mm to 7.7 mm.

1.6.4.3 Materials properties

A vast number of material characteristics are required when using CFD or Nodal approaches to evaluate the hygrothermal behavior of buildings. For instance, common material parameters used as an initial input for hygrothermal simulation include specific heat, thermal conductivity, water vapor permeability, apparent density, water absorption coefficient, sorption isotherm, and hydraulic conductivity.

Temperature, humidity, and moisture content can all have an impact on the values of the aforementioned factors. In fact, they may alter proportionally as a result of these elements or the opposite. For instance, COMSOL Multiphysics' [82] simulation of the hygrothermal behavior of a hygroscopic wall requires the material's water content, liquid and vapor permeability, diffusion coefficient, suction pressure, as well as thermal parameters like thermal conductivity and specific heat [88]. The accuracy of the simulation depends on the sorption isotherm and hysteresis effect, two phenomena that have been observed in hygroscopic materials. Below is a description of the models explaining these two phenomena.

1.6.4.4 Sorption isotherm

The water sorption isotherm depicts the thermodynamic interaction between water motion and the equilibrium moisture content of a porous structure medium under constant ambient settings, with the exception of humidity.

The two distinct processes of adsorption and desorption define the equilibrium water content as a function of ambient relative humidity at a certain temperature (**Figure 1.7**). As a result, isotherm curves may be regarded as one of the most significant moisture diffusion features of porous construction materials. Hence, either an adsorption or a desorption process can result in the generation of sorption isotherms.

A gas is frequently adsorbed and desorption from a porous surface occurs after the generation of phase change heat. The relationships between the adsorbent and adsorbate influence this. During adsorption, heat is released into the environment, and during desorption, it is recovered back into the system.

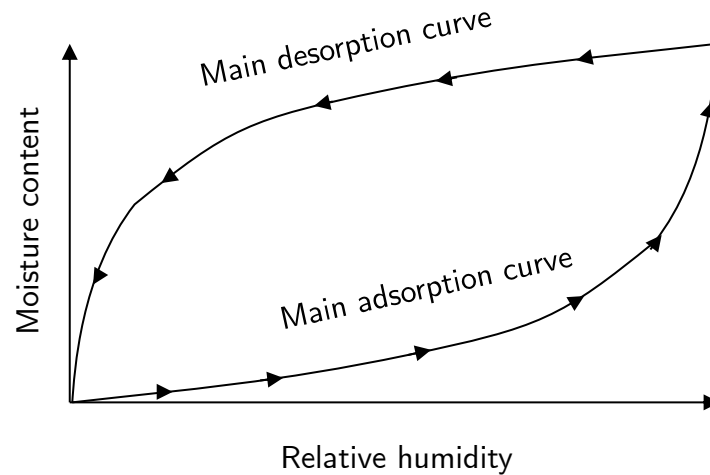


Figure 1.7 Humidity sorption isotherm as a function of relative humidity [138]

To explain sorption isotherms, a number of mathematical models have been proposed, such as linearity or non-linearity models using partial coefficients as parameters. The model only has a reasonable prediction value for a certain range of moisture activity, and it is not always appropriate for all types of hygroscopic materials.

Semi-empirical equations with two or three reasonable setting can be used to define the moisture sorption isotherms. The Langmuir, Van Genuchten, and other equations have also been used to explain sorption isotherms in building materials, although the GAB formula and the BET equations are the most often utilized. Several studies [12], [14] employed the Clausius-Clapeyron equation to characterize the sorption curves as a function of temperature.

1.6.4.4.1 Brunauer, Emmett, and Teller (BET) Model

The BET model was proposed by Brunauer, Emmett, and Teller and has since been the model most frequently employed to explain sorption curves for hygroscopic materials [60]. This idea is essential to understand multilayer sorption isotherms, and its model is as follows:

$$w = \frac{X_0 c \phi}{(1 - \phi)(1 - \phi + c \phi)} \quad 1.7$$

Where c denotes the energy absorption differential between molecules in the first layer and molecules in successive layers and represents the specific heat of sorption. ϕ is the relative humidity. X_0 is the monolayer moisture content, as that is the point where the water is attached to every ionic group.

1.6.4.4.2 Guggenheim-Anderson-de Boer (GAB) model

The equation for this model was established by Guggenheim [95], Anderson [96], and De Boer [97] separately in 1966, 1946, and 1953, respectively. The GAB model of physical adsorption is an improvement on the Langmuir [98] and BET models and offers various advantages over the others due to the inclusion of a strong theoretical framework. The adsorbed molecules in the second layer, according to this concept, are in a different state from those in the liquid state, but they are in the same condition as those in the upper layers that were produced later. For the categorized adsorber molecules, these authors suggested a second sorption technique.

For any isotherm sorption curve development based on the GAB model, the typical chemical potential difference between the molecules in this second layer and those in the pure liquid state is represented by a third factor, designated as k . As a result, the present model is written as.

$$w = \frac{X_0 c_g k_g \phi}{(1 - k_g \phi)(1 - k_g \phi + k_g c_g \phi)} \quad 1.8$$

The adsorption constants, c_g and k_g , are proportional to the energies of interaction between the initial and final adsorbed molecules at each sorption scale, where X_0 is the monolayer moisture content. Thus, they may potentially be stated as shown in the following equation.

$$c = c_0 e^{\left(\frac{H_0 - H_n}{RT}\right)} \quad k = k_0 e^{\left(\frac{H_n - H_l}{RT}\right)}$$

Where H_0 , H_n , and H_l , respectively, indicate the molar sorption enthalpies of the monolayer, the layer that comes after it, and the bulk liquid.. The entropic correction factors are often defined as c_0 and k_0 . The ideal gas constant is equal to R and T is the absolute temperature. It's important to remember that when K equals 1, the GAB model becomes the BET equation.

The explicit consideration of thermodynamic state functions makes the GAB model a popular choice for modeling isothermal sorption curves. As a result, sorption activity may be explained in a wide range of possible values between 0 % and 90 %. The GAB model underestimates the moisture content values at relative humidity levels above 93 %, particularly when there is a lot of moisture activity in liquid form. Numerous research [13], [16], [17], [40], [57] have approximated sorption isotherms using this model.

1.6.4.4.3 Van Genuchten model

When fitting empirical isothermal sorption curves of hygroscopic materials [15], [41], [91], the Van Genuchten model [99] is frequently employed since it is simple and clear.

$$\theta = \theta_r + \frac{(\theta_s - \theta_r)}{(1 + (\alpha h)^n)^m} \quad 1.9$$

With $m = 1 - (1/n)$ and $n > 1$. Where h is the capillary pressure, θ_r is the residual moisture content, θ_s is the saturated moisture content. A , m and n are the improvement factors.

1.6.4.5 Hysteresis effect

One of the most significant elements impacting moisture transport inside building materials is the hysteresis of water vapor sorption isotherms, which has long been noted. The primary adsorption and desorption evolution lines are shown by sorption curves. When drying and wetting processes take place, sorption isotherms will change away from the primary pathway, causing a phenomenon known as sorption hysteresis (**Figure 1.8**). Numerous investigations have discovered that there is a hysteresis effect between desorption and adsorption throughout the whole spectrum of relative humidity.

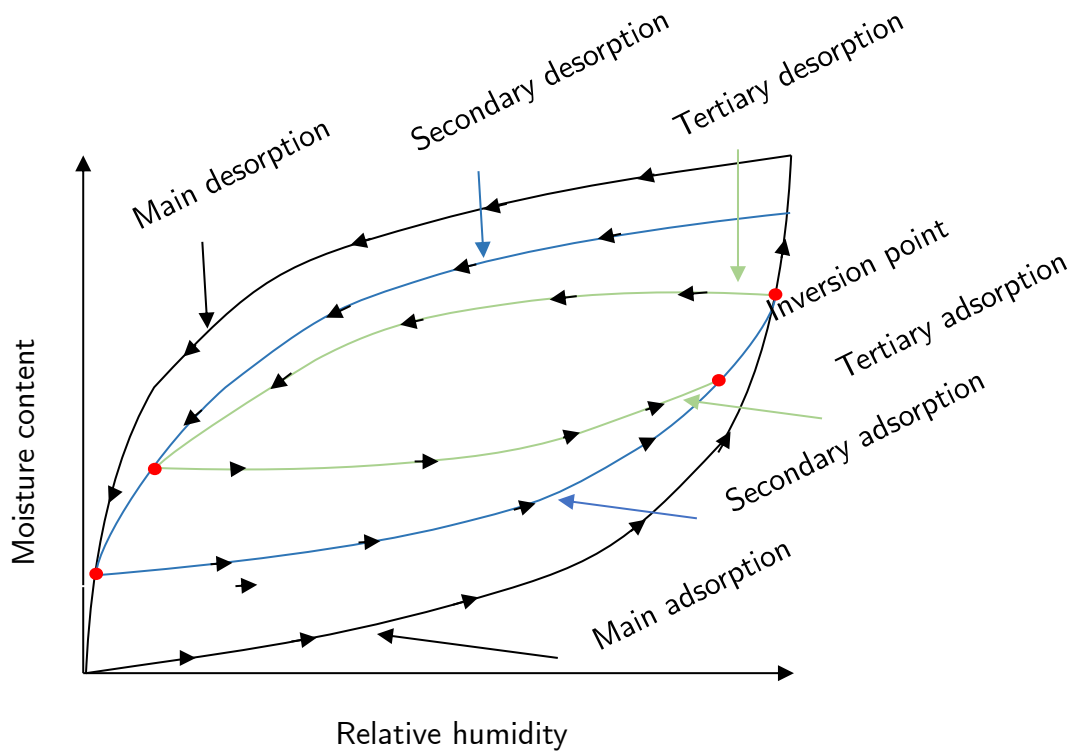


Figure 1.8 Schematic representation of the intermediate variations of the hysteresis phenomenon of the sorption curves [138]

Some approaches neglect the hysteresis effect and utilize the primary sorption isotherm to simulate moisture transport throughout adsorption and desorption cycles. However, in order to improve numerical findings, such as those from the work by Moujalled et al. [15], hysteresis consideration in numerical simulations has lately attracted a lot of attention.

The hygrothermal behavior of the building was investigated experimentally and numerically by the authors using an actual building envelope. The hysteresis is simulated in MATLAB since WUFI cannot account for it in their co-simulation study, which shows high agreement between simulations and experiments. Maaroufi et al. [100] investigated the effects of the sorption hysteresis phenomena on heat and moisture movement in expanded polystyrene concrete. They incorporated the coupled heat and moisture transfer model to COMSOL Multiphysics with the hysteresis model on MATLAB. Their associated model reduces the mismatch between the numerical and experimental data from 28 % to less than 7 % while improving knowledge of hygrothermal dynamics. The models for sorption hysteresis cycles are then provided.

1.6.4.5.1 Mualem II model

The scanning curves can be predicted from two boundary curves using the Mualem II model [101]. On the boundary wetting curve, the principal drying scanning curve begins at a suction ψ_1 , and it can be computed as follows:

$$\theta(\psi_{\min}, \psi_1, \psi) = \theta_w(\psi) + \frac{[\theta_w(\psi_1) - \theta_w(\psi)]}{[\theta_u - \theta_w(\psi)]} [\theta_d(\psi) - \theta_w(\psi)] \quad 1.10$$

Where θ_u is the water content at the point where the two boundary curves meet, and $\theta_w(\psi)$ and $\theta_d(\psi)$ are the water contents on the frontier of the wetting and drying curves at suction, respectively. This equation yields the principal wetting scanning curve.

$$\theta(\psi_{\max}, \psi_1, \psi) = \theta_w(\psi) + \frac{[\theta_u - \theta_w(\psi)]}{[\theta_u - \theta_w(\psi_1)]} [\theta_d(\psi_1) - \theta_w(\psi_1)] \quad 1.11$$

After a sequence of alternate drainage and adsorption cycles, the wetting is expressed as follows.

$$\begin{aligned} \theta(\psi_{\min}, \psi_1, \psi_2, \dots, \psi_N, \psi) &= \theta_w(\psi) + \frac{[\theta_d(\psi_N) - \theta_w(\psi_N)]}{[\theta_u - \theta_w(\psi_N)]} [\theta_w(\psi_{N-1}) - \theta_w(\psi)] \\ &+ \sum_{i=1}^{(N/2)-1} \frac{[\theta_d(\psi_{2i}) - \theta_w(\psi_{2i})]}{[\theta_u - \theta_w(\psi_{2i})]} [\theta_w(\psi_{2i-1}) - \theta_w(\psi_{2i+1})] \end{aligned} \quad 1.12$$

And after a series of alternating desorption and adsorption operations, the drainage is expressed as follows.

$$\begin{aligned} \theta(\psi_{\min}, \psi_1, \psi_2, \dots, \psi_N, \psi) &= \theta_w(\psi) + \frac{[\theta_d(\psi) - \theta_w(\psi)]}{[\theta_u - \theta_w(\psi)]} [\theta_w(\psi_N) - \theta_w(\psi)] \\ &+ \sum_{i=1}^{(N-1)/2} \frac{[\theta_d(\psi_{2i}) - \theta_w(\psi_{2i})]}{[\theta_u - \theta_w(\psi_{2i})]} [\theta_w(\psi_{2i-1}) - \theta_w(\psi_{2i+1})] \end{aligned} \quad 1.13$$

The sorption cycles of hygroscopic building materials' adsorption and desorption have been

studied using this model to account for the hysteresis effect [16], [17], [57], [62], [92].

1.6.4.5.2 Pedersen Model

Rode-Pedersen [102] makes the assumption that the intermediate curves change asymptotically in the direction of the primary adsorption or desorption curves, depending on the complexity of the motion of the water content microenvironment in the material. In Pedersen's model, the fundamental adsorption and desorption cycles as well as the principal adsorption and desorption curves must be established experimentally. The analytical approximation of the water capabilities of the intermediate adsorption/desorption curves can be described as follows once the water capacities for the primary curves are identified.

$$u_{new} < u_{old} \quad || \quad \xi_{hys} = \frac{(u - u_a)^2 \xi_d + 0.1(u - u_d)^2 \xi_a}{(u_d - u_a)^2} \quad 1.14$$

$$u_{new} > u_{old} \quad || \quad \xi_{hys} = \frac{0.1(u - u_a)^2 \xi_d + (u - u_d)^2 \xi_a}{(u_d - u_a)^2} \quad 1.15$$

Where ξ_{hys} is the moisture potential at hysteresis, ξ_a is the adsorption humidity ability at the current relative humidity, ξ_d is the desorption moisture at the current relative humidity, u is the current moisture content, and u_a and u_d are the corresponding adsorption and desorption moisture contents to the current relative humidity value.

1.6.4.5.3 Huang's hysteresis model

In order to describe intermediate sorption curves in soils, Huang et al. [103] developed a novel hysteresis model based on the Kool and Parker model [104]. The adsorption and desorption curves can be represented [105] after a series of alternate sorption cycles:

$$\text{Adsorption} \quad || \quad u(RH, i) = u_r(i) + (u_s(i) - u_r(i)) \frac{u_{ads}(RH)}{u_{sat}} \quad 1.16$$

$$\text{Desorption} \quad || \quad u(RH, i) = u_r(i) + (u_s(i) - u_r(i)) \frac{u_{des}(RH)}{u_{sat}} \quad 1.17$$

The major adsorption and desorption curves are denoted by the symbols u_{ads} and u_{des} , respectively, where $u_r(i)$ and $u_s(i)$ represent the residual and saturated moisture contents of the scanning curves, respectively.

1.6.4.6 Boundary and initial conditions

Along with coupled equations for the physical description of heat and moisture transfer, boundary

conditions are frequently crucial for the output's reliability for the numerical resolving of the mathematical models. The inner temperature, external environment, and boundary conditions between elements must all be considered for both nodal and CFD techniques. For a simulation to be successful, boundary interactions at the interfaces of control volumes (fluid or solid domain) must be properly pre-processed. The interior and outside environments, the heat balance on indoor and outdoor wall surfaces, and the vapor balance on indoor and outdoor wall interfaces are all described using the models that are shown below.

1.6.4.6.1 Exterior environment

The outer ambient air or outside atmosphere is commonly specified in terms of hourly meteorological information for most HAM models. The climatic data that the majority of hygrothermal softwares require on an hourly basis include the temperature and relative humidity of the exterior air, solar radiation incident on the ground, and rain load incident on the outer walls. Additionally, typical meteorological information like wind speed and direction is needed for hygrothermal models. All of the aforementioned information can be obtained by using a weather station [15], making predictions using weather software tools, or by applying quantitative analysis to meteorological datasets [35], [44], [61], [71], [91]. The CFD technique, however, finds it challenging to characterize climatic phenomena like rain load without utilizing additional physical model equations, which might extend calculation times. As a result, the majority of study papers [12], [15], [40], [94] incorporate imposed climate conditions in the form of equations. With a computation time step Δt that is substantially less than the nodal technique, often ranging from a few seconds to a few minutes, but typically less than 5-6 minutes [10], the CFD method gives straightforward calculations for wind scenarios such as speed and orientation.

1.6.4.6.2 Interior environment

The interior environment, commonly referred to as the indoor ambient atmosphere, is defined by the dynamic values of temperature and relative humidity. To evaluate thermal comfort indices, there are a few standards for interior climate regulation modeling (ISO, ASHRAE, etc.). Thermal comfort indices make it possible to assess the building's energy efficiency. The building envelope's hygrothermal balance is shown below.

1.6.4.6.3 Outside Surface Heat Balance

The following equation represents the building energy balance equation.

$$-\lambda \left. \frac{\partial T}{\partial x} \right|_{ext} = h_{c,ext} (T_{air,ext} - T_{surface,ext}) + Q_{rad.sky} + j_v L_v \quad 1.18$$

Where j_v is the mass flow density of moisture vapor diffusion, $h_{c,ext}$ is the convective heat exchange

coefficient of the exterior face, and L_v is the latent heat of evaporation. The first two sentences on the right-hand side explain the convective and radiative heat transfers with the surrounding air. The third element, which exclusively considers the latent amount of the energy conveyed by the water vapor, deals with its specific enthalpy. The sensible element is neglected. As a result, zero is established as the reference temperature for the sensible specific enthalpy.

1.6.4.6.4 Vapor and capillary balance on outdoor wall surface

The following equation represents the relationship.

$$-\delta_p \left. \frac{\partial P}{\partial x} \right|_{\text{ext}} = \beta_{v,\text{ext}} (P_{\text{vap.air.ext}} - P_{\text{vap.surface.ext}}) \quad 1.19$$

The term on the right-hand side represents the convective moisture transfer with the surrounding air. The convective mass transfer coefficient, which depends on the air velocity at the surface, and the water vapor permeability, denoted by the letters δ_p and β_v , respectively, in the mentioned equation. Since the vertical wall has a wet surface condition, it is frequently believed that there is no liquid flow at the interior boundary surface. The assumption also remains true for the outside boundary surface in the absence of wind-driven precipitation. Otherwise, rain may cover the outer wall's surface, which gradually saturates. There are two scenarios: either the incidence rain is insufficient to completely saturate the outer wall layer, or the whole moisture supply is absorbed by the wall.

$$m_w = k_w \frac{\partial P}{\partial z}$$

The incidence rain on the exterior wall layer exceeds the capillary transfer rate limit, and the surplus moisture is drained from the surface.

$$m_{\text{rain}} = k_w \frac{\partial P}{\partial z}$$

Where K_w is the permeability of liquid water. m_w and m_{rain} are the mass fluxes for liquid water and rain, respectively.

1.6.4.6.5 Inside Surface Heat Balance

With the exception of the radiative exchange, which results from interior sources that emit radiation. This balance is described using the similar boundary conditions as for the exterior surface.

$$-\lambda \left. \frac{\partial T}{\partial x} \right|_{\text{int}} = h_{c,\text{int}} (T_{\text{air.int}} - T_{\text{surface.int}}) + Q_{\text{rad.int}} + j_v L_v \quad 1.20$$

In this case, the first two terms on the right-hand side of equation (1.20) explain the convective

and radiative heat exchanges with the surrounding air. The third term describes the enthalpy of the passage of water vapor through the building membranes.

$$Q_{rad.int} = \frac{W_r}{\sum_i A_i} + h_{r.int} (T_{surrounding} - T_i) \quad 1.21$$

Where W_r stands for the sum of all the volume area's radiative heat sources. The second term indicates the radiative heat transfer from the surrounding medium, where $T_{surrounding}$ denotes the mean surface temperature of all surfaces in a space. In this instance, the portion that travels through a transparent material, like a window, is considered as a heat loss. The temperature of the air within is T_i .

1.6.4.6.6 Vapor balance on indoor wall surface

The balance is expressed by the following equation.

$$-\delta_p \left. \frac{\partial P}{\partial x} \right|_{int} = \beta_{v.int} (P_{vap.air.int} - P_{vap.surface.int}) \quad 1.22$$

The same fundamentals that apply to boundary conditions on an outside surface apply here, with the exception that inside air is involved. In some situations, the moisture convective transfer coefficient can be associated with the heat convection coefficient of the inside environment. Considering sorption and hysteresis models, the kind of boundary conditions applied, and the different elements that may be employed in the computations. A thorough review of the literature (**Table 1.8**) reveals that the issue of hygrothermal bridges has not yet been addressed.

1.6.4.6.7 Discussion on the physical models

The sections that came before this one detailed a number of physical techniques for simulating building energy. We showed in the previous cases that the notions of each strategy and each physical methodology has its own application domain. The most precise and illustrative method is the CFD. It makes it possible to describe every component of the building envelope in great detail. It is especially effective at simulating the convective exchange that takes place in a large zone volume. However, it is challenging to represent all physical phenomena using CFD, mostly due to the lengthy computation periods. Therefore, it must be used in conjunction with the nodal technique as it is performed in EnergyPlus or TRNSYS. In contrast to the CFD simulation, the physical phenomena is shown in a less accurate manner, nodal modeling is ideally suited to take global resolution into account as uniform field parameters.

When a physical simplification is conceptually achievable, the goals change to linearizing as many physical equations as possible in order to improve the basic computing model of the solution processes. **Table 1.7** compares the two most widely used methodologies that have been tested and utilized to replicate the behavior of buildings in a prior research.

Table 1.7 Main difference between CFD and Nodal approach [138]

Nodal approach	CFD approach
Flow between zones, outputs, inputs	Detailed modeling of air flow and its parameters within zones.
Heat balances, thermal dispersion (Including thermal bridges, under crawl space...)	More efficient modeling of the physics phenomenon within the solid and volume domains.
Energy balance equations.	Reynolds Average Navier Stokes Equations. Large Eddy Simulation. Direct Numerical Simulation.
Less complex resolution method, faster calculations.	Detailed calculations requiring a longer resolution time.
1 node = 1 zone = 1 Mesh	Meshing a whole volume into few thousands to few millions of small elements or volumes.
Climate data, includes temperature, relative humidity, solar radiation, rain load and etc.	Describing climatic conditions such as rain load needs the use of other physical model equations.

Section **1.6.4** identifies the boundary conditions and inputs of material parameters required for hygrothermal simulation. We have included a list of recommendations to follow when simulating a single area of a building envelope or a multizone design since the goal of most hygrothermal models is to contain adequate and correct data for a good and smooth simulation running. The accuracy of earlier strategy works and their confirmation by benchmarks should ideally serve as the foundation for the software's performance in analyzing a specific single element's or multi-zone building's hygrothermal behavior. Choosing a tool based on the numerical modeling solvers and inputs of the program is recommended if this is not achievable. Future researchers would need to select hygrothermal simulation methods that perfectly matching their objectives because different software has different hygrothermal features, strengths, and limitations. Such as the capacity to model heat and moisture transfers by air or diffusion via enclosures in 1D, 2D, or 3D dimensions or the capability to simulate a great number of zones in an acceptable amount of time.

- Accurately calculating and validating outcomes.
- Enabling efficient data entry and verification.
- Understanding every input required for the simulation.
- Having the flexibility to solve uncommon problem forms.
- Delivering rapid output post-processing.

Table 1.8 Synthesis of parameters and application models for hygrothermal behavior simulation of porous media [138]

Study	Hygrothermal bridges	Sorption model	Hysteresis Model	Calculation method	Numerical Dimensions	EMPD Model	Solar Radiation	Heat and moisture convection	Experimental validation	Boundary conditions type
Zhang et al. [40]	x	GAB	x	Programming on MATLAB Künzel model	2D &3D	x	x	x	✓	Dirichlet
Reuge et al. [41]	x	Van Genuchten	x	Not indicated	1D	x	x	✓	✓	Neumann
Alioua et al. [17]	x	GAB	Mualem II	Finite element	1D	x	Defined as radiation coefficient	✓	✓	Neumann
Promis et al. [16]	x	GAB	Mualem II	Finite element	3D	x	x	✓	✓	Neumann
Moujalled et al. [15]	x	Van Genuchten	Huang	Finite difference	1D	x	✓	✓	✓	Neumann
Colinart et al. [14]	x	Clausius-Clapeyron equation GAB model	x	x	1D	x	✓	✓	✓	Neumann
Seng et al. [13]	x	GAB	x	Finite element	1D	x	x	✓	✓	Neumann and Dirichlet
Lelievre et al. [57]	x	GAB	Pedersen and Mualem II	Finite element	1D	x	✓	✓	✓	Neumann
Van Belleghem et al. [62]	x	✓	Mualem II	Finite volume	2D	x	x	✓	✓	Dirichlet and Neumann

1.7 Statistical methods using Deep Learning

Deep learning is the main focus of the computer science topic known as artificial intelligence. Also referred to as a computer methodology based on data analysis. Despite the fact that AI refers to a variety of complex mathematical and processing techniques, which enable models to learn from the data they gather and utilize that knowledge to execute a number of essential tasks. Artificial neural networks (ANN), a subset of artificial intelligence, are discussed in this section. Everything we require to understand neural networks, including their layers, neurons, connections, weights, and activation mechanisms, is provided. Additionally, it covers the modeling guidelines for ANN architects. The development of ANN is described in depth and every aspect of neuron network processing is shown in the following subsections.

1.7.1 Deep Learning modeling

The capacity of artificial neural networks to directly learn from incoming data and solve complicated problems has led to their widespread usage in a number of disciplines. A neural network is a type of data processing model that takes its origins from the way a human brain can abstractly understand and learn from observations.

A dynamically parallel distributed processor formed of fundamental processing units, known as an ANN, has a natural ability to encode experimental data and make it accessible for study. ANN and LSTM (long short-term memory) is frequently employed as a proxy model or as a method based on an estimate of the response surface due to its resilience in handling quantitative and nonlinear simulation issues, such as feature predictions and identifications.

A multitude of inputs, outputs, hidden neurons, and hidden layers make up the architecture of an ANN. In terms of reliability, learning time, and applicability, this does not imply that an ANN with a one hidden layer is the optimum option. The ideal ANN architecture for a certain collection of input and output data cannot truly be determined by a defined rule.

1.7.2 Artificial Neural Networks principles

ANNs are without a doubt one of the most important soft-computing techniques for general energy issues [106], [107]. There are several plausible reasons why this is the case. It has the capacity to accurately comprehend the fundamental interactions of any ranges of input and output information even without necessity of a physical model. The complexity of the underlying connection, such as non-linearity, numerous variables and contexts, external disorder, and confusing input and output data, does not significantly affect the capability of this technique. Learning techniques for the ANN building energy engineer led to the development of this fundamental competence, which is called as pattern recognition.

Furthermore, the approach is built to be problem resilient owing to the massive simultaneous processing of data performed by the network's several processing elements. Additionally, the methodology can adapt to changes in the parameters thanks to its capacity for learning. The ANN can manage time-dependent operations and dynamic simulation using neuro-controllers.

Energy engineering is now able to do very sophisticated predictive model analyses and calculations, such as the nonlinearity of heat and moisture convection movement at boundary layers, which are now outside the scope of conventional physical analysis.

1.7.3 Artificial Neural Networks architectures

The structure of an artificial neural network is made up of layers of neurons. The input layer is the initial layer of neurons, X_i (**Figure 1.9**), and it receives input signals from the environment to generate output. The network's output results, y_j , are produced by the final layer of neurons Y_j . The majority of the computations are carried out by hidden layers of neurons that are situated between the input and output layers. Artificial connections are used to operate relations among each layer and the one beneath it.

Recurrent (feedback) networks and feed-forward networks are two categories of ANN that may be distinguished dependent on their attachment patterns [108], Precisely specific set of output values is produced from a given input by a feed-forward network. Unidirectional interactions exist between layers in the most popular class of feed-forward networks. These networks are identified by their memorylessness, which refers to the fact that the network's past state has no consequence on the way it responds to an input. A dynamic system is a recurrent or feedback network. A new input pattern causes the neuron outputs to be computed. The feedback channels then allow the inputs to each neuron to adapt, bringing the network to a new state.

1.7.3.1 Weights

Each neuron in the preceding layer is connected to a neuron in the layer next to it, and this connection is given a weight that has two indices. The first index of the weight is determined by the receiving neuron number, while the second index is determined by the sending neuron number. The relationship between the single input layer neuron and the second hidden layer neuron is taken into consideration when applying the weight.

1.7.3.2 Bias

Each neuron layer can be responsible for the bias, u_j , as any incoming information might be affected in some way. The linear component of each neuron's output measurement can more clearly follow the estimated function design owing to biases.

The following mathematical formulas can be used to explain the artificial neuron model.

$$u_j = \sum_{i=1}^n w_{i,j} x_i \qquad v_j = u_j + b_j \qquad Y_j = \varphi(v_j)$$

Where x_1, x_2, \dots, x_n are the input signals. $w_{1,j}, w_{2,j}, \dots, w_{i,j}$ are the corresponding synaptic weights of the neuron j . b_j is the bias weight at layer level j . u_j is the output of the linear coupler as a result of the input signals. $\varphi(\dots)$ is the activation function. v_j is the induced local field. and Y_j is the signal produced by the neuron.

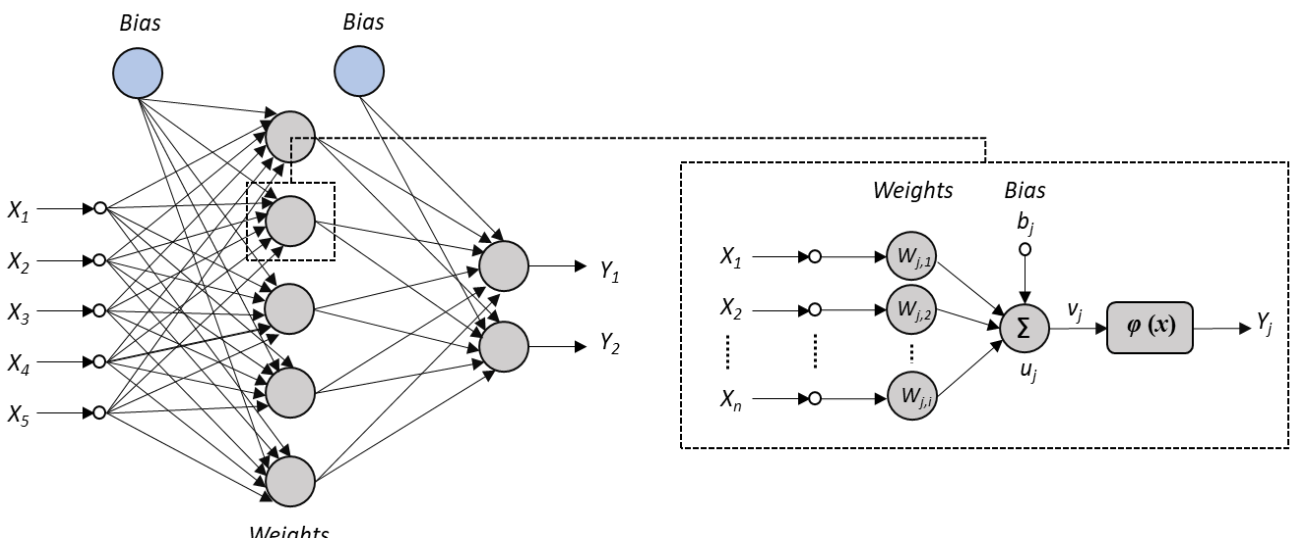


Figure 1.9 Feed-Forward of Artificial Neural Network architect with a nonlinear model of a neuron [138]

1.7.3.3 Activation function $\varphi(x)$

A non-linear activation function of the inputs is used to specify the output state of each neuron, which can be either active ("on" or "1") or inactive ("off" or "0"). Numerous activation functions have been utilized with ANN. Their usefulness is affected by a number of factors, including the range in which they operate without submitting to saturation very quickly, the rate at which the function changes as its argument changes, and the primary computational objectives [109].

The threshold function, sometimes referred to as the Heaviside function, is one of the most frequently utilized activation functions (**Figure 1.10**). With such a function, the neuron's output is 0 in the case of a negative input and 1 in all other cases. The logistic sigmoid is another frequently used function, and the variation of δ controls how suddenly it transitions between its two asymptotic values. Although it is also utilized as an activation function, the hyperbolic tangent function does not permit changing the unexpectedness of the transition. As a result, the inputs to the network are often standardized on a certain interval since particular activation functions operate best on that interval, on which the input data are normalized.

Thus, activation functions like the threshold function, the logistic sigmoid function, the hyperbolic tangent, the Gaussian, and others are used in a variety of investigations. It's possible for the activation function to change from one hidden layer to the next. The most popular and widely used activation function is the logistic sigmoid function, which features continuous derivatives to get around computing challenges.

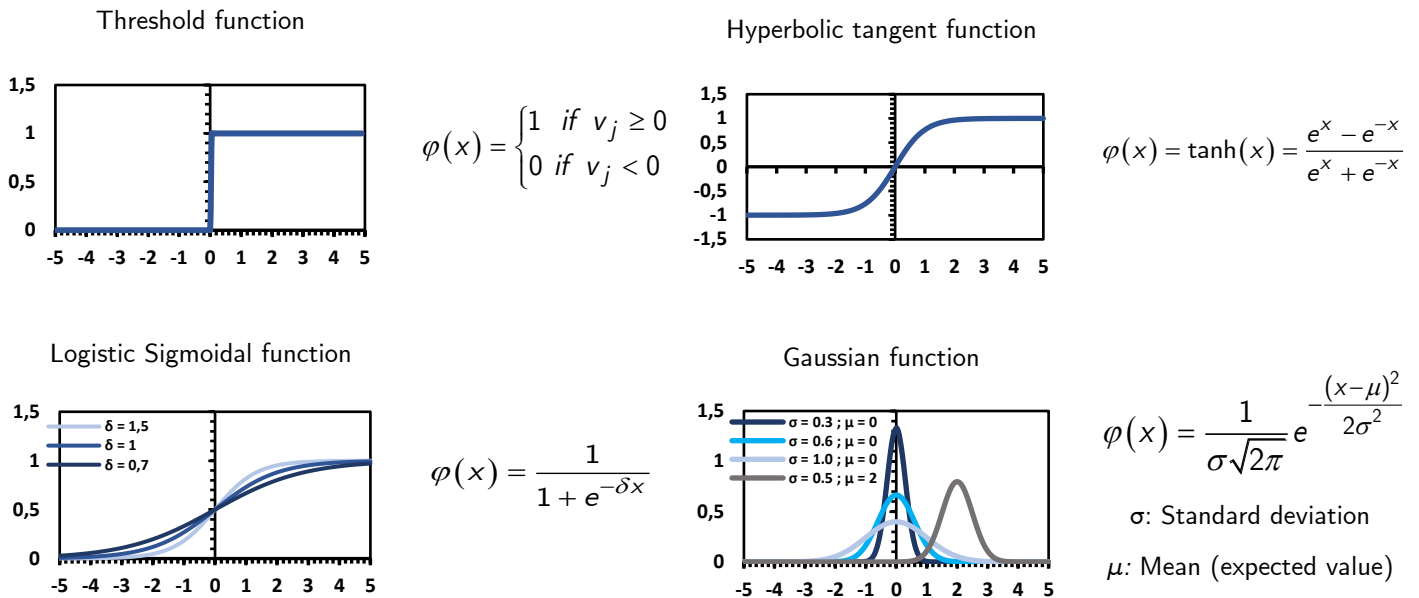


Figure 1.10 Different activation functions of a neuron [138]

1.7.4 Learning methods in Artificial Intelligence

An artificial intelligence network may learn sophisticated links among inputs and outputs from a variety of mixed data. Making ANN functions effective requires providing data for pre-processing investigation and before network training. In this situation, data scaling may be utilized due to the clear considerable disparity between data input and neural network output. The artificial neural network typically uses training data to determine the connectivity weights. This technique is highly attractive since it allows the network's weights to be updated iteratively, which enhances performance over time, and because ANNs may maximize the value of the data that is presented. Instead of adhering to a set of rules established by a predetermined case of studies, ANNs prefer to learn basic idea rules, such as input-output connections, from a sorted number of representative examples. As a result, under some circumstances, this statistical modeling is more trustworthy than the conventional physical modeling. The amount of change made to the weights and biases must be kept as low as possible according to the network's learning rate. However, oscillatory error behaviors might occasionally block the ANN from producing the expected results. The teaching data is often used to train the network in the range of 70 to 80 percent, with the remaining portion being utilized to check the network's correctness.

In order to identify the updating process and employ a learning algorithm that refers to the intended technique to optimize the weights depending on requirements, we must understand how the network weights are adjusted (**Figure 1.11**). The two main learning ideas are learning with a teacher (supervised learning) and learning without a teacher (unsupervised, and reinforced learning) [110]. When learning with a teacher, the network is provided a proper output response for each input set of data, which enables the network's weights to produce outcomes that are roughly equivalent to the known valid replies.

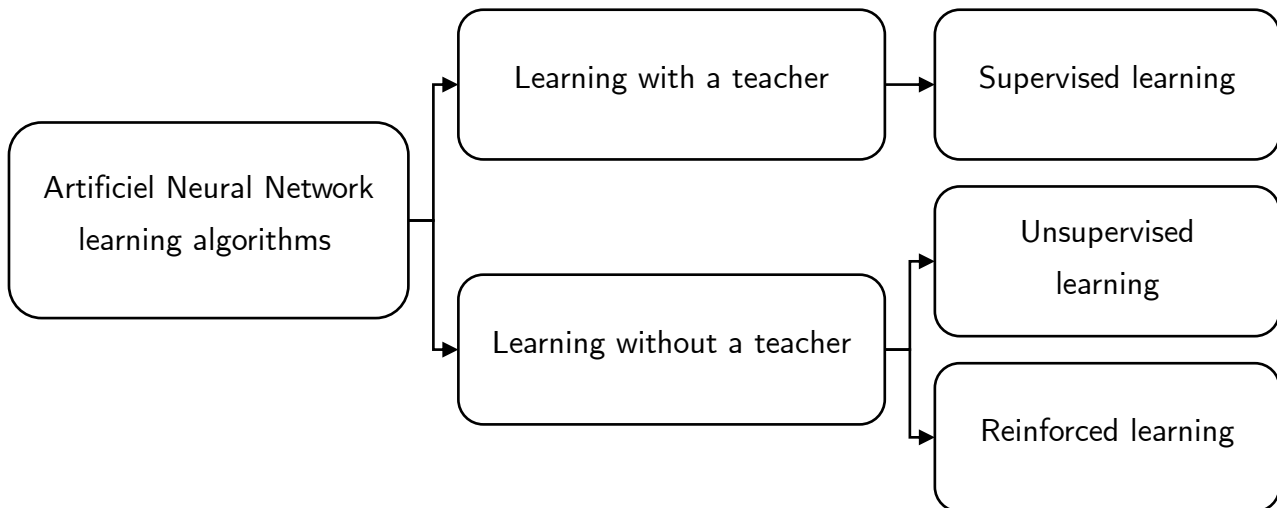


Figure 1.11 Different learning method of ANN [138]

Reinforcement learning, as a form of learning without a teacher, uses a network to develop the optimum architecture for an ANN model without providing the network with the actual solutions. Instead, it provides the network with important criteria on the outputs' accuracy. Contrarily, learning without a teacher or in an unsupervised context would not require a correct answer for the training procedure's input data. It explores the underlying structure of the data, or relationships between variables, classifies structures based on similarities, and enables researchers to occasionally do unsupervised learning using a competitive-learning strategy. As an example, consider a neural network with two layers. The input layer receives the validation data, while the competitive layer is composed of neurons that interact with one another.

1.7.4.1 Statistical comparison and error-correction

The inaccuracy of the output variables can be quantified in a variety of ways through comparison of the estimated provided data with the numeric output results. Therefore, a statistical comparison of simulated and experimental results can be conducted using statistical estimators such the Root Mean Square Error (RMSE) and the coefficient of determination (R^2) in order to assess the reliability of the deep learning training model for coupled heat and moisture transfer.

- **Root mean square error (RMSE)**

During the learning phase, the effectiveness of deep learning model in representing a particular set of observed data can be assessed by computing the RMSE values of the output results.

$$RMSE = \sqrt{\frac{\sum_{i=1}^N (P_i - A_i)^2}{N}} \quad 1.23$$

Where N is the number of measurements in the data set, A_i is the actual measured or experimental data, and P_i is the estimated network output.

- **Coefficient of determination (R^2)**

The linear connection between the output of the predictor variable and the given computed data is quantified by the coefficient of determination. It is expressed in the following way.

$$R^2 = 1 - \frac{SSE}{SST} \quad 1.24$$

$$SSE = \sum_{i=1}^N (P_i - A_i)^2 \quad 1.25$$

$$SST = \sum_{i=1}^N (P_i - \bar{A}_i)^2 \quad 1.26$$

P_i is the predicted network output, A_i the actual measured or experimental data, and \bar{A}_i is their corresponding average values.

1.7.5 Deep Learning approach for building energy simulation

The application of the deep learning technique to model overall thermal behavior of buildings is covered in a number of academic publications. Only the three studies by Tijssens et al. (2019) [111], (2021) [112], and O. May Tzuc et al. [113] (2021) utilize ANN to evaluate the hygrothermal behavior of building materials, for example, Sözer et Aldin [114] and Chegari et al. [115] use it to predict the interior air temperature.

The initial investigation (**Table 1.9**) emphasizes on the use of ANN (multilayer perceptron (MLP), recurrent (RNN), and convolutional networks (CNN)) to forecast hygrothermal reaction time series based on climatic dataset. The authors demonstrate that the intricate patterns of the hygrothermal sensitivity can only be captured by recurrent (RNN) and convolutional networks (CNN). The convolutional network outperformed the recurrent network impressively and taught 10 times quicker for the present application case. The performance of the various neural networks discussed above is investigated by using them to forecast the stochastic hygrothermal behavior of a large masonry wall.

In the second research, the same authors employed the same methodology and hygrothermal behavior technique but just a different type of wall, a wood frame wall [112], as opposed to the ancient huge masonry type wall of their earlier paper [111]. Using a supervised ANN learning technique, 70 % of the training experimental data are utilized to adapt the prediction model to the performance of the output results. The sophistication of the neural network throughout the development of the multi-output model was primarily influenced by the hygrothermal parameter that presented the most assessment challenge, such as the humidity within the wall.

Table 1.9 Summary of building hygrothermal simulation studies based on the ANN approach [138]

Study	ANN Approach	Building scale			ANN architect	Learning methods	Activation function	Statistical comparison
		Material	Wall	Envelope				
May Tzuc et al. [113]	✓	×	✓	×	Feed-forward networks	Supervised learning with experimental data	Tangent sigmoid function	RMSE / MAPE / R ²
Tijskens et al. [111]	✓	×	✓	×	Feed-Forward Back networks	Supervised/unsupervised learning	Not indicated	RMSE / MAPE / R ²

The authors come to the conclusion that ANN modeling has shown to be a reliable method that enables researchers to understand the behavior within concrete without the use of demanding and complex factors. They were unable to identify any usage of the ANN technique for the hygrothermal behavior of bio-based materials in the literature.

1.7.5.1 Strength and weakness of the deep learning approach

A large amount of data and extremely complicated parameterization are needed to cover the whole design area for a building's performance. For instance, it will be challenging to parameterize a three-story structure with various floor sizes and geometries, and a high number of parameters will make it harder to locate sufficient representative data. As a result, an ANN technique only needs a minimal number of inputs, most of which are connected to external conditions.

Consequently, the ANNs are severely constrained by the requirement for a pertinent database. In fact, it is crucial to train the ANN using a thorough learning foundation that includes comprehensive and representative data. Additionally, it is challenging to comprehend physical phenomena using these models, such as changes in hygrothermal behavior caused by climatic factors, occupant behavior, set-point temperature, etc.

However, understanding of material properties like sorption, hysteresis, thermal conductivity, and specific heat is not necessary when employing ANNs for hygrothermal simulations. but simply the temperature, global relative humidity (RH), and relative humidity of the materials.

1.8 Existing data for validation

Model validation's primary objective is to make sure that the model is accurate, along with the governing equations and boundary conditions. Three aspects can be used to appropriately validate a hygrothermal simulation model. (i) to compare the physical model performance to the analytical solution to ensure that the latter is accurate. (ii) to contrast the estimations with further numerical data from the literature that have previously undergone validation. (iii) to model the dynamic hygrothermal responses of a building envelope subjected to an actual external climate and to validate it using experimental data. The model validation of the building envelope part is judged accurate if the numerical and experimental outputs are in accordance.

1.8.1 Analytical validation

Analytical validation is an accurate and reliable validation method, but it can only be applied when it is possible to find an analytical answer. An empirical solution is challenging to find since the governing equations for multilayer enclosures are significantly nonlinear and connected to one another. For this reason, it is preferable to analytically evaluate the coupled heat and moisture model at the one-dimensional scale using already-published data, as those in the benchmarks presented by Hagentoft et al. [68].

1.8.2 Numerical-Numerical Validation

There are several categories into which this validation technique might be divided. It can be compared to numerical findings from prior research publications [30], [31], or it can be a conforming validation of already-produced simulated outputs from hygrothermal simulation software, such as WUFI plus for the nodal approach or the COMSOL Multiphysics benchmarks for the CFD approach [88]. We can either rely on self-programming outcomes if we employ a programming approach such FORTRAN programming with difference finite discretization.

1.8.3 Experimental Validation

The most effective and trustworthy method for validating coupled heat and moisture transport models is still experimentation. The outputs of the computational model are evaluated with the outcomes of experiments to assess the accuracy of the model calculation. Academics have run several experiments pertinent to model validation.

Conclusion of the chapter

For the purpose of validating hygrothermal models for building materials and envelopes, recent experimental research split the three scales of the building, material, wall, and enclosure into these three categories. The capacity to manage convective boundary conditions, which are unique to the tunnel dispositive, is the main distinction between the climate chamber [17], [45] and air tunnel [92], [116] facilities that may be utilized to investigate the hygrothermal reactions of a single material exposing under controlled environments. On the one hand, the wall scale may be divided into two categories, those subjected to temperature-controlled chamber environment and those exposed to outdoor weather. The experimental method used to confirm the accuracy of the numerical modeling may be categorized into two types, putting the wall under a predefined climate setting [10], [14], or putting it in a real climate. Depending on the case study, both single- and multi-layer walls might be included in this classification.

Rafidiarison et al. [117] provide sets of experimental data for single and multi-layer walls using hygroscopic materials to support one-dimensional heat and moisture transmission models. Their experiments were conducted in a twin climate room with oscillation cycles and basic to complex climate settings. Their study's findings may be utilized to confirm the accuracy of any hygrothermal computational simulation.

1.9 Conclusion of the chapter

We investigated techniques in this work that other researchers can implement. Nevertheless, no research offered a comprehensive view of hygrothermal behavior simulation techniques for hygroscopic structures. To better comprehend the building performance testing through comparisons and to estimate the actual impact of moisture transfer on thermal comfort, energy modelers and decision-makers can greatly benefit from understanding the provided conclusion. The utilization of comprehensive, in-depth physical and data-driven models in this study, as well as the benefits and drawbacks of each model, are among its strong points. Our research adds to the basic knowledge on hygrothermal modeling techniques for residential hygroscopic buildings. Numerous numerical methods have been investigated and shown to be capable of delivering accurate results. It's crucial to keep in mind that the simulations account for exceedingly challenging non-linear interaction and dynamics scenarios.

The outcomes may differ from one simulation to the next due to a variance in the computation methodology. These influencing parameters include things like the numerical scheme, the equation-solving technique, the mesh size, and the boundary conditions with diverse sets of potential inputs. It is difficult to accurately simulate the hygrothermal behavior of hygroscopic building materials, which may affect the feasibility of retrofit solutions that adhere to conventional thermal rules. In fact, a bad simulation might result in bad assumptions, which could result in bad actions when upgrading buildings to increase their energy efficiency.

Conclusion of the chapter

In order to compute the combined heat and moisture transport processes, this research reveals a sizable gap in real building energy simulation software. It shows that most softwares simplifies the calculation procedures by ignoring envelope moisture buffering, which results in inaccurate energy simulations. In order to replicate the hygrothermal behavior of structures made of two different types of hygroscopic materials

- Physical models that are based on equations for the hygrothermal balance and physical understanding of the structure. These are frequently acquired using energy simulation tools like COMSOL Multiphysics or WUFI.
- Statistical models that solely employ measurable input/output data and statistical estimate techniques like ANN, CNN, and LSTM models.

Every method may indeed, although, have advantages and disadvantages. There are two subcategories of physical models.

- The CFD method, which splits each zone into many control volumes.
- The nodal method considers each designated zone to be a homogenous volume with constant physical parameters.

The advantages of one tool might not be present in the other tool in particular situations, making the combination of the two tools the "optimum" model and necessitating a coupling approach. In order to achieve a co-simulation between two separate softwares that takes into consideration coupled heat and moisture transfer at various building dimensions, we have included the research that were able to accomplish these. According to the review, a well-established approach is required to estimate the hygrothermal boundary conditions for material or building scales.

Although there are analytical methods to characterize the hygrothermal behavior of permeable materials in the literature, they do not adequately capture the complexity of the time-varying outside humidity, temperature, and incident sun radiation. The main drawback of these methods is that they don't take into account the complexity of actual structures, which have a variety of heat and mass fluxes. The deep learning approaches, which rely on statistical analyses of building hygrothermal activity, are also presented in this work. Several other neural network models, including the multilayer perceptron (MLP), recurrent (RNN), and convolutional networks (CNN), have been investigated in the literature. These techniques are especially helpful when geometry, material, and envelope physical parameters are not given.

Physical modeling requires more construction knowledge than deep learning modeling, which is typically more difficult to apply. The data gathered in this work, in conclusion, provide instruction to researchers and engineers working on building modeling and can contribute to the design and rehabilitation studies of hygroscopic building materials.

Conclusion of the chapter

As is evident, there is disagreement in the literature on the applicability of the hygrothermal behavior of structures made of porous materials (bio-based materials for example). There have been few research done on simulating the hygrothermal behavior of a whole building using a hygroscopic material while taking into consideration the residents and HVAC systems. The wall scale was the only thing that was studied. A knowledge gap about hygrothermal bridges of porous enclosure also shown by the literature review.

Chapter 2.

Basic notions of heat and mass transfer

Contents

2.1	INTRODUCTION TO THE CHAPTER	62
2.2	PARTIAL DIFFERENTIAL EQUATIONS TO FINITE DIFFERENCE EQUATIONS	62
2.2.1	Classification of partial differential equations	63
2.2.2	Boundary condition types	64
2.2.3	Heat and mass transport equations.....	65
2.3	MODES OF HEAT TRANSFER	66
2.3.1	Conductive transfer	66
2.3.1.1	One-dimensional stationary conduction, Fourier law	66
2.3.1.2	Analytical resolution of the one-dimensional unsteady conduction	67
2.3.1.2.1	Infinite plane wall with Dirichlet boundary condition	67
2.3.1.2.1.1	Separation of variables method	67
2.3.1.2.1.2	Laplace transformation method	70
2.3.1.2.2	Infinite plane wall with Neumann boundary condition	72
2.3.1.3	Numerical resolution of the one-dimensional unsteady conduction.....	74
2.3.1.3.1	Partial differential equations for heat transfer	75
2.3.1.3.2	Explicit scheme	76
2.3.1.3.3	Implicit scheme	78
2.3.1.3.4	Crank and Nicolson scheme	79
2.3.2	Convective transfer.....	80
2.3.2.1	Method of dimensionless analysis, Buckingham π theorem.....	81
2.3.2.2	Determination of convective exchange coefficient for a plane wall.....	84
2.3.3	Radiative transfer	86
2.3.3.1	Radiative properties of real bodies	86
2.3.3.2	Solar radiation	90
2.3.3.2.1	ASHRAE Clear sky equations for solar radiation	90
2.3.3.2.2	Clear-Sky Solar Radiation	91
2.3.3.2.3	Calculation of Clear-Sky Solar Irradiance Incident on receiving surface	94
2.4	MODES OF MASS TRANSFER	96
2.4.1	Mass diffusion	96
2.4.1.1	Fick's Law	96
2.4.1.2	Diffusion coefficient	98
2.4.1.3	Diffusion of fluids through porous media	99
2.4.1.4	One-dimensional stationary mass diffusion.....	100
2.4.1.5	One-dimensional unsteady mass diffusion	103
2.4.2	Mass convection.....	108

2.4.2.1	Dimensional analysis applied to convective mass transfer	108
2.5	DEVELOPED COUPLED HEAT AND MASS TRANSFER MODELS.....	109
2.5.1	Common models of coupled heat and mass transfer	110
2.5.1.1	Philip and De Vries model.....	110
2.5.1.2	Luikov Model.....	110
2.5.1.3	Whitaker model	111
2.5.1.4	Künzel model.....	111
2.5.1.5	Mendes model.....	112
2.6	CONCLUSION OF THE CHAPTER	113

2.1 Introduction to the chapter

Employing numerical techniques flexible enough to replicate the associated transfer events is required for the intended multi-scale investigation. The energy performance of these energy systems and buildings needs to be assessed. We have to work on determining the amount of heat that can be passed through building components and transferred to adjacent structures. Calculating heat and mass transmission at the wall and building scales is necessary for this assignment. It is necessary to establish an effective method for quantifying dynamic energy and heat transfer from walls to buildings. Within the parameters of this term, a thorough examination of the thermal and hydric interactions between the building enclosure and the environment is being conducted to determine the effects of energy distribution inside the envelopes. Quantifying the energy performances of building enclosures, such as walls, is crucial for predicting their efficiency and overall performance in capturing and distributing thermal energy between various sizes. While doing so, flexibility should be maintained to allow for the introduction of complex material elements at different scales, such as the scale of a building or even a wall.

The uncoupled mass and heat transfer models in the program do not offer this flexibility throughout all scales. The fundamental ideas behind the various physical transfer phenomena must be addressed before developing more complex models. These include the concepts of heat capacity, mass diffusion, and thermal resistance, which are fundamental to both conventional thermal analysis and contemporary methods for energy analysis in complicated geometries like buildings. It is crucial to understand the reciprocal dependencies among some of these phenomena along with the relationships between the theories and the behavior of other phenomena on a limited basis, such as fluid dynamics, heat transfer, and mass transfer.

In this chapter, each fundamental physical model is thoroughly explained. Along with additional considerations that must be addressed when using an analytical or numerical resolution for physical heat and mass transfer in certain conditions. The mathematical foundation for the varied forms of heat and mass transport is provided in the contents of the following chapter. This topic is explained using several examples, including both simple and advanced computations.

2.2 Partial differential equations to finite difference equations

We will explore the most popular approaches to solving partial differential equations in this manner. The Laplace transform, separation of variables, Fourier series, and parameter variation are among the most used approaches. We will go through the various approaches in depth, including their advantages and disadvantages in terms of efficiency and dependability. As more information becomes available, we will examine the numerous approaches available to solve a specific PDE (Partial differential equations) after starting with the simplest approach.

The sequence in which the fundamental mathematical models are expressed as partial differential equations is determined by the maximum degree of partial derivatives occurring in the equation. Ordinary differential equations, hyperbolic, parabolic, and elliptic differential equations are examples of partial differential equation models.

$$a \frac{\partial f}{\partial x}(x, y) - bf(x, y) = 0 \quad \text{First-order PDE} \quad \mathbf{2.1}$$

$$a \frac{\partial^2 f}{\partial x^2}(x, y) - bf(x, y) = 0 \quad \text{Second-order PDE} \quad \mathbf{2.2}$$

Unless the relationships between the function f as well as its partial derivatives are a linear combination, the system of equations is classified as linear. When it comprises just changeable functions and their partial derivatives, it is said to be homogeneous. It is considered quasi-linear when it is linear in terms of to the greatest power of partial derivatives in each element.

$$\frac{\partial f}{\partial t}(x, t) + b \frac{\partial f}{\partial x}(x, t) = 0 \quad \text{Linear, first order and homogeneous PDE} \quad \mathbf{2.3}$$

$$f \frac{\partial f}{\partial t}(x, t) + a \frac{\partial f}{\partial x}(x, t) + f^2 = b \quad \text{Non-linear, first-order and inhomogeneous PDE} \quad \mathbf{2.4}$$

$$\frac{\partial f}{\partial t}(x, t) + f \frac{\partial f}{\partial x}(x, t) - b \frac{\partial^2 f}{\partial x^2}(x, t) = 0 \quad \text{Quasi-linear, second order and homogeneous PDE} \quad \mathbf{2.5}$$

$$\frac{\partial^2 f}{\partial x^2}(x, t) + \frac{\partial^2 f}{\partial t^2}(x, t) = 0 \quad \text{Second order homogeneous nonlinear PDE} \quad \mathbf{2.6}$$

2.2.1 Classification of partial differential equations

Applications based on partial differential equations for heat and mass transfer in 1D or 2D are of special interest to us. Three categories can be used to group them:

$$a \frac{\partial^2 f}{\partial x^2} + b \frac{\partial^2 f}{\partial x \partial y} + c \frac{\partial^2 f}{\partial y^2} + d \frac{\partial f}{\partial x} + e \frac{\partial f}{\partial y} + gf = 0 \quad \mathbf{2.7}$$

$$b^2 - 4ac < 0 \quad \text{Elliptic equation} \quad \mathbf{2.8}$$

$$b^2 - 4ac = 0 \quad \text{Parabolic equation} \quad \mathbf{2.9}$$

$$b^2 - 4ac > 0 \quad \text{Hyperbolic equation} \quad \mathbf{2.10}$$

- **Elliptic equation**

Elliptic equations, which describe usually steady physical applications, are time independent equilibrium solutions.

$$\Delta f = \frac{\partial^2 f}{\partial x^2} + \frac{\partial^2 f}{\partial y^2} = g(x, y) \quad 2.11$$

When it is homogeneous, $g(x, y) = 0$, it is referred to as Laplace's equation, and when $g(x, y) > 0$, it is considered as Poisson's equation. It can be used to represent a perfect, incompressible and steady irrotational flow in 2D.

- **Parabolic equation**

Equations for propagation with a regularizing effect are termed parabolic issues. An illustration of a parabolic equation is as follows.

$$\frac{\partial f}{\partial t} - \alpha \frac{\partial^2 f}{\partial x^2} = g(x, t) \quad 2.12$$

The temperature or molar concentration may be represented by the variable $f(x, t)$ in the pure diffusion of heat or mass equation in one dimension. The source term is represented by the variable g . The subsequent convection and diffusion equations can be investigated for a 1D flow and a second order linear PDE.

$$\frac{\partial f}{\partial t} + U_0 \frac{\partial f}{\partial x} - \nu \frac{\partial^2 f}{\partial x^2} = 0 \quad 2.13$$

- **Hyperbolic equation**

Hyperbolic equations discuss issues of finite velocity development or propagation. Here is an illustration of a hyperbolic equation. Hence, an equation for a one-dimensional wave is shown in the equation above.

$$\frac{\partial^2 f}{\partial x^2} = \frac{1}{c^2} \frac{\partial^2 f}{\partial t^2} \quad 2.14$$

2.2.2 Boundary condition types

- **Dirichlet boundary condition**

The variable is specified as follows for a boundary portion limit or section.

$$f(x \in \partial\Omega, t) = g(x, y) \quad 2.15$$

- **Neumann boundary condition**

The values are for the gradient of the variable in the direction perpendicular to the boundary.

$$\frac{\partial f}{\partial n}(x \in \partial\Omega, t) = g(x, y) \quad 2.16$$

- **Continuity and generalized transport equation**

In many natural processes, transport mechanisms by diffusion and convection control the flux of

energy. In general, and for the majority of engineering applications, heat transfer occurs when the temperature gradient changes within the domain. A fluid or solid's density, specific heat, and thermal conductivity are frequently taken for granted to be constants. It is possible to investigate the governing equation in a domain with a fluid-filled interface. The domain location and time are indicated by $x \in \Omega$ and \underline{t} , respectively.

In the most general case, the fluid density $\rho = \rho(x,t)$ depends on time and place. The fluid velocity field is denoted by $V = V(x,t)$, and the theory of mass conservation assumes that.

$$\frac{\partial \rho}{\partial t} + \bar{\nabla}(\rho \bar{V}) = 0 \tag{2.17}$$

As a result, the general transport equation may be expressed as follows in differential form.

$$\rho \frac{\partial \phi}{\partial t} + \bar{V} \rho \bar{\nabla}(\phi) = \bar{\nabla}(\Gamma_{\phi} \bar{\nabla} \phi) + S_{\phi} \tag{2.18}$$

The entire structure of this equation provides numerous opportunities to investigate the solution's results for a variety of behavioral cases, including steady/unsteady conditions, pure convection, pure diffusion, and even a source term. It also allows for the design of straightforward test problems that can be solved analytically or numerically in a wide range of physics fields, including heat and mass transfer.

2.2.3 Heat and mass transport equations

The unstable state and source elements in the second-order diffusion-convection equation provide the base denominator for the energy equation. The temperature term, which is written as $T(x,t)$, is stated as an independent variable in the energy equation.

$$\rho c_p \frac{\partial T}{\partial t} + \bar{V} \rho c_p \bar{\nabla}(T) = \bar{\nabla}(\lambda \bar{\nabla} T) + S \tag{2.19}$$

Thus, c_p is the thermal heat capacity and λ is the thermal conductivity, both of which are taken to be constant and independent of temperature. S stands for the domain heat source, while V represents the convection transport term's velocity vector. The mass conservation theories serve as the foundation for the moisture transport equations. Describe the equilibrium between the change in mass within volume V and the net fluxes of mass over the surrounding surface S .

Take the constant volume V in space that is covered by surface $V = S$ as an example. We can obtain the mass transport equation from a mass balance on a finite control volume V , similar to the heat transport method. The mass transfer equation for the species can therefore be written as follows.

$$\frac{\partial W}{\partial t} + \vec{V} \nabla (W) = \nabla (D_i \nabla W) + S_W \tag{2.20}$$

Furthermore, it may be written based on the molar concentration.

$$\frac{\partial C}{\partial t} + \vec{V} \nabla (C) = \nabla (D_i \nabla C) + S_C \tag{2.21}$$

Where D_i is the diffusion coefficient, which is often considered to be constant in the formulas above, and S is the number of species or moles produced per unit of time and volume.

2.3 Modes of heat transfer

2.3.1 Conductive transfer

2.3.1.1 One-dimensional stationary conduction, Fourier law

Heat transfer with a consistent heat flow and a stable spatial temperature distribution is referred to as steady-state thermal conduction. The amount of heat transmitted and the specific temperature distribution change transiently when a body undergoes heating or cooling operation.

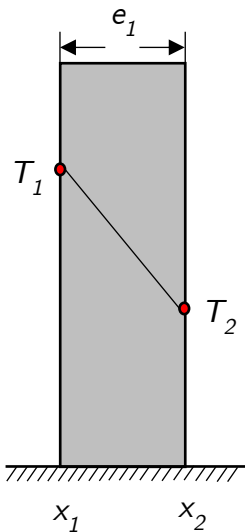


Figure 2.1 Heat conduction in a plane wall [118]

The corresponding boundary conditions are.

$$\begin{aligned} x_1 = 0 & \quad T(x) = T_1 \\ x_2 = L & \quad T(x) = T_2 \end{aligned}$$

The heat equation is as follows once the regime is stationary and the conductive heat propagation is one-dimensional.

$$\frac{\partial^2 T}{\partial x^2} = 0 \tag{2.22}$$

Integration yields the following results.

$$T(x) = Ax + b \tag{2.23}$$

Hence, the temperature distribution takes on the form.

$$T(x) = T_1 - (T_1 - T_2) \frac{x}{L} \tag{2.24}$$

The heat flow caused by a material's temperature difference is described by the Fourier law.

$$\dot{q} = \lambda \nabla T = \lambda \frac{\partial T}{\partial x} \tag{2.25}$$

The spatial coordinate in the 1D approach is x . Both the thermal conductivity and temperature gradient in space affect the heat flux proportionally. It spreads in a direction opposite to the

temperature gradient. Moreover, n is the normal constituent of the space vector passing through this surface, and q is the normal element of the heat flux vector passed through the area.

The following describes the heat ratio on a surface.

$$\dot{Q} = \int_S \dot{q} \, ds \tag{2.26}$$

Along with the adiabatic theory, which holds that heat loss is negligible, at the summit and bottom of the wall vertically. assuming a constant property of the material's physics, such thermal conductivity, and a straightforward heat flux in the x direction. The integration of equation 2.26 takes a form such as the following.

$$\dot{Q} = \int_{x_1}^{x_2} \dot{q} \, ds = \int_{T_1}^{T_2} -\lambda S dT = \frac{\lambda}{e_1} S (T_1 - T_2) \tag{2.27}$$

Plane walls usually have several layers, including building envelopes, cold chamber insulation, and housing walls. The picture below shows a wall made up of n layers with different thermal conductivities and thicknesses.

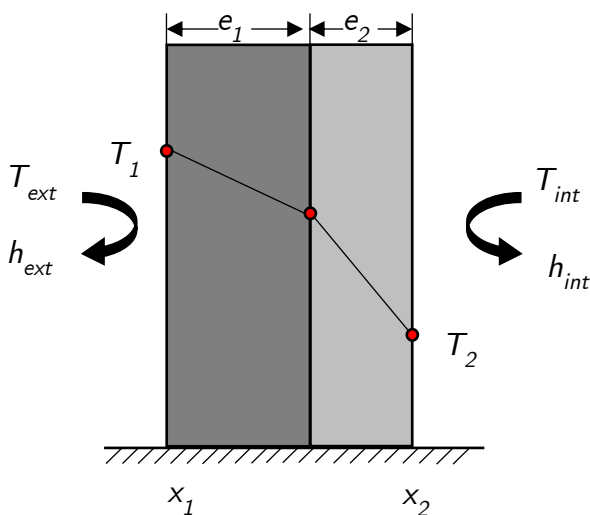


Figure 2.2 Heat conduction through a multilayer wall

The same calculations used to obtain a plane wall's heat transfer coefficient may be used to determine the global heat transfer coefficient.

$$\dot{Q} = US(T_{ext} - T_{int}) \tag{2.28}$$

The global heat transfer coefficient U is.

$$U = \frac{1}{\frac{1}{h_{ext}} + \sum_{i=1}^n \frac{e_i}{\lambda_i} + \frac{1}{h_{int}}} \tag{2.29}$$

2.3.1.2 Analytical resolution of the one-dimensional unsteady conduction

2.3.1.2.1 Infinite plane wall with Dirichlet boundary condition

The body's temporal and spatial temperature distribution will undoubtedly vary if a subject with starting temperature T_i is placed in an environment with changing temperature. A process of transient heat conduction occurs throughout this last one.

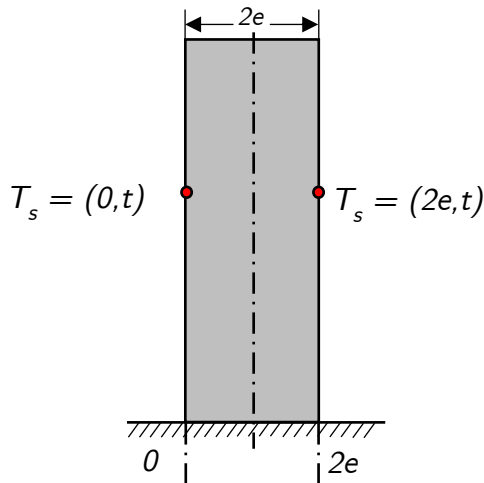
2.3.1.2.1.1 Separation of variables method

The differential equation describing the temporal and spatial distribution of the wall's temperature may be stated as follows, since only heat transmission in the x direction is feasible

due to the infinite side dimensions of the wall (the Y and Z directions).

$$\frac{\partial T}{\partial t} = \alpha \frac{\partial^2 T}{\partial x^2} \quad \text{with} \quad \alpha = \frac{\lambda}{\rho c_p} \quad \text{2.30}$$

The material's thermal diffusivity is indicated by the letter " α ". It measures in $\text{m}^2 \text{s}^{-1}$. The differential equation shows that when a material is chilled or warmed from the outside, its thermal diffusivity has the most impact on the time and space temperature distribution.



The associated boundary conditions.

$$\left\{ \begin{array}{l} \frac{\partial T}{\partial x}(e, t) = 0 \\ T(0, t) = T_s \\ T(2e, t) = T_s \\ T(x, 0) = T_i \end{array} \right.$$

Figure 2.3 Infinite wall with constant surface temperature

The equation 2.30 can be expressed by incorporating the change of variable $\theta(x,t) = T(x,t) - T_s$.

$$\frac{\partial \theta}{\partial t} = \alpha \frac{\partial^2 \theta}{\partial x^2} \quad \text{2.31}$$

The boundary conditions change to.

$$\left\{ \begin{array}{l} \frac{\partial \theta}{\partial x}(e, t) = 0 \\ \theta(0, t) = 0 \\ \theta(2e, t) = 0 \\ \theta(x, 0) = T_i - T_s \end{array} \right.$$

We can use the variable separation approach of x and t with $\theta(x,t) = X(x)\tau(t)$ since there is just one non-homogeneous boundary condition.

$$\alpha \tau \frac{\partial^2 X}{\partial x^2} = X \frac{\partial \tau}{\partial t} \rightarrow \frac{1}{X} \frac{\partial^2 X}{\partial x^2} = \frac{1}{\alpha \tau} \frac{\partial \tau}{\partial t} = -K^2 \quad \text{2.32}$$

We infer that.

$$\frac{\partial^2 X}{\partial x^2} + K^2 X = 0 \rightarrow X(x) = C_1 \cos(K.x) + C_2 \sin(K.x) \quad 2.33$$

$$\frac{\partial \tau}{\partial t} + \alpha K^2 \tau = 0 \rightarrow \tau(t) = C_3 \exp(-\alpha K^2 t) \quad 2.34$$

Therefore,

$$\theta(x, t) = [C_1 \cos(K.x) + C_2 \sin(K.x)] C_3 \exp(-\alpha K^2 t) \quad 2.35$$

The boundary condition $\theta(0, t) = 0$ allows us to determine the coefficient C_1 .

$$[C_1 \cos(K.x) + 0] C_3 \exp(-\alpha K^2 t) = 0 \rightarrow \cos(0) = 1 \text{ Hence } C_1 = 0 \quad 2.36$$

Hence.

$$\theta(x, t) = [C_2 \sin(K.x)] C_3 \exp(-\alpha K^2 t) \quad 2.37$$

The boundary condition for symmetry can be expressed as follows.

$$\frac{\partial \theta(x, t)}{\partial x} = [C_2 \sin(K.e)] = 0 \quad 2.38$$

There are an unlimited number of possible solutions to the equation, which have the following form.

$$K_n = (2n + 1) \frac{\pi}{2e} \quad \text{With} \quad n \in [0 \rightarrow +\infty] \quad 2.39$$

In light of the fact that we have a solution for each value of $K_n \in [0 \rightarrow +\infty]$, we can express the general solution as follows using the approach of variable separation.

$$\theta(x, t) = \sum_{n=0}^{\infty} [C_n \sin(K_n.x)] \exp(-\alpha K_n^2 t) \quad 2.40$$

The initial condition $\theta(x, 0) = \theta_i = T_i - T_s$ serves as the foundation for calculating the coefficients C_n .

$$\theta(x, 0) = \theta_i = \sum_{n=0}^{\infty} [C_n \sin(K_n.x)] \quad 2.41$$

We multiply the two parts of the equation (2.41) by the quantity $(K_m x)$ and integrates it on the interval $[0, e]$ (symmetry), then we obtain.

$$\int_0^e \theta_i \sin(K_m \cdot x) dx = \int_0^e \sin(K_m \cdot x) \sin(K_n \cdot x) dx \quad 2.42$$

If $n \neq m$ we obtain the orthogonality of the eigenfunctions.

$$C_n = \frac{\int_0^e \theta_i \sin(K_n \cdot x) dx}{\int_0^e \sin^2(K_n \cdot x) dx} = \frac{\frac{\theta_i}{K_n}}{\frac{e}{2}} = \frac{2\theta_i}{K_n e} = \frac{4\theta_i}{(2n+1)\pi} \quad 2.43$$

Finally, the solution of the equation 2.41 is.

$$\theta(x, t) = \theta_i \sum_{n=0}^{\infty} [C_n \sin(K_n \cdot x)] \exp(-\alpha K_n^2 t) \quad 2.44$$

$$T(x, t) = T_s + (T_i - T_s) \sum_{n=0}^{\infty} \frac{\pi}{4} \left(\frac{1}{2n+1} \right) \left(\sin \left((2n+1) \frac{\pi}{2e} \cdot x \right) \right) \exp \left(-\alpha \left((2n+1) \frac{\pi}{2e} \right)^2 t \right) \quad 2.45$$

2.3.1.2.1.2 Laplace transformation method

As before, we continue to look at the possibility of an open-ended wall (According to the Y and Z directions) with symmetry, which has an initial temperature T_i at the time $t=0$ as well as a surface temperature T_s at $x = \pm e$.

The associated boundary conditions.

$$\left\{ \begin{array}{l} \frac{\partial T}{\partial x}(0, t) = 0 \\ T(+e, t) = T_s \\ T(-e, t) = T_s \\ T(x, 0) = T_i \end{array} \right.$$

The equation can be expressed as follows by incorporating the new change of variable $\theta(x, t) = T(x, t) - T_i$, as before.

$$\frac{\partial \theta}{\partial t} = \alpha \frac{\partial^2 \theta}{\partial x^2} \quad 2.46$$

The boundary conditions change to.

$$\left\{ \begin{array}{l} \frac{\partial \theta}{\partial x}(0, t) = 0 \\ \theta(e, 0) = T_s - T_i \\ \theta(-e, 0) = T_s - T_i \\ \theta(x, 0) = 0 \end{array} \right.$$

We define $\bar{\theta}(x, p) = \mathcal{L}\{\theta(x, t)\}$ as the Laplace transform of variable change $\theta(x, t)$.

Equation **2.46** of Laplace transform yields the following results.

$$\frac{d^2 \bar{\theta}}{dx^2} = \frac{1}{\alpha} [p\bar{\theta} - \theta(x, 0)] \quad \text{with } \theta(x, 0) = 0 \tag{2.47}$$

The equation **2.46** can be expressed as follows.

$$\frac{d^2 \bar{\theta}}{dx^2} - k^2 \bar{\theta} = 0 \quad \text{with } k = \sqrt{\frac{p}{\alpha}} \tag{2.48}$$

Then, the solution of the equation **2.48** is.

$$\bar{\theta}(x, p) = C_1 \cosh(k.x) + C_2 \sinh(k.x) \tag{2.49}$$

The symmetry boundary condition $\frac{\partial \theta}{\partial x}(0, p) = 0$ shows that $C_2 = 0$, so the equation **2.49** can be written as follows.

$$\bar{\theta}(x, p) = C_1 \cosh(k.x) \tag{2.50}$$

The boundary condition $\theta(e, t) = T_s - T_i \xrightarrow{\mathcal{L}} \theta(e, p) = \frac{T_s - T_i}{p}$, allows us to calculate the coefficient C_1 of the equation **2.50**, hence.

$$C_1 = \frac{T_s - T_i}{p \cosh(k.e)} \tag{2.51}$$

Therefore.

$$\bar{\theta}(x, p) = \frac{(T_s - T_i) \cosh(k.x)}{p \cosh(k.e)} \tag{2.52}$$

We know that $\cosh(x) = \frac{e^x + e^{-x}}{2}$ and using the development $\frac{1}{1+x} = \sum_{n=0}^{\infty} (-1)^n x^n$.

We get the following formulas.

$$\cosh(k.x) = \frac{e^{k.x} + e^{-k.x}}{2}, \quad \cosh(k.e) = \frac{e^{k.e} + e^{-k.e}}{2}, \quad \frac{1}{1 + e^{-2.k.e}} = \sum_{n=0}^{\infty} (-1)^n e^{-2.k.e.n}$$

The equation 2.52 is written as follows.

$$\bar{\theta}(x,p) = \frac{(T_s - T_i)}{p} \frac{e^{k.x} + e^{-k.x}}{e^{k.e}(1 + e^{-2.e.k})} = \frac{(T_s - T_i)}{p} \left(e^{-k(e-x)} + e^{-k(e+x)} \right) \sum_{n=0}^{\infty} (-1)^n e^{-2.e.k.n} \quad 2.53$$

The inverse Laplace transformation leads to.

$$\frac{e^{(k.x)}}{p} \xrightarrow{\mathcal{L}^{-1}} \operatorname{erfc}\left(\frac{x}{2\sqrt{\alpha.t}}\right) \quad 2.54$$

$$\bar{\theta}(x,p) \xrightarrow{\mathcal{L}^{-1}} \theta(x,t) = T(x,t) - T_i \quad 2.55$$

$$T(x,t) = T_i + (T_s - T_i) \left[\sum_{n=0}^{\infty} (-1)^n \operatorname{erfc}\left(\frac{(2n+1)e-x}{2\sqrt{\alpha.t}}\right) + \sum_{n=0}^{\infty} (-1)^n \operatorname{erfc}\left(\frac{(2n+1)e+x}{2\sqrt{\alpha.t}}\right) \right] \quad 2.56$$

2.3.1.2.2 Infinite plane wall with Neumann boundary condition

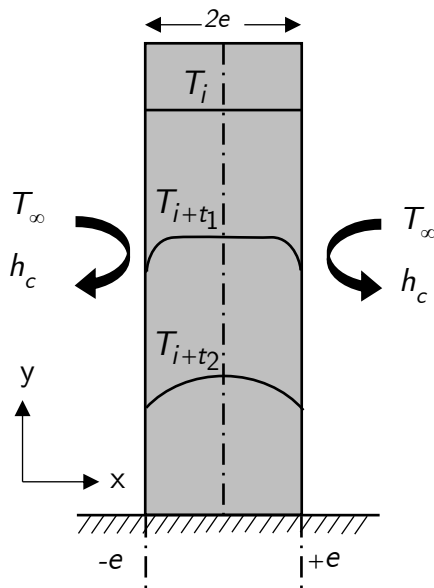


Figure 2.4 Infinite wall with convective exchange on the surfaces

The associated boundary conditions.

$$\left\{ \begin{array}{l} \frac{\partial T}{\partial x}(0,t) = 0 \\ -\lambda \frac{\partial T}{\partial x}(e,t) = h_{\infty} (T(e,t) - T_{\infty}) \\ T(x,0) = T_i \end{array} \right.$$

By introducing the change of variable, as before, $\theta(x,t) = T(x,t) - T_{\infty}$, so the equation 2.30 can be written as follows.

$$\frac{\partial \theta}{\partial t} = \alpha \frac{\partial^2 \theta}{\partial x^2} \quad 2.57$$

We continue with the same example of an opened-end plane wall (according to the Y and Z directions) with the symmetry hypothesis, this wall has an initial temperature of T_i at time $t = 0$ and will be submerged in a fluid with a lower temperature T_{∞} . Heat will therefore be transmitted to the environment via the wall's surface. The boundary conditions change to.

$$\left\{ \begin{array}{l} \frac{\partial \theta}{\partial x}(0, t) = 0 \\ -\lambda \frac{\partial \theta}{\partial x}(e, t) = h_{\infty} \theta_e \\ \theta(x, 0) = \theta_{ii} \end{array} \right\}$$

Because we have only one non-homogeneous boundary condition, we can implement the method of variable separation of x and t with $\theta(x, t) = X(x)\tau(t)$ and proceed the same way as for the Dirichlet boundary condition, consequently.

$$\theta(x, t) = [C_1 \cos(K.x) + C_2 \sin(K.x)] \exp(-\alpha K^2 t) \tag{2.58}$$

Visit the page (67) for the variable separation technique's solution process to learn more about the method. The boundary condition $-\lambda \frac{\partial \theta(e, t)}{\partial x} = h_{\infty} \theta(e, t)$ helps us to find the coefficient C_1 .

$$[-C_1 \sin(0) + C_2 \cos(0)] C_3 \exp(-\alpha K^2 t) = 0 \rightarrow \cos(0) = 1 \quad \text{so} \quad C_2 = 0 \tag{2.59}$$

Thus.

$$\theta(x, t) = [C_1 \cos(K.x)] \exp(-\alpha K^2 t) \tag{2.60}$$

$$\frac{\partial \theta(e, t)}{\partial x} = -C_1 \sin(K.e) \exp(-\alpha K^2 t) \tag{2.61}$$

The boundary condition $-\lambda \frac{\partial \theta(e, t)}{\partial x} = h_{\infty} \theta(e, t)$, allows to deduce.

$$\lambda C_1 \sin(K.e) K \exp(-\alpha K^2 t) = h_{\infty} C_1 \cos(K.e) \exp(-\alpha K^2 t) \tag{2.62}$$

$$\frac{\sin(K.e)}{\cos(K.e)} K = \frac{h_{\infty}}{\lambda} \rightarrow K \tan(K.e) = \frac{h_{\infty}}{\lambda} \tag{2.63}$$

Thus, for each value of $K_n \in [0 \rightarrow \infty]$, the equation 2.63 provides a limitless number of solutions. The following is the general form of the solution to the general equation 2.60.

$$\theta(x, t) = \sum_{n=0}^{\infty} [C_n \cos(K_n.x)] \exp(-\alpha K_n^2 t) \tag{2.64}$$

Using the boundary condition for $t = 0$ and multiplying the two parts of the equation 2.64 by the quantity $\cos(K_m.x)$, we get (orthogonal functions), so we have.

$$\int_0^e \theta_i \cos(K_m \cdot x) dx = \int_0^e C_m \cos(K_m \cdot x) \cos(K_n \cdot x) dx \quad 2.65$$

$$\int_0^e C_m \cdot \cos(K_m \cdot x) \cos(K_n \cdot x) dx = \int_0^e C_m \cos^2(K_n \cdot x) dx = C_m \int_0^e \frac{1}{2} + \frac{1}{2} \cos(2K_n \cdot x) dx \quad 2.66$$

$$C_m \int_0^e \frac{1}{2} + \frac{1}{2} \cos(2K_n \cdot x) dx = C_m \left(\left[\frac{(e)}{2} \right] + \left[\frac{\sin(2K_n \cdot e)}{4K_n} \right] \right) \quad 2.67$$

$$\int_0^e \theta_e \cos(K_m \cdot x) dx = \theta_e \left[\frac{\sin(K_n \cdot e)}{K_n} \right] \quad 2.68$$

In accordance with the definition of "double-angle," $\sin(2x) = \frac{2 \tan(x)}{1 + \tan^2(x)}$ and with

$$\tan(k_n \cdot e) = \frac{h_\infty}{\lambda k_n}.$$

$$C_m \left(\left[\frac{(e)}{2} \right] + \left[\frac{1}{4K_n} \frac{2 \tan(K_n \cdot e)}{1 + \tan^2(K_n \cdot e)} \right] \right) = \theta_i \frac{\sin(K_n \cdot e)}{K_n} \quad 2.69$$

$$C_m = \theta_i \frac{\sin(K_n \cdot e)}{k_n} 2 \left(\frac{e \left(\frac{h_\infty}{\lambda \cdot e} + \frac{h_\infty^2}{\lambda^2} + K_n^2 \right)}{K_n^2 + \frac{h_\infty^2}{\lambda^2}} \right)^{-1} \quad 2.70$$

Finally, we obtain at the temperature distribution equation.

$$T(x,t) = T_\infty + (T_i - T_\infty) 2 \sum_{n=0}^{\infty} \frac{\sin(K_n \cdot e)}{K_n} \left(\frac{e \left(\frac{h_\infty}{\lambda \cdot e} + \frac{h_\infty^2}{\lambda^2} + K_n^2 \right)}{K_n^2 + \frac{h_\infty^2}{\lambda^2}} \right)^{-1} \cos(K_n \cdot x) e^{(-\alpha K_n^2 t)} \quad 2.71$$

2.3.1.3 Numerical resolution of the one-dimensional unsteady conduction

The choice of numerical methods, such as the finite volume or element finite approach, determines the capacity to calculate the temperature distribution in complex one-dimensional or multidimensional thermal conduction geometries. In this section, some of the foundations of numerical solution that simply use the finite difference approach will be presented.

2.3.1.3.1 Partial differential equations for heat transfer

The choice of a specific finite discretization method in the solution of partial differential equations with finite differences also depends on the kind of partial differential equation being solved.

$$A \frac{\partial^2 \phi}{\partial x^2} + B \frac{\partial^2 \phi}{\partial x \partial y} + C \frac{\partial^2 \phi}{\partial y^2} + D \frac{\partial \phi}{\partial x} + E \frac{\partial \phi}{\partial y} + F \phi + S(x, y) = 0 \tag{2.72}$$

The following formula is used to represent the 2D heat transfer equation when the two-dimensional Laplace's equation is elliptic, which is shown by setting $A = 1$, $B = 0$, and $C = 1$.

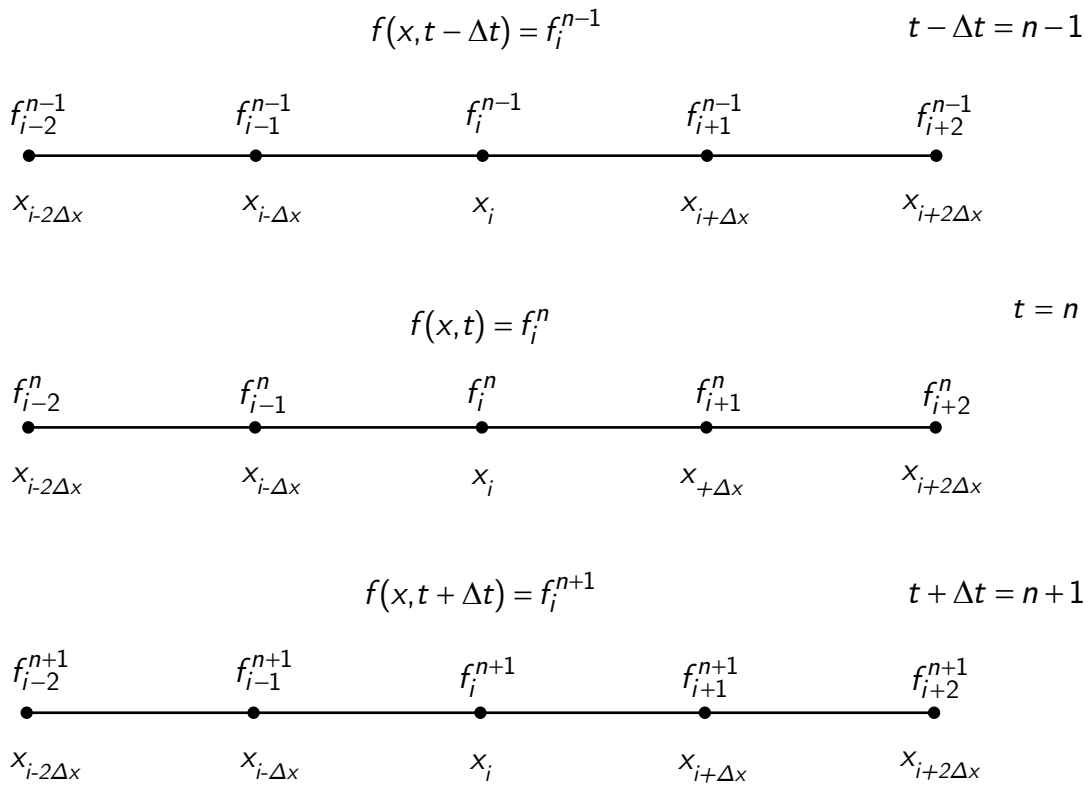
$$\frac{\partial^2 T}{\partial x^2} + \frac{\partial^2 T}{\partial y^2} = 0 \tag{2.73}$$

By making t the independent variable and setting $A = 1$, $B = 0$, and $C = 0$. It is possible to see that the one-dimensional time-dependent heat conduction equation is parabolic.

$$\frac{\partial T}{\partial t} = \alpha \frac{\partial^2 T}{\partial x^2} \tag{2.74}$$

- Expression of the derivatives

Considering the concept of the derivative of a generic function $f(x)$ at a specific point $x = x_i$ can help explain the concept of the finite difference formulation of a derivative.



- **Approximation of first derivative by finite difference**

$$f'_i = \frac{f_{i+1} - f_i}{\Delta x} + 0(\Delta x) \quad \text{Forward scheme} \quad \mathbf{2.75}$$

$$f'_i = \frac{f_i - f_{i-1}}{\Delta x} + 0(\Delta x) \quad \text{Backward scheme} \quad \mathbf{2.76}$$

$$f'_i = \frac{f_{i+1} - f_{i-1}}{\Delta x} + 0((\Delta x)^2) \quad \text{Centered scheme} \quad \mathbf{2.77}$$

- **Approximation of second derivative by finite difference**

$$f''_i = \frac{f_i - 2f_{i+1} + f_{i+2}}{(\Delta x)^2} + 0((\Delta x)^2) \quad \text{Forward scheme} \quad \mathbf{2.78}$$

$$f''_i = \frac{f_{i-2} - 2f_{i-1} + f_i}{(\Delta x)^2} + 0((\Delta x)^2) \quad \text{Backward scheme} \quad \mathbf{2.79}$$

$$f''_i = \frac{f_{i-1} - 2f_i + f_{i+1}}{(\Delta x)^2} + 0((\Delta x)^2) \quad \text{Centered scheme} \quad \mathbf{2.80}$$

2.3.1.3.2 Explicit scheme

Contemplate about the one-dimensional issue of heat conduction in a 1 m long bar. The heat equation **2.74**, where α is the thermal diffusivity, is verified by the temperature field $T(x,t)$.

- **Dirichlet Boundary Conditions**

Two boundary conditions are added to this heat equation at the ends of the wall, with $2e=L=1$ for literary simplifying (see **Figure 2.3**).

$$\left\{ \begin{array}{l} T(0,t) = T_g = T_s \\ T(2e,t) = T_d = T_s \\ T(x,0) = T_o \end{array} \right\}$$

For evaluating the time derivative, we use a forward scheme of order 1, and for calculating the second derivative in space, we use a centered scheme of order 2.

$$\left(\frac{\partial T}{\partial t} \right)_i^n = \frac{T_i^{n+1} - T_i^n}{\Delta t} \quad \mathbf{2.81}$$

$$\left(\frac{\partial^2 T}{\partial x^2} \right)_i^n = \frac{T_{i+1}^n - 2T_i^n + T_{i-1}^n}{\Delta x^2} \quad \mathbf{2.82}$$

In imposing $K = \alpha \frac{\Delta t}{\Delta x^2}$. The equation **2.74** can be written in the following form for the interior

nodes with $n = 0, 1, 2, \dots$ and $i = 1, 2, \dots, N-1$:

$$T_i^{n+1} = kT_{i-1}^n + (1 - 2k)T_i^n + kT_{i+1}^n$$

N being the quantity of discretized nodes over the wall interval. Suppose that the temperatures are prescribed at the boundaries $i = 0$ and $i = N$. We have $T_0^n = T_g = T_s$.

$$T_N^n = T_d = T_s$$

Therefore.

$$\begin{bmatrix} T_i \\ \vdots \\ T_{i-1} \end{bmatrix}^{n+1} = \begin{bmatrix} 1-2k & k & 0 & 0 \\ k & \ddots & \ddots & 0 \\ 0 & \ddots & \ddots & k \\ 0 & 0 & k & 1-2k \end{bmatrix} \begin{bmatrix} T_i \\ \vdots \\ T_{i-1} \end{bmatrix}^n + k \begin{bmatrix} T_g \\ 0 \\ 0 \\ T_d \end{bmatrix} \tag{2.83}$$

With $i = [1, \dots, N]$.

Stability criteria, derived from the dominating diagonal matrix, is as follow.

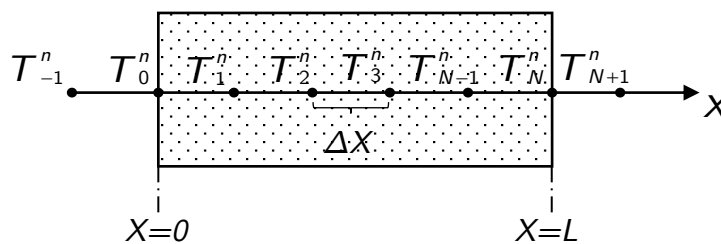
$$1 - 2k > 0 \Rightarrow \Delta t < \frac{1}{2} \frac{\Delta x^2}{\alpha}$$

- **Neumann boundary conditions (convective type)**

Take into account the boundary interfaces $x = 0$ and $x = 2e$ that are prone to heat convection at ambient temperature T_∞ with heat transfer coefficient h_∞ . We have.

$$\lambda \frac{\partial T}{\partial x} = h_\infty (T(x, t) - T_\infty) \tag{2.84}$$

For the second derivative in space, we employ a centered, order 2 based scheme.



$$-\lambda \frac{T_1^n - T_{-1}^n}{2\Delta x} = h_{\infty,0} (T_{\infty,0} - T_0^n) \quad \text{for } i = 0 \tag{2.85}$$

$$-\lambda \frac{T_{N+1}^n - T_{N-1}^n}{2\Delta x} = h_{\infty,N} (T_N^n - T_{\infty,N}) \quad \text{for } i = N \tag{2.86}$$

We will use the discretized equation of heat for the current case of study at the node $i = 0$ and

$i = N$, we obtain.

$$i = 0 \quad T_0^{n+1} = k.T_{-1}^n + (1 - 2k)T_0^n + k.T_1^n \quad 2.87$$

$$i = N \quad T_N^{n+1} = k.T_{N-1}^n + (1 - 2k)T_N^n + k.T_{N+1}^n \quad 2.88$$

To eliminate the temperature at the node $i = -1$ and $i = N+1$ outside the solid domain, we will adhere to the resolution-step process: We have the boundary condition equation at:

$$i = 0 \quad 0 = \frac{\lambda}{2.\Delta x} T_{-1}^n + h_{\infty,o}T_0^n - \frac{\lambda}{2.\Delta x} T_1^n - h_{\infty,o}T_{\infty,o} \quad 2.89$$

We pose, $\Psi = \frac{2}{\rho c_p} \frac{\Delta t}{\Delta x}$, and we multiple the equation **2.89** by Ψ , so we get.

$$i = 0 \quad 0 = K T_{-1}^n + \Psi h_{\infty,o} T_0^n - k T_1^n - \Psi h_{\infty,o} T_{\infty,o} \quad 2.90$$

We subtract the equation **2.89** from the equation **2.87** to eliminate the term T_{-1}^n , we have now.

$$i = 0 \quad T_0^{n+1} = (1 - 2k - \Psi h_{\infty,o}) T_0^n + 2k T_1^n + \Psi h_{\infty,o} T_{\infty,o} \quad 2.91$$

The same methodology to determine the equation of heat at the boundary $i = N$, and we get.

$$i = N \quad T_N^{n+1} = (1 - 2k - \Psi h_{\infty,N}) T_N^n + 2k T_{N-1}^n + \Psi h_{\infty,N} T_{\infty,N} \quad 2.92$$

With, $k = \frac{\lambda}{\rho c_p} \frac{\Delta t}{(\Delta x)^2}$ and $i = [0, \dots, N]$.

$$\begin{bmatrix} T_i \\ \vdots \\ T_N \end{bmatrix}^{n+1} = \begin{bmatrix} 1-2k-\Psi h_{\infty,o} & 2k & 0 & 0 & 0 & 0 & 0 \\ k & 1-2k & k & \ddots & \ddots & \ddots & 0 \\ 0 & \ddots & \ddots & \ddots & \ddots & \ddots & 0 \\ 0 & \ddots & \ddots & \ddots & \ddots & \ddots & 0 \\ 0 & \ddots & \ddots & \ddots & k & 1-2k & k \\ 0 & 0 & 0 & 0 & 0 & 2k & 1-2k-\Psi h_{\infty,N} \end{bmatrix} \begin{bmatrix} T_i \\ \vdots \\ T_N \end{bmatrix}^n + \begin{bmatrix} \Psi h_{\infty,o} T_{\infty,o} \\ 0 \\ \vdots \\ 0 \\ \Psi h_{\infty,N} T_{\infty,N} \end{bmatrix} \quad 2.93$$

2.3.1.3.3 Implicit scheme

We employ a centered scheme of order 2 for the second derivative in space and a backward scheme of order 1 again for determination of the time derivative.

$$\left(\frac{\partial T}{\partial t} \right)_i^{n+1} = \frac{T_i^{n+1} - T_i^n}{\Delta t} \quad 2.94$$

$$\left(\frac{\partial^2 T}{\partial x^2} \right)_i^{n+1} = \frac{T_{i+1}^{n+1} - 2T_i^{n+1} + T_{i-1}^{n+1}}{\Delta x^2} \quad 2.95$$

Equation **2.74** can be written as follows for the interior nodes, using $K = \alpha \frac{\Delta t}{\Delta x^2}$, with $n = 0, 1,$

2, ... and $i = 1, 2, \dots, N-1$.

$$(1 + 2k)T_i^{n+1} - kT_{i-1}^{n+1} - kT_{i+1}^{n+1} = T_i^n \tag{2.96}$$

- **Dirichlet Boundary Conditions**

In the preceding situation of explicit scheme, for the exact Dirichlet-type boundary conditions.

$$T_o^{n+1} = T_g = T_s$$

$$T_N^{n+1} = T_d = T_s$$

The following matrix form can be used to express the equation.

$$\begin{bmatrix} 1 + 2k & -k & 0 & 0 \\ -k & \ddots & \ddots & 0 \\ 0 & \ddots & \ddots & -k \\ 0 & 0 & -k & 1 + 2k \end{bmatrix} \begin{bmatrix} T_i \\ \vdots \\ \vdots \\ T_{i-1} \end{bmatrix}^{n+1} = \begin{bmatrix} T_i \\ \vdots \\ \vdots \\ T_{i-1} \end{bmatrix}^n + k \begin{bmatrix} T_g \\ 0 \\ 0 \\ T_d \end{bmatrix} \tag{2.97}$$

With $i = [1, \dots, M]$, the implicit scheme is unconditionally stable.

2.3.1.3.4 Crank and Nicolson scheme

The temperatures at time intervals t_n and t_{n+1} are employed in this procedure. However, over the interval of time between these two periods, $t_{n-\Delta t/2}$ and $t_{n+\Delta t/2}$, the differential equation of heat is discretized. This allows for the correct central difference scheme to be used to approximation the derivative $(\partial\theta/\partial t)^{k+1/2}$

$$\left(\frac{\partial T}{\partial x}\right)_i^{n+1/2} = \frac{T_i^{n+1} - T_i^n}{\Delta t} + O(\Delta t^2) \tag{2.98}$$

$$\left(\frac{\partial^2 T}{\partial x^2}\right)_i^{n+1/2} = \frac{1}{2} \left(\frac{T_{i+1}^{n+1} - 2T_i^{n+1} + T_{i-1}^{n+1}}{\Delta x^2} + \frac{T_{i+1}^n - 2T_i^n + T_{i-1}^n}{\Delta x^2} \right) + O(\Delta x^2) \tag{2.99}$$

This is beneficial since using an implicit difference technique enables the use of bigger time steps and necessitates a closer approximation of the derivative in regard to time.

$$(2 + 2k)T_i^{n+1} - KT_{i-1}^{n+1} - kT_{i+1}^{n+1} = (2 - 2k)T_i^n + KT_{i-1}^n + kT_{i+1}^n \tag{2.100}$$

The differential equation **2.100** can be written as above, using $K = \alpha \frac{\Delta t}{\Delta x^2}$, for the interior nodes with $n = 0, 1, 2, \dots$ et $i = 1, 2, \dots, N-1$.

- Dirichlet Boundary Conditions

The grid is selected so that $x = 0$ and $x = N$ correspond with the two borders in the event that the temperatures at the boundaries are known. This suggests that.

$$T_0^{n+1} = T_0^n = T_g = T_{surface}$$

$$T_N^{n+1} = T_N^n = T_d = T_{surface}$$

The initial equation of the tridiagonal system has the following form.

$$(2 + 2k)T_1^{n+1} - kT_2^{n+1} = (2 - 2k)T_1^n + kT_2^n + k(T_0^n + T_0^{n+1}) \tag{2.101}$$

Whereas the last equation will be.

$$(2 + 2k)T_{N-1}^{n+1} - kT_{N-2}^{n+1} = (2 - 2k)T_{N-1}^n + kT_{N-2}^n + k(T_N^n + T_N^{n+1}) \tag{2.102}$$

The equation can be written in the following matrix form.

$$\begin{bmatrix} 2+2k & -k & 0 & 0 \\ -k & \ddots & \ddots & 0 \\ 0 & \ddots & \ddots & -k \\ 0 & 0 & -k & 2+2k \end{bmatrix} \begin{bmatrix} T_i \\ \vdots \\ \vdots \\ T_{i-1} \end{bmatrix}^{n+1} = \begin{bmatrix} 2-2k & k & 0 & 0 \\ k & \ddots & \ddots & 0 \\ 0 & \ddots & \ddots & k \\ 0 & 0 & k & 2-2k \end{bmatrix} \begin{bmatrix} T_i \\ \vdots \\ \vdots \\ T_{i-1} \end{bmatrix}^n + k \begin{bmatrix} T_{i-1}^n + T_{i-1}^{n+1} \\ \vdots \\ \vdots \\ T_N^n + T_N^{n+1} \end{bmatrix} \tag{2.103}$$

With $i = [1, \dots, M]$, the Crank-Nicholson scheme is unconditionally stable.

2.3.2 Convective transfer

Convective mode transfer is the term used to describe simultaneous heat transfers in a fluid domain. This type of heat exchange takes place in non-solid medium, where it is often common. In most situations, a differentiation is made between forced flow and free flow. An external force, such as a pump or fan, can cause a flow, is defined as forced flow. In contrast, a free flow results from density variations induced by differences in concentration, pressure or temperature of any fluid fields.

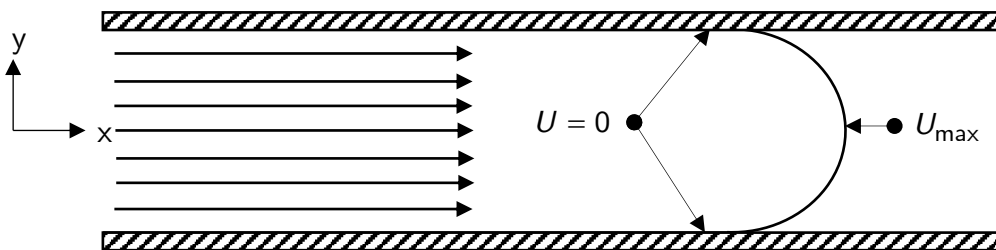


Figure 2.5 Schematic of a laminar flow

In the laminar regime, the flow is composed of almost independent layers, as in **Figure 2.5**.

Therefore, heat exchange occurs between two parallel and contiguous fluid wires.

- Conduction is only possible if the direction is normal to the fluid lines.
- Convection transfer will take place if we can evaluate a path that is not normal to the flow streamlines.

When there is turbulence, the flow is not uniform and follows a random appearance.

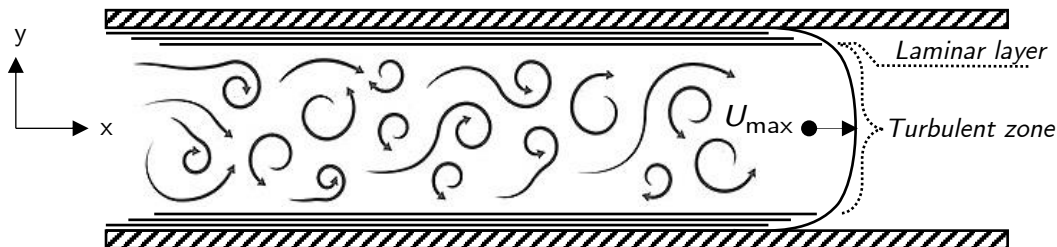


Figure 2.6 Schematic of a turbulent flow

In the turbulent zone, heat exchange happens in all directions via convection and conduction. Outside the boundary layers of the flow fronts, it is demonstrated that molecular conduction is often minimal when it comes to convection and turbulent diffusion (fluid blending caused by turbulent agitation).

2.3.2.1 Method of dimensionless analysis, Buckingham π theorem

Partial differential equations can be employed to outline the transfer processes involved in convection heat transfer. Essentially, the velocity (3D), pressure and temperature need to be solved. In this configuration, we require five equations to determine them, that can be obtained from the conservation equations of movement and energy. The links between these equations, the significant characteristic of dimensionless numbers, and the method by which they can be used to calculate heat transfer coefficients, are extensively illustrated in the subsequent paragraphs. The difficulty can be reduced as follows once we can mathematically define a physical rule by representing a physical variable as a function of a specific number of other independent physical variables G_2, \dots, G_n , i.e. if $G_1 = f(G_2, G_3, \dots, G_n)$ or $f(G_1, G_2, \dots, G_n) = 0$

- For every element G_i , we create a dimensional equation based on the basic dimensions. Therefore, n equations are needed to characterize all physical quantities, and these equations need p basic dimensions.
- We choose p among these n variables and use them as the fundamental equations. Each basic dimension must be represented in the group of p equations at least once, quite apart from the random selection of the equations.
- Subgroups π , also known as "reduced quantities," are then used to represent the final $(n-p)$ equations. Following that, we arrive at the following simplified equation.

$$g(p_1, p_2, \dots, p_{n-p}) = 0$$

A group π is the correlation between the product of the fundamental equations and a dimensional expression for a physical quantity that is not included in the list of basic equations. Each of them has been given a particular degree of power.

$$\pi_i = \frac{[G_i]}{[G_1]^{a_i} [G_2]^{b_i} \dots [G_p]^{e_i}}$$

M, L, T, θ and Q are the basic dimensions for each one that appears in the denominator. The coefficients are added together and matched to the exponential of the same dimension that appears in the main equation of the physical quantity in the numerator.

As a result, we are left with a linear series of p equations, the solution of which enables us to know the p exponents of the governing equations of the denominator. The ratio π can then be expressed in terms of the physical parameters connected to the initial dimensional equations.

- **Equation of momentum**

This equation represents the outcome of a force equilibrium on a mass object moving through a fluid.

$$\frac{dV}{dt} = -\frac{1}{\rho} (\nabla(P) + \rho g + \sum \nabla(\tau)) \tag{2.104}$$

←

Pressure gradient

↓

External forces

↘

Viscous forces

The equation **2.104** can be expressed in 1D, for direction x , by writing it as long as we exclude the external forces and assume a stable state.

$$\rho V_x \frac{\partial V_x}{\partial x} = -\frac{\partial P}{\partial x} + \sum \frac{\partial \tau}{\partial x} \tag{2.105}$$

Newton's law provides a definition of the shear stress as $\tau = \mu \frac{\partial V_x}{\partial x}$, therefore.

$$\rho V_x \frac{\partial V_x}{\partial x} = -\frac{\partial P}{\partial x} + \sum \mu \frac{\partial^2 V_x}{\partial x^2} \tag{2.106}$$

All parameters describing the state and geometry of the particular flow may be reduced to one integer by trying to work out this equation. It is often transferred in a dimensionless state to initiate the transformation. Trying to link all variables to defining parameters achieves this.

Then, implementing the following change of variable.

$$V_x^* = \frac{V_x}{V} \qquad x^* = \frac{x}{L} \qquad P_x^* = \frac{P}{V^2 \rho}$$

The number of fundamental dimensions is three, Time T , Length L and Mass M .

Parameters	Physical dimensions	Fundamental dimensions
x	m	L
V	$m \text{ s}^{-1}$	$L \text{ T}^{-1}$
P	$\text{Kg m}^{-1} \text{ s}^{-2}$	$M \text{ L}^{-1} \text{ T}^{-2}$

The following is the result of adding the dimensionless variables to the equation of movement.

$$V_x^* \frac{\partial V_x^*}{\partial x^*} = -\frac{\partial P^*}{\partial x^*} + \frac{\mu}{V \rho L} \sum \frac{\partial^2 V_x^*}{\partial x^{2*}} \qquad \mathbf{2.107}$$

Therefore.

$$\text{Re} = \frac{\rho V L}{\mu} \qquad \mathbf{2.108}$$

We will always get the same findings for the dependent variables with the same Reynolds number. On the other hand, we may deduce that distinct differential equation solutions for various fluids, states, or geometries are only brought about by various Reynolds numbers.

- **Heat equation**

The energy equation will be developed. Dimensionless variables will be introduced, and we'll look for more distinctive dimensionless numbers. The 3-dimensional differential equation for the temperature distribution in a steady fluid system without a source term is where we will begin.

We make the following variable changes.

$$T^* = \frac{T}{T_f - T_s} \qquad t^* = t \frac{V}{L} \qquad x^* = \frac{x}{L} \qquad V_x^* = \frac{V_x}{V}$$

$$\frac{V(T_f - T_s)}{L} \left(\frac{\partial T^*}{\partial t^*} + V_x^* \frac{\partial T^*}{\partial x^*} + V_y^* \frac{\partial T^*}{\partial y^*} + V_z^* \frac{\partial T^*}{\partial z^*} \right) = \frac{\lambda}{c_p \rho} \frac{(T_f - T_s)}{L^2} \left(\frac{\partial^2 T^*}{\partial x^{*2}} + \frac{\partial^2 T^*}{\partial y^{*2}} + \frac{\partial^2 T^*}{\partial z^{*2}} \right)$$

$$\left(\frac{\partial T^*}{\partial t^*} + V_x^* \frac{\partial T^*}{\partial x^*} + V_y^* \frac{\partial T^*}{\partial y^*} + V_z^* \frac{\partial T^*}{\partial z^*} \right) = \frac{\alpha}{VL} \left(\frac{\partial^2 T^*}{\partial x^{*2}} + \frac{\partial^2 T^*}{\partial y^{*2}} + \frac{\partial^2 T^*}{\partial z^{*2}} \right) \quad 2.109$$

The right side of the equation can be rearranged to have the first term in the following scheme.

$$\frac{\alpha}{VL} = \frac{\mu}{VL} \frac{\alpha}{\mu} = \frac{\mu}{VL\rho} \frac{\alpha\rho}{\mu} = \frac{\mu}{VL\rho} \frac{\lambda}{c_p \mu} = \frac{1}{\text{Re}} \frac{1}{\text{Pr}} \quad 2.110$$

Thus,

$$\text{Pr} = \frac{c_p \mu}{\lambda} \quad 2.111$$

In addition to the Reynolds number. The Prandtl number is a novel dimensionless number.

Assume a fluid running through a pipe with a temperature T_f and a wall temperature T_s . The heat flux is described as follows at any location.

$$\dot{q} = h(T_f - T_s) \quad 2.112$$

Applying the assumption that heat is transferred by conduction through the laminar sublayer (a few millimeters from the wall), the result is as follows.

$$-\lambda \frac{\partial T}{\partial x} \Big|_{x=0} = h(T_f - T_s) \quad \text{and} \quad h = -\lambda \frac{\frac{\partial T}{\partial x} \Big|_{x=0}}{(T_f - T_s)} \quad 2.113$$

Inserting the dimensionless variables.

$$h = -\lambda \frac{\frac{(T_f - T_s)}{L} \frac{\partial T^*}{\partial x^*} \Big|_{x=0}}{(T_f - T_s)} \quad 2.114$$

The recently obtained dimensionless heat transfer coefficient is called Nusselt number.

$$\text{Nu} = - \left(\frac{\partial T^*}{\partial x^*} \Big|_{x^*=1} \right) = \frac{hL}{\lambda} \quad 2.115$$

2.3.2.2 Determination of convective exchange coefficient for a plane wall

- **Horizontal wall, flat plate approach**

A fluid moving over a flat plate transferring heat is rather rare in engineering applications. The calculation of heat transfer coefficients is less complicated in this simplified case than for many other complex bodies.

$$h = \frac{Nu_L \lambda}{L} \quad 2.116$$

L is the wall length in the flow direction.

The same equation applies to a **laminar flow** on a horizontal wall that is warmed or cooled from the start edge straight ahead [119].

$$Nu_L = 0.644 (Pr)^{\frac{1}{3}} (Re_L)^{\frac{1}{2}} \quad \text{with} \quad \begin{array}{l} Re_L < 10^5 \\ 0.5 \leq Pr \leq 1000 \end{array} \quad 2.117$$

For **turbulent flow**, the empirical correlation is [119].

$$Nu_L = \frac{0.037 (Re_L)^{\frac{4}{5}} Pr}{1 + 2.443 (Re_L)^{-\frac{1}{10}} \left((Pr)^{\frac{2}{3}} - 1 \right)} \quad \text{with} \quad \begin{array}{l} 5 \cdot 10^5 < Re_L < 10^7 \\ 0.6 \leq Pr \leq 2000 \end{array} \quad 2.118$$

There are other empirical relationships between the Nusselt number and the Rayleigh number, as well as for different cooling or heating scenarios ([119], P422).

$$Nu_L = 0.54 Ra^{\frac{1}{4}} \quad \text{with} \quad 10^4 \leq Ra \leq 10^7 \quad 2.119$$

$$Nu_L = 0.15 Ra^{\frac{1}{3}} \quad \text{with} \quad 10^7 < Ra \leq 10^{11} \quad 2.120$$

The correlations **2.119** and **2.120** hold true for horizontal walls that have either an upper hot side or a lower cooled side.

$$Nu_L = 0.27 Ra^{\frac{1}{4}} \quad \text{with} \quad 10^5 \leq Ra \leq 10^{10} \quad 2.121$$

For a horizontal wall that is heated on the bottom side or cooled on the top side, the correlation **2.121** remains valid.

- **Vertical wall, natural convection**

An ascending flow forms when a heated flat vertical wall of height l is present because the fluid's density in the boundary layer next to the wall is lower, making it float. On the other hand, a descendent flow takes place at a cooled wall.

The uplifting and resistive forces are almost equal in a steady-state condition. After a specific length, the flow changes from laminar to turbulent. The temperature and density of the fluid in the boundary layers vary with the distance to the wall.

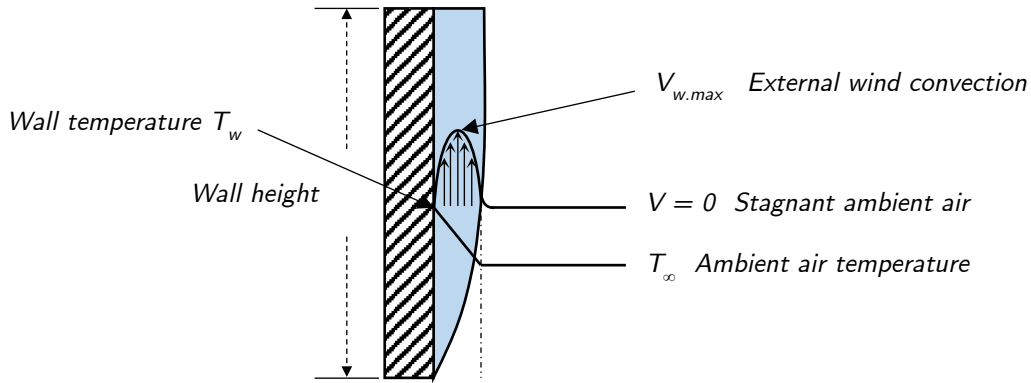


Figure 2.7 Free convection at a plain vertical wall

The subsequent empirical association is put forth [118] for plain vertical walls.

$$Nu_L = \frac{0.825 + 0.387(Ra)^{\frac{1}{6}}}{\left(1 + 0.671(Pr)^{\frac{9}{16}}\right)^{\frac{8}{27}}} \quad \text{with} \quad \begin{matrix} 0.1 < Ra < 10^{12} \\ 0.001 \leq Pr \leq \infty \end{matrix} \quad \mathbf{2.122}$$

Rayleigh numbers are determined by the wall's height, L [119].

$$Ra = PrGr = Pr \frac{\beta_{\infty}(T_s - T_{\infty})gL^3}{\nu^2} \quad \mathbf{2.123}$$

β is the coefficient of thermal expansion (K^{-1}), g is the gravity acceleration ($m\ s^{-2}$), L is wall length (m), ν is kinematic viscosity ($m^2\ s^{-1}$), T_s is surface temperature (K) and T_{∞} is air temperature.

2.3.3 Radiative transfer

The fundamental rules of thermal radiation are distinct from those of conduction and convective heat transfer. Since electromagnetic waves also transmit energy in void space, heat transmission of radiation is not dependent on the existence of material. As for the wave propagation at various directions in space, much more thought must be given to the dispersion of the radiation based on their wavelength dependency.

2.3.3.1 Radiative properties of real bodies

Radiation waves can be entirely or partially reflected, transmitted, or received at the surface of a body, according on its surface characteristics. The ratios of radiation transmitted, reflected, and absorbed are as follows τ , ρ and α . The three ratios are always added up to one.

$$\alpha + \rho + \tau = 1$$

Anything for which temperature is greater than absolute zero releases electromagnetic radiation.

One of the properties of the body is the ability to emit. At a specific temperature, such a black body may generate electromagnetic waves with the greatest intensity. The emissivity ϵ of a body affects its capacity to radiate electromagnetic waves at a given temperature. The emissivity is the difference between the emission spectra of the object at a specific temperature and the black body's emission intensity at the exact temperature.

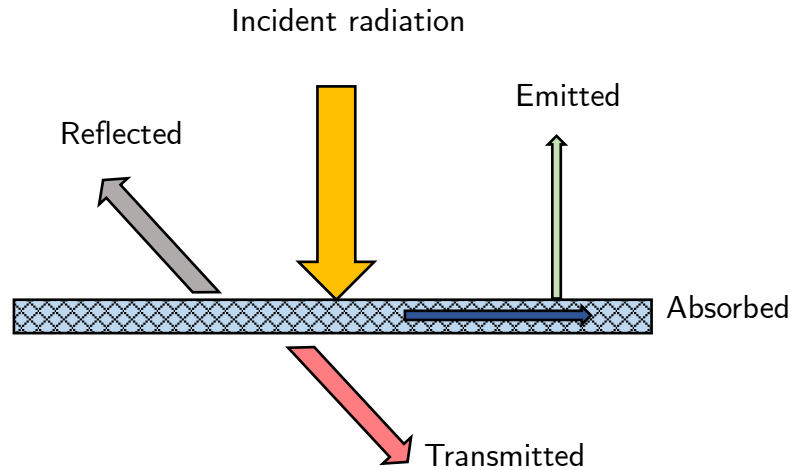


Figure 2.8 Radiative behavior of a surface [120]

Kirchhoff's Law states that the absorptivity and emissivity are equivalent for a gray and diffuse surface. (This last one radiative characteristics are direction and frequency independent). For $\alpha = \epsilon$, we can conclude that.

$$\alpha = \epsilon = 1 \quad \text{For a black surface (Hence } \rho = 0 \text{ and } \tau = 0) \quad \mathbf{2.124}$$

$$\alpha + \rho = 1 \quad \text{For an opaque surface (Hence } \tau = 0) \quad \mathbf{2.125}$$

Typically, emissivity rises according to body temperature.

- **Radiative flux density**

The fundamental radiative flux density is denoted by the following expression [120].

$$d\phi = L(T, \vec{\Omega}) d\Omega \cos \theta \quad \mathbf{2.126}$$

$L(T, \vec{\Omega})$ is the total luminance and $d\Omega$ is the solid angle. The radiative flux produced by a planar surface can be calculated using this expression. The following statements establish the basic solid angle for a point.

$$d\Omega = \sin \theta d\theta d\gamma$$

The flux density that a flat surface emits into a hemispherical space is thus expressed as.

$$\varphi = \int_{\Omega=2\pi} d\varphi = L \int_0^{2\pi} d\psi \int_0^{\pi/2} \sin\theta \cos\theta d\theta = \pi L \tag{2.127}$$

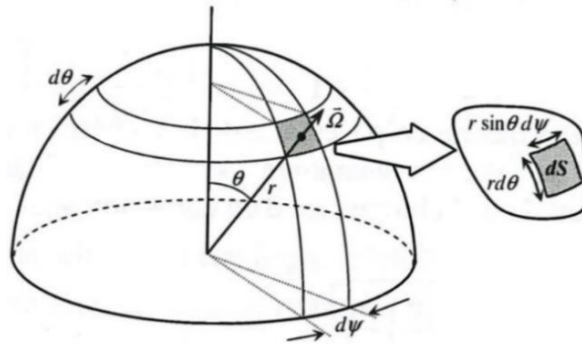


Figure 2.9 Hemispheric space [120]

In terms of total luminance is expressed as.

$$L(T, \bar{\Omega}) = \int_{\nu=0}^{\infty} L_{\nu}(T, \bar{\Omega}) d\nu \tag{2.128}$$

$L_{\nu}(T, \bar{\Omega})$ Spectral luminance.

The equation is expressed as follows to obtain the global luminance of the black body $L^{\circ}(T)$ and in accordance with Stefan Boltzmann 's law.

$$L^{\circ}(T) = \int_{\nu=0}^{\infty} L_{\nu}^{\circ}(T) d\nu \tag{2.129}$$

According to Planck's theory, a black body's spectral luminance is expressed as follows.

$$L_{\nu}^{\circ}(T) = \frac{2h\nu^2}{c_0^2 \left(\exp\left(\frac{h\nu}{KT}\right) - 1 \right)} \tag{2.130}$$

h is Planck's constant, ν is the frequency, K is Boltzmann constant, c_0 is the velocity of propagation of radiation in vacuum and T is the absolute temperature of the black body.

We insert the expression $x = \frac{h\nu}{KT}$ in the equation 2.129 it becomes as follow.

$$L^{\circ}(T) = \frac{2h}{c_0^2} \left(\frac{KT}{h} \right) \int_{x=0}^{\infty} \frac{x^3}{e^x - 1} dx \tag{2.131}$$

With,

$$\int_{x=0}^{\infty} \frac{x^3}{e^x - 1} dx = \frac{\pi^4}{15} \quad 2.132$$

Then,

$$L^o(T) = \frac{\sigma T^4}{\pi} \quad 2.133$$

And,

$$\sigma = \frac{2\pi^5 K^4}{15c_0^5 h^3} = 5,67.10^{-8} \left(\frac{W}{m^2 K^4} \right) \quad 2.134$$

σ is Stefan-Boltzmann constant.

The overall radiative flux density released by a black body in emptiness volume is represented as follows.

$$\varphi^o(T) = \pi L^o(T) = \sigma T^4 \quad 2.135$$

Consider that the black body has zero emissivity.

• **Radiative exchange between a flat surface and a transparent medium (Ambient)**

The heat flux between both surface S and the surroundings can be expressed using Stephan's law as follows.

$$\Phi(w) = \varepsilon \sigma A (T_s^4 - T_\infty^4) \quad 2.136$$

A is the exchange area, σ is the Stefan-Boltzmann coefficient, ε is the emissivity of the surface ($\varepsilon=1$ for a black body) T_s is the surface temperature and T_∞ is the ambient temperature. Once the temperature difference $T_s - T_\infty$ is still modest, equation **2.136** can be linearized by assuming only with finite expansion of the the $T_s^4 - T_\infty^4$ factor.

$$x^4 - y^4 = (x - y)(x + y)(x^2 + y^2) \quad 2.137$$

With,

$$T_m = \frac{T_s - T_\infty}{2} \approx T_s \approx T_\infty \quad 2.138$$

Therefore,

$$T_s^4 - T_\infty^4 = (T_s - T_\infty) (T_s + T_\infty)(T_s^2 + T_\infty^2) \approx 4T_m^3 (T_s - T_\infty) \quad 2.139$$

Then, the equation can be written as.

$$\Phi(w) = h_r A (T_s - T_\infty) \quad \text{with} \quad h_r = 4\varepsilon\sigma T_m^3 \quad \mathbf{2.140}$$

A is the exchange area, h_r is the radiative exchange coefficient ($W\ m^{-2}\ K^{-1}$) and T_m is the average temperature.

2.3.3.2 Solar radiation

2.3.3.2.1 ASHRAE Clear sky equations for solar radiation

Current radiation load calculation methods require their estimation at various times, which can be done with the method described in the section above. The approach employs the clear sky optical depths τ_b and τ_d given in the ASHRAE Revised Clear Sky model.

There are a number of calculating techniques for heat gains in HVAC systems and solar energy uses that depend on an understanding of clear-sky solar radiation at different times of the year and day.

- Extraterritorial Solar Radiation

Throughout the entire year, the extraterrestrial radiant flux E_o fluctuates according on the sun-earth distance. The following equation can be used to approximate the amount of extraterrestrial solar irradiance that strikes a surface which is perpendicular to the sun's radiation.

$$E_o = E_{sc} \left[1 + 0.033 \cos \left(360 \left(\frac{n-2}{365} \right) \right) \right] \quad \mathbf{2.141}$$

E_{sc} is the solar constant, with a value of $1376\ W\ m^{-2}$, and n is the day of the year (Iqbal 1983).

Table 2.1 Approximate Extraterritorial Solar Radiation data for 21st day of Each Month

Month	21 st Day of each month	E_o ($W\ m^{-2}$)
Jan	21	1410
Feb	52	1397
Mar	80	1378
Apr	111	1354
May	141	1334
Jun	172	1323
Jul	202	1324
Aug	233	1336
Sep	264	1357
Oct	294	1380
Nov	325	1400
Dec	355	1411

2.3.3.2.2 Clear-Sky Solar Radiation

- **Revised Model**

On a clear day, the beam (direct) and diffuse portions of solar radiation describe it. The diffuse element accounts for radiation coming from the rest of the sky, whereas the direct element indicates the portion of solar energy directly derived from the solar sphere. These two elements are computed as follows.

$$E_b = E_o \exp(-\tau_b m^{ab}) \quad 2.142$$

$$E_d = E_o \exp(-\tau_d m^{ad}) \quad 2.143$$

Where E_b is the beam normal irradiance ($W m^{-2}$), E_d is the diffuse horizontal irradiance ($W m^{-2}$), E_o is the extraterrestrial normal irradiance ($W m^{-2}$), m is the air mass, ab is the beam air mass exponents, ad is the diffuse air mass exponents, τ_b is the beam optical depths, τ_d is the diffuse optical depths.

- **Air mass model**

The ratio between the mass of the atmosphere along the current earth/sun trajectory and the mass which might occur if the sun were overhead is known as the relative air mass m . (Kasten and Young 1989 [121]), (θ_z is the zenith angle $^\circ$).

$$m = \left(\cos \theta_z + 0.50572(96.07995 + \theta_z)^{-1.6364} \right)^{-1} \quad 2.144$$

The following empirical correlations link τ_b and τ_d to the air mass coefficients ab and ad .

$$ab = 1.454 - 0.406\tau_b - 0.268\tau_d + 0.021\tau_b\tau_d \quad 2.145$$

$$ad = 0.507 - 0.205\tau_b - 0.080\tau_d + 0.190\tau_b\tau_d \quad 2.146$$

Only the ASHRAE manual bibliography presents the beam and diffusive optical depths (τ_b and τ_d).

- **1985 Model**

As advised by ASHRAE (1985), the old model may be used if any parameters in the new model are unavailable. The following equations are used, in order, to determine I the global radiation, I_{bn} the normal sun beam radiation on horizontal surfaces, and I_d the diffuse radiation on the horizontal surface on a non-cloudy day.

$$I = I_{bn} \cos \theta_z + I_d \tag{2.147}$$

$$I_{bn} = A \exp\left(-\frac{B}{\cos \theta_z}\right) \tag{2.148}$$

$$I_d = CI_{bn} \tag{2.149}$$

The following equation may be used to compute θ_z , which stands for zenith angle [122].

$$\cos \theta_z = \cos \delta \cos L \cos H + \sin \delta \sin L \tag{2.150}$$

where δ is the solar declination, L is the latitude of the station, and H is the hour angle.

A is the apparent solar-radiation coefficient, B is the atmospheric extinction factor, and C is the diffuse sky constant.

Table 2.2 Constants for ASHRAE equations for the 21st day of each month

Month	21 st Day of each month	A ($W\ m^{-2}$)	B	C
Jan	21	1229.48	0.142	0.058
Feb	52	1213.71	0.144	0.060
Mar	80	1185.34	0.156	0.071
Apr	111	1134.90	0.180	0.097
May	141	1103.38	0.196	0.121
Jun	172	1087.61	0.205	0.134
Jul	202	1084.46	0.207	0.136
Aug	233	1106.53	0.201	0.122
Sep	264	1150.66	0.177	0.092
Oct	294	1191.65	0.160	0.073
Nov	325	1220.02	0.149	0.063
Dec	355	1232.63	0.142	0.057

To be applicable for every day of the year, the values of A , B , and C are adapted to a trigonometric function of cosine for all the years day number n [123].

$$A = 1162.12 + 77.032 \cos\left(n \frac{360}{365}\right) \quad 2.151$$

$$B = 0.171076 - 0.0348944 \cos\left(n \frac{360}{365}\right) \quad 2.152$$

$$C = 0.0897334 - 0.0412439 \cos\left(n \frac{360}{365}\right) \quad 2.153$$

- **Solar declination**

Every year, the solar declination changes. With their irregular lengths of daylight and night, these variations lead to the passing of the seasons. The precision of the following equation is enough to.

$$\delta = 23.45 \sin\left(360 \frac{n + 284}{365}\right) \quad 2.154$$

- **Apparent solar time**

The apparent solar time (AST) is determined as follows.

$$AST = LST + \frac{ET}{60} + \left(\frac{LON - LSM}{15}\right) \quad 2.155$$

Where *AST* is the apparent solar time (decimal hours), *LST* is the local standard time (decimal hours) *ET* is the equation of time, *LSM* is the longitude of local standard time meridian, and *LON* is the longitude of site

- **Equation of time**

The following expression roughly approximates the formula of time (Iqbal, 1983).

$$ET = 2.2918 \left[0.0075 + 0.1868 \cos(\Gamma) - 3.2077 \sin(\Gamma) - 1.4615 \cos(2\Gamma) - 4.089 \sin(\Gamma) \right] \quad 2.156$$

With,

$$\Gamma = 360 \frac{n - 1}{365} \quad 2.157$$

- **Longitude of local standard time meridian**

Time zone and standard meridian longitude are associated as follows.

$$LSM = 15TZ \quad 2.158$$

- **Hour Angle**

The hour angle, abbreviated *H*, is the degree-based expression for the angular position of the sun from the local meridian induced by the earth's rotation.

$$H = 15(AST - 12) \tag{2.159}$$

Sun Position (Altitude and azimuth)

The sun's altitude β , which is above the horizontal, and azimuth ϕ , which is calculated from the south, are easy ways to describe the sun's location in the sky.

$$\sin \beta = \cos L \cos \delta \cos H + \sin L \sin \delta \tag{2.160}$$

Where L is the local latitude of the site.

The sun azimuth angle ϕ is the angle at which the beam of radiation projected on the horizontal surface displaced from the south.

$$\cos \phi = \frac{\sin L \cos \delta \cos H - \sin \delta \cos L}{\cos \beta} \tag{2.161}$$

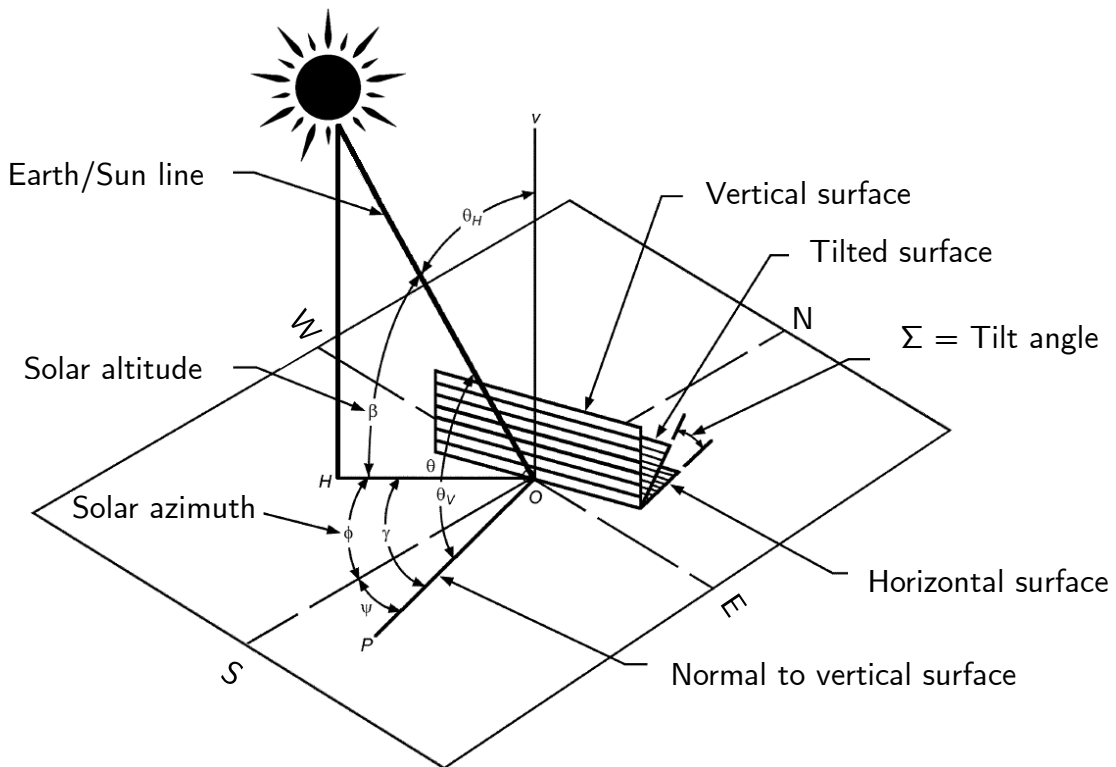


Figure 2.10 Solar angles for vertical and horizontal surfaces [124]

2.3.3.2.3 Calculation of Clear-Sky Solar Irradiance Incident on receiving surface

The three elements that make up the total clear-sky irradiance E_t that reaches the receiving surface are, the ground-reflected element $E_{t,r}$ coming from the land in front of the receipt surface, the diffuse element $E_{t,d}$ arriving from the sky dome, and the beam component $E_{t,b}$ getting from the solar spheric. Thereby.

$$E_t = E_{t,b} + E_{t,d} + E_{t,r} \tag{2.162}$$

$$E_{t,b} = E_b \cos \theta \tag{2.163}$$

θ is the angle of incidence. Only when $\cos \theta > 0$ the correlation is valid. Otherwise, $E_{t,b} = 0$.

$$E_{t,d} = E_d (Y \sin \Sigma + \cos \Sigma) \quad \text{if} \quad \Sigma \leq 90^\circ \tag{2.164}$$

$$E_{t,d} = E_d (Y \sin \Sigma) \quad \text{if} \quad \Sigma > 90^\circ \tag{2.165}$$

With $Y = \max \left[0.45 ; 0.55 + 0.437 \cos \theta + 0.313 \cos^2 \theta \right]$ and Σ is the tilt angle.

$$E_{t,r} = (E_b \sin \beta + E_d) \rho_g \frac{1 + \cos \beta}{2} \tag{2.166}$$

Where ρ_g is ground reflectance, often taken to be 0.2 for a typical mixture of ground surfaces.

Table 2.3 Different world time zones

Name	Description	Time Zone	LSM
GMT	Greenwich Mean Time	0	0
UTC	Universal Coordinated Time	0	0
ECT	European Central Time	1	15
EET	Eastern European Time	2	30
ART	(Arabic) Egypt Standard Time	2	30
EAT	Eastern African Time	3	45
MET	Middle East Time	+3.5	52,5
NET	Near East Time	4	60
PLT	Pakistan Lahore Time	5	75
IST	India Standard Time	+5.5	82,5
BST	Bangladesh Standard Time	6	90
VST	Vietnam Standard Time	7	105
CTT	China Taiwan Time	8	120
JST	Japan Standard Time	9	135
ACT	Australia Central Time	+9.5	142,5
AET	Australia Eastern Time	10	150
SST	Solomon Standard Time	11	165
NST	New Zealand Standard Time	12	180
MIT	Midway Islands Time	-11	-165
HST	Hawaii Standard Time	-10	-150
AST	Alaska Standard Time	-9	-135
PST	Pacific Standard Time	-8	-120
PNT	Phoenix Standard Time	-7	-105

MST	Mountain Standard Time	-7	-105
CST	Central Standard Time	-6	-90
EST	Eastern Standard Time	-5	-75
IET	Indiana Eastern Standard Time	-5	-75
PRT	Puerto Rico and US Virgin Islands Time	-4	-60
CNT	Canada Newfoundland Time	-3.5	-52,5
AGT	Argentina Standard Time	-3	-45
BET	Brazil Eastern Time	-3	-45
CAT	Central African Time	-1	-15

2.4 Modes of mass transfer

Mass transfer is the movement of one or more substances inside a phase or over a phase boundary in a combination of fluid or solid materials. Pressure, temperature, or concentration gradients are among the primary driving forces of mass transfer. The most common of these three forces, the concentration gradient, will be addressed in the following sections. As we know from experience, a mixture's constituent parts travel from areas of higher concentration to those of lower concentration.

2.4.1 Mass diffusion

2.4.1.1 Fick's Law

Consider the system displayed below, where distinct elements *B* and *C* are originally divided by a thin barrier while they are both at the same pressure and temperature. The two components diffuse through one another once the barrier has been eliminated.

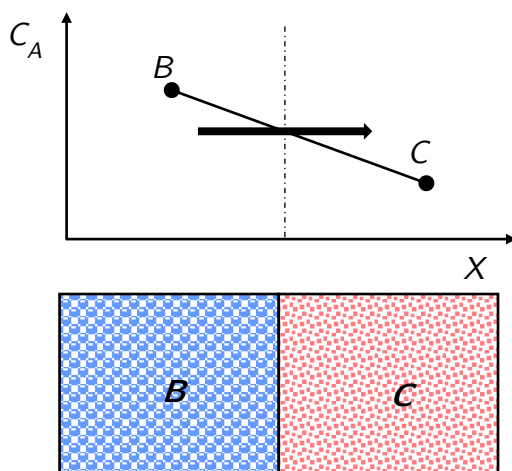


Figure 2.11 Mass diffusion of gases [125]

The component *B* concentration gradient in that direction is directly related to the same component mass diffusion rate m_B , which is expressed as follows.

$$\dot{m}_B = -SD_{BC} \frac{dC_B}{dx} \quad 2.167$$

S area through which the mass diffuses m^2 , D_{BC} diffusion coefficient $m^2 s^{-1}$, C_B mass concentration of the component *B* ($Kg m^{-3}$), \dot{m}_B mass diffusion rate ($Kg s^{-1}$)

The diffusion coefficient, in terms of physics, denotes the amount of the substance passing across

a unit surface area in a unit of time when a gradient of concentration occurs. Experimental methods are frequently used to calculate diffusion coefficients. Because molecules in fluids may move around readily, the diffusion coefficient in gases is higher than that in solids. Due to the effect of molecular force fields and an increase in collisions, which results in less molecular liberty of movement, diffusion in liquids and solids is more challenging to happen.

- **Fick's law expressed in mass**

The densities of a species ρ_i and the mixture ρ , respectively, are provided by the following formulas for volume V .

$$\rho_i = \frac{m_i}{V} \quad 2.168$$

And

$$\rho = \frac{m}{V} = \sum \frac{m_i}{V} = \sum \rho_i \quad 2.169$$

Through using mass fraction of species i the mass concentration can be stated in non-dimensional form as follows.

$$w_i = \frac{m_i}{m} = \frac{m_i / V}{m / V} = \frac{\rho_i}{\rho} \longrightarrow \sum w_i = 1 \quad 2.170$$

Therefore

$$\frac{\dot{m}_B}{S} = -\rho D_{BC} \frac{d(\rho_B / \rho)}{dx} = -\rho D_{BC} \frac{d(w_B)}{dx} \quad \left(\frac{kg}{m^2s} \right) \quad 2.171$$

- **Fick's law expressed in molar concentration**

The molar concentration is determined by once more taking into account the proportion V of the species i and the mixture.

$$C_i = \frac{N_i}{V} \quad 2.172$$

And

$$C = \frac{N}{V} = \sum \frac{N_i}{V} = \sum C_i \quad 2.173$$

By utilizing the molar fraction y as the molar fraction of molecule I the molar concentration may be written in a dimensionless form as follows.

$$y_i = \frac{N_i}{N} = \frac{N_i / V}{N / V} = \frac{C_i}{C} \longrightarrow \sum y_i = 1 \quad 2.174$$

Therefore,

$$\frac{\dot{N}_B}{S} = -CD_{BC} \frac{d(C_B / C)}{dx} = -CD_{BC} \frac{d(y_B)}{dx} \quad \left(\frac{\text{mol}}{\text{m}^2\text{s}} \right) \quad 2.175$$

C is the total molar concentration (mol m^{-3})

• **Fick's law expressed in terms of partial pressure**

Partial pressures can be used to express Fick's law for gases. By using the gas B 's characteristic equation, we get at.

$$p_B = \rho_B R_B T = \rho_B \left(\frac{R_o}{M_B} \right) T \longrightarrow \rho_B = \frac{p_B M_B}{R_o T} \quad 2.176$$

R_o is the perfect gas constant ($\text{J mol}^{-1} \text{K}^{-1}$)

According to the equation **2.167**. With $\rho_B = C_B$ we get.

$$\frac{\dot{m}_B}{S} = -D_{BC} \frac{d \left(\frac{p_B M_B}{R_o T} \right)}{dx} = -D_{BC} \left(\frac{M_B}{R_o T} \right) \frac{dp_B}{dx} \quad 2.177$$

For the gases B and C , Fick's law for isothermal diffusion is either expressed as follows.

$$\dot{N}_B = \frac{\dot{m}_B}{M_B} = -D_{BC} \left(\frac{S}{R_o T} \right) \frac{dp_B}{dx} \quad 2.178$$

$$\dot{N}_C = \frac{\dot{m}_C}{M_C} = -D_{CB} \left(\frac{S}{R_o T} \right) \frac{dp_C}{dx} \quad 2.179$$

Where N is the number of moles.

Equation **2.167** is integrated to give us the mass flow of the B component.

$$\frac{\dot{m}_B}{S} = -D_{BC} \left(\frac{M_B}{R_o T} \right) \frac{p_{B2} - p_{B1}}{\Delta x} \quad 2.180$$

2.4.1.2 Diffusion coefficient

The diffusion coefficient is a transfer parameter that relies on the system's function's type, pressure and temperature (T, p). The Kinetic hypothesis of gases has been applied to demonstrate that the dependency of the diffusion coefficient on pressure and temperature for a

$$D_{AB} = p^{-1} T^{\frac{3}{2}} \longrightarrow \frac{D_{AB,1}}{D_{AB,2}} = \frac{P_2}{P_1} \left(\frac{T_1}{T_2} \right)^{\frac{3}{2}} \quad 2.181$$

binary mixture may be derived from the relationship above under the assumption of ideal gas behavior.

2.4.1.3 Diffusion of fluids through porous media

Through the pore holes, the permeable gas penetrates the solid and travels through the porous channels while continuing to exist in the gas phase. No penetration of the solid matrix exists, and the diffusion is strictly considered Fickian. A couple things need to be taken into account while describing this procedure. The diffusion coefficient is decreased by a factor equal to the solid's void ϵ percent when the cross-sectional area that is accessible for diffusion is reduced in the first place. Here, the value of ϵ , which varies from 0 to 1, is given as the proportion of the open cross-sectional area to the overall cross-sectional area. The second reason is brought on by the porous pathway's winding structure, which is frequently connected to these media. Instead of flowing through the material directly, gas molecules are made to twist aleatory across it, eventually popping into complete shut-in area known as "dead-end pores" (Figure 2.12c). Overall, the diffusion channel is lengthened, which lowers the net diffusion rate.

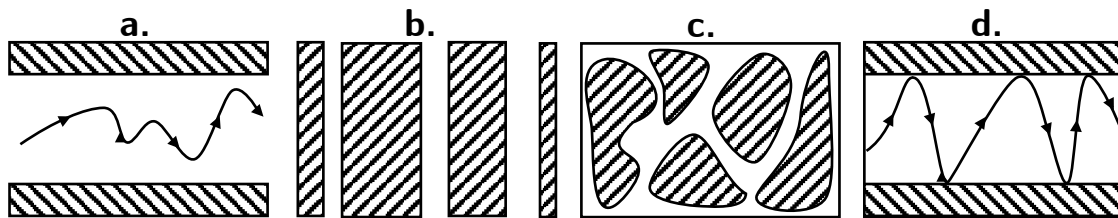


Figure 2.12 Diffusion in a porous medium: (a) molecular diffusion, (b) straight pores, (c) tortuous pores with branching, (d) Knüdsen diffusion [126].

The deformation factor τ , which has a value larger than uniformity, accounts for both the prolonging of the path and the impact of dead-end pores. The diffusion coefficient combines these two effects to provide an effective and decreased diffusivity D_e , from which we may derive the following expression [126].

$$D_e = \frac{D\epsilon}{\tau} \tag{2.182}$$

D then continues to be the common diffusivity that applies to empty space. In combination with Fick's law, which keeps its original form, D_e is used.

$$\frac{N}{S} = -D_e \frac{dC}{dx} \tag{2.183}$$

For various porous media, the typical void fraction ranges from 0.1 to 0.5, with 0.3 serving as a reliable average. The range of tortuosity is 1.5 to 10, with sporadic excursions to higher numbers. In the lack of accurate data, a value of $\tau = 4$ provides a fair beginning approximation.

The free-space diffusivity is decreased by roughly an order of magnitude when the cross-sectional area and diffusion channel are both extended. As a result, the previously calculated oxygen diffusion in air, which was put at $0.2 \text{ cm}^2 \text{ s}^{-1}$, is now around $0.02 \text{ cm}^2 \text{ s}^{-1}$.

However, the diffusion process goes through a change known as Knudsen diffusion when the pore dimension drops under the mean free path value. The problematic collisions now take place between the gas particles and the capillary wall, instead of among the gas molecules themselves. The gas molecules are deflected in a different direction by the trajectory, which is still random but now twisting between the pore walls. (**Figure 2.12d**). Knudsen diffusion also relies on the size of the pore. However, it still changes linearly with temperature and inversely with molar mass M . The appropriate expression is provided by.

$$D_K = 9700r_p \left(\frac{T}{M}\right)^{1/2} \left(\frac{cm^2}{s}\right) \quad 2.184$$

2.4.1.4 One-dimensional stationary mass diffusion

- Constant surface concentration

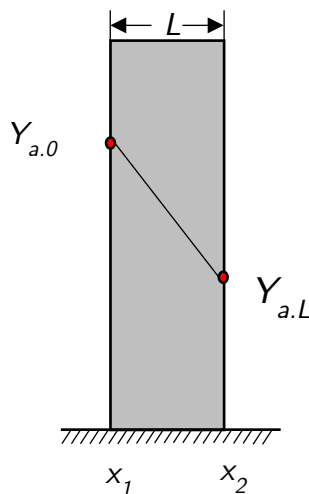


Figure 2.13 Mass diffusion through a wall

Consider that both the diffusion coefficient D_{AB} and the whole molar concentration c are unchanged. The continuity equation for species A may be expressed as follows.

$$\frac{N_{Ax}}{S} = -c D_{AB} \frac{dy_A}{dx} \quad 2.185$$

We have: $N_{Ax}=N_{Ax}(X)$ et $N_{Ay}=N_{Az}=0$,
Therefore.

$$\frac{dN_{Ax}}{dx} = 0 \longrightarrow N_{Ax} = C^{te}$$

As shown in **Figure 2.13**, consider the normal 1D diffusion of species A through a square barrier (species B) of thickness L . For $x = 0$ and $x = L$, species A 's mole fractions in the solid phase are $y_{a.0}$ and $y_{a.L}$, respectively, with $y_{a.0} > y_{a.L}$. However, it is crucial to find out the rate at which species A gets the moles through the wall. Then,

$$\frac{d}{dx} \left(\frac{dy_A}{dx} \right) = 0 \quad 2.186$$

Based on the following boundary conditions.

$$x = 0 \longrightarrow y_A = y_{A0}$$

$$x = L \longrightarrow y_A = y_{AL}$$

The solution of the equation **2.186** is.

$$y_A(x) = \frac{y_{AL} - y_{Ao}}{L} x + y_{Ao} \quad 2.187$$

The following definition applies to species A 's molar flux density.

$$N_{Ax} = C D_{AB} \left(\frac{y_{Ao} - y_{AL}}{L} \right) = D_{AB} \left(\frac{C_{Ao} - C_{AL}}{L} \right) \quad \left(\frac{\text{mol}}{\text{m}^2 \text{s}} \right) \quad 2.188$$

- **Mass convective exchange on surfaces**

- **Mass Biot number**

Consider the movement of species A over a solid-fluid interface from the solid matrix (species B) to the fluid medium. Therefore, A 's molar flow is homogenous at the interface.

$$N_{A|solide \rightarrow \text{interface}} = N_{A|\text{interface} \rightarrow \text{fluide}} \quad 2.189$$

Mass diffusive flux density is expressed as follows.

$$N_{A|solide \rightarrow \text{interface}} = -D_{AB} (\nabla C)_{\text{solide}} \quad 2.190$$

Mass convective flux density is written as follows.

$$N_{A|\text{interface} \rightarrow \text{solide}} = h_m (\Delta C)_{\text{fluide}} \quad 2.191$$

Then equation **2.189** becomes.

$$-D_{AB} (\nabla C)_{\text{solide}} = h_m (\Delta C)_{\text{fluide}} \quad 2.192$$

$$D_{AB} \frac{(\Delta C)_{\text{solide}}}{L} = h_m (\Delta C)_{\text{fluide}} \quad 2.193$$

Therefore, we find out the mass number of Biot.

$$Bi_m = \frac{(\Delta C)_{\text{solide}}}{(\Delta C)_{\text{fluide}}} = \frac{h_m L}{D_{AB}} \quad 2.194$$

L is the characteristic wall length in x direction, h_m is the mass convective exchange coefficient and D_{AB} is the mass diffusivity.

The concentration dispersion in the fluid is significantly larger than that in the solid once $Bi_m \ll 1$. Otherwise, both the concentration distribution in the solid media and the mass transfer barrier in the fluid domain are interpreted as being uniform.

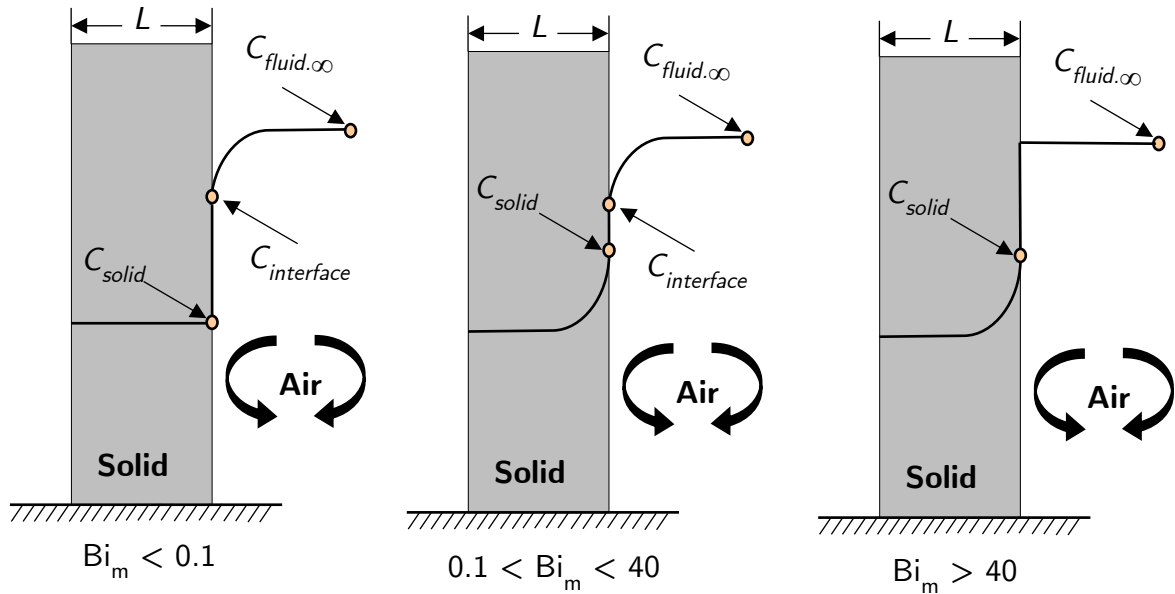


Figure 2.14 Effect of the mass Biot number on the concentration distribution [127]

- Case of $Bi_m > 40$

We consider the concentrations in the fluids at the surfaces at $x=0$ and $x=L$, respectively, to be $C_{A,\infty 1}$ and $C_{A,\infty 2}$. It is therefore important to link C_{A0} and C_{AL} to $C_{A1,\infty}$ and $C_{A2,\infty}$. as it is much simpler to quantify the fluid concentrations.

In this scenario, the fluid phase mass transfer resistances are insignificant. Otherwise, there isn't any alteration in the concentration of the gas phases. A partition coefficient (K_A) correlates the concentrations levels of species A in the solid material to the concentrations of fluids near the wall under equilibrium as follows:

$$K_A = \frac{C_{A|x=0}}{C_{A1,\infty}} = \frac{C_{A|x=L}}{C_{A2,\infty}} \tag{2.195}$$

Therefore.

$$N_A = S \cdot K_A \cdot D_{AB} \cdot \left(\frac{C_{A2,\infty} - C_{A1,\infty}}{L} \right) \left(\frac{mol}{s} \right) \tag{2.196}$$

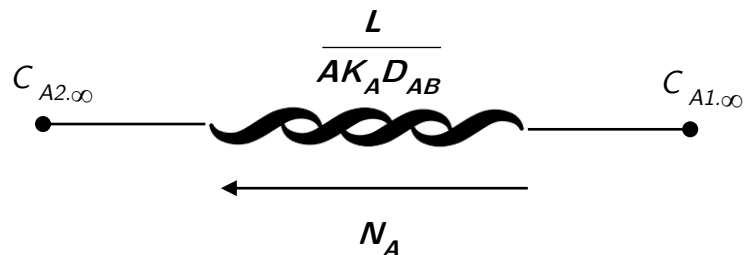


Figure 2.15 Analogy of electrical circuits for mass transfer with number of Biot > 40 [127]

Alternatively, equation 2.196 can be written in terms of the partial pressure terms.

$$N_A = S K_A D_{AB} \sigma \left(\frac{P_{A2,\infty} - P_{A1,\infty}}{L} \right) \quad \left(\frac{\text{mol}}{\text{s}} \right) \quad 2.197$$

S is the area through which the mass diffuses, D_{AB} is the diffusion coefficient, σ is the coefficient of solubility, K_A is the partition coefficient, $P_{A\infty}$ Partial vapor pressure of the fluid.

The equation 2.197 allows for the deduction of the permeability term.

- **Case of $0.1 < Bi_m < 40$**

The saturation distributions of element A in this instance are stated as follows for both the solid and the boundary surface.

$$K_A = \frac{C_{A|x=0}}{C_{A|interface.0}^{fluide}} = \frac{C_{A|x=L}}{C_{A|interface.L}^{fluide}} \quad 2.198$$

Thus,

$$N_A = S K_A D_{AB} \left(\frac{C_{A2,\infty} - C_{A1,\infty}}{L} \right) \quad \left(\frac{\text{mol}}{\text{s}} \right) \quad 2.199$$

Newton's law of mass transfer states that the convective molecular transmission rate of component A at the interface $x=0$ is similar to the one at $x=L$. This is represented by the following equation.

$$N_A = S h_{m1} (C_{A1,\infty} - C_{A|interface.0}^{fluide}) = S h_{m2} (C_{A|interface.L}^{fluide} - C_{A2,\infty}) \quad \left(\frac{\text{mol}}{\text{s}} \right) \quad 2.200$$

The species A molar transfer rate is therefore expressed as.

$$N_A = \frac{1}{\left(\frac{1}{S h_{m1}} + \frac{L}{A K_A D_{AB}} + \frac{1}{S h_{m2}} \right)} (C_{A1,\infty} - C_{A2,\infty}) \quad \left(\frac{\text{mol}}{\text{s}} \right) \quad 2.201$$

S is the area through which the mass diffuses, D_{AB} is the diffusion coefficient, K_A is the partition coefficient, h_{m1} is the mass convective exchange coefficient at $x = 0$ (m s^{-1}) and h_{m2} is the mass convective exchange coefficient at $x = L$ (m s^{-1}).

2.4.1.5 One-dimensional unsteady mass diffusion

For any species concentration, the following physical definitions are provided for each variable in the continuity equation.

$$\underbrace{\frac{\partial C_A}{\partial t}}_{\text{Unsteady term}} + \underbrace{v \nabla C_A}_{\text{Convective term}} = \underbrace{D_{AB} \nabla^2 C_A}_{\text{Diffusif term}} + \underbrace{S_A}_{\text{Source term}} \quad 2.202$$

• Laplace transform method

Considering the species *B* of vertical wall in **Figure 2.16**, which has a thickness of $2L$. At a value of C_{A0} for $t = 0$, the concentration of species *A* in the wall is initially homogeneous.

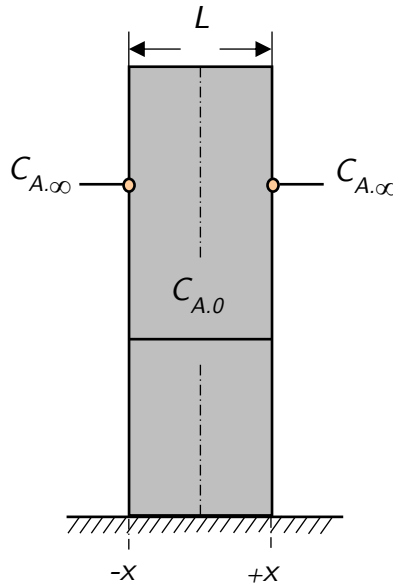


Figure 2.16 Mass transfer in a plane wall

Boundaries at $x = +L$ and $x = -L$ are confronted to a fluid containing a concentration of $C_{A,∞}$, where $C_{A,∞} \gg C_{A0}$, at time $t = 0$. The quantity of species *A* that has been absorbed into the wall over time is what we are mostly interested in. To achieve this, it is necessary to identify how the distribution of component concentration *A* concentration in the wall changes according to location x and time t .

$$\frac{\partial C_A}{\partial t} = D_{AB} \frac{\partial^2 C_A}{\partial x^2} \tag{2.203}$$

The relevant initial and boundary conditions are.

- $Bi_m > 40$

Suppose that the Biot number is more than 40, leading to limit mass convection and negligible resistance of transfer in the fluid phase, as well as $C_{A,∞}$ for the proportion of species *A* in the surrounding fluid at the solid-fluid interface. A partition coefficient (K_A) in equilibrium combines the levels of species *A* on each side of the contact as follows:

$$C_{A|interface}^{solide} = K_A C_{A,∞} \tag{2.204}$$

$$C_{A|interface}^{solide} = C_{A|interface}^{fluide} \tag{2.205}$$

The species continuity equation can be described as follows, emphasizing that the major part is dispersing in the x direction.

$$\left\{ \begin{array}{l} C_A(x,t) = C_{A0} \quad \text{for } t = 0 \\ C_A(x,t) = K_A C_{A,\infty} \quad \text{for } x = +L \\ C_A(x,t) = K_A C_{A,\infty} \quad \text{for } x = -L \end{array} \right\}$$

We provide the non-dimensional numbers for variable changes as follows.

$$\theta = \frac{K_A C_{A,\infty} - C_A(x,t)}{K_A C_{A,\infty} - C_{A0}} \quad \tau = \frac{D_{AB} \cdot t}{L^2} \quad X = \frac{x}{L} \tag{2.206}$$

τ describes the Fourier dimensionless number.

So, the equation 2.203 and the associated boundary conditions becomes.

$$\left\{ \begin{array}{l} X = 0 \quad \frac{\partial \theta}{\partial X} = 1 \\ X = 1 \quad \theta = 0 \\ \tau = 0 \quad \theta = 1 \end{array} \right\}$$

$$\frac{\partial \theta}{\partial \tau} = \frac{\partial^2 \theta}{\partial X^2} \tag{2.207}$$

The Laplace transform of the equation 2.207 is.

$$\mathcal{L}\left[\frac{\partial \theta}{\partial \tau}\right] = s\mathcal{L}[\theta] - \theta(\tau = 0) \longrightarrow \mathcal{L}\left[\frac{\partial \theta}{\partial \tau}\right] = s\bar{\theta} - 1 \tag{2.208}$$

$$\mathcal{L}\left[\frac{\partial^2 \theta}{\partial X^2}\right] = \frac{\partial^2 \bar{\theta}}{\partial X^2} \tag{2.209}$$

$$\frac{\partial^2 \bar{\theta}}{\partial X^2} = s\bar{\theta} - 1 \tag{2.210}$$

The boundary conditions in the Laplace domain are.

$$\left\{ \begin{array}{l} X = 0 \quad \frac{\partial \bar{\theta}}{\partial X} = 1 \\ X = 1 \quad \bar{\theta} = 0 \end{array} \right\}$$

The differential equation 2.210 (Laplace) has a unique solution in the form.

$$\bar{\theta} = \frac{1}{p} - \frac{\cosh(X\sqrt{p})}{p \sinh(\sqrt{p})} \tag{2.211}$$

We get the following results by applying the inverse Laplace transforms to the two terms of the

equation 2.211.

$$\frac{1}{p} \xrightarrow{\mathcal{L}^{-1}} 1$$

$$\frac{\cosh(X\sqrt{p})}{p \sinh(a\sqrt{p})} \xrightarrow{\mathcal{L}^{-1}} 1 + \frac{4}{\pi} \sum_{n=1}^{\infty} \frac{(-1)^n}{(2n-1)} e^{-\left(\frac{(2n-1)\pi}{2a}\right)^2 \tau} \cos\left(\frac{(2n-1)\pi}{2a} X\right) \quad 2.212$$

Therefore.

$$C_A(x,t) = K_A C_{A\infty} - (K_A C_{A\infty} - C_{A0}) \left[\frac{4}{\pi} \sum_{n=1}^{\infty} \frac{(-1)^n}{(2n-1)} e^{-\left(\frac{(2n-1)\pi}{2}\right)^2 \frac{D_{AB}t}{L^2}} \cos\left(\frac{(2n-1)\pi}{2} \frac{x}{L}\right) \right] \quad 2.213$$

According to the formula below, the molar flux density at the surfaces is as follow.

$$N_{Ax}|_{x=L} = -D_{AB} S \left. \frac{\partial C_A(x,t)}{\partial x} \right|_{x=L} \quad \left(\frac{\text{mol}}{\text{s}} \right) \quad 2.214$$

$$N_{Ax}|_{x=L} = D_{AB} (K_A C_{A\infty} - C_{A0}) \frac{S}{L} 2 \sum_{n=1}^{\infty} e^{-\left(\frac{(2n-1)\pi}{2}\right)^2 \frac{D_{AB}t}{L^2}} \quad \left(\frac{\text{mol}}{\text{s}} \right) \quad 2.215$$

- **Boundary conditions of Dirichlet**

The same procedures we undertook earlier for a Biot number $Bi_m > 40$ will be followed, but this time we'll take into account a uniform boundary condition on the surface of the wall, therefore the mass transfer equation and related initial and boundary conditions are provided in the following format.

$$\frac{\partial C_A}{\partial t} = D_{AB} \frac{\partial^2 C_A}{\partial x^2} \quad 2.216$$

$$\left\{ \begin{array}{l} C_A(x,t) = C_{A0} \text{ for } t = 0 \\ C_A(x,t) = C_{A,L} \text{ for } x = +L \\ \frac{\partial C_A(x,t)}{\partial x} = 0 \text{ for } x = 0 \end{array} \right.$$

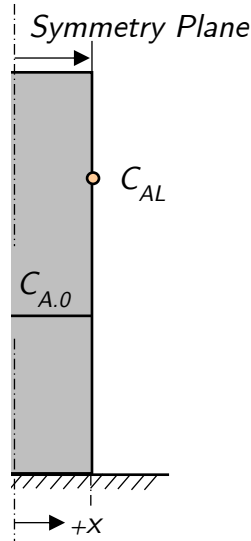


Figure 2.17 Semi-infinite domain of a plane wall

We perform a change of variable for the non-dimension number θ .

$$\theta = C_A(x,t) - C_{A,0} \tag{2.217}$$

Consequently, equation 2.216 and the corresponding boundary conditions are transformed into.

$$\frac{\partial \theta}{\partial t} = D_{AB} \frac{\partial^2 \theta}{\partial x^2} \tag{2.218}$$

$$\left\{ \begin{array}{l} x = 0 \quad \frac{\partial \theta}{\partial x} = 0 \\ x = L \quad \theta = \theta_L \\ t = 0 \quad \theta = 0 \end{array} \right.$$

The differential equation has the following ultimate solution.

$$\theta(x,t) = \theta_L \left[\sum_{n=0}^{\infty} (-1)^n \operatorname{erfc} \left(\frac{(2n+1)L-x}{2\sqrt{D_{AB}t}} \right) + \sum_{n=0}^{\infty} (-1)^n \operatorname{erfc} \left(\frac{(2n+1)L+x}{2\sqrt{D_{AB}t}} \right) \right] \tag{2.219}$$

Hence.

$$C_A(x,t) = C_{A,0} + (C_{A,L} - C_{A,0}) \left[\sum_{n=0}^{\infty} (-1)^n \operatorname{erfc} \left(\frac{(2n+1)L-x}{2\sqrt{D_{AB}t}} \right) + \sum_{n=0}^{\infty} (-1)^n \operatorname{erfc} \left(\frac{(2n+1)L+x}{2\sqrt{D_{AB}t}} \right) \right] \tag{2.220}$$

The approach for solving the 1D mass equation (through a wall) 2.216 is the same as for solving the 1D temperature equation (through a plane wall) by Laplace's method and for Dirichlet type boundary conditions, so for more information on solving, you can follow the steps on the p.70.

2.4.2 Mass convection

The following equation provides the description of mass transfer by convection.

$$N_A = S h_m \Delta C_A \quad 2.221$$

Where h_m is the mass transfer coefficient.

The equation is comparable to the previously mentioned convective heat transfer equation. When the fluid is under a driven fluid flow, it is alluded to as forced convection mass transfer, similar to the case of convective heat transfer. Natural convection mass transfer happens when the only reason for the mass transfer is a difference in density brought over by changes in pressure or temperature. The intensity of concentration difference ΔC_B , the sort of air movement (laminar or turbulent), the physical characteristics of the materials employed and the geometry of the system, all affect the value of the mass transfer coefficient. The convective mass transfer formula in terms of partial pressure difference is described as shown below (when using the hypothesis $C_A = \rho_A = (p_B/RT)$).

$$N_A = S h_m \left(\frac{p_{B1}}{RT_1} + \frac{p_{B2}}{RT_2} \right) \quad 2.222$$

2.4.2.1 Dimensional analysis applied to convective mass transfer

The Sherwood and Schmidt numbers are the two principal dimensionless groups of importance for mass transportation. These are their descriptions.

$$Sh = \frac{h_m L}{D} \quad \text{and} \quad Sc = \frac{\mu}{\rho D} \quad 2.223$$

L is the wall size (m), D is the diffusion coefficient ($\text{m}^2 \text{s}^{-1}$), h_m is the mass convective exchange coefficient (m s^{-1}), μ is the mass convective exchange coefficient at $x=0$ ($\text{Pa s} = \text{kg m}^{-1} \text{s}^{-1}$) and ρ is the density of the fluid (kg m^{-3}). It is possible to think of the Sherwood number as indicating the proportion of diffusive to convective movement. This is also present in the heat transfer field in form of a Nusselt number.

The Schmidt number, which is similar to the commonly used Prandtl number in the heat transfer domain, is a ratio of physical properties pertinent to the system. The Reynolds number, which measures the proportion of convective transfer to viscous effects and is generally used to define flow conditions (laminar, transient, or turbulent). The Peclet number and the Stanton number are two further nondimensional groups that are also employed, but less often. The two numbers are assemblages of further dimensionless groupings, which commonly occur simultaneously. As a result, the Reynolds and Schmidt numbers are frequently combined to form the Peclet number.

$$Pe = ReSc = \frac{\rho VL}{\mu} \frac{\mu}{\rho D} = \frac{LV}{D} \quad 2.224$$

The Sherwood, Reynolds, and Schmidt numbers, which also frequently appear together, are combined to form the Stanton number. It's outlined as.

$$St = \frac{Sh}{Re Sc} = \frac{h_m}{V} \quad 2.225$$

V is the flow velocity (m s⁻¹)

• **Empirical correlations of mass transfers on a plane wall**

For flow across a flat plate, the local mass convective transfer coefficient's convective mass correlations are.

Laminar [125] $Sh_x = \frac{h_m x}{D} = 0.332(Re_x)^{1/2} (Sc)^{1/3} \quad Re \leq 5 \cdot 10^5 \quad 2.226$

Turbulent [125] $Sh_x = \frac{h_m x}{D} = 0.0296(Re_x)^{4/5} (Sc)^{1/3} \quad Re > 10^8 \quad 2.227$

The mean values, the correlations are.

Laminar [125] $Sh_L = \frac{h_m L}{D} = 0.664(Re_L)^{1/2} (Sc)^{1/3} \quad Re \leq 5 \cdot 10^5 \quad 2.228$

Turbulent [125] $Sh_L = \frac{h_m L}{D} = 0.037(Re_L)^{4/5} (Sc)^{1/3} \quad Re > 10^8 \quad 2.229$

• **Summary of dimensionless numbers used in mass and heat transfer processes**

Table 2.4 Summary of dimensionless numbers

Heat transfer		Mass transfer	
Nusselt number	$Nu = \frac{hL}{\lambda}$	Sherwood number	$Sh = \frac{k_c L}{D}$
Prandtl number	$Pr = \frac{C_p \mu}{\lambda}$	Schmidt number	$Sc = \frac{\mu}{\rho D}$
Reynolds number	$Re = \frac{\rho VL}{\mu}$	Reynolds number	$Re = \frac{\rho VL}{\mu}$

2.5 Developed coupled heat and mass transfer models

Models for heat and mass movement are created using the laws of mass and energy conservation. The unifying elements throughout the various hygrothermal theories for porous building enclosures and materials are the forces that drive moisture migration. Modern hygrothermal models incorporate a variety of moisture-related driving factors, including moisture content, capillary pressure, partial water vapor pressure, relative humidity, and air moisture content.

2.5.1 Common models of coupled heat and mass transfer

2.5.1.1 Philip and De Vries model

The first combined moisture and heat models were created in 1957 by Philip and De Vries [21]. It was established using their concept regarding the relationship between temperature and moisture transport in soil. The fundamental differential equation for the movement of moisture in a porous medium is given in terms of the volumetric water content and the temperature T . They are indeed the major transport's driving factors for the heat and moisture transfer equation.

$$\frac{\partial \theta}{\partial t} = \nabla(D_{\theta} \nabla \theta) + \nabla(D_T \nabla T) + \frac{\partial K_h}{\partial z} \quad 2.230$$

$$D_{\theta} = D_{\theta,liq} + D_{\theta,vap}$$

$$D_T = D_{T,liq} + D_{T,vap}$$

Where D_T and D_{θ} are the corresponding moisture diffusion coefficients for the temperature and moisture gradients, respectively. The moisture diffusion coefficients for transfers of moisture in liquid and vapor phases, respectively, are D_{liq} and D_{vap} . The hydraulic conductivity, k_h , is typically linked to gravity forces. The heat transfer formula is expressed as follows:

$$C \frac{\partial T}{\partial t} = \nabla(\lambda \nabla T) - L_v \nabla(D_{\theta,vap} \nabla \theta) \quad 2.231$$

Where $D_{\theta,vap}$ is the vapor diffusion coefficient associated with the moisture gradient, C is the total heat capacity, and λ is the thermal conductivity. The diffusion energy of steam is the main heat source term accounted for in the Philip and De Vries equation.

2.5.1.2 Luikov Model

For both isothermal and non-isothermal processes, Luikov proposed a model concentrating on the thermodynamics of irreversible systems in 1966 [23]. This model was built on a strong descriptive investigation that made macroscopic predictions about the movement of heat and moisture in capillary porous materials. The relative moisture content u and temperature T are the driving forces behind the coupled heat and moisture transport. Under non-isothermal circumstances, the moisture transfer equation for porous medium may be expressed as follows.

$$\frac{\partial u}{\partial t} + \tau_{rm} \frac{\partial^2 u}{\partial t^2} = D_m \nabla(\nabla u + \delta \nabla T) \quad 2.232$$

Where τ_{rm} is the time at which moisture spreads through the capillary porous medium, D_m is the porous media's moisture diffusion coefficient, and δ is the thermogradient coefficient.

The difference between this model and standard moisture modeling is the extra factor on the right-hand side of the equation, which describes moisture capillary activities. The heat transfer equation for porous material is as follows.

$$\frac{\partial T}{\partial t} = \alpha \nabla(\nabla T) + \frac{E}{C_p} L \frac{\partial u}{\partial t} \quad 2.233$$

Here, L is the latent heat of evaporation, E is the phase conversion number, and α is the heat diffusion coefficient ($\lambda \rho^{-1} C_p^{-1}$).

2.5.1.3 Whitaker model

Whitaker offered out a more extensive theory in 1977 [22], describing transport equations for each phase (solid, liquid, and gas) in terms of the local average volume behavior at the macroscopic and microscopic levels. A model with the dependent variables moisture X and temperature T serves as the foundation for this theory. The moisture differential equation is.

$$\rho_s \frac{\partial X}{\partial t} = \nabla(\rho_s f D_v \nabla W_v + D_b \nabla \rho_v - \rho_w \bar{V}_w) \quad 2.234$$

X is the bulk moisture content in that case. W_v is the vapor mass fraction, D_v and D_b are the water vapor and bound water diffusivities, respectively, and V_w is the liquid phase velocity [128]. ρ_v , ρ_w , ρ_s are respectively the density of water vapor, liquid phase, and solid phase. The following is a representation of the heat differential equation.

$$\frac{\partial(\varepsilon_w \rho_w H_w + \varepsilon_g \rho_v H_v + \varepsilon_s \rho_s H_s + \bar{\rho}_b \bar{H}_b)}{\partial t} = \nabla(\lambda \nabla T) + H_v \rho_g f D_v \nabla W_v + H_b D_b \nabla \rho_v - H_w \rho_w \bar{V}_w \quad 2.235$$

H_w, H_v, H_s and H_b stand for, respectively, the enthalpies of water in its liquid, vapor, solid, and bound states. The volume fractions of liquid, vapor, and solid are denoted by ε_b , ε_v and ε_s respectively, while the porous medium's thermal conductivity is designated by λ .

2.5.1.4 Künzel model

Although it was founded on Kiel's theorem, Künzel produced a new model in 1995 that was remarkably comparable to others created in earlier decades [24]. In this paradigm, Künzel made an effort to define the coupled heat and moisture transmission in building components using the terminology relative humidity and temperature T as the main driving factors.

$$\frac{dw}{d\phi} \frac{\partial \phi}{\partial t} = \nabla(D_\phi \nabla \phi + \delta_p \nabla(\phi p_{sat})) \quad 2.236$$

Where $(dw/d\phi)$ is the porous material's capability to trap moisture, D_ϕ is its liquid conduction

coefficient, δ is its ability to let water vapor through to the outside world (water vapor permeability), ϕ is its relative humidity, and p_{sat} is its water vapor saturation pressure. The Künzel model for heat transfer proposes the expression below.

$$\frac{dH}{dT} \frac{\partial T}{\partial t} = \nabla(\lambda \nabla T) + h_v \nabla(\delta_p \nabla(\phi p_{sat})) \quad 2.237$$

Where h_v is the enthalpy of water evaporation, λ is the thermal conductivity, and (dH/dT) is the heat storage capacity of the porous medium.

2.5.1.5 Mendes model

Mendes introduced a novel hygrothermal model in 1999 based on the equations of Philip and De Vries, but he employed the volumetric moisture content and temperature gradient T as the main driving factors for the coupled heat and moisture transport equations [25]. The following is how the moisture transfer equation is currently expressed:

$$\frac{\partial \theta}{\partial t} = \nabla(D_T \nabla T + D_\theta \nabla \theta) \quad 2.238$$

Where θ is the volumetric moisture content and D_T and D_θ are the total moisture diffusion coefficients of liquid and vapor phases that are related to the temperature gradient and the moisture gradient, respectively. Mendes suggests the following equation for heat transfers.

$$\rho c_p \frac{\partial T}{\partial t} = \nabla(\lambda \nabla T) + L \nabla(D_{T,vap} \nabla T + D_{\theta,vap} \nabla \theta) \quad 2.239$$

Where L is the latent heat of evaporation, λ is the thermal conductivity of the material, c_p is the specific heat of the dry material, $D_{\theta,vap}$ and $D_{T,vap}$ are the vapor diffusion coefficients related to the moisture content and temperature gradients, respectively, and ρ is the material's density.

Mendes et al. developed a novel approach in 2002 for resolving equations involving highly coupled heat and mass flow in hygroscopic material. Due to changes in temperature and moisture content, he was capable to linearize the vapor exchange between both the wall and the surrounding air, which cut down on the time needed to calculate the numerical solution.

2.6 Conclusion of the chapter

Whatever the complexities of the subject, the models proposed above presently provide a general enough diversity to make modeling simple. In the upcoming chapters, they will be heavily used to both identify parameters and contribute to the interpretation of experimental data in order to better understand hygrothermal phenomena. To completely describe these effects, a broader approach to theoretical analysis is required.

These model systems can become more sophisticated as a result, which can lead to new discoveries, deeper understanding, and eventually more complicated designs with fewer thermal failures. This initiative ultimately aims to provide new methodologies for predicting the energy performance of low-carbon buildings. The creation of appropriate numerical algorithms that are based on earlier theoretical investigations and experimental/numerical techniques is required to achieve this aim. This synthesis of the literature has shown that efficient coupled heat, air, and moisture transfer models must be developed in order to accurately represent the hygrothermal behavior of buildings and, consequently, to enhance predictions of the energy balance caused by an excess of moisture in the building. Fortunately, techniques for predicting the flow of heat, moisture, and air inside the building envelope are available. These models may be used to determine a structure's performance under a variety of boundary conditions, such as temperature, solar radiation, and inside humidity levels.

An approach for incorporating a multilayer wall model (2D or 3D) in a dynamic simulation tool of a building was developed as a result of parametrizing work that was done in this respect. This simulation takes heat and mass transfers into account (temperature, air and humidity). Thus, the temperature and humidity in each of the walls, as well as the ambient conditions of the outside air (wind, rain, etc.), are computed using physical characteristics and boundary conditions. The thermal building modeling tool receives these characteristics from the model in order to perform dynamic simulations. These simulations trace how heat moves between layers through internal and exterior barriers, as well as its interactions with the environment alongside proper consideration for the radiative transmission between the walls. Additionally, consideration was given to the material's hydric and thermophysical qualities which varied with its hygrothermal condition. By simplifying the hygrothermal transfer model at the building scale and simulating typical thermal behavior modeling in conjunction with artificial intelligence, it is possible to convert the outcomes of a typical dynamic thermal simulation into a full hygrothermal simulation at the building scale.

Chapter 3.

Characterization of a novel geo-based material for multilayered wall and highlighting of sorption curve linearization on the coupled heat and mass transfer

Contents

3.1	INTRODUCTION TO THE CHAPTER	115
3.2	AIM OF CHAPTER	117
3.3	EXPERIMENTAL SETUP AND MATERIAL ELABORATION	117
3.3.1	Characterization techniques.....	118
3.3.2	Natural fiber.....	118
3.3.3	Structural earth.....	119
3.3.4	Lightened earth.....	120
3.3.5	Soils preparation	120
3.3.6	Material properties measurement.....	121
3.3.6.1	Water vapor permeability, porosity and vapor resistance factor.....	121
3.3.6.2	Thermal conductivity, heat capacity and dry density	122
3.3.6.3	Sorption isotherm curves.....	122
3.4	MECHANICAL AND HYGROTHERMAL PROPERTIES	123
3.4.1	Hygrothermal properties of the structural part (Structural Cob. SC).....	123
3.4.2	Hygrothermal properties of the insulating part (Coffee Lightened Clay. CLC).....	124
3.4.3	Material compression strength.....	128
3.5	NUMERICAL SIMULATION OF HYGROTHERMAL BEHAVIOR	130
3.5.1	Geometry, boundary conditions and mesh generating.....	130
3.5.2	Mathematical modeling and sorption linearization due to hysteresis effect.....	133
3.5.3	Model validation of linearization effect on sorption curve with experimental data	138
3.5.3.1	Scenario 1. Temperature variation with constant humidity	139
3.5.3.2	Scenario 2. Humidity variation with constant temperature.....	141
3.5.4	Hygrothermal performance evaluation of CLC and SC wall	143
3.5.4.1	Scenario 1. Temperature variation with constant humidity	144
3.5.4.2	Scenario 2. Humidity variation with isotherm condition	145
3.5.4.3	Heat flow transfer through the CLC+SC wall for isotherm and isohydric scenario ..	147
3.6	CONCLUSION OF THE CHAPTER AND DISCUSSION	149
3.6.1	Summary of main results.....	149
3.6.2	Discussion on model limitations and perspectives.....	150

3.1 Introduction to the chapter

Coffee production procedures produce wastes called coffee ground wastes (CGW). In this work, we suggest substantially valuing them as building materials. We specifically focus on the mechanical and hygrothermal properties of earthen cob constructions that incorporate varying levels of CGW. Our findings show that the introduction of coffee ground wastes to cob improves both its compressive and thermos-hydric properties. It is noted that the thermal characteristics of the lightened earth have been improved, and the hydric load in the air has been efficiently controlled while still retaining appropriate mechanical qualities.

In order to comprehend the effect on the energy performance potential of cob specimens, hygrothermal behavior is assessed using numerical analysis. To speed up computation and enhance outcomes, a linearization of the sorption curve is used to simplify the simulation approaches. Experimental data used to validate the strategy and reveals a potential advance over earlier methods. The suggested approach can be quickly and effectively used to investigate the energy performance of hygroscopic low carbon materials and examine their hygrothermal behavior, which are strictly associated with the energy performance of a building.

Numerous ancient clay constructions are still seen today in North Africa and the Middle East, where they have been built for over ten thousand years [129]. Use of clay as a main building material is referred to as "earthen construction." It can be seen as a single natural construction idea or as a group of technologies that provide more thermos-hydric comfort, endurance, and ecological sustainability than more conventional modern construction techniques [130]. Earth building is being used by communities and individuals all around the world to reduce their effects on carbon dioxide emissions in the atmosphere and global temperature rise [131]. The common earth-building techniques that use clay as a building material involve mud bricks, rammed earth, cob, poured earth, and compacted ground [132]. One of most traditional forms of constructing with clay, soil, water, and fibers is called cob and is commonly used in Brittany and Normandy (in France) [133]. Cob is an ancient construction technique that uses sand, molded earthen clods, and fibers like straw and reed. In order to reduce self-generating shrinkage in earth materials and provide the best thermal performance, fibrous materials, especially reed, are frequently employed. Lightened earth combinations have a considerable ability to interact with moisture, according to several studies. Combinations of earth, straw and hemp are among the insulating materials with the highest amount of water buffering value and good ability to control moisture in defined areas. Numerous environmental factors can have an impact on the structural response of cob constructions. The material's mechanical characteristics are weakened by increased water content, which can be brought on by rising humidity levels or a leaking roof, and this causes the fibers to swell. Therefore, at the fiber-matrix contact, voids or microcracks might form [134].

The hygrothermal activity of cob structures depends on a number of variables that can occasionally be out of our control. It might be difficult to find a model that accurately describes the hygrothermal performance of buildings. Indeed, complex and non-linear systems controlled by their environment determine their dynamics. There are various phenomenological techniques that are used to describe completely coupled heat and mass movements in building enclosures, and these approaches often differ in the transfer capabilities they employ. For example, the temperature is referred to as a traditional transfer potential when discussing heat transfer. Otherwise, several models have been established using various mass transfer driving parameters, such as water content [135], vapor pressure [136], vapor content [137] and relative humidity [17], to represent the transport of moisture.

However, determining the sorption curve hysteresis represents the primary challenge in utilizing physical models to represent the complete hygrothermal behavior simulation. In order to predict the hygrothermal behavior of low carbon buildings, Hamdaoui et al. 2021 research [138] presented many hysteresis models and their impacts on moisture activity. At both the wall and building scales, the sorption curve hysteresis is generally ignored in the conventional numerical calculations. The simplified Mualem model [139], [140] has been utilized in numerous research [141], [142] and is one of the few models that takes into consideration the sorption hysteresis of hygroscopic media such as the material used in construction [143].

Only a few numerical methods, such as COMSOL Multiphysics, are utilized in the literature to account for the hysteresis effect. This final one, for instance, was utilized by Alioua et al. [17] to predict the hygrothermal behavior of date palm concretes (DPC). When hysteresis is taken into account, they show that moisture transfer estimates in DPC is improved.

In both constant and transient phases, with and without moisture adsorption hysteresis, Promis et al. [141] analyzed the situation. If the relative humidity range stays below the capillary condensation point, hysteresis can be disregarded in steady state. Hysteresis consideration, however, raises the complexity of the model and the simulation's computational time [144]. Furthermore, some researchers demonstrate that non-hysteresis simulation can produce errors of up to 20–30 % in the prediction of moisture content for wood sorption performance [145].

In this study, we suggest a numerical investigation of the material's hygrothermal behavior utilizing linearization of the sorption curve in order to reach the optimum combination between lowering model complexity [144] and boosting accuracy. Without the need for extra equations to simulate the hysteresis effect, the program can increase the outputs' consistency. Experimental data from Alioua et al. [17] were first used to validate the impact of linearization of sorption curves. The effectiveness of this technique is evaluated on a multilayer wall made of Coffee Lightening Clay (CLC) and Structural Cob (SC), for which hygroscopic, thermal, and mechanical characterizations are carried out at various replacement levels. Similar methods to those employed

Aim of the chapter

Traditional German and Brittany cob buildings are utilized to produce the cob materials [146]. In this building architecture, an extra layer is employed.

A mixture of two wall construction layers formed of earth components is taken into consideration to adhere to building regulations. The two layers consist of a load-bearing layer with a higher density and an insulating membrane including a high fiber content. Cob walls' mechanical properties, thermal conductivity, and heat capacity are all measured on a lab scale.

3.2 Aim of the chapter

After analyzing the pertinent recent literature, we subdivided the study for this section of the thesis into a number of parts, each of which is constituted up of a number of sub-sections, as we shall see in more detail below.

- Formulation and experimental characterization. In this section, two material formulations (i) Coffee Lightening Clay (CLC) and (ii) Structural Cob (SC) have been investigated, Hygroscopic, thermal, and mechanical characterizations were carried out at different levels of substitution.
- Investigation and discussion are conducted on experimental outcomes regarding the hygrothermal properties of materials created for insulating and structural walls.
- Conducting a campaign of numerical simulations to study the hygrothermal behavior while optimizing the modeling approach and accounting for the linearized hysteresis impact In this section, wall scale experimental data from Alioua et al. [17] are used to validate the output numerical data.
- The approach is tested using WUFI Plus software for a double layer wall (CLC and SC) after it has been proven in terms of its hygrothermal performance.

3.3 Experimental setup and material elaboration

Coffee ground wastes (CGW) are made up of several arabica coffee species. CGW were gathered from our coffee lounge (Caen, Normandy, France). The waste material from raw coffee grounds was immediately sifted and crushed to a particle size of 63 microns after being collected and dried for 24 hours at 105 °C. **Table 3.1** provides a summary of the basic physicochemical characteristics of CGW.

Table 3.1 Physicochemical properties of Coffee Ground Wastes [165]

	Porosity (%)	Bulk density (kg m ⁻³)	Water absorption (%)	pH
CGW	52.1	468 ± 3	0.9	6.1 ± 0.01

The mean values are provided, and it is assumed that the measurement errors will be under 10 %. Approximately, half of the weight of raw CGW is made up of cellulose and hemicellulose (**Table 3.2**), with lignin making up the remaining weight. 14.2 % of proteins, 9.5 % of lipids, and 2.1 % of ash are examples of other biochemicals.

Table 3.2 Biochemical composition of coffee ground wastes [165]

Composition	Weight (wt. %)
Proteins	15.3
Cellulose	26.2
Hemicellulose	23.8
Lignin	24.9
Lipids	7.7
Ashes	2.1

3.3.1 Characterization techniques

The results of the bibliographic analysis demonstrated that the components of the cob had certain ideal properties. Since the goal of this study is to create a composite of earth-fibers that is near to the cob and has a high energy efficiency, it is necessary to evaluate these different components (earth, fibers) in order to determine the ideal composite mixtures that will produce the best mechanical and thermo-hydric results. In terms of improving the supply and give local products priority, it should be highlighted that the materials utilized are completely from the Normandy region.

However, various regions of France have access to resources of a similar nature. Thus, the study seeks to characterize the primary materials, the creation of the various formulations, and manufacturing conditions for the samples, are all covered in this chapter. The numerical simulation techniques that will be used to examine the hygrothermal behavior of the composites at the wall scale are also covered in detail in the following subsections, with a focus on a novel linearization strategy.

3.3.2 Natural fiber

As reinforcing and insulator components, natural fibers were used (**Table 3.3**). Local Laulne (Normandy) farmers supplied the fibers utilized in this investigation (Normandy). We employed the wheat straws to create the Structural Cob (SC). The thermal conductivity of used fiber ranges from 0.035 to 0.054 W m⁻¹ K⁻¹ [133]. The reed fiber was utilized for the Coffee Lightening

Clay (CLC). They may be found easily and are reasonably priced. Their distribution could have a less negative effect on the environment because of their entirely biodegradable qualities and low CO₂ emissions degree when in comparison to synthetic fibers. Reed is a generally suitable insulating material with a thermal conductivity of around 0.05 W m⁻¹ K⁻¹ [147].

Table 3.3 Physical properties of reed and wheat straw fibers [1]

	Diameter (mm)	Density (kg m ⁻³)	Initial water content (%)	Tensile strength (MPa)
Straw	1-4	1408 ± 5	10.7	23.9 ± 3.5
Reed	1-4	1294 ± 5	8.5	117 ± 9

3.3.3 Structural earth

The principal ionic compounds in the structural earth employed in this study are mostly silicon, aluminum, iron, and sodium (**Table 3.4**). To sum up, silty soil is the predominant of the structural soil utilized for solid construction. In fact, it is made of unaltered minerals like silicates and quartz flakes (micas, feldspars, smectites and serpentines).

Table 3.4 Chemical composition of structural soil [1]

Element	Wt. %
Silicon dioxide (SiO ₂)	65.89
Aluminum oxide (Al ₂ O ₃)	14.23
Ferric oxide (Fe ₂ O ₃)	6.65
Magnesium oxide (MgO)	4.08
Potassium oxide (K ₂ O)	2.17
Titanium dioxide (TiO ₂)	2.08
Calcium oxide (CaO)	1.27
Sodium oxide (Na ₂ O)	1.11
Manganese oxide (MnO)	0.16
Phosphorus Pentoxide (P ₂ O ₅)	0.14
Sulfur trioxide (SO ₃)	<0.1
Loss on ignition	2.26

3.3.4 Lightened earth

Kaolinite and illite with a small amount of chlorite constitute the lighter earth. Kaolinite affords the clay its moldability when mixed with water [148]. The chemical content and mechanical properties of the utilized lightened earth are presented in **Table 3.5**.

Table 3.5 Chemical composition and mechanical properties of lightened earth [1]

Element	Wt. %
Silicon dioxide (SiO ₂)	59.73
Aluminum oxide (Al ₂ O ₃)	20.25
Ferric oxide (Fe ₂ O ₃)	6.09
Calcium oxide (CaO)	5.33
Magnesium oxide (MgO)	3.16
Sodium oxide (Na ₂ O)	0.1
Potassium oxide (K ₂ O)	2.05
Sulfur trioxide (SO ₃)	<0.1
Phosphorus Pentoxide (P ₂ O ₅)	<0.1
Cl ⁻	0.18
Loss on ignition	3.10
Physical properties	
Plasticity limit (%)	42.5
Plasticity index (%)	15.3
Absolute density (g cm ⁻³)	2.73

3.3.5 Soils preparation

The soils were dried in a high-temperature oven heated to 105 °C for 24 hours to remove the absorbed water before being ground to a fine powder (<63µm). According to earlier studies, the land has a wider particle size distribution. Lightened and structured earth particles with diameters smaller than 2 mm must constitute around 98 percent of the total particles when preparing the earth for the creation of the mixture. The bio-based composites Coffee Lightning Clay (CLC) and Structural Cob (SC) are made of typical natural components. Cob, sand, fiber, and CGW

are used to create the insulating component, while clay, sand, fiber, and CGW are used to create the structural component. To mix CLC with coffee grounds wastes, local water supply with a pH of 7.68 was employed for the formulation of materials (**Table 3.6**).

For this experiment, it was decided to use the soil-fiber-CGW mixes with the best thermal properties. Therefore, a mixture of 20 % used coffee grounds for CLC and 0 % for SC was selected (**Table 3.6**). In fact, compared to the ordinary Cob, the SC material's addition of CGW has a very low compressive strength. This outcome is a result of the silty, low-calcium character of the soil that was employed. Our test specimens showed no signs of crack initiation, and their shrinkage after 28 days was under 1 %.

Table 3.6 Mixture proportion of the developed structural and insulating wall parts made of coffee ground wastes [165]

	Coffee lightened clay (CLC)				
	0 %	5 %	10 %	15 %	20 %
Lightened clay	1	0.95	0.9	0.85	0.8
Coffee grinds	0	0.05	0.1	0.15	0.2
Reed	0.25	0.25	0.25	0.25	0.25
Structural Cob (SC)					
Structural cob	0.67				
Coffee grinds	0				
Sand	0.33				
Straw	0.02				

3.3.6 Material properties measurement

In order to perform numerical analysis on the hygrothermal behavior of CLC/SC multilayered walls, the computer simulations used in this work require for input a variety of material features such as sorption isotherms, vapor resistance factors, thermal conductivity, heat capacity, and so on. Therefore, as described in the next subsections, these parameters were established empirically in compliance with norms.

3.3.6.1 Water vapor permeability, porosity and vapor resistance factor

A hygroscopic wall's capability to permit vapor movement in the inside pores of a hygroscopic

media while we have a permanent changing in relative humidity, is referred to as water vapor permeability. Numerous studies have been conducted to calculate vapor resistance factors.

Practically dry cups method (NF EN ISO 12572) [149], which corresponds to an operational technique with relative humidity ranges between 0 % and 50 %. In order to perform this test, relative humidity gradients must be created between two sides of a specimen that is fully sealed. Once this has been done, the daily mass variance must be observed until it becomes constant. On the other hand, the method described in the NF ISO 5017 standard was used to determine porosity [150]. The resistance factor and water vapor permeability of highly porous low carbon material was calculated using the following formulas.

$$G = \frac{m_2 - m_1}{t_2 - t_1} \quad (\text{kg s}^{-1}) \quad \text{Flow rate of water vapor, where } m \text{ is the mass of the sample at time } t. \quad 3.1$$

$$w = \frac{G}{A \Delta P_v} \quad (\text{kg m}^{-2} \text{ s}^{-1} \text{ Pa}^{-1}) \quad \text{Water vapor Permeance, where } \Delta P_v \text{ is the difference in water vapor pressure between the samples, and } A \text{ is its area.} \quad 3.2$$

$$z = \frac{1}{w} \quad (\text{m}^2 \text{ s Pa kg}^{-1}) \quad \text{Water vapor resistance.} \quad 3.3$$

$$\delta = w d \quad (\text{kg m}^{-1} \text{ s}^{-1} \text{ Pa}^{-1}) \quad \text{Water vapor permeability, where } d \text{ is the average thickness of specimen.} \quad 3.4$$

$$\mu = \frac{\delta_{air}}{\delta} \quad (-) \quad \text{Water vapor resistance factor} \quad 3.5$$

3.3.6.2 Thermal conductivity, heat capacity and dry density

For an experimental investigation or for numerical estimations of energy performance, using the current formula can make it easier to determine the thermal conductivity of the insulation wall as a function of temperature and CGW concentration.

The specific heat capacity (C_p) of a cob wall under constant pressure is used to determine how well it can store thermal energy. The Differential Scanning Calorimetry technique (DSC, NETZSCH STA 449 F3), that also complies with ISO 11357-4, was used to quantify C_p [151]. Data have been gathered at a heating rate of $1^\circ\text{C}\cdot\text{min}^{-1}$ and between -20°C and 30°C . The specific surface area of the cob samples was calculated using the BET method, and the absolute density of all raw materials was assessed using a helium pycnometer (Accupyc II 1340).

3.3.6.3 Sorption isotherm curves

The isothermal sorption curve of biobased walls is an important factor due to the high porosity of the plant fibers incorporated in it. Based on NF EN ISO 12571 [152], this adsorption/desorption curve shows the way in which the water content inside the material

changes as a function of relative humidity at a constant test temperature. The standard utilized in the experimental investigations outlines two procedures for evaluating the hygroscopic sorption characteristics of porous building materials and products. Either by using desiccators and weight cups (desiccator technique) or a climatic chamber by applying a fluctuation in relative humidity until equilibrium is attained inside the material.

3.4 Mechanical and hygrothermal properties

In this section, we examined and compared our results to experimental data for various earth fiber materials, as well as lightened earth and clay for different densities, in order to determine the hygrothermal performance of our built-earth walls. The calculation of densities, specific heat capacities, and isothermal sorption curves is covered in the following subsections.

Especially considering the fact that all of the results come from the same material, the insulating components' hygroscopic values are very different from those of the structural elements. Consequently, we prioritize the insulation component for more investigation.

3.4.1 Hygrothermal properties of the structural part (Structural Cob. SC)

All of the SC materials' hygrothermal parameters are listed in **Table 3.7**, making it easy to conduct numerical simulations or perform experimental research on their behavior.

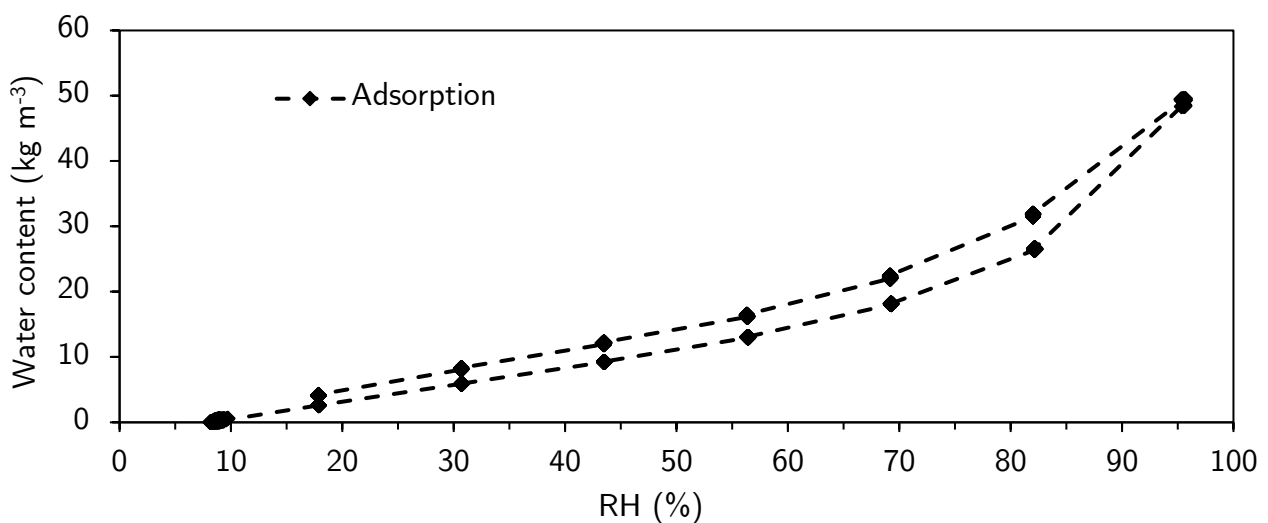


Figure 3.1 Sorption curve of Structural Cob (SC with 0 % of coffee ground wastes) [165]

The employed SC material's moisture sorption curve displays type II isotherm characteristic and has a sigmoidal shape [153] (**Figure 3.1**). Such activity is typical of cobs, which contain earth fiber, and is clearly related to the hygroscopic appearance of this substance.

Due to the increased porosity of the CLC material, the moisture content of the SC material is almost two thirds that of the first one (**Figure 3.3**), as would be expected for an insulating wall as compared to a structural element.

Table 3.7 Hygrothermal properties of Structural Cob (SC 0 %) [165]

Properties	Value
Dry density ρ (kg m ⁻³)	1384
Dry thermal conductivity λ (W m ⁻¹ K ⁻¹)	0.33 at 10°C
Vapor resistance factor (dry cup) μ [-]	8.385
Dry specific heat C_p (J kg ⁻¹ K ⁻¹)	865.2
Porosity	0.34
Water vapor permeance w (kg m ⁻² s ⁻¹ Pa ⁻¹)	3.518 10 ⁻¹⁰

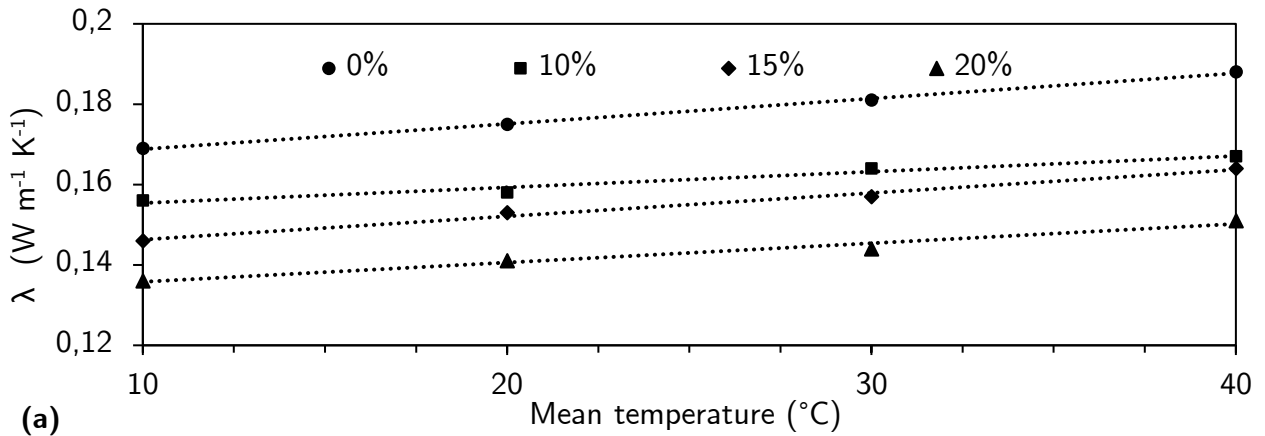
3.4.2 Hygrothermal properties of the insulating part (Coffee Lightened Clay. CLC)

For temperatures ranges between 10°C and 40°C, the thermal conductivity of the clay samples without the addition of CGW varies between 0.169 and 0.188 W m⁻¹ K⁻¹ (**Figure 3.2a**). Such values drop from 0.167 W m⁻¹ K⁻¹ to 0.156 W m⁻¹ K⁻¹ within the same temperature gradient with a 10 % increase in CGW. These findings demonstrate that the thermal conductivity of the CLC is decreased by the incorporation of CGW into the earth matrix. The optimum tested addition of 20 % CGW appears to be the best improves of the material's thermal insulation. Thermal conductivity decreased with the addition of 20 % of CGW by 24.2 % at 10 °C and 24.5 % at 40 °C as compared to pure cob. For the insulating element, thermal conductivity varies with temperature and the percentage of coffee ground wastes. In this work, thermal conductivity as a factor of (CGW) and (T) was approximated using the following equation.

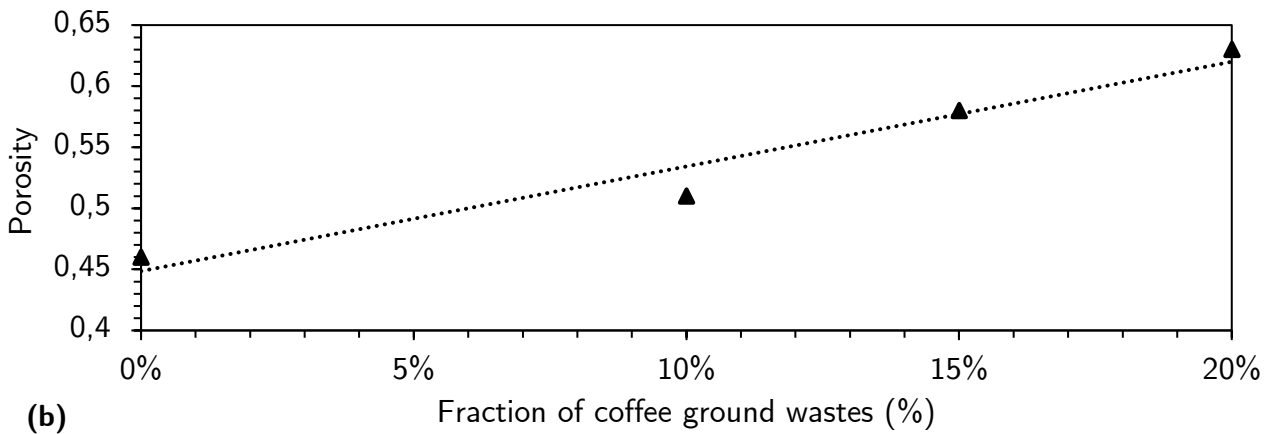
$$\lambda = [0,1511(CGW)^{-0,016} + 1,9 \cdot 10^{-3}(CGW)^{0,984} - 1,2 \cdot 10^{-4}(CGW)^{1,984}] \left(\frac{T}{T_{ref}}\right)^{0,068} \quad 3.6$$

Where T is the mean ambient temperature in degrees Celsius, T_{ref} is equal to 10°C, and CGW is the percentage of coffee ground wastes (ranges from 0 to 1). The 20 wt % sample of CLC was chosen for the subsequent analysis because it had the lowest thermal conductivity.

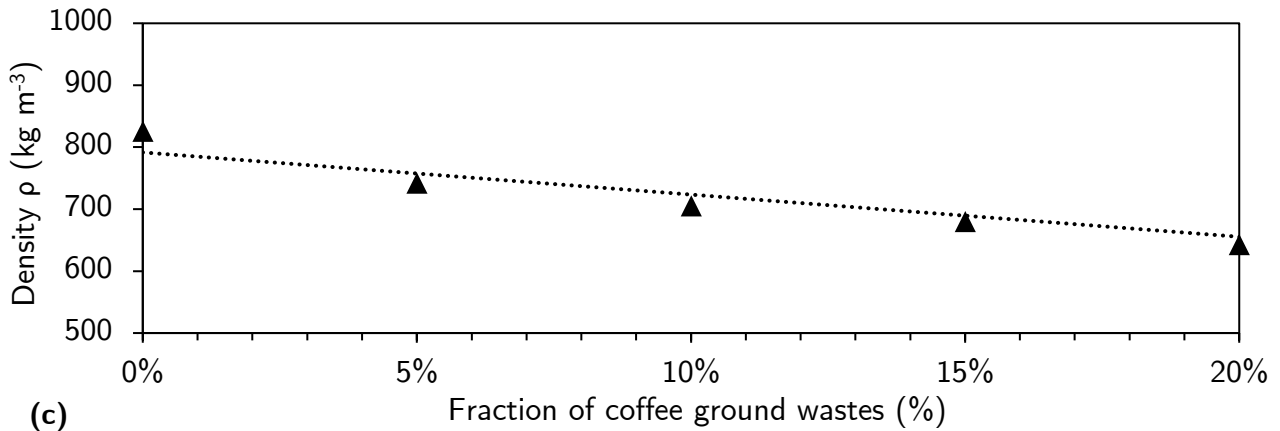
Figure 3.2b shows that the apparent porosity of CLC ranged from 46 % to 63 %, while the material's bulk density dropped by roughly 26 % (**Figure 3.2c**). Since coffee waste has been added, the density of CLC has declined. Since CGW has a lower density than cob, this has resulted in a significant weight reduction when it comes to applications in the field of civil engineering. The increased porosity that occurs from the CGW addition to cob contributes to the specimens' reduced heat conductivity. In our scenario, air fills the pores, and we know that it has a lower thermal conductivity than the solid materials under consideration, which lowers the thermal conductivity of the samples.



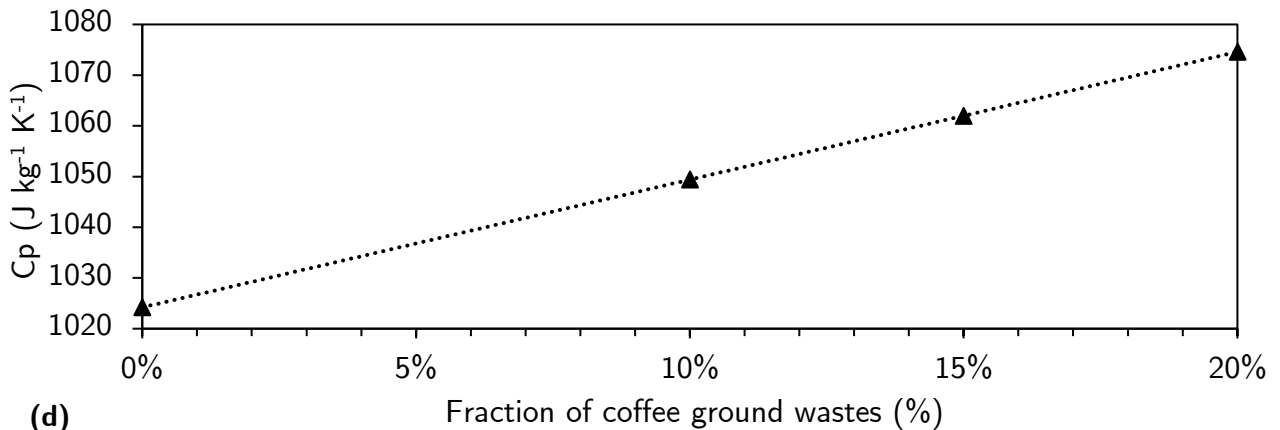
(a)



(b)



(c)



(d)

Figure 3.2 (a) Thermal conductivity, (b) Porosity, (c) Density, and specific heat (d) of Coffee Lightened Clay for various amounts of CGW in CLC [165]

The thermal conductivity values dropped by up to 24.2 % at 10°C, suggesting that there are further opportunities for efficiency gains improvements in construction applications. We found that the densities and porosities of the samples are clearly related to their thermal conductivities, and further incorporation of CGW in the CLC might be researched to further explore this impact. In accordance with the NF ISO 5017 standard [150], porosity is assessed by measuring the mass of a dried test sample, its actual mass when immersed in a solution that it has been soaked just under vacuum environments, and its mass in air while remaining saturated with the liquid. While 20 % of CGW is used in the formulation design, we observe a porosity rise from 0.45 without CGW in the CLC wall to nearly 0.63 (Figure 3.2b), which is a 40 % increase.

With the addition of CGW, the specific heat capacity (Figure 3.2d) rises as well, achieving nearly 1075 J kg⁻¹ K⁻¹ for 20 % in CLC, a considerably large number when compared to the earth-fiber mixture. Generally, materials with greater specific heat capacities are needed to improve insulating applications in building. Our tests demonstrate that soil-fiber-coffee mixes outperform conventional cobs with straightforward soil-fiber combinations in terms of Cp values. All the CLC specimens had remarkably identical moisture sorption curves (Figure 3.3), which After CGW is added to the samples, the water content marginally increases.

This can be influenced by a range of factors, including the sample's porosity, which has a substantial impact on the activities and interactions of water molecules within the porous structure. When attempting to calculate the water diffusion inside porous media using a different method, such as the Knüdsen model, a thorough understanding of the adsorption/desorption process might result in an appropriate hypothesis. It is advised to consistently rely on the experimental research on these parameters since the underlying phenomena is rather challenging to fully comprehend.

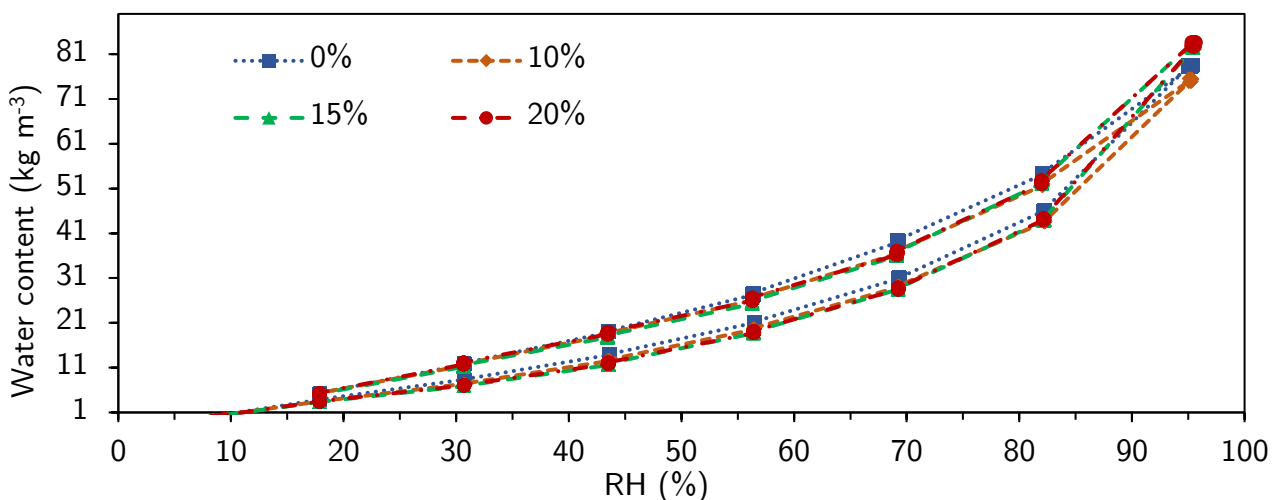


Figure 3.3 Moisture sorption isotherm curve of Coffee Lightened Clay (CLC with different portions of coffee ground wastes) [165]

In comparison to conventional building materials, CLC and SC are extremely hygroscopic and absorb a significant amount of water. Due to its high porosity and low density, CLC offers excellent insulating and hydric properties. In **Figure 3.4**, the water vapor resistance factor decreases from 6.06 to 5.5 as the coffee waste proportion increases.

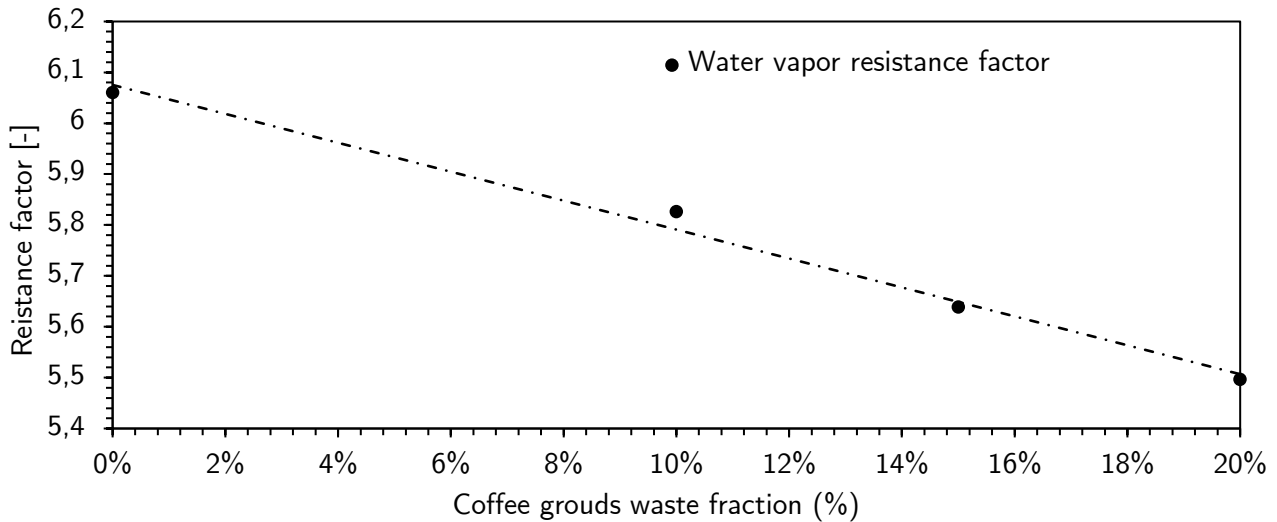


Figure 3.4 Water vapor resistance factor of CLC samples upon CGW additions [165]

The water vapor permeability of bio-composites determines their ability to transfer water vapor under a variety of relative humidity conditions. The evaluation for water vapor permeability was determined in compliance with French norm NF EN ISO 12571 [152]. The specimens were coated along both edges with aluminum sheets and gel wax, and the variation in relative humidity between the surfaces of their inside and outside was then noted.

For 0 % and 20 % CGW, respectively, the water permeability (δ) of CLC samples rises steadily and linearly with the amount of coffee grounds introduced, approximately from $2.97 \cdot 10^{-11}$ to $3.27 \cdot 10^{-11} \text{ kg m}^{-1} \text{ s}^{-1} \text{ Pa}^{-1}$ as mentioned in **Figure 3.5**.

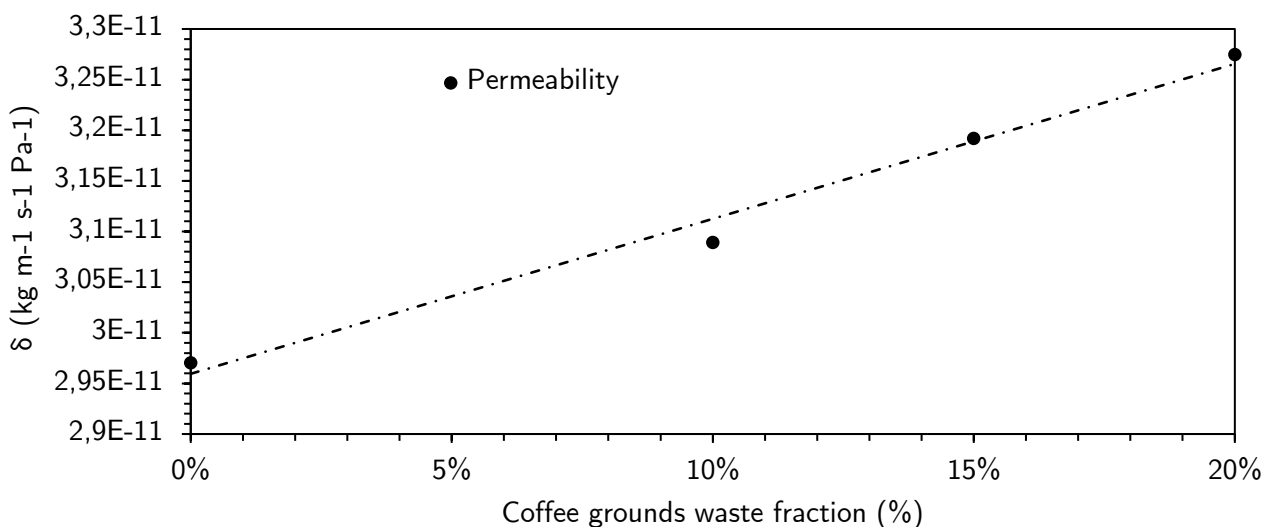


Figure 3.5 Permeability of CLC samples upon CGW additions [165]

3.4.3 Material compression strength

Before water was gradually added while mixing constantly to create a uniform fresh composite solution, all the dry ingredients were well blended. In order to prevent cavitation or empty holes in the enclosed shell, the mix was then gradually created layer by layer for either cylindrical or parallelepiped molds (see **Figure 3.6**). One day later, the built-up blocks were taken out of the molds. A month of dehydration in the lab was conducted at 50 % RH and 20°C environments. Throughout the drying process, temperature and relative humidity were monitored often to make sure they were steady. In addition to the absence of any adhesion between the components of the combination, the compression tests on the cylinders revealed no particle rupture. As a result, the compressive strength among these created materials is limited to the highest measured stress. A prior investigation determined the greatest compressive strength for longitudinal deformations between 1.5 and 7.5 %. From 2 % to 4 % of deformation, Cob illustrates a maximum compression stress of 1.2 MPa (**Figure 3.7b**). As predicted, these deformation values reached low loads of 5 to 10 times for the insulating parts compared to the structural cob composite. Nevertheless, upon the addition of more than 15 % of CGW, the compressive strength improves significantly (**Figure 3.7a**), although the thermal conductivity of CLC decreases (**Figure 3.2a**). Consequently, the CGW inclusion promotes both mechanical and insulating qualities.

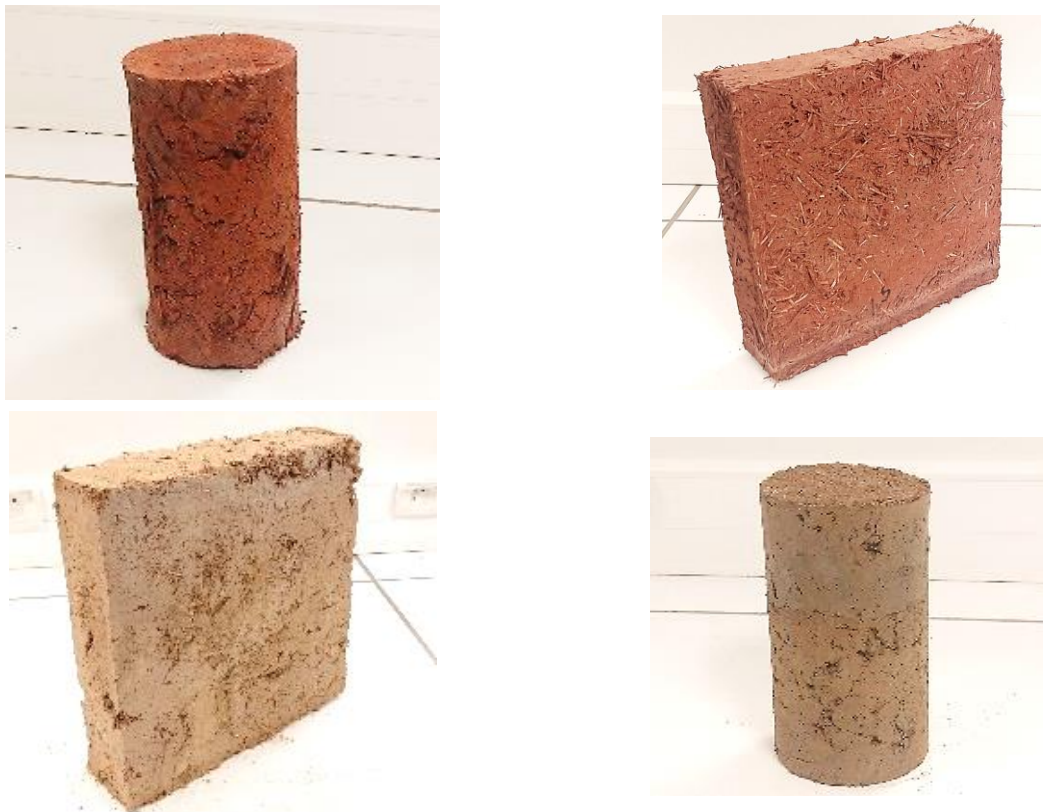


Figure 3.6 Coffee lightened clay and Structural cob samples used for mechanical ($\text{Ø}11 \text{ cm} \times 22 \text{ cm}$) and thermal ($30 \times 30 \times 4 \text{ cm}$) tests [165]

A Schenck 4-column press with a hydraulic cylinder that can conduct traction, compression, shear, and flexion experiments with forces up to 3000 kN was employed for the compression testing. It is primarily utilized for mechanical testing of building materials applied on cylindrical specimens with the following dimensions, 11 cm of diameter and 22 cm of height. The test configuration was established on a displacement rate of 0.05 kN/s and a maximum deflection length of 10 cm. In comparison to other specimens, the mixes of CLC with 15 % CGW consistently exhibit the highest strength following higher deformations of up to 5 % (**Figure 3.7a**).

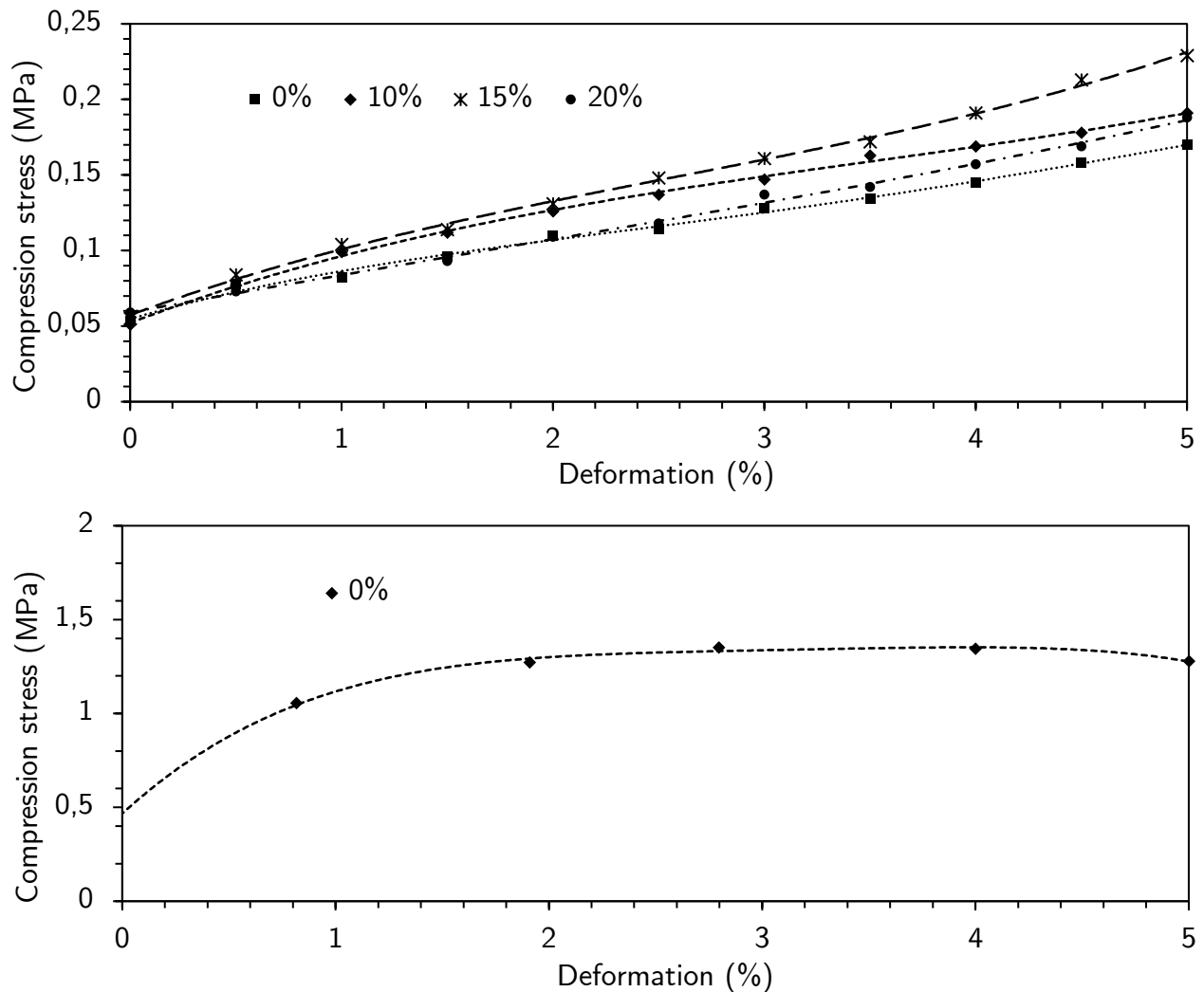


Figure 3.7 CLC (a) and SC (b) compression strength tests as a function of deformation [165]

This behavior is brought on by CGW's improved ground, fiber, and lignin adhesion, which prevents fracture extension. Consolidation is required to improve the mechanical characteristics of lighter earth since it is known to have differential settlements and also have poor shear strength. Therefore, lignin, the main constituent of the coffee cellulose that is empty of carbohydrates and is crucial for its hard structure, can be credited for CGW's stabilizing action in this study [154].

Lignin makes for around 24.9 % of the dry matter of the biomass in the CGW (**Table 3.2**). Lignin is considered a non-carbohydrate-based polymer which is hugely significant hydrophilic material due to its capacity to absorb and keep a large amount of water inside its structure. Lignin undergoes hydrolytic depolymerization, resulting in reduced molecular weight, lower alkyl-aryl ether, and higher phenolic OH-content molecules [155].

At a relative humidity of 95 %, the mass change for the CLC 20 % and CLC 0 % specimens is approximately 82 kg m^{-3} and 78 kg m^{-3} , respectively (**Figure 3.3**). The SC specimen's retention curve value at 95 % relative humidity is close to 50 kg m^{-3} , which is nearly equivalent to 60 % of the CLC material's overall adsorption capacity (**Figure 3.1**).

Our findings are compatible with those of Sena da Fonseca et al. (2014) [156], who looked into the application of CGWs in clays for the manufacture of ceramic bricks. Clay pastes holding 5, 10, 15, and 20 % CGWs have been investigated for use in the bio-based specimens.

The addition of CGW to the mixture enhanced the apparent porosity and water absorption. With the addition of CGWs, the samples' thermal conductivity was also decreased. Thermal conductivity decreased by 70 % when 20 % CGW is added to the earth. Eliche-Quesada et al. (2011) [157] also investigated how CGW may be used to make clay bricks instead of clay. Using CGWs up to 2 % caused the bricks to have open cell porosity, which decreased thermal insulating. Nevertheless, using CGWs at higher concentrations (3-5 %) caused lower density and greater pore volume (closed-cell porosity), which offered better insulating capacity and the right amount of mechanical resistance. When compared to the pure specimen, the addition of CGW causes the density to drop and the total permeability of the clay to rise, however this often results in a reduction in the samples' compressive strength. Therefore, based on the research findings, compressive strength increases with the addition of CGW up to 15 %. As soil conditioners and stabilizers, biopolymers like lignin have been proven to increase the compressive performance and water retention of aggregate particles [158]. Their efficiency can be significantly boosted by strategically injecting the polymer into pores that fall within a certain size range [158]. As one might suppose, the ability of a molecule to stabilize soil aggregates increases with molecule size. For these factors, we think that the addition of CGW to our CLC specimens causes the pores in the material to open up and allow lignin to enter, enhancing the compression strength.

3.5 Numerical simulation of hygrothermal behavior

3.5.1 Geometry, boundary conditions and mesh generating

The boundary conditions on a fine enough mesh are defined on a 2D geometry, which is used for the simulations of hygrothermal phenomena (**Figure 3.8**). To create the proper geometry and boundary conditions and to completely fit the requirements of the energy simulation programs,

any CAD (Computer-Aided Design) software used for the pre-processing method must have the flexible numeric format. It is necessary to convert geometric data created in "Native CAD" format to a WUFI Plus application-compatible format, such as WPS. Building energy simulation software's pre-processors can all read CAD data in various forms.

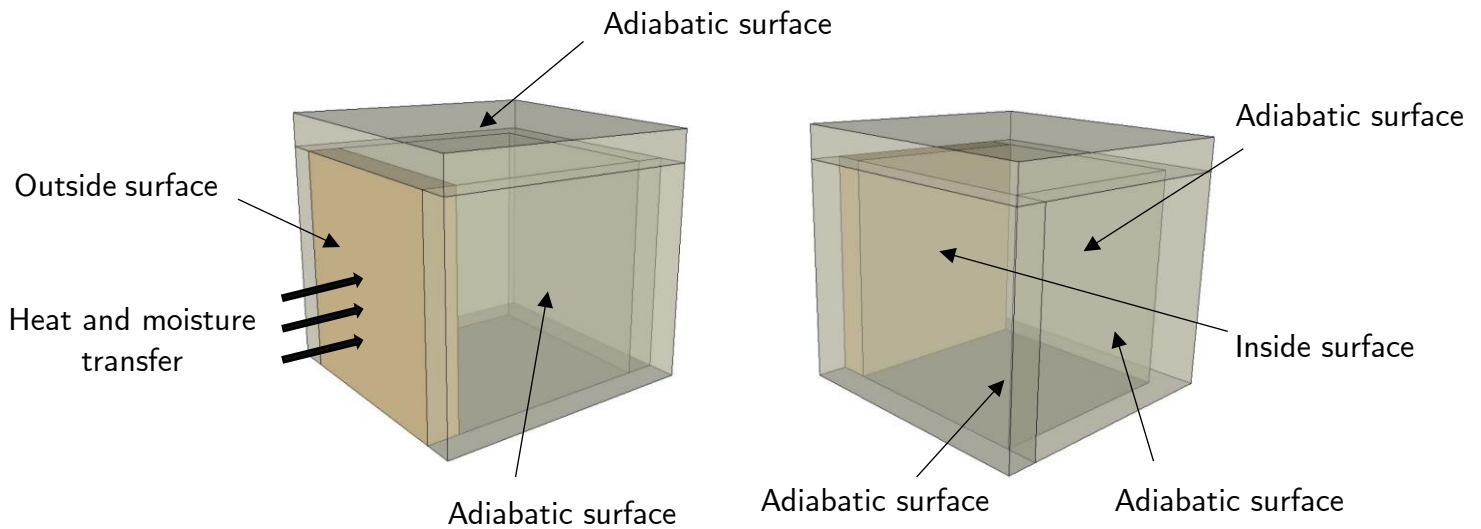


Figure 3.8 Scheme of geometry and boundary conditions for numerical simulation [165]

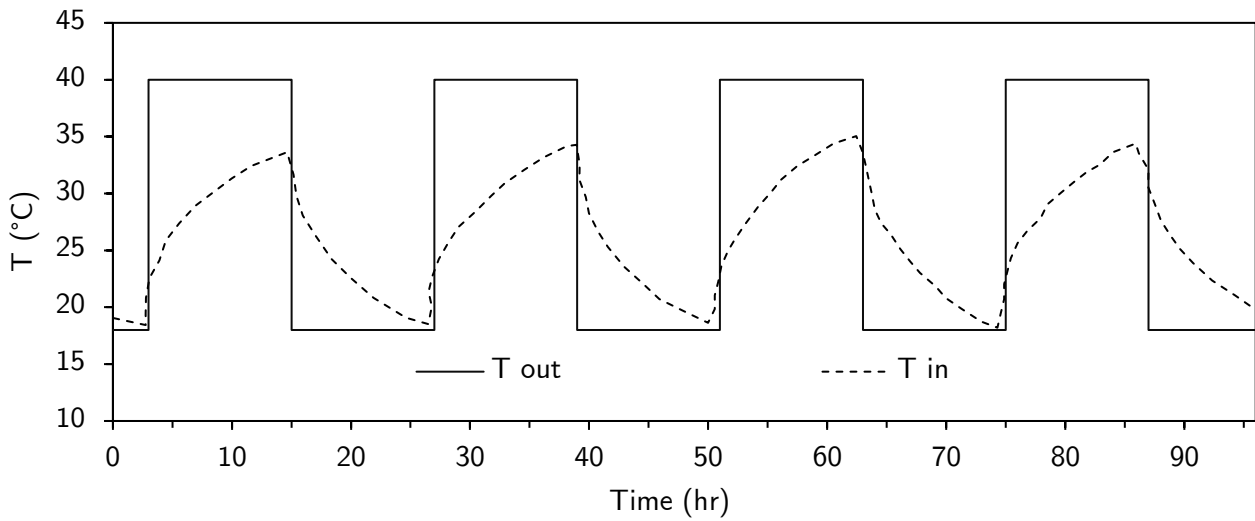
The format must be listed as one of the accepted formats by the program. The upper and lower boundaries of the field variables are defined by the boundary conditions of any basic problem. These are the functional factors that control how these parameters behave.

A proper simulation setup is just as crucial as a robust set of boundary conditions. A boundary condition, as demonstrated in **Figure 3.8** and **Figure 3.10** in terms of temperature and relative humidity fluctuations at the stated outer surface boundary condition, shows that "it is known what happens" on a certain border.

For model validation, we introduced temporal changes in temperature and relative humidity to the outside surfaces of the walls with imposed patterns of 95 hours and 500 hours, respectively (**Figure 3.9**, adapted from [17]). Surfaces inside the state were continuously exposed to ambient temperatures of 23 °C and 50 % relative humidity. The system is initially in an equilibrium condition at 23 °C and 50 % RH. The internal variables are then relieved while external environments are applied in conformity with the T and RH scenario.

The system is always reset to its initial state (23°C and 50 % RH) before any simulation commences. The experimental setup's restraints are imposed on us at the boundaries, providing that the hypothetical condition is coherent with the simulations' real configuration. While ignoring radiative fluxes and rain loads on the exterior and interior walls, we investigate the scenario of heat and mass convective exchanges at interfaces fluid/solid in this study.

Scenario 1



Scenario 2

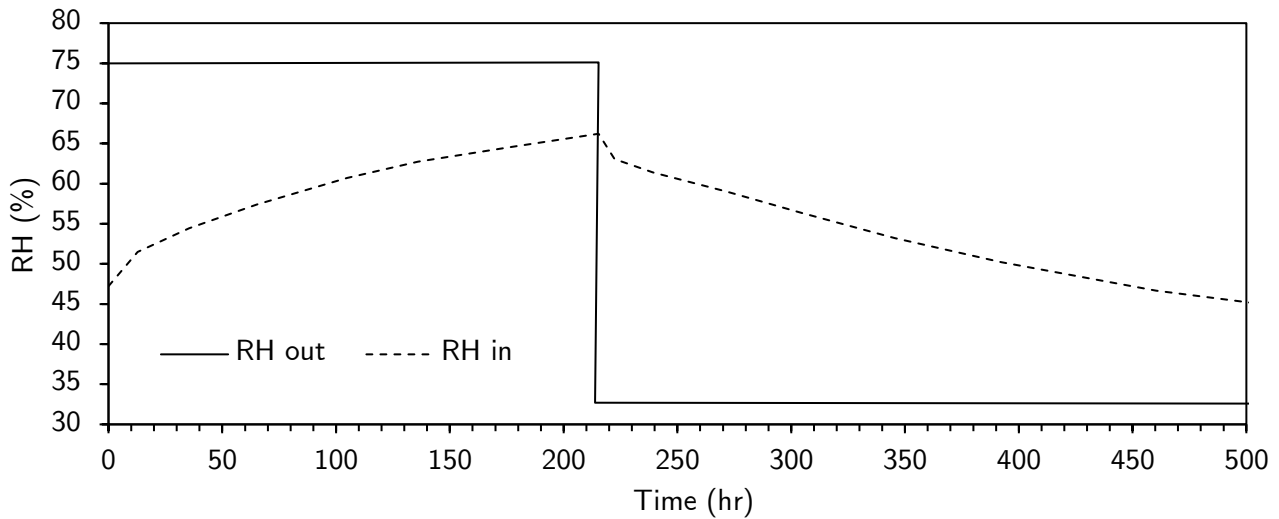


Figure 3.9 Outdoor and indoor climatic boundary conditions for the isothermal (RH=50 %) and isohydric (T=23°C) scenario, Alioua et al [17] (Refitted from original) [165]

The following equations illustrate how Neumann boundary conditions are defined.

Outside surface.

$$-\lambda \frac{\partial T}{\partial x} \Big|_{out} = h_{c,out} (T_{air,out} - T_{surface,out}) \quad 3.7$$

$$-\delta_p \frac{\partial P}{\partial x} \Big|_{out} = \beta_{v,out} (P_{vap,air,out} - P_{vap,surface,out}) \quad 3.8$$

Inside surface.

$$-\lambda \frac{\partial T}{\partial x} \Big|_{in} = h_{c,in} (T_{air,in} - T_{surface,in}) \quad 3.9$$

$$-\delta_p \frac{\partial P}{\partial x} \Big|_{in} = \beta_{v,in} (P_{vap,air,in} - P_{vap,surface,in}) \quad 3.10$$

δ_p is the permeability of the porous material to water vapor, while h_c is the convective transfer

constant. Based on the wall quality and rugosity, the WUFI program automatically calculates the water vapor convection coefficient β_v .

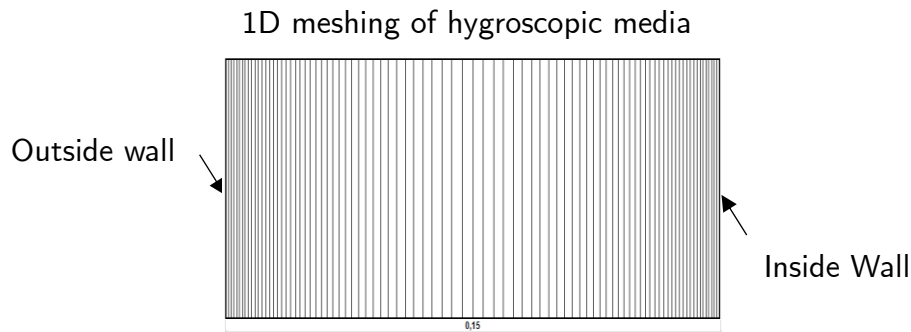


Figure 3.10 1D wall meshing along the X axis [165]

For the modeling of temperature and humidity variations inside the hygroscopic wall, a 1D meshing was deployed (**Figure 3.10**). To accurately reflect this gradient both close to the edges and further away from them, the mesh layers are not constant. The program automatically generates small cells or meshes to fill the space in order to model the coupled heat and moisture movement (**Figure 3.10**). Each cell represents a distinct area that represents the local temperature and humidity, and together they create a mesh.

For reliable numerical stability and precise solutions, a high-quality mesh must be produced. In the context of auto-generating, software programmers ensure that a good mesh size is created in order to effectively achieve the equations solution's stability and convergence. For the modeling of temperature and humidity gradients within the hygroscopic wall, a 1D meshing was implemented (**Figure 3.10**).

3.5.2 Mathematical modeling and sorption linearization due to hysteresis effect

- Künzel model for the 1D dimension

The modeling technique used in our case study replicates the hygrothermal response of hygroscopic building components using the Künzel model. It also tries [159] demonstrate the combined heat and moisture movements in building enclosures using the terms of relative humidity ϕ and temperature T gradient as the main driving forces. Equations for the mass transport and heat transfer models are expressed as follows.

$$\frac{dw}{d\phi} \frac{\partial \phi}{\partial t} = \frac{\partial}{\partial x} \left(D_{\phi} \frac{\partial \phi}{\partial x} + \delta_p \frac{\partial}{\partial x} (\phi p_{sat}) \right) \quad 3.11$$

Where D_{ϕ} is the liquid diffusion coefficient, δ_p is the porous material's water vapor permeability, ϕ is the relative humidity, and p_{sat} is the water vapor saturation pressure, $(dw/d\phi)$ is the porous material's capacity to store moisture as shown by the moisture sorption curve of the material

under consideration.

$$\frac{dH}{dT} \frac{\partial T}{\partial t} = \frac{\partial}{\partial x} \left(\lambda_T \frac{\partial T}{\partial x} \right) + h_v \frac{\partial}{\partial x} \left(\delta_p \frac{\partial}{\partial x} (\phi p_{sat}) \right) \quad 3.12$$

h_v is the water's evaporation enthalpy, (dH/dT) is the porous material's capacity to store heat and λ_T is its thermal conductivity.

- **Hysteresis effect**

Most of the porous materials have a noticeable moisture sorption curve hysteresis. During repeated wetting - drying processes, capillary pressures hold a large quantity of water into gaps. In order to include this aspect in calculations for heat and mass transport, many models have been proposed in the literature to determine intermediate fluctuations of water content between the primary adsorption-desorption curves (Hamdaoui et al. [138]). Hysteresis effects have not been implemented into any simulation software's computational techniques. Any given hysteresis model must be addressed synchronously with the heat and moisture equations.

As a result, coupling with some other software code is necessary, usually highly difficult, and requires for considerable programming ability. This approach also requires a lot of computation time. We suggest simplifying the curve sorption by paying attention to the hysteresis phenomena in order to make the simulation parameterization easier. Based on prior research on the impact of hysteresis on various material constructions, it is evident that type II sorption curve materials exhibit the same behavior after several wetting-drying cycles, regardless of their adsorption/desorption special capability (and for RH in the 30 %-80 % range), as illustrated on **Figure 3.11**. The section after this one goes even further into details about this feature.

- **Sorption linearization due to hysteresis effect**

According to Hamdaoui et al. [138], many sorption hysteresis models are utilized to explain the ink-bottle pore effect and other phenomena involving physic-chemically interacting small-volume particles. These models have demonstrated their effectiveness in enhancing the outcomes of numerical investigations. However, all their calculation durations and their attachment to certain scenarios and settings are their principal drawbacks.

The "pumping effect" is a type of hysteretic activity that usually occurs through the use of conceptual hysteresis models. It illustrates how the quantifiable scanning sorption curves deviate from the closure main one. In other words, during a succession of adsorption / desorption processes, there is a specific water content value for each degree of relative humidity. As a result, a substance that has been repeatedly wet and dried ought to return to its initial humidity levels and moisture content. In order to evaluate the experimental and numerical hygrothermal behavior

of hemp and rape straw concretes while taking into account hysteresis phenomena, Promis et al. [141] employed the Comsol Multiphysics program. The authors used a hysteresis model based on the adsorption curve of the observed material to show how the water content changed as a function of Relative humidity in rape straw concretes (**Figure 3.11**).

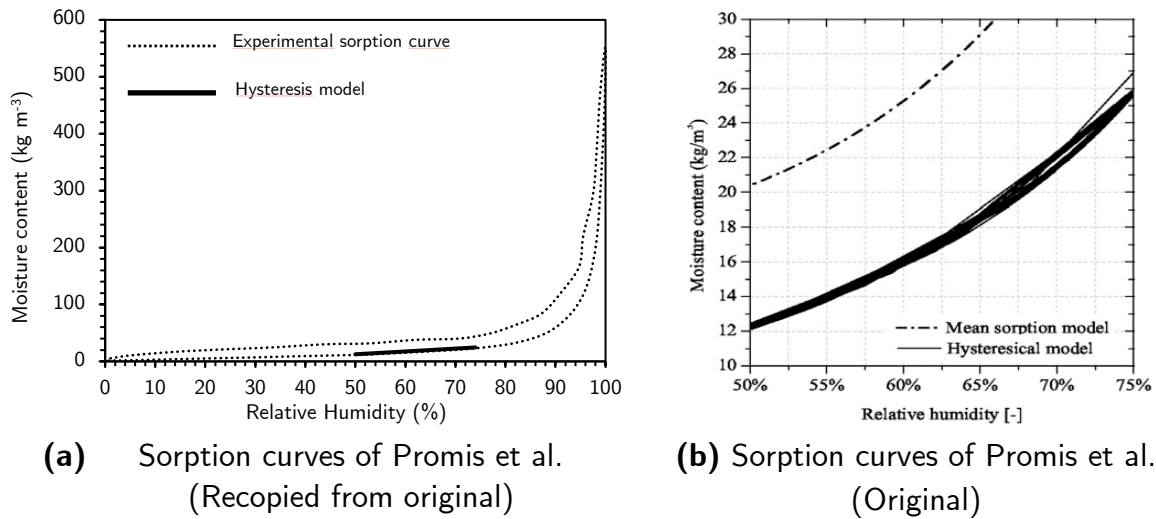


Figure 3.11 Water vapor sorption hysteresis phenomena behavior of Promis et al. [141]

The moisture hysteresis is nearly on the adsorption curve for a relative humidity interval of 50 % to 75 %, and when additional cycles are added, it begins to take on a linear character. Based on Promis et al works [141], we draw the conclusion that, for relative humidity less than 80 % and more than 50 % in this case, hysteresis appears to have a negligible effect on hydric behavior (**Figure 3.11a**). Satisfactory outcomes can be obtained by using a linear adsorption curve.

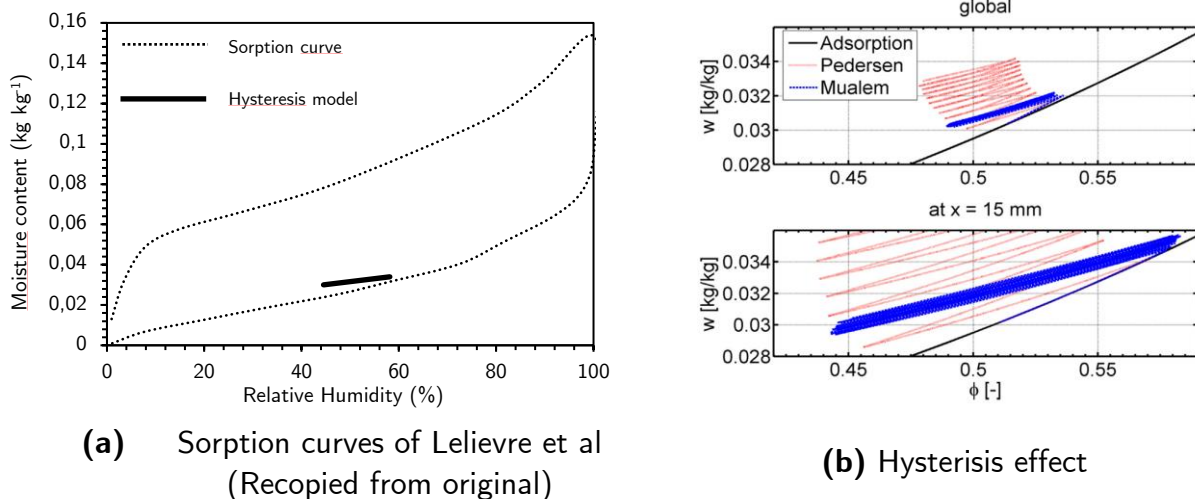
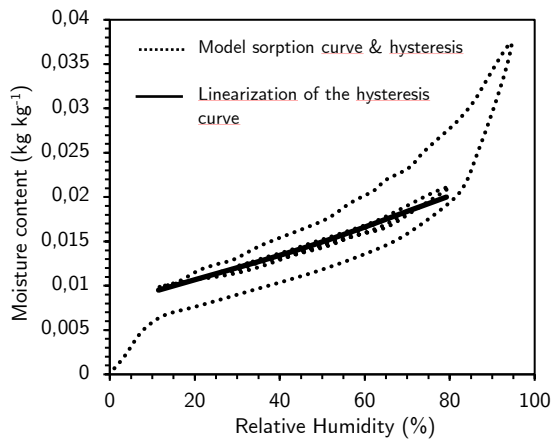


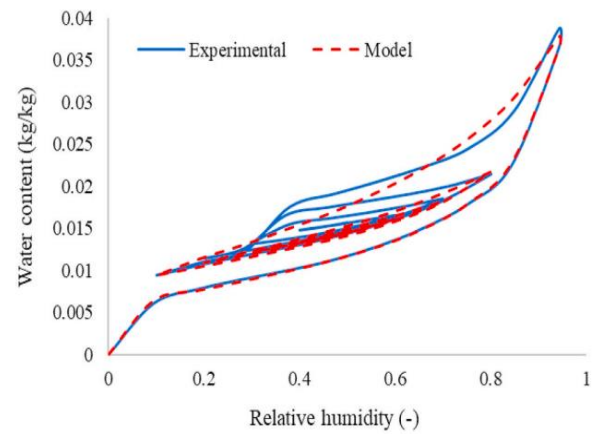
Figure 3.12 Water vapor sorption hysteresis phenomena behavior of Lelievre et al [142]

Lelievre et al [142]'s numerical analysis of heat and moisture transport for equivalent materials carried phase transition and hysteresis effects into consideration. **Figure 3.12b** shows how the

authors illustrate that Mualem's model seems to be more appropriate than Pedersen's to simulate sorption-desorption cycles. Thus, with a humidity buffer comprised between 40 % and 60 %, their sorption curve assumes a linear shape after several cycles of adsorption/desorption, as shown on **Figure 3.12a**.



(b) Sorption curve of Maaroufi et al. (Modified from original)



(a) original sorption curve

Figure 3.13 Water vapor sorption hysteresis phenomena behavior of Maaroufi et al. [100]

On the other hand, Maaroufi et al. [100] tried to show how the sorption hysteresis phenomenon affected the movement of heat and moisture in expanded polystyrene concrete (**Figure 3.13a**). They created a model of combined heat and mass transfer that accounts for the sorption hysteresis phenomenon. They showed that bringing the hysteresis into consideration improves comprehension of the hygrothermal behavior of construction materials by highlighting and comparing their numerical calculations with and without the hysteresis to experiment data.

In contrast to other studies, their hysteresis model was tested on a large range of relative humidity that attains a high proportion close to 95 %, where hygroscopic material will experience overloading in terms of water content. This describes why the mean segment of the adsorption/desorption curves is positioned almost in the middle and not close to the main adsorption curve. The most significant is that the sorption curve tends to assume a linear variance with a greater amount of humidification and evaporation cycles (**Figure 3.13b**).

Rémond et al. [160] provide a novel formulation to evaluate water sorption hysteresis in lignocellulosic materials by incorporating the idea of a gripped box in their simple hysteresis model. Just two changeable parameters must be fitted to the observed measurements for their model to work. The hysteresis phenomenon between a certain range of relative humidity may be described by the curves of a linear format across the mean sorption curve, which can be modified depending on the situation. Two points are established, one on the desorption curve passing by

the mean sorption curve and the other on the adsorption curve.

This strategy has limitations if we have a lot of wetting/drying cycles with a low relative humidity margin of less than 20 %. In several investigations [103], [161], it was shown and proven that the shift point from desorption toward the adsorption curve might be placed significantly below the desorption curve. Their model has to be connected in the current computational softw, which, depending on the coupling mechanism, may increase computation time.

Based on earlier research, we propose in this study a methodology for linearizing the hysteresis loops utilizing the key points at 80 % and 30 % of RH of the initial adsorption curve. Mainly, the RH inside the material in real situations is not completely saturated with moisture contents, as shown by the first position of the linearized curve at 80 % RH on the first adsorption curve (**Figure 3.14**).

It is presumable that adsorption occurs initially in the first hysteresis cycle, followed by desorption. The second coordinate of the linearized curve at 30 % RH is given the amount of the water content at this level of humidity by adding a ΔW % of difference between the initial adsorption and desorption curves at 30 % (12 % for the Mualem model and 10 % for the Promis model).

**Table 3.8 Hygrothermal properties of Date Palm Concrete (DPC)
(Taken from Alioua et al. study [17]) [165]**

Property	Value	Reference
Dry density (kg m ⁻³)	954	[162]
Dry thermal conductivity (W m ⁻¹ K ⁻¹)	0.185	[162]
Vapor resistance factor (dry cup) [-]	6.310	[163]
Water sorption coefficient (kg m ⁻² s ^{-1/2})	0.165	[162]
Dry specific heat (J kg ⁻¹ K ⁻¹)	1500	[164]
Moisture supplement of thermal conductivity (-)	10.190	[162]
Vapor resistance factor (-)	5.570	[164]
Water content at free saturation (kg m ⁻³)	429	[162]

We tested our method using data from Alioua et al. [17] at different depths (3, 7.5 and 12.5 cm). The sorption curve [17] is suitable for this application. Add a ΔW of 15 % to the first point, which is at 80 % of RH, and the second point, which is at 30 % of RH. After doing a sensitivity analysis between 10 % and 20 %, the decision to use 15 % was chosen.

The ideal arrangement has a value of 15 %. Following linearization, the findings discovered for this technique are confronted with those discovered by Alioua et al [17] (with and without the hysteresis effect). The Date Palm Concrete's (DPC) hygrothermal characteristics used in this study modeling investigation are shown in **Table 3.8**.

Based on the fitted sorption curve with the GAB model, the linearized mathematical equation is expressed as follows to calculate the water content of the material.

$$W_{lin}(\phi) = \left[2GAB_{ads}(80\%) - \frac{17}{10}GAB_{ads}(30\%) - \frac{3}{10}GAB_{des}(30\%) \right] \times (\phi) + \left[\frac{68}{50}GAB_{ads}(30\%) + \frac{12}{50}GAB_{des}(30\%) - \frac{3}{5}GAB_{ads}(80\%) \right] \tag{3.13}$$

Where ϕ is the relative humidity situated between 0.3 and 0.8, GAB_{ads} is the first main adsorption curve fitted with GAB model and GAB_{des} is the first main desorption curve fitted with the GAB model.

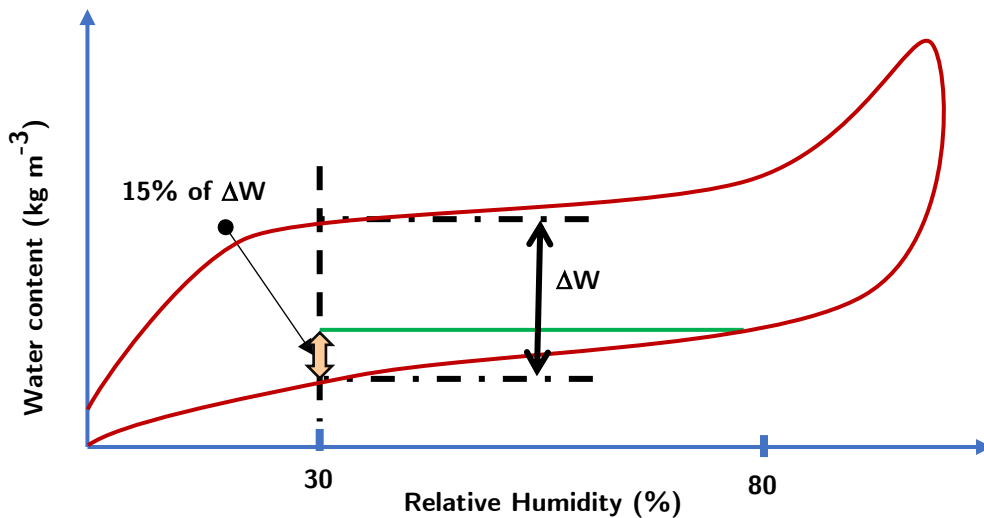


Figure 3.14 Moisture sorption isotherm linearized of Date Palm Concrete (DPC) (Refitted and modified from original [17]) [165]

The experimental section of the research into the mechanical and hydrothermal characteristics of bio-based materials was undertaken using the methods shown in **Figure 3.15**. By optimizing the simulation and taking into consideration the impact of hysteresis in difficult climatic circumstances, numerical analysis was performed to investigate the material's energy performance.

3.5.3 Model validation of linearization effect on sorption curve with experimental data

One of the earliest academics, Mendes et al. [31] used a linearization strategy to improve the calculation of hygrothermal behavior and simplify a challenging physical phenomenon. The vapor transmission between the wall and the surrounding air was linearized by the scientists. The relevant numerical outputs can be calculated more quickly using this method. In our situation, we have attempted to linearize the sorption curve based on how often occurring adsorption and desorption cycles affect the hysteresis effect.

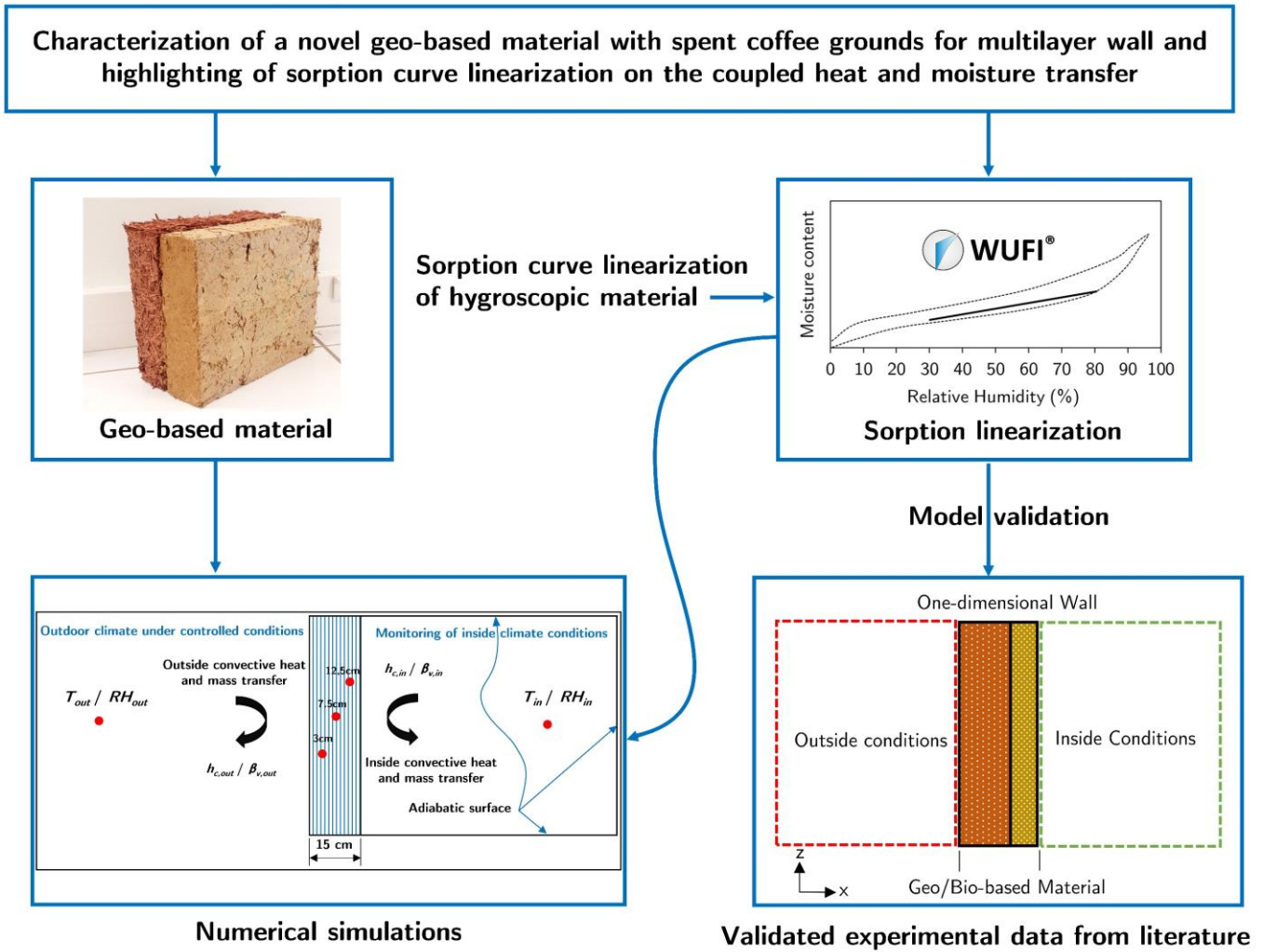


Figure 3.15 Conceptual study plan [165]

The following repeated wetting and drying processes for a predetermined relative humidity interval, which must be found between 30 % and 80 %, have been used to linearize the sorption curve. We furthermore carried in to the account of the linearization for sorption curves of type II-isotherm [153] and materials with porosities ranging from 0.3 to 0.9. Consequently, it has been studied how heat and moisture are transmitted in DPC (Date Palm Concrete) [166], CLC (Coffee Lightened Clay), and SC (Structural Cob). Air indicators, (T&RH), at the inside/outside environment as well as temperature and relative humidity distributions throughout the layer thickness of wall were continuously measured during the trials.

3.5.3.1 Scenario 1. Temperature variation with constant humidity

We can really perform numerically (Figure 3.16) the temperature variations at depths ranging from 3 to 12.5 cm inside the wall applying the temperature profile of Scenario 1 (Figure 3.9a), applying temperature and relative humidity value system at boundaries (from the experiments [163], [166]), and using initial conditions ($T=23\text{ }^{\circ}\text{C}$ and $\text{RH}=50\%$).

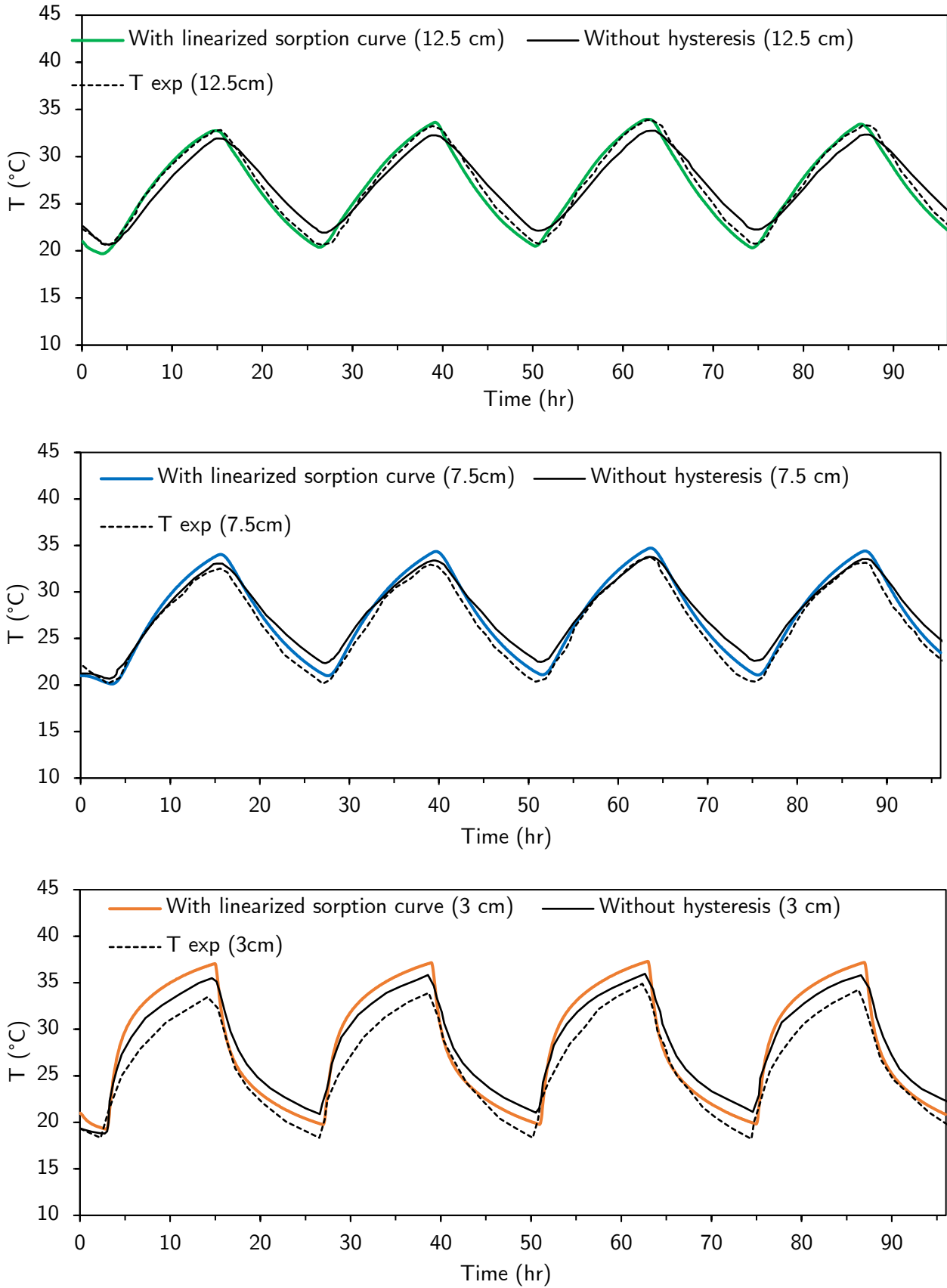


Figure 3.16 Numerical and experimental temperature variations at various depths within the DPC wall by taken into account the linearization of hysteresis effect [165]

In particular at deeper depths, the temperature profiles reproduce more accurately with linearized hysteresis compared to without it. In our study, however, the largest disparities between the numerical and actual measurements are found at a depth of 3 cm and are 2 °C and 2.8 °C for the higher and lower temperatures, respectively.

Even at 3 cm deep, the linearization model's temperature estimations are verified by the root mean square error (**Table 3.9**). The errors were practically cut in half by the linearization for the rest of two deeper depths. Simulations without the hysteresis effect consistently underestimate the amount of water absorbed along the adsorption curve (**Figure 3.17**), in comparison to experimental data, with the RH curve of Scenario 2 (**Figure 3.9b**). In accordance with observations, the curves without hysteresis in **Figure 3.17a** maintain an excessive amount of water inside the wall during desorption.

The predicted RH profiles at intermediate depths greatly improve when the linearization model of the sorption curve is incorporated in the simulations. Linearization marginally tends to reduce overestimation of water absorption during adsorption for the deepest depth of 12.5 cm, but does not considerably differ from the standard hysteresis simulation during desorption. At the shallowest depths, linearization tends to reduce the amount of water absorbed, favoring a sharper RH simulation during adsorption, but a relatively high-water desorption in comparison to tests and conventional hysteresis simulation. As shown by Alioua et al. [17], the hysteresis effect does not significantly affect accuracy at 3 cm wall depth, which is also a valid statement with our linearization methodology. These attitudes are represented in the total RMSE values, with the greatest gap between experience and simulations for the two deepest depths.

Table 3.9 Model comparison and validation for scenario 1 [165]

Wall depth (cm)	Without hysteresis effect		With linearized sorption curve	
	Data sources compare	RMSE	Data sources compare	RMSE
12.5	Exp – num (Without hysteresis)	1.024	Exp – num (Linearization)	0.575
7.5	Exp – num (Without hysteresis)	1.409	Exp – num (Linearization)	0.862
3.0	Exp – num (Without hysteresis)	2.076	Exp – num (Linearization)	2.042

3.5.3.2 Scenario 2. Humidity variation with constant temperature

Simulations without the hysteresis effect consistently underestimate the amount of water absorbed along the adsorption curve (**Figure 3.17**), in comparison to experimental data, with the application of RH distribution of Scenario 2 (**Figure 3.9b**).

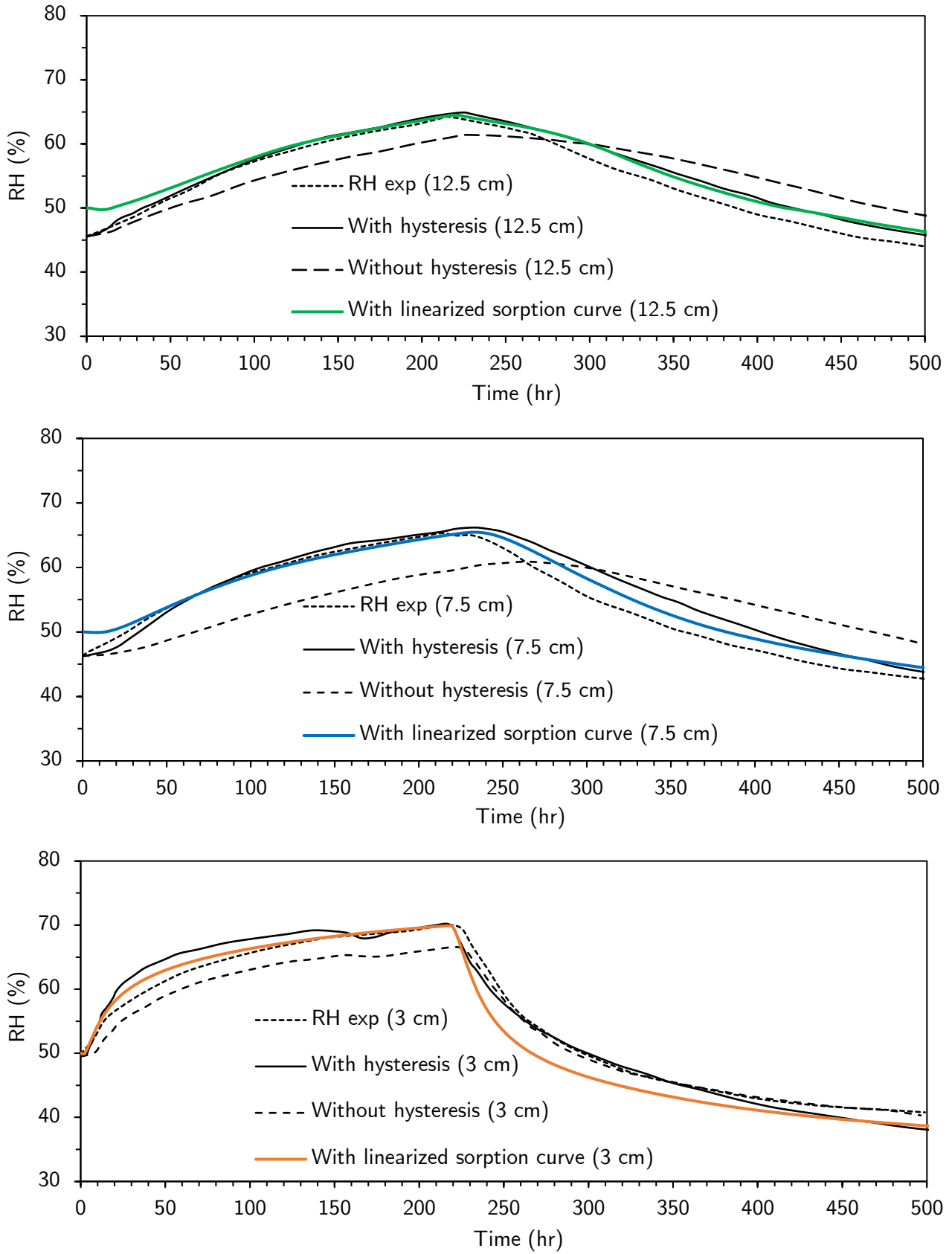


Figure 3.17 Numerical and experimental humidity variations at various depths within the DPC wall by taken into account the linearization of hysteresis effect [165]

In contrast to observations, the curves without hysteresis in **Figure 3.17a** maintain an excessive amount of water inside the wall during desorption. The predicted RH profiles at intermediate depths greatly improve when the linearization approach of the sorption curve is incorporated into the simulations. Linearization marginally overestimates water absorption during adsorption for the deepest depth of 12.5 cm but does not considerably differ from the standard hysteresis simulation during desorption.

Table 3.10 Model comparison and validation for scenario 2 [165]

Wall depth (cm)	Without hysteresis effect		With hysteresis effect		Linearized sorption curve	
	Data source compare	RMSE	Data source compare	RMS E	Data source compare	RMSE
12.5	Exp – num	3.535	Exp – num (hysteresis)	1.572	Exp – num (Linearization)	1.564
7.5	Exp – num	5.586	Exp – num (hysteresis)	2.389	Exp – num (Linearization)	1.529
3.0	Exp – num	2.025	Exp – num (hysteresis)	2.008	Exp – num (Linearization)	2.325

Linearization tends to reduce water absorption at the lowest depths, favoring superior RH simulations during adsorption but a relatively high-water desorption in comparison to experiments and conventional hysteresis simulations. The differences between real data and simulations outputs at tall depths are illustrated in the total RMSE values (**Table 3.10**), that represent these tendencies. At 3 cm wall depth, as shown by Alioua et al. [17], the hysteresis phenomenon does not significantly affect reliability, which is also a true fact with our linearization strategy.

3.5.4 Hygrothermal performance evaluation of CLC and SC wall

The simulations of WUFI Plus were performed to a dual wall construction made up of the previously mentioned SC and CLC elements.

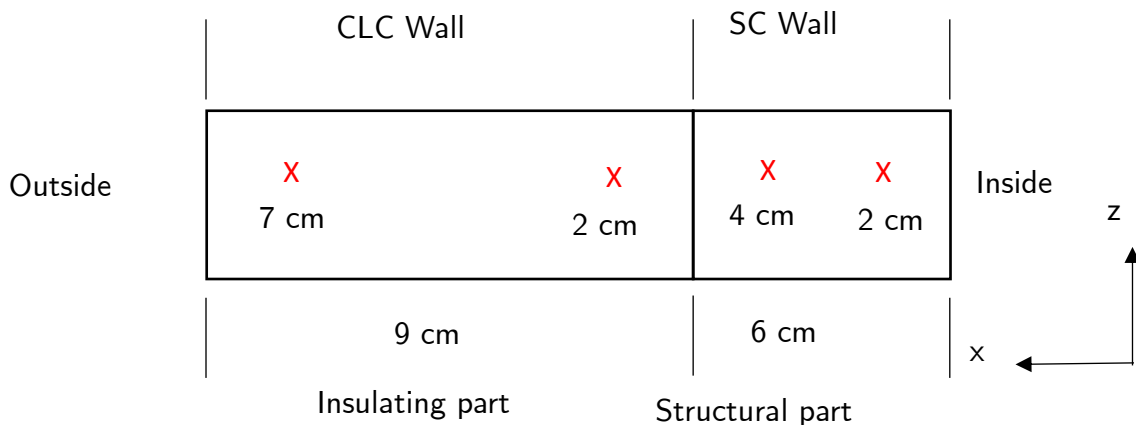


Figure 3.18 Schematics of the multilayer wall composed of SC+CLC and the measured points [165]

This final one's material inputs include appropriate sorption isotherms, vapor resistance factors, thermal conductivity, and heat capacity (**Figure 3.1, Figure 3.2 and Figure 3.3**).

3.5.4.1 Scenario 1. Temperature variation with constant humidity

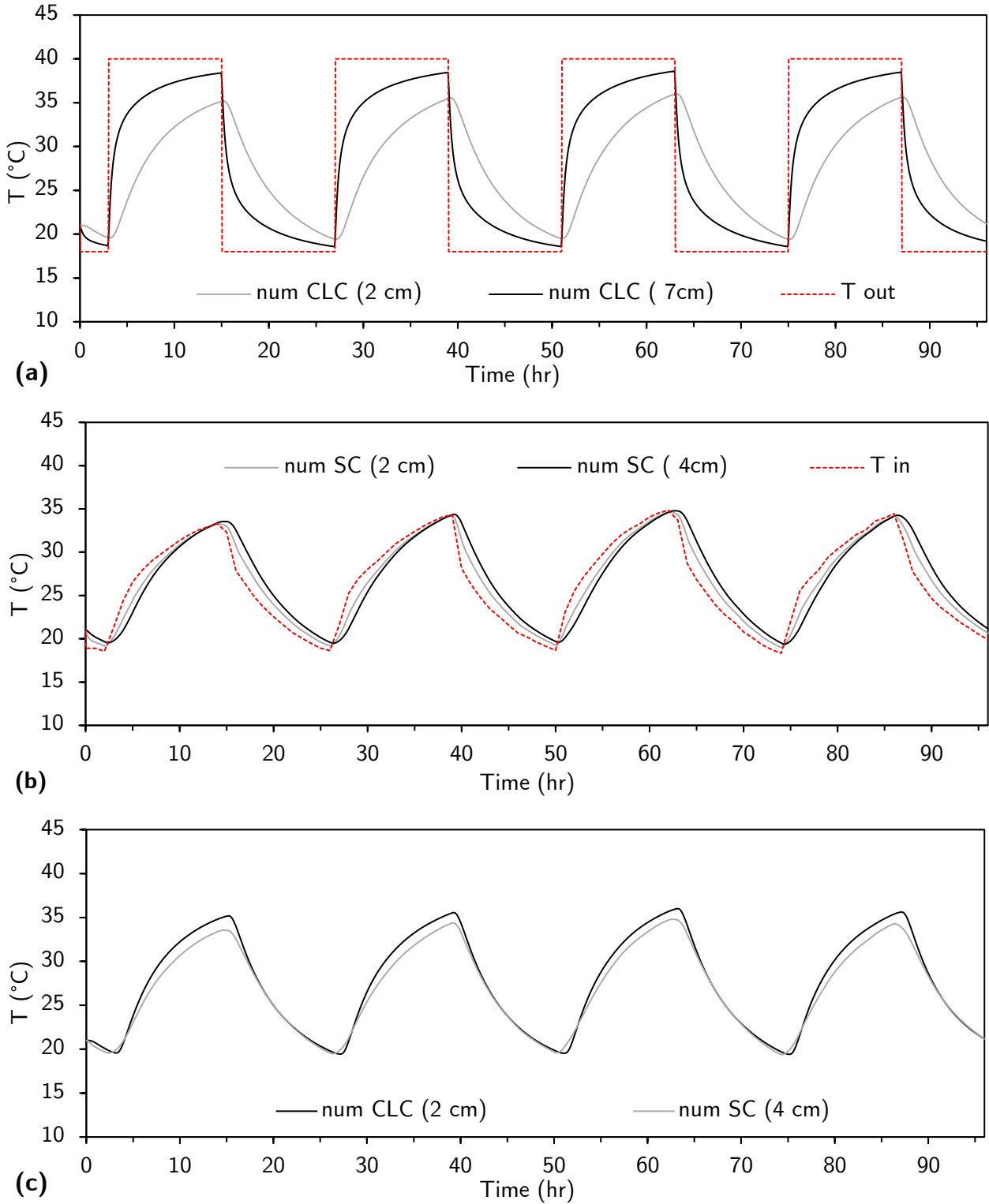


Figure 3.19 Numerical investigation of temperature variations at various depths within the SC+CLC multilayered wall by considered the linearization of hysteresis effect [165]

The SC and CLC layers of the wall exhibit differing thermal behavior, particularly near the surfaces. Between the two wall limits, where we can detect an apparent delay in the thermal performance of the wall produced by the quick change in outside temperature, the CLC part (**Figure 3.19a**) exhibits a striking reduction in amplitude. After 12 hours, the CLC experiences a strong development of heat that reaches 38.5°C at a distance of 7 cm from the outside environment, while only 34°C is attained at a distance of 2 cm deeper in the wall (**Figure 3.19b**). Due to their proximity, there is a negligible maximum temperature difference between the 2 cm CLC and 4 cm SC measured locations (**Figure 3.19c**). Additionally, the inside surface is vulnerable to temperature variations. In comparison to the 7 cm of the CLC wall, the temperature drops once further at 2 cm for the SC wall and hits 32.9°C (**Figure 3.19b**).

3.5.4.2 Scenario 2. Humidity variation with isotherm condition

In this case, the interior temperature is maintained at 23°C while the exterior wall is exposed to changes in RH. The outer wall is subjected to sequential 75 % and 33 % RH phases for 216 hours. Evolutions of the interior relative humidity at the different depths have been simulated. Closer to the inner of the SC wall, changes have a lesser magnitude (**Figure 3.20b**). Additionally, a notable delay in reaction is seen between 2 cm and 4 cm SC, indicating a greater structural wall moisture resistance.

The difference in sorption between the two depths is due to the SC at 2 cm absorbing the largest quantity of moisture (60 %) after 216 hours, whereas at 4 cm, the material is still absorbing moisture. For DCP, this behavior has not been reported [163]. Additionally, compared to 2 cm, the RH drops at 4 cm more quickly during the desorption phase.

A similar pattern is shown for the CLC (**Figure 3.20a**), where a responsive delay between 2 cm and 7 cm is seen for RH standing oscillations. This delay is less evident than in the SC wall due to the CLC's higher water permeability. In comparison to the other position further inside the wall, the relative humidity rises at the point close to the wall's outside more quickly during the adsorption phase, reaching a maximum of 65 %.

Regarding SC, the absorption and desorption processes at the CLC wall are different at the two depths. Variations in indoor and outdoor relative humidity have a light impact on the intersection between CLC and SC. Contrary to the findings in **Figure 3.20**, **Figure 3.21** demonstrates that the RH variations for the two positions at 4 cm (SC) and 2 cm (CLC) are expressing similar hygroscopic behaviors, with the only reason for the minor differences in humidity between the two positions being their close proximity to one another within the double wall structure.

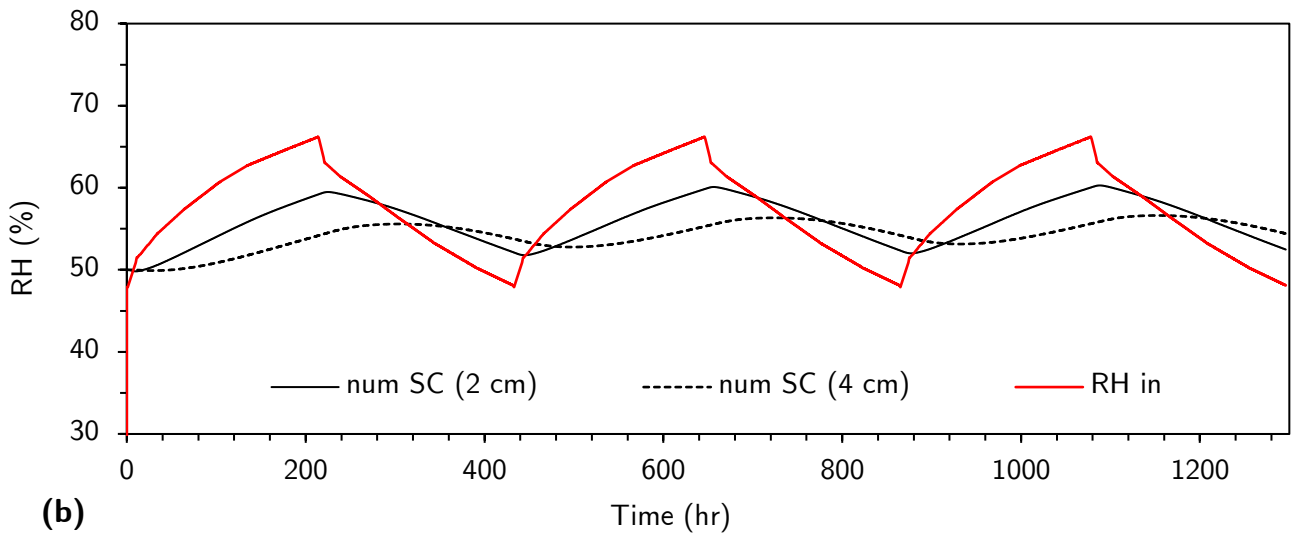
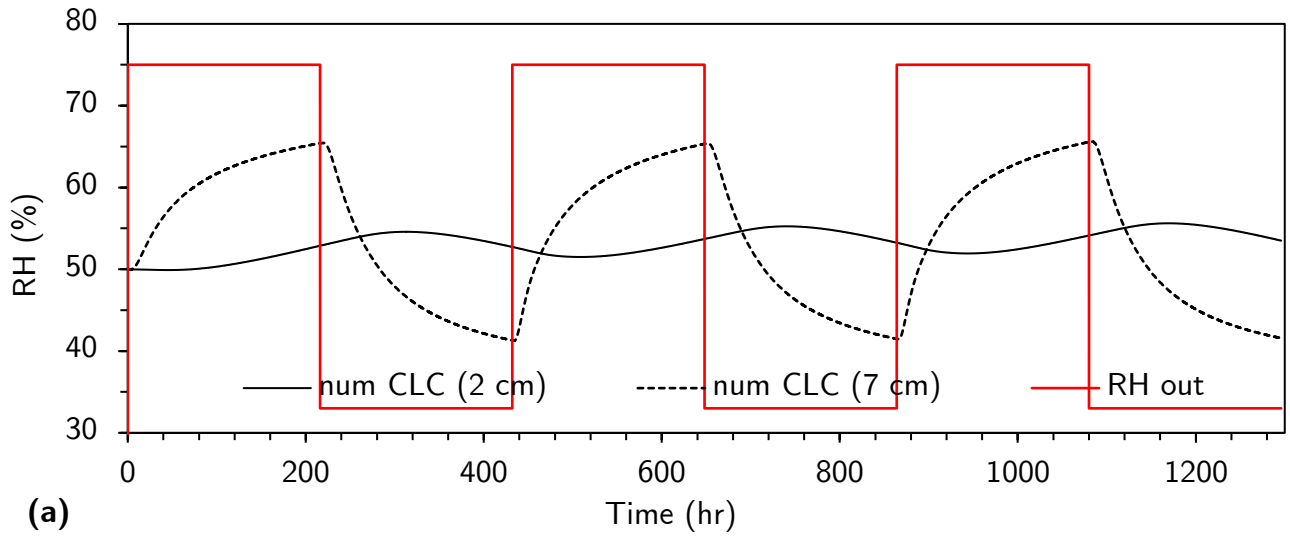


Figure 3.20 Numerical investigation of humidity variations at various depths within the SC+CLC multilayered wall using linearization of the RH hysteresis cycle [165]

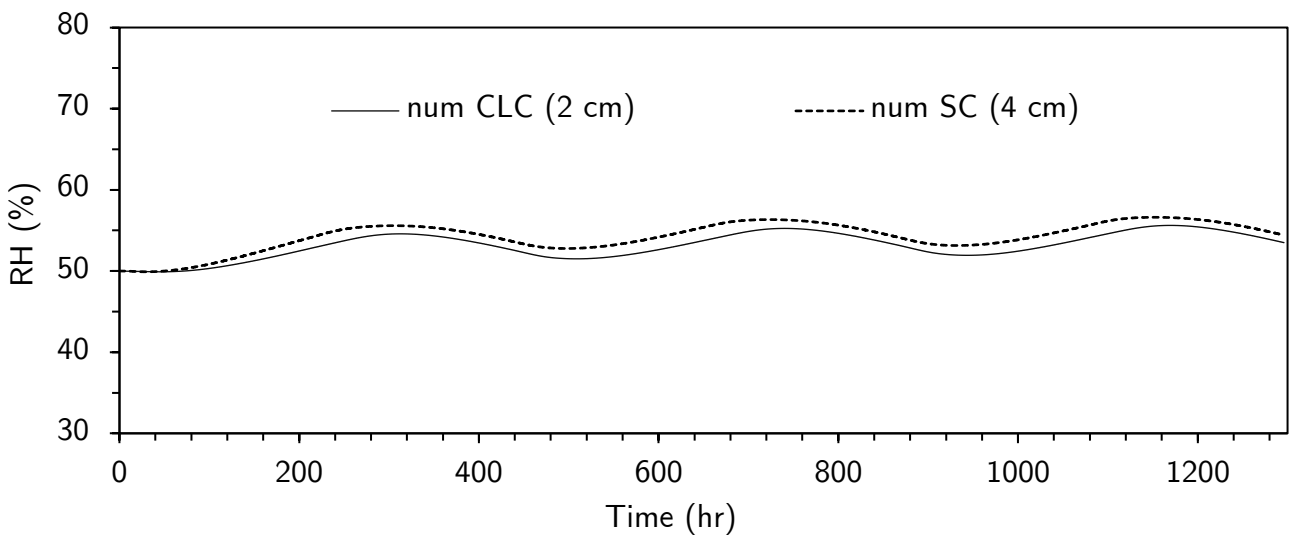


Figure 3.21 Moisture behavior of the interface between CLC and SC walls [165]

3.5.4.3 Heat flow transfer through the CLC+SC wall for isotherm and isohydric scenario

A heat diffusion density is produced via hygrothermal transfer, which is often not measured. **Figure 3.22** illustrates the heat flux produced for the SC+CLC wall of 0 % and 20 % of coffee ground wastes in the insulation CLC wall for this application. These simulations demonstrate that the CLC+SC wall with CGW, owing to the strong variation in temperature and humidity, enables less heat to transfer than without the addition of CGW in the material (**Figure 3.22a** and **Figure 3.22b**). This discrepancy in the instance of **Figure 3.22a** is brought caused by waste coffee grounds' reduction of the wall's thermal conductivity. A distinct pattern can be seen in **Figure 3.22b**, in which the heat flux density gain practically rises (with CGW included) due to the increased porosity caused by the incorporation of biomass wastes (see **Figure 3.2b**). Since water has a high phase change enthalpy, adding CGW causes the wall to catch additional moisture. This moisture will be transferred to the wall as energy.

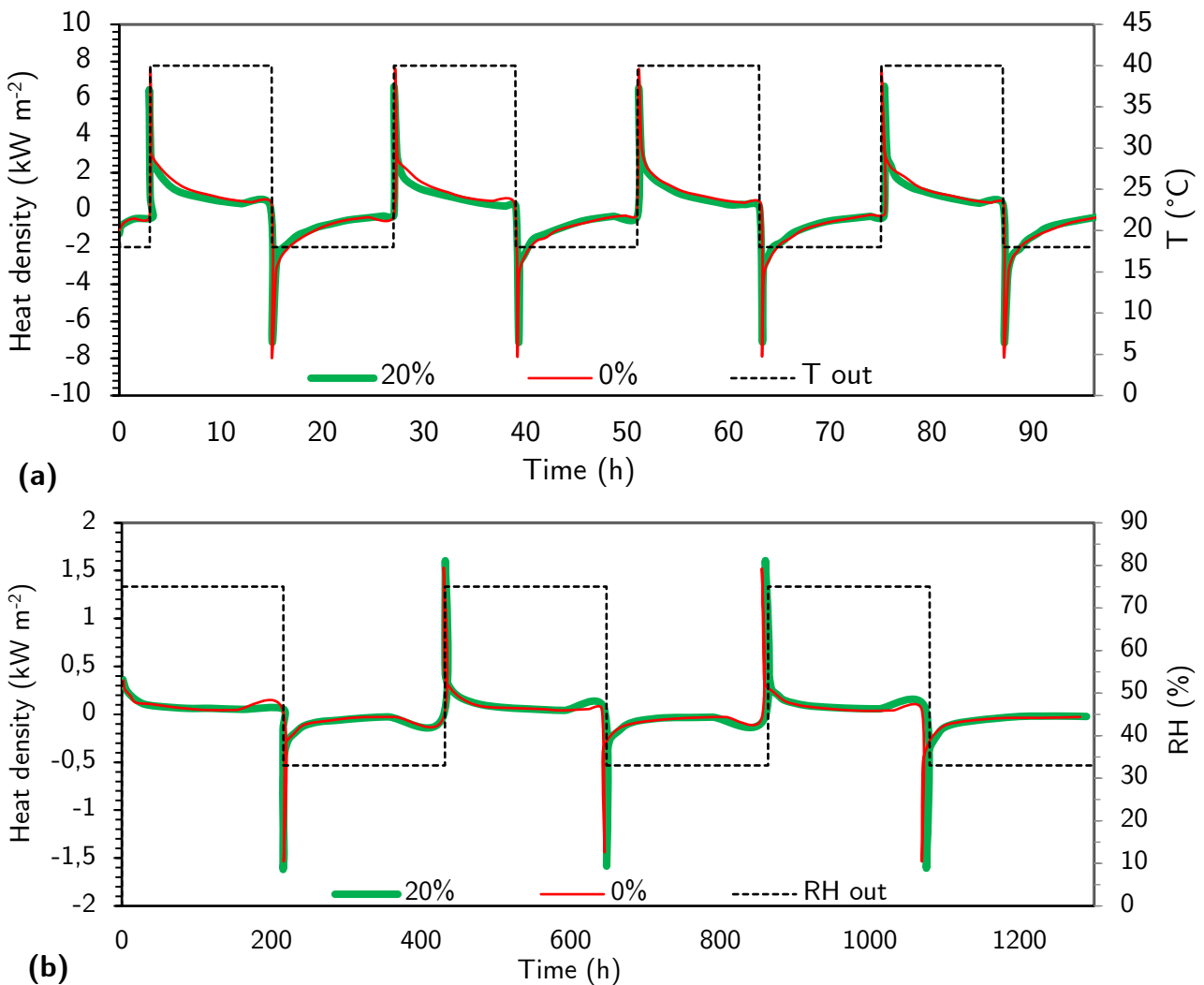


Figure 3.22 Quantitative analysis of the energy performance of multilayered wall (SC+CLC) for isotherm (a) and isohydric (b) scenarios [165]

For isotherm and isohydric scenarios, numerical results depict dynamic fluctuations of the heat flow through the SC+CLC wall façade. In **Figure 3.22a**, the temperature ranged from 18 to 40°C while the relative humidity was maintained at 50 %. We saw two phases: (i) the heat peak period, which coincided with the temperature peak, and (ii) the heat release period, which occurred as the temperature declined.

The peak is greater in the case of the CLC wall containing 0 % coffee ground wastes (7.48 kW m⁻²) compared to the case with 20 % coffee ground wastes, as can be seen in the first phase (6.62 kW m⁻²). However, as the temperature drops, the opposite result is noticed. Compared to a wall with no coffee grounds, one with 20 % coffee grounds dissipates less heat.

The enhancement of the wall's thermal conductivity and heat capacity by CGW is connected to the capability to absorb and release heat. This variance causes a dynamic variation in the amount of heat going through the wall of 12 % over a predetermined time period (at time 3h).

For, fully comprehension of the energy behavior in terms of moisture residues, we used an isotherm scenario for the second experiment (**Figure 3.22b**), maintaining a constant air temperature on both sides at 23 °C and simply varying the relative humidity from 33 % to 75 % for multiple cycles. With this final one, we can find out how much heat is passed via a wall when a moisture gradient is imposed between two surfaces, as well as how much the variation in porosity affects the heat flow.

The heat flow density, as seen in **Figure 3.22b**, peaks at 1.61 kW m⁻² and 1.53 kW m⁻², respectively, for a proportion of 20 % and 0 % of coffee ground wastes in the CLC membrane formulation. The variation in internal structure in the sense of material porosity accounts for this heat peak. **Figure 3.2b** shows that the roughness ranges between 0.46 and 0.63 for the CLC wall with 0 % and 20 % coffee ground wastes, which corresponds to a 37 % increase in porosity. This fluctuation causes a dynamic variation of 8 % in the rate of heat flow through the wall over a certain time period. Our research leads us to the conclusion that the inclusion of CGW enhances porosity, which makes the absorption/desorption cycle easier and allows more heat to flow through owing to the enthalpy of phase transition.

3.6 Conclusion of the chapter and discussion

The major goal of this study was to assess the mechanical and hydrothermal characteristics of cob walls that contained CGW in varying amounts. By using up to 20 % CGW in the isolating cob matrix, the material performs better in terms of heat storage capacity, thermal insulation, and compressive strength. This investigation has shown that CGW has the potential to be used as a construction material in high relative humidity since it offers an affordable and environmentally friendly alternative to enhance the performance of existing structures. When compared to typical cob building materials, the CLC wall with CGW's compressive strength and hygrothermal performance allow the cob wall thickness to be lowered. As a result, less material is needed to assemble walls, which lowers the cost of construction.

Additionally, it allows for thinner insulation to be used and shortens the construction process. The widespread valorization of CGW may significantly contribute to the achievement of sustainable development goals, provided that such reserves are not used more effectively elsewhere. After a computational investigation of the effect of sorption isotherm linearization on the hygrothermal behavior of porous walls constructed of low carbon material, the approach was proven experimentally. The experimental data reinforce the numerical analysis and demonstrate that even in the presence of a considerable hysteresis effect, the sorption curves of porous walls with CGW may be linearized. Hysteresis linearization is a powerful and time-efficient approach for thermal engineers to carry out more precise building performance assessments. The estimations for comfort and energy usage would thus be more precise and realistic in terms of building efficiency.

When it comes to heat and mass transfers at various depths, the suggested technique is comparatively accurate. The linearization of the hysteretic sorption curve considerably improves the simulation reliability. The numerical study also supported the idea that this method generates more precise results than common heat- and mass-transfer techniques. It should be emphasized that the approach necessitates the knowledge of the sorption isotherm for the target material, as well as the linearization of the isotherm at some point throughout the procedure. This approach was discovered to be helpful in clarifying the hygrothermal behavior of the walls with CGW.

3.6.1 Summary of main results

The hygrothermal performance of the CLC wall employing CGW was investigated in this work both numerically and experimentally. The findings show that employing CGW as an insulating material greatly enhances wall performance. Additionally, the hysteresis effect takes on greater interest, which enhances the ability to forecast wall performance. The simulations also show that the prediction of the hygrothermal performance of hygroscopic walls is much improved in

terms of comfort when using linearized sorption curves. Additionally, this development needs to contribute to more accurate calculations of energy usage and comfort in structures constructed from natural resources.

3.6.2 Discussion on model limitations and perspectives

The model presented in this study has limitations and can be developed. The effect of external variables, such as wind speed, on the efficiency of hygroscopic walls was not investigated in this study. In addition, the usage of an empirical coefficient for the CGW's heat and mass transport should be explored. Future research should be conducted to investigate these aspects and their impact on the hygrothermal behavior of hygroscopic building enclosures.

Finally, it should be mentioned that while this procedure can be applied to any hygroscopic material, it has only been conducted so for this research study on CLC & SC walls. The linearization of the sorption curve is possible for materials with porosities ranging from 0.1 to 0.9 and a humidity range of 30 % to 80 %.

Chapter 4.

A novel methodology for integrating artificial intelligence into building energy simulation to investigate hygrothermal behavior at the building scale

Contents

4.1	SUMMARY OF THE CHAPTER	153
4.2	INTRODUCTION TO THE CHAPTER	153
4.3	STUDY METHODOLOGY	156
4.4	LAB-SCALED BUILDING EARTHEN PROTOTYPE	158
4.4.1	Understanding difference between thermal and hygrothermal transfers in buildings.....	161
4.4.2	Basic notions of nodal approach for whole building energy simulation (BES).....	162
4.4.2.1	Computing and simulation strategy of thermal method.....	163
4.4.2.2	Thermal simulation parameters definition.....	163
4.4.2.2.1	Conduction through the walls.....	163
4.4.2.2.2	Outside and inside surface heat balance.....	166
4.4.2.2.3	Sky and solar calculations.....	167
4.4.2.2.4	Shading calculations.....	167
4.4.2.2.5	Infiltration/ventilation.....	168
4.4.2.2.6	Zone gain heat loads.....	169
4.4.2.2.7	HVAC sizing simulation.....	169
4.4.3	Fundamentals of coupled heat and mass transfer.....	169
4.4.4	Deep learning modeling.....	170
4.4.5	Coupling method between physical models and deep learning.....	174
4.5	RESULTS AND DISCUSSIONS OF DEVELOPED APPROACH	177
4.5.1	Sensitivity analysis.....	178
4.5.2	Outputs of the standard building energy simulation (BES).....	179
4.5.3	Thermal physical model coupled with ANN (deep learning) to transform outputs into hygrothermal Data.....	181
4.5.4	Coupled thermal physical model with LSTM (deep learning) to transform outputs into hygrothermal Data.....	182
4.6	ENERGY PERFORMANCE OF STUDIED EARTHEN CONSTRUCTION BUILDING	184
4.6.1	Needs for air conditioning.....	184
4.6.2	Basic method for estimating the cooling loads.....	185
4.6.3	Ideal Air-Conditioner system pre-sizing (basic simplified method).....	192

4.6.4	Energy performance of our building based on the outputs of different dynamic simulation approaches	194
4.7	APPLICATION OF THE NOVEL CO-SIMULATION TECHNIQUE TO A REAL BUILDING	199
4.7.1	Pre-processing and DATA gathering.....	199
4.7.2	Monitoring and analysis of building behavior.....	202
4.7.2.1	Instrumentation and locations	202
4.7.2.2	Energy use and internal loads.....	203
4.7.2.3	Experimental measurement data.....	205
4.7.3	Outputs of the fundamental building energy simulation (BES)	206
4.7.4	Transformed hygrothermal data resulting from the combination of ANN model and standard BES	208
4.7.5	Transformed hygrothermal data resulting from the combination of LSTM model and standard BES	209
4.7.6	Energy performance of earthen constructed buildings based on the outputs of different dynamic simulation approaches	211
4.8	CONCLUSION OF THE CHAPTER AND DISCUSSION	215
4.8.1	Summary of main results.....	215
4.8.2	Discussion on building energy modeling and Deep Learning co-simulation	216

4.1 Summary of the chapter

The thermal and hydric simulation of porous construction materials presents a significant challenge in regard to ethical decision-making as well as adhering to current laws and standards. In order to reduce humidity oscillations in buildings and to reduce energy consumption by lowering the heat transmission through building walls, hygroscopic materials are being employed more frequently. Prospective low-carbon buildings may have substantial challenges because of issues with the building envelope caused by humidity adsorption/desorption. In order to further the practical approach to building enclosure design and to lower the possibility of recurrent failures, a large full-scale experiment and a novel numerical modeling methodology were developed in order to evaluate the hygrothermal behavior of earthen buildings.

The research is concentrated on developing a combined, standardized approach for hygrothermal modeling of hygroscopic material. It improves comprehension of coupled heat and mass transport behavior, which aids in selecting the best practical strategy or idea. Therefore, novel and effective numerical simulation methodologies require additional investigation in order to handle tough challenges and minimize the mathematical sophistication of generating models. We may distinguish between two different types of models: data-driven models, which required the development of a prediction model using deep learning algorithms, and conventional physical models, which rely on the solution of equations that replicate the thermal behavior of the entire structure. The objective of merging the several models is to obtain results that are more reliable for buildings that experience temperature and relative humidity change while demanding less investigation into material properties, particularly for hydric characterization. In order to collect experimental evidence for the numerical model's evaluation and to serve as a highlight for analyzing the structure's overall hygrothermal response, a realistic one-zone building in 3D dimensions subjected to realistic climatic conditions was constructed. By combining a simple thermal nodal model with deep learning in the current work, we will provide a one-step dynamic technique for modeling the hygrothermal behavior of a specific recommended material. Then, the numerical calculations and the result of the experiments were compared. The analysis will give a more precise estimate of how the entire building will react to the effects of temperature variations and moisture buffering. The model may be used for a variety of architectural and new building projects, including temperature and relative humidity assessment and measurement.

4.2 Introduction to the chapter

The application of new sustainable materials is one of the top concerns in building construction within ecological development context. In actuality, it has some consequences for energy demand, harmful emissions, and the degradation of natural resources [167]. In this situation, bio-based materials seem to offer a practical solution to these difficulties [168].

Buildings can greatly decrease their greenhouse gas emissions by using bio-based materials, which has been proven to be a realistic option. Innovative materials made of natural fibers were used in the building industry as a solution to this energy crisis, including date palm [164], [169], hemp [170]–[173], and straw [174]–[177]. These bio-based renovation materials are also referred to as hygroscopic materials because of their high porosity and permeability. These characteristics result in a decrease in heat conductivity, density, and an effective buffering effect, each of which helps to keep the interior hygrothermal environments within a restricted range and cut down on energy use [177].

This sort of materials' dynamic energy simulation is a significant challenge, not only in consideration of norms and regulations but also in the context of decision-making (Projects for construction and remodeling, material selection, etc). Because of the nonlinear character and direct interaction between mass and heat activities, predicting porous material behavior is in fact complicated and challenging [178]. In recent years, there has been a rise in the need for modeling software to determine the associated heat and moisture interactions of building systems and envelopes.

The core of research is still carried out using large empirical models, which include a number of analytical concepts correlating thermodynamics principles of mass transfer and temperature-dependent movement coefficients. Porous materials are complicated and challenging to describe because of their nonlinear behavior and strong relationship between mass and heat transport. As a result, a variety of methods for simulating the dynamic thermal performance and energy use of buildings have been established. Most of these tools, like the Effective Moisture Penetration Depth model (EMPD) and the Conduction Transfer Function model (CTF), do not consider coupled heat and moisture fluxes in the wall or accurately represent them [178], [179]. These methods just take into consideration heat transfer or heat and moisture transfer separately. The literature has thus recommended a range of techniques, including the co-simulation approach, for a better assessment of the hygrothermal performance of the buildings [138].

This strategy makes use of two simulation programs, one for simulating building energy and another for properly reproducing mass and heat transfer in the building enclosure [180]. The hygrothermal performance of buildings made of bio-based materials has been studied using co-simulation in the literature [63], [180], [181]. TRNSYS is one of the applications used for dynamic thermal simulation of buildings. The hygrothermal transfer, however, has not yet been incorporated into the software. The dynamical thermo-hydric exchange between the interior air and the building envelope is not taken into consideration by the TRNSYS moisture storage models. This indicates that the hygrothermal response of porous construction materials cannot be correctly predicted by this model [180].

In order to anticipate the general performance of buildings, numerous studies in the literature, including those by Ferroukhi et al. [180], integrate the modeling software COMSOL Multiphysics and TRNSYS. Similar to this, Steeman et al. [63] talk about how to include a hygrothermal model in TRNSYS. The authors coupled heat, air, and mass transport (HAM) in porous materials using the implicit temporal discretization technique of TRNSYS. Due to its adaptability, the proposed coupled model may simulate multilayered walls with various boundary conditions for modeling actual construction applications.

However, it is well acknowledged that applying these models to ascertain non-isothermal moisture in porous materials presents several significant difficulties. One of the deficiencies that might occur is that the moisture content profile is not uniform at the interface of two distinct porous media because of the varying hygroscopic activity. Second, both potentials affect the moisture and heat diffusion coefficient in the conventional physical model. It is also difficult to experiment to find the dual dependence parameters. The strongly coupled governing equations are also difficult theoretically. The dynamic modeling of heat and mass transmission is a challenging undertaking since there are many variables that can affect how well hygrothermal behavior performs. There are a lot of factors related to heat and mass movement that are sometimes far beyond our control. Finding a model that effectively captures the behavior of bio-based materials can be challenging. Identifying the material's hygrothermal properties in order to feed the model. The main problem with the physical models that are discussed in the literature, nevertheless, is in this area. Discretization also increases computation times. In practice, two different categories of models can be identified.

White-box models are founded on the system's physical properties and the energy balance algorithms. They are produced by energy simulation programs like TRNSYS, EnergyPlus, WUFI, COMSOL Multiphysics, etc. Data-driven models frequently eliminate theory physical models and fully rely on input/output data that has been gathered and statistical prediction techniques like Artificial Neural Networks (ANN) or long short-term memory networks (LSTM).

However, it was shown that there is a deficiency of understanding regarding data-driven applications to forecast the hygrothermal response of bio-based materials. Based on a survey of the literature, we discovered limited publications on hygrothermal analysis applications of machine learning (ML) and artificial neural networks (ANN). A switching-linear (PWARX) model and three research on the usage of ANN [111]–[113] models are the only other studies that specifically mention them. In their work, M. H. Benzaama et al. [182] highlighted the advantages of data-driven models over physical models. The disadvantages and benefits of physical and data-driven models were discussed by the writers. The prospect of fusing physical models with data-driven models hasn't been investigated, yet.

Study methodology

Due to this and in order to benefit from each approach, we suggest in this study that a coupling strategy between a deep learning algorithm (ANN and LSTM) and the Building Energy Simulation (BES) method be used (TRNSYS tools). There has been no research on this pairing of LSTM and BES for the analysis of the hygrothermal performance of bio-based constructions. The major goal is to reduce the knowledge gap and propose a dynamic model that can overcome challenges in comparison to physical models, like offering a convincing description of heat and mass transport for bio-based structures, with less inputs and quicker computations.

As of right now, there are no research available to look at the interactions between an artificial intelligence algorithm and TRNSYS software for simulating the hygrothermal behavior of bio-based houses. Therefore, the research issue is, how can the hygrothermal simulation of bio-based structures be computed more quickly while still providing a physical understanding? How does the TRNSYS heat transfer model be upgraded to include the missing mass transfer data using artificial intelligence? Exists a process for converting thermal behavior that TRNSYS simulates into coupled heat and mass transfer? What variables have an impact on the co-simulation?

In order to anticipate the hygrothermal dynamics of bio-based buildings, this study introduces a unique method that combines traditional thermal simulation on TRNSYS with machine learning to provide hygrothermal outputs. A laboratory-scaled earthen prototype measuring 59 cm in length, 61 cm in width, and 44 cm in height is being used to test and confirm this method.

The listed below are the primary objectives of this study:

- To learn the fundamental theories behind the thermal behavior of hygroscopic enclosures and AI learning models.
- To showcase the physical and artificial intelligence models used in hygrothermal simulation.
- Outline how heat and mass transfer are related, as well as how deep learning would be utilized to combine the two.
- To demonstrate the effectiveness of hygrothermal simulations applied to porous structure envelopes under actual climatic circumstances.
- To show how machine learning may be incorporated into software for dynamic thermal modeling.

The objective of this study is to develop a model that forecasts the ambient temperature and humidity progression in a highly porous earthen building enclosure. In order to anticipate the thermal behavior of buildings, physics-based and deep learning algorithms will be presented.

4.3 Study methodology

We have created a strategy that describes our study technique in accordance with a survey of the applicable current literature.

Study methodology

There are numerous features to the theoretical study design for this research. Our working technique is divided into three main stages (**Figure 1.2**), that are each made up of a number of procedures which are described in the sections below.

- First step: Using the basic thermal properties of the material and the base physics of pure heat transmission, analyze and parameterize a typical thermal computation of the entire building.
- Second step: Demonstrating numerous machine learning models, with an emphasis on ANN and LSTM, and describing their advantages and disadvantages.
- In the third stage, data-driven modeling is combined with the outputs of physical models to transform the outcomes of the thermal simulation into hygrothermal data.

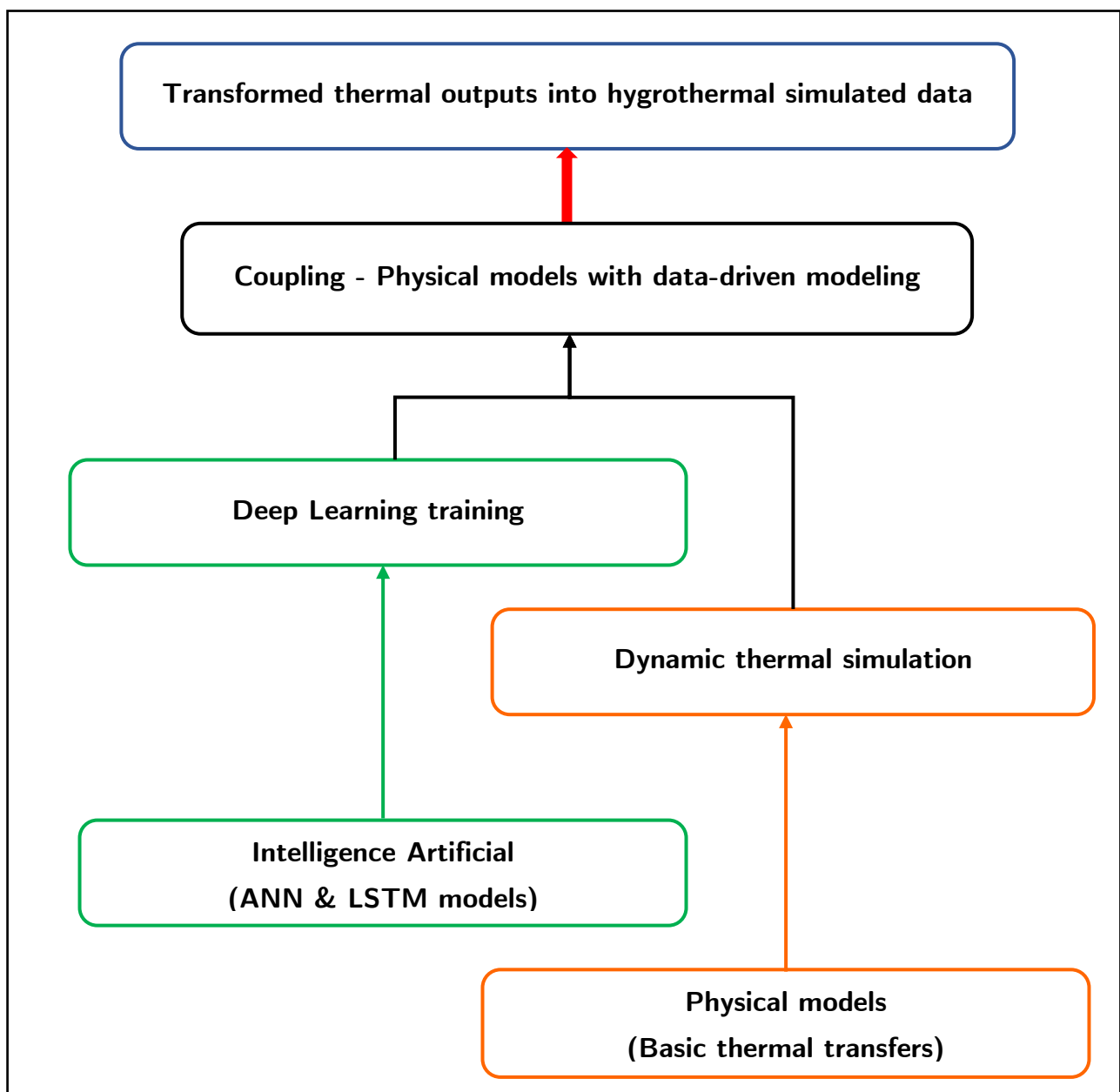


Figure 4.1 Schematic overview of hygrothermal simulation approaches

4.4 Lab-scaled building earthen prototype

Low-carbon construction materials are often produced using resources derived from bio-based sources or straw/rammed earth. The handling of carbon and the control of pollution are considerably aided by these mixes, which may be thought of as substantial volumes of low-carbon materials and industrial organic wastes [32].

Industries and governmental authorities with appropriate jurisdiction take a stand their deployment in newly designed and renovated buildings and structures. As a result, a specific class of building materials that utilize natural fibers [33] and produce enormous porosities to significantly lower their heat conductivity have been developed for the construction sector.

An insulating layer and a structural base make up the prototype's two layers. Both walls' constructions are mostly made of silty soil, algae, sand, straw, and water, in varying proportions to suit building rule standards. The following physical properties [1] of the material were evaluated and listed in **Table 4.1**.

Table 4.1 Mixture proportion of the developed structural and insulating wall parts made of Algae [1]

	Algae Structural Cob (ASC)	Algae lightened clay (ALC)
	5 %	20 %
Structural cob	62 %	00 %
Lightened clay	00 %	80 %
Algae (Laminaria Digitata Seaweed)	05 %	20 %
Reed	00 %	25 %
Straw	02 %	00 %
Sand	33 %	00 %

Several experiments were carried out utilizing the dry cup technique, which itself is founded on the standard NF EN ISO 12572 [149] and refers to relative humidity limits of 0 % to 50 %. This test requires the generation of relative humidity gradients between the two sides of an isolated, side-by-side sample. After doing this, it is necessary to monitor the daily mass variation until it stagnates. The porosity of several specimens was measured using the NF ISO 5017 [150] standard. In our illustration, the heat conductivity of the insulating and building elements is influenced by the temperature and the quantity of Laminaria digitata seaweed (Algae).

After conducting laboratory experiments, the optimal thermal conductivity values were established as constant values for the reduced heat transfer rate capacity (see **Table 4.2**). The traditional approach was used to estimate the dry density. Consequently, a cob wall's specific heat capacity is examined in order to gauge how well it can store thermal energy (C_p).

According to ISO 11357-4 [151], the C_p was determined using differential scanning calorimetry (DSC, NETZSCH STA 449 F3). Data was collected at a temperature increase of 1°C per minute between -20°C and 30°C .

Table 4.2 Hygrothermal properties on dry materials of the structural and insulation walls [1]

Properties	Insulation Clay	Structural Cob
Dry density (kg m^{-3})	643	1250
Dry thermal conductivity ($\text{W m}^{-1} \text{K}^{-1}$)	0.116	0.45
Vapor resistance factor (dry cup) [-]	6.07	6.2
Dry specific heat ($\text{J kg}^{-1} \text{K}^{-1}$)	827	1325
Porosity	0.6	0.5

The ALC and ASC specimens' moisture sorption curves are quite similar to one another (**Figure 4.2**) and exhibit type II isothermal behavior [153], which is characteristic of porous construction materials and is also seen in regular cob/clay. This specific curve, which was created utilizing the standard (NF EN ISO 12571) [152], demonstrates how the water content increases when algae are introduced to the two building walls.

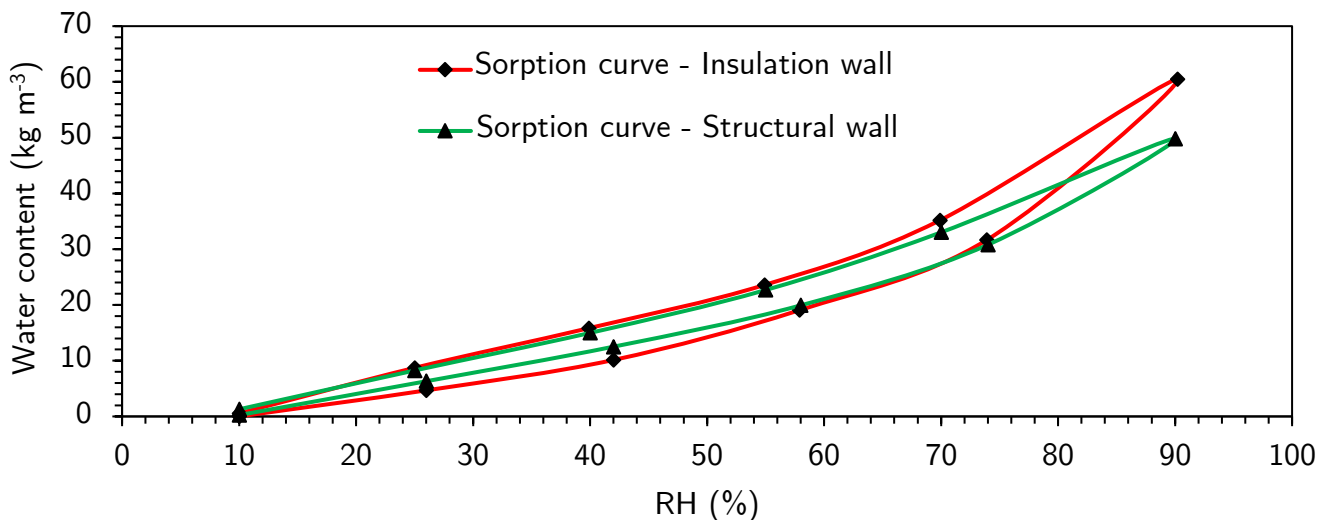


Figure 4.2 Sorption curve of the simulated materials for the structural (a) and insulating (b) wall parts [1]

Many variables may be utilized to explain it, including the sample's porosity, which has a substantial influence on the collision of water molecules within the micropores. A detailed explanation of the adsorption/desorption mechanism would lead to an accurate hypothesis while aiming to determine water diffusion within porous material using a different technique, such as the Knüdsen model [65]. Always relying on the experimental study of these components is advised because the underlying phenomenon is challenging to completely understand.

Lab-scaled building earthen prototype

Additionally, we see that near the offending material, the sorption curve tends to retain more moisture. It can be justified by the abundance of algae, which have a great ability to absorb water.

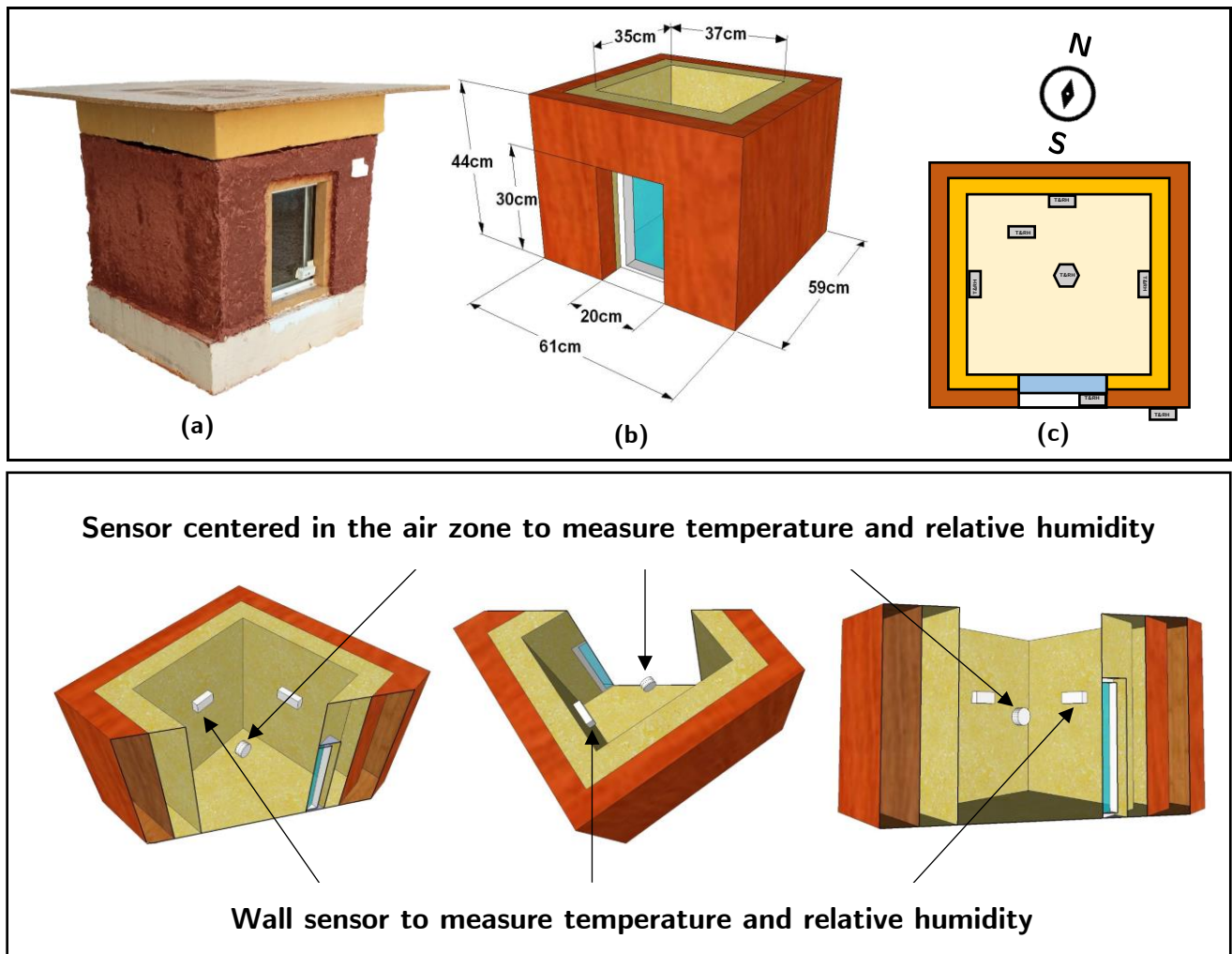


Figure 4.3 Basic structure of lab-scale building and location of measurement points inside and outside at different positions [1]

A lab-scaled prototype was created with dimensions of 59 cm long, 61 cm wide, and 44 cm high in order to explore the hygrothermal behavior (Figure 4.3b). **Figure 4.3a** shows how a window frame that is oriented toward the south and covers 6 % of the total lateral surfaces has been constructed to reduce summertime overheating and boost wintertime solar gain. The prototype comprises of a structural cob layer that is 6 cm thick, followed by an insulating cob layer that is 6 cm in thickness. Polyurethane is used as insulation for the floor and roof. **Figure 4.3c** shows the positioning of the sensors, which are placed at various points.

The prototype's central, south, north, east, and west sides all had temperature and humidity sensors fitted. We also installed sensors in the external facades (north and south). Additionally the weather conditions were gauged.

Table 4.3 Sensors technical data

Range of humidity	From 0% to 100%.
Range of Temperature	From -40 °C to 125 °C
Precision	± 3% (max) between 0 and 80% of relative humidity ± 0.4°C (max), from -10 °C to 85 °C of temperature
Radio coverage	100 m outdoors and 20 m indoors

In this research. The prototype serves as a tool to evaluate and test the numerical strategy. We wouldn't divulge into specifics regarding how the content was manufactured and characterized. On the latter, another in-depth study is being conducted.

4.4.1 Understanding difference between thermal and hygrothermal transfers in buildings

The thermal simulation of buildings performance is used to determine the amount of energy required to heat and cool a structure using a variety of subsystems and energy sources. This is achieved by simulating the responses of the building's energy systems under various operating and environmental conditions. The main part of the simulation is a model of the structure based on basic heat balance ideas [66].

Table 4.4 Difference between thermal and hygrothermal simulation

	Thermal simulation	Hygrothermal simulation
Weather conditions and solar radiation impact	✓	✓
Energy consumption (Only due to heat load forms)	✓	✓
(Due to mass phase change latent enthalpy)	x	✓
Air energy loads (Heat and mass loads)	✓	✓
Wall moisture buffering behavior	x	✓
Monitoring comfort temperature	✓ (No description of the energy balance due to the phase change during mass transfer)	✓
Monitoring comfort humidity	X (No interaction with building enclosure moisture buffering)	✓
Hygroscopic envelope heat conduction	✓	✓
Hygroscopic envelope mass diffusion	x	✓
Enclosure heat convection	✓	✓
Enclosure mass convection	x	✓

Hygrothermal behavior, on the other hand, is based on the idea of coupled heat and mass transfers in porous and permeable building materials, which are intricately linked with complicated nonlinear systems of equations.

The development of a reliable model to describe the hygrothermal behavior of buildings made of hygroscopic materials is difficult. The contrast between thermal and hygrothermal transfers in buildings must thus be understood before going further into how the two phenomena are associated (see **Table 4.4**).

4.4.2 Basic notions of the nodal approach for whole building energy simulation (BES)

Our investigation's main objectives are to offer a programming method that is manageable from the perspectives of both developers and programmers. In order to reduce the program's basic literacy requirements for adding models. The programming and simulation methodologies were intentionally intended to be as self-contained and adaptable as feasible. By doing this, we will use fewer inputs and have a bigger influence on the subject of heat load calculations and building energy audits. Once physical models and deep learning are effectively combined, it will also be easier to understand how a building's overall energy performance responds to environmental factors. The following explanation gives the initial heat and mass transmission and boundary conditions of a wall:

Exterior surface:

$$-\lambda \frac{\partial T}{\partial x} \Big|_{\text{ext}} = h_c (T_{\text{air,ext}} - T_{\text{surface,ext}}) \quad 4.1$$

$$-\delta_p \frac{\partial P}{\partial x} \Big|_{\text{ext}} = \beta_v (P_{\text{vap,air,ext}} - P_{\text{vap,surface,ext}}) \quad 4.2$$

Interior surface:

$$-\lambda \frac{\partial T}{\partial x} \Big|_{\text{int}} = h_c (T_{\text{air,int}} - T_{\text{surface,int}}) \quad 4.3$$

$$-\delta_p \frac{\partial P}{\partial x} \Big|_{\text{int}} = \beta_v (P_{\text{vap,air,int}} - P_{\text{vap,surface,int}}) \quad 4.4$$

Initial conditions:

$$T(x,0) = T_{\text{int}} \quad 4.5$$

$$P(x,0) = P_{\text{int}} \quad 4.6$$

Where λ is the thermal conductivity of the wall. δ_p is the water vapor permeability of porous material. h_c is the convective transfer coefficient. The water vapor convection coefficient β_v is based on the wall quality and rugosity.

4.4.2.1 Computing and simulation strategy of thermal method

When running a building thermal dynamic simulation, different sizing and parameter settings are completed first, followed by the climate periods, design days, and execution periods. Building energy modeling programs include a lot of data, and the underlying systems need some time to acquire and analyze that relevant information. Before starting the final estimations, the model might need to undertake a number of sizing calculations and carefully plan the size of the element (in the case of a full building energy performance study).

Additionally, it's critical to understand that testing and tracking are important considerations in the development of any new computational technique. Even though certain programming paradigms contain new codes, the vast majority of the heat balance code used in fundamental programs skips mass transfer via walls.

It should be noted that this method has experienced considerable rearchitecting algorithms. An attempt had been made to employ a program coupling to consolidate, modularize, and replace the in-data sets. The ultimate goal is to modernize it in order to comply with present programming standards without adding additional code. The software is tested at each step along the way using a range of input files and settings to ensure that modifications made to the program that were intended to be algorithmic independent have not influenced the result. This process has increased program credibility and been remarkably efficient. Additionally, it may be shown that the new coupling mechanism is at least as dependable as its predecessors by making comparisons to earlier experimental data.

4.4.2.2 Thermal simulation parameters definition

4.4.2.2.1 Conduction through the walls

Conduction transfer functions (CTFs) are widely used to estimate the global conduction heat transfer of a building in order to calculate the capacity and heat exchange. They may conveniently be included into any methods for calculating the energy performance of buildings to accomplish conduction estimations. The Laplace transform (LP), state-space (SS), and frequency-domain regression (FDR) are the three most used methods for obtaining CTF coefficients.

Studying the conduction heat diffusion through the building envelope is one of the primary theoretical techniques for determining the cooling/heating loads and energy needs for a defined volume. Several methods are used to compute the dynamic thermal behavior parameters of building structures, such as the conduction transfer function (CTF) and periodic/temperature response variables. The dynamic thermal behavior of a construction is described by the conduction transfer function (CTF). It also serves as the basis for calculating out the heat loss capability.

In contemporary building simulation tools including TRNSYS, EnergyPlus, and others, they are then utilized in conjunction with meteorological data to predict the heat transfer through the structures as well as space cooling load calculations. The precision of the dynamic thermal behavior variable outputs has a direct influence on building load and/or energy calculations.

In energy estimations, full building scale simulations, and investigation. The conduction heat transfer is often modeled as a one-dimensional, transient mode with constant material properties. Equation shows the simplified 1D unsteady heat diffusion equation alone without source and convection elements.

$$\frac{\partial T(x,t)}{\partial t} = \alpha \frac{\partial^2 T(x,t)}{\partial x^2} \quad 4.7$$

T standing for temperature. Thermodynamic diffusivity is α . X and t represent the direction of the heat flow and time, respectively.

As a function of the material's thermal conductivity and the temperature difference across a certain thickness, Fourier's law equation, which describes conductive heat transfer, is expressed as follows.

$$Q = -\lambda \frac{\partial T(x,t)}{\partial x} \quad 4.8$$

Where Q is the heat flow and λ is thermal conductivity.

Formula (8) is a partial differential equation that can be mathematically solved. The problem is frequently handled theoretically utilizing multiple conduction transfer function (CTF) as an independent technique [183].

Depending on the building surface's properties, CTFs reveal the material's thermal reactivity. The process generates a straightforward linear equation that, when combined with the current temperature, the historical and the present heat flow patterns, precisely describes the actual heat transfer:

$$Q_{out,t} = -\sum_{n=0}^{N_y} Y_n T_{in/surface,t-n\Delta t} + \sum_{n=0}^{N_x} X_n T_{out/surface,t-n\Delta t} + \sum_{n=0}^{N_\phi} \phi_n q_{out,t-n\Delta t} \quad 4.9$$

$$Q_{in,t} = -\sum_{n=0}^{N_z} Z_n T_{in/surface,t-n\Delta t} + \sum_{n=0}^{N_y} Y_n T_{out/surface,t-n\Delta t} + \sum_{n=0}^{N_\phi} \phi_n q_{in,t-n\Delta t} \quad 4.10$$

$T_{in,surface}$ and $T_{out,surface}$ are the temperatures of the internal and external surfaces, respectively. The letters X_n , Y_n , and Z_n stand for the surface-to-surface exterior, cross, and interior CTF coefficients, respectively.

The symbols N_x , N_y , and N_z , stand for the number of exteriors, cross, and internal CTF components, respectively. The heat flow at the outside and inner surfaces is represented by the variables Q_{out} and Q_{in} , respectively. The number of statements in the flux history is N_ϕ . The subscript Δt refers for the time step, and the letter t for the current time. The letter ϕ_n stands for the flow coefficient.

The approach can be applied faster and with less programming effort because of its linear connection. The CTFs are typically predefined [184] and irrespective of temperature (Available only for standard thermal simulation and not applicable for coupled heat and mass transfer simulation). The state space approach is the main technique used in building energy simulation for CTF calculations (Ceylan and Myers 1980 [185], Seem 1987 [186], Ouyang and Haghghat 1991 [187]). The preceding linear matrix formulas [188] define the fundamental state space system as follows:

$$\frac{d}{dt}[x] = [A][x] + [B][u] \quad 4.11$$

$$[y] = [c][x] + [D][u] \quad 4.12$$

Where x is a vector of state variables. u is a vector of inputs. y is the output vector. t is time, and A , B , C , and D are coefficient matrices.

The vector (x) of the system variables in an equation system can be eliminated using matrix algebra. Consequently, both the input vector (u) and the output vector may have a direct relationship to the dynamical patterns of the input and output values (y). The transient heat conduction equation is solved using this approach [188] by applying a finite difference discretization to all layers of the investigated building component. In this case, inputs include both the inside and external building temperatures. The resulting heat flow over both surfaces serves as an input, and the nodal temperatures are the outputs. As a result, the state space description based on finite difference variables can resemble such as this one:

$$\frac{d}{dt} \begin{bmatrix} T_1 \\ \vdots \\ T_n \end{bmatrix} = [A] \begin{bmatrix} T_1 \\ \vdots \\ T_n \end{bmatrix} + [B] \begin{bmatrix} T_{in} \\ T_{out} \end{bmatrix} \quad 4.13$$

$$\begin{bmatrix} Q_{in} \\ Q_{out} \end{bmatrix} = [C] \begin{bmatrix} T_1 \\ \vdots \\ T_n \end{bmatrix} + [D] \begin{bmatrix} T_{in} \\ T_{out} \end{bmatrix} \quad 4.14$$

Where T_{in} and T_{out} are the interior and exterior environmental temperatures. $T_1, T_2, \dots, T_{n-1}, T_n$ are the finite difference nodal temperatures. n is the number of nodes and Q_{in} and Q_{out} are the

heat fluxes (desired output). The resultant finite difference thermal equation for a conventional one-layer solid block featuring two interior nodes on both surfaces (in & out) and the same convection at both sides is displayed below.

$$C \frac{d}{dt} [T_{out,surface}] = hS [T_{out} - T_{in,surface}] + \frac{T_{in,surface} - T_{out,surface}}{R} \quad 4.15$$

$$C \frac{d}{dt} [T_{in,surface}] = \frac{T_{out,surface} - T_{in,surface}}{R} - hS [T_{in,surface} - T_{in}] \quad 4.16$$

The formula $R = (e \lambda^{-1} S^{-1})$ describes thermal resistance. The symbol for heat capacity is C . The wall's thermal conductivity is λ , its surface is S , and the layer's thickness is e . The construction materials have a density of ρ . The heat capacity of a wall is c_p .

Matrixed standardization:

$$\frac{d}{dt} \begin{bmatrix} T_{in,surface} \\ T_{out,surface} \end{bmatrix} = - \begin{bmatrix} \frac{hS}{C} + \frac{1}{RC} & -\frac{1}{RC} \\ -\frac{1}{RC} & \frac{hS}{C} + \frac{1}{RC} \end{bmatrix} \begin{bmatrix} T_{in,surface} \\ T_{out,surface} \end{bmatrix} + \begin{bmatrix} \frac{hS}{C} & 0 \\ 0 & \frac{hS}{C} \end{bmatrix} \begin{bmatrix} T_{out} \\ T_{in} \end{bmatrix} \quad 4.17$$

$$\begin{bmatrix} Q_{in} \\ Q_{out} \end{bmatrix} = - \begin{bmatrix} 0 & -h \\ h & 0 \end{bmatrix} \begin{bmatrix} T_{in,surface} \\ T_{out,surface} \end{bmatrix} + \begin{bmatrix} 0 & h \\ -h & 0 \end{bmatrix} \begin{bmatrix} T_{out} \\ T_{in} \end{bmatrix} \quad 4.18$$

The fundamental aspect of the state space method is that the nodal temperatures, which are state space variables, may be eliminated using matrix algebra to create a matrix equation that primarily explains the results (heat fluxes) as a consequence of the inputs (environmental temperatures). Therefore, it is not required to find the solutions in the Laplace domain. Additionally, the resulting matrix form has a greater physical meaning than the intricate functions demanded by the Laplace transform technique.

4.4.2.2.2 Outside and inside surface heat balance

The external face's heat balance is expressed as follows.

$$Q_{abs,rad,out} + Q_{net,rad,exch,out} + Q_{conv,out} + Q_{cond,out/in} = 0 \quad 4.19$$

The heat flow of absorbed direct and diffuse solar radiation (short wavelength) is the first component, the heat flux from net long wavelength (thermal) radiation exchange with the atmosphere and surrounding regions is the second, convection with the external air is the third, and conduction diffusivity through the wall is the fourth and final element. All other elements are positive for net flows towards the face, with the exception of the conduction term, which is commonly stated to be positive in the path from the outside to the inside of the wall. The first three parameters are frequently merged using optimized techniques that take into account the

sol-air temperature. Each of these components of the heat balance is introduced in further depth.

The term for absorbed direct and diffuse solar radiation is affected by a number of variables, including location, surface tilt, material coloration, environmental conditions, and others. The net longwave radiation is made up of the elements of radiation exchanges with the ground, sky, and air. The linearized radiative heat transfer coefficients are more compatible with the heat balance equation. While the prior section discussed the conduction heat transfer term, the conventional formulation used for understanding the principles of thermal transfer is employed to represent the heat transfer from surface convection.

The approach for calculating internal heat balance is based on the inner sides of zone surfaces. The four interrelated heat transfer variables of conduction through the building element, convection to the air, receipted and reflected of short-wave radiation, and long-wave radiant exchange are frequently employed to model this heat balance.

The incident short wave radiation is made up of solar radiation that enters via glass and interior emissivity from objects such lamps. The longwave radiation exchange involves the absorption and emission of low temperature radiation from sources such all other zone walls, equipment, and people. The heat balance might be written as follows on the inside face:

$$Q_{abs,rad,in} + Q_{xch,rad,in} + Q_{conv,in} + Q_{cond,out/in} = 0 \quad 4.20$$

$Q_{abs,rad,in}$ is the total of the radiation exchange between surfaces and from equipment/people in a certain air zone. $Q_{xch,rad,in}$ is the incident irradiation emitted from the outside on the interior surfaces that passed via windows. $Q_{cond,out/in}$ is the heat flux conduction from inside, and $Q_{conv,in}$ is the convective heat exchange between the facade surfaces and the inner zone air.

4.4.2.2.3 Sky and solar calculations

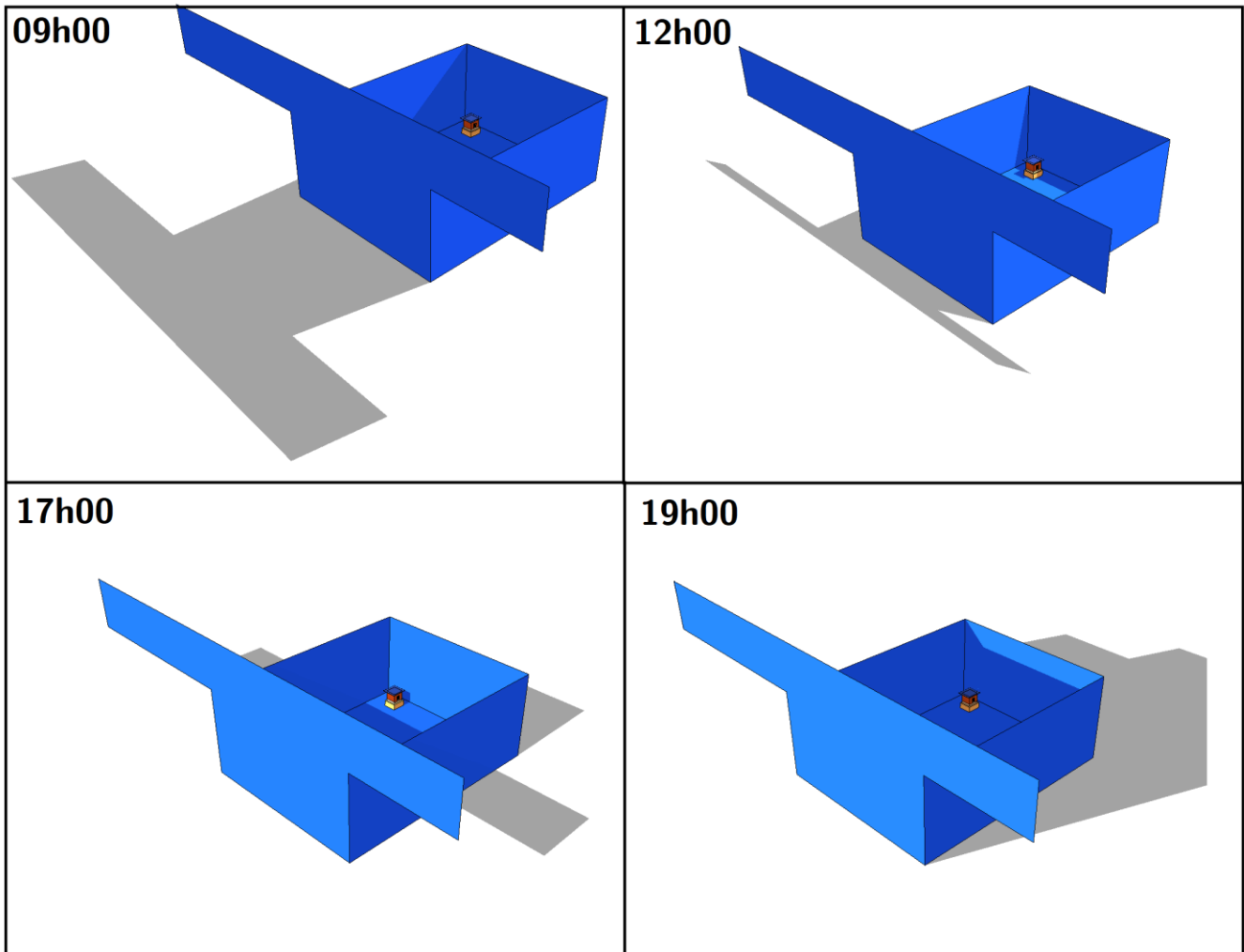
Diffuse solar radiation coming from the sky impacting on an exterior surface is calculated while taking into account the anisotropic radiance dispersion of the sky (horizontal or titled).

Two values that define the sky's state are used to estimate the ratios of these distributions: the clearness factor and brightness factor, which are derived from the sun's position and other solar attributes from the weather file.

4.4.2.2.4 Shading calculations

Predicting heat gains in buildings caused by solar radiation requires knowledge of the amount of each section of the facility is covered and the percentage that is exposed to direct sunshine. The quantity of each surface that is exposed to sunlight changes throughout the day in accordance with the sun's location. The shadow methods are used to compute these sunny areas.

The computing shadowing principles may differ from software to software, but for a good shadowing method, the choice of it must be compatible with the real situations.



Date : 07/06/2022 - City : Caen, Normandy, France

Figure 4.4 Shade profile during the whole day taking into account the actual conditions in relation to the building site

4.4.2.2.5 Infiltration/ventilation

Any external air that penetrates through infiltration is assumed to immediately mix with the air in the zone. Estimating the amount of infiltration air is extremely difficult and uncertain. The most common technique uses the current simulation time steps of outside temperature to convert the infiltration volume from the number of air changes per hour and incorporate it in the zone air heat balance. Infiltration is the unanticipated entry of air from the surrounding atmosphere into a thermal zone. In very tiny quantities, architectural elements, gaps surrounding windows, the opening and shutting of outside doors all contribute to the infiltration phenomenon. In this model, the user enters a design rate of flow that may be based on a number of different approaches, but the engineering process ultimately determines which model is the proper one.

Ventilation is the controlled flow of air from the external ambient into a thermal zone in order to provide some non-mechanical conditioning. Simple ventilation may be controlled by a schedule and the determination of minimum, maximum, and delta temperatures. The temperatures might be either a single constant number or a time-varying schedule over the length of the simulation.

4.4.2.2.6 Zone gain heat loads

Internal heat gains from persons, equipment, and artificial light often have a substantial impact on the thermal balance of the zone. Users of the BES (building energy simulation) can specify heat gains for a wide range of equipment types, such as people, illumination, gas and electric equipment, as well as a few more types. The total heat gain comes from these sources' convective, radiant, and latent gains in the right amounts. Convective gains are the designation for sudden temperature rises in the zone air. Radiant gains are dispersed over the zone's surfaces, where they are predominantly absorbed and then released back into the space, depending on the surface heat balances (with a small percentage transmitted through the surface).

4.4.2.2.7 HVAC sizing simulation

Once the zone heat balancing model is run on the computer during the zone sizing periods, we speak about optimal loads sizing simulations. However, since the space heat balance model is performed during the sizing processes for equipment load calculations, we make use of the ideal system load simulations. An HVAC sizing simulation is a sort of simulation that does thorough simulations utilizing the most recent component sizes and operational HVAC systems by employing duplicates of previous sizing periods. The complex sizing algorithms monitor activities that occurred during particular size periods, alert software and subsystems to rerun their size calculations, and determine whether new size results are necessary. The process can be repeated iteratively.

4.4.3 Fundamentals of coupled heat and mass transfer

The transfer of moisture and heat over building envelopes may be described using transport equations for energy and mass conservation. Energy balance equations may measure heat transfer involving conduction, convection, and radiation [66]. While natural, outside, or manually generated air fluxes can cause air-moisture convection. Mass balance calculations take into account liquid flow, moisture convection, and vapor diffusion [67]. The term appearance of heat, air, and moisture transfers (HAM) refers to these interactions in any investigation of the entire building envelope's hygrothermal performance [68]. The various element of the in/outdoor climate conditions and the building envelope interact physically in the manner as shown in **Figure 4.5**.

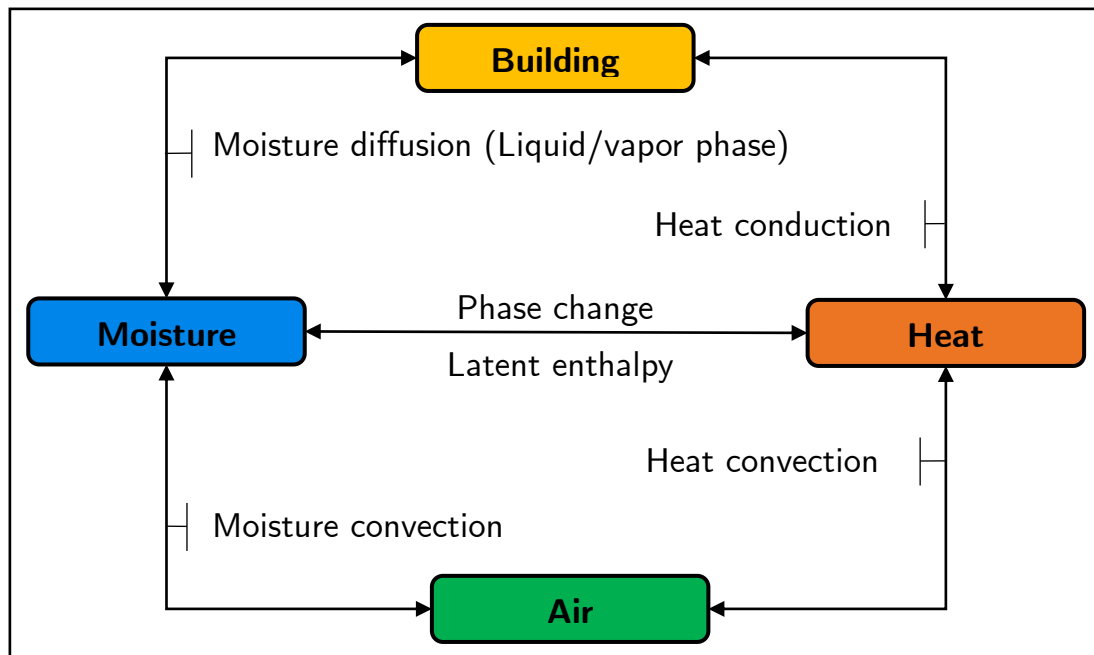


Figure 4.5 Different forms of physical interaction between the building envelope and the heat, air and moisture [138]

The literature describes a number of computer-based techniques for examining the thermal behavior of buildings. The complexity of models varies greatly with respect to the fundamental concepts of mathematics and physics. The complexity of the model considers the following elements: aspects of heat and moisture diffusion (1D, 2D, or 3D), system dynamics regime (steady-state, quasi-static, or transient), and conceptual understanding. Besides to the availability of numerous details, such as construction details, temperature, building dimensions, and meteorological conditions, can determines the level of sophistication of the model. Every well-known thermal simulation program uses a variety of techniques, combining computational mathematical techniques with physical models (which usually disregard mass movement and just incorporate heat balance calculations), to address the physical issue quantitatively. The finite volume, finite difference, or finite element methods can be applied. The ANN or LSTM approach, a machine learning-based statistical modeling technique, also made a contribution to the core topic of the current work. The Künzle model [24] is the most widely used physical model in the literature for modeling the coupled heat and mass transfer of bio-based materials.

4.4.4 Deep learning modeling

The literature's most popular data-driven model for analyzing the thermal performance of building heating is the artificial neural network (ANN). An artificial neuron is a simplified and numerically oriented version of a biological neuron. The information processing function of this neuron is handled by a mathematical entity [189]. An example of the typical architecture of an ANN model is shown below. The three aspects of the artificial neuronal approach are shown in **Figure 4.6**.

- The synapses that are associated to weights.
- Processing component known as a "summing junction" that aggregates input synaptic weighting data and alters them by adding a bias factor (b_k).
- A function called activation (φ) controls how strong the signal is when it leaves the cell.

The neuron k can possibly be explained by the equations below:

$$u_k = \sum_{j=1}^m X_j w_{k,j} \quad 4.21$$

$$v_k = u_k + b_k \quad 4.22$$

$$Y_k = \varphi \left(\sum_{j=1}^m X_j w_{k,j} + b_k \right) \quad 4.23$$

Where the linear yield of the original signal is represented by u_k and v_k is the weighted sum of the input signal that has been altered using b_k . The activation function φ is a set of mathematical equations that governs how the neuron k outputs a signal. The weighted and bias-corrected inputs are added to produce the final output signal (Y_k),

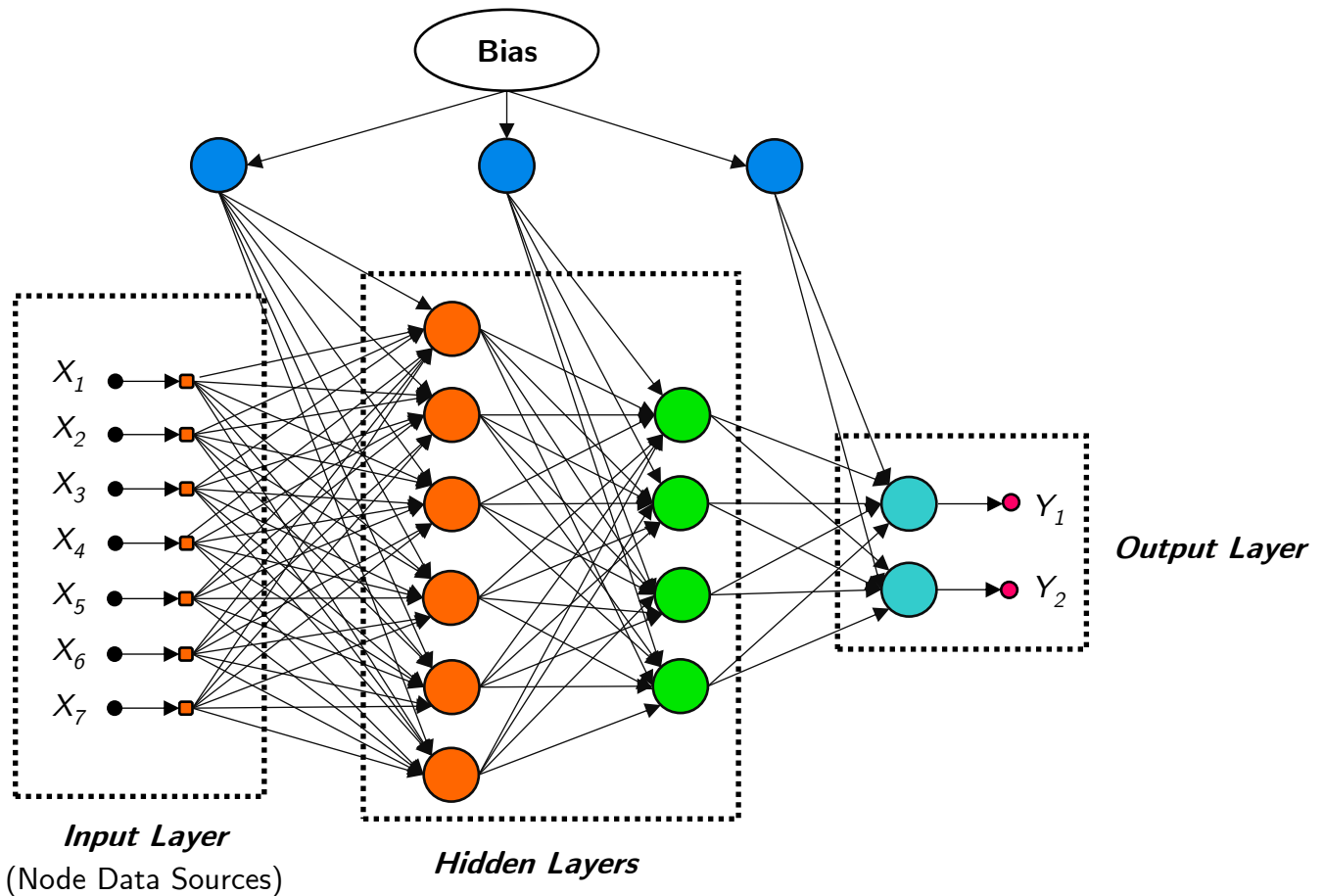


Figure 4.6 Simplified representation of an ANN model [138]

There are four main groups that make up the activation function [189]. The threshold function equivalent to Heaviside function, the identification function known as the linear function, the Logistic sigmoid function and the Hyperbolic tangent function. A number of ANN types, such as Convolutional Neural Networks (CNN) and Long Short-Term Memory (LSTM), have been described in the literature. The output of a CNN, on the other hand, is not dependent on the

output from previous time intervals; it doesn't maintain the same memory as the output of an LSTM. However, CNN gets access to a variety of inputs from earlier in time because of the stacked residual blocks. This network has an advantage over LSTMs in that output may be performed in parallel, which enhances both training and predicting. Furthermore, CNNs are better suitable for pattern recognitions, but LSTM networks would be more ideal for data sequences that need taking into account historical inputs while developing forecasts.

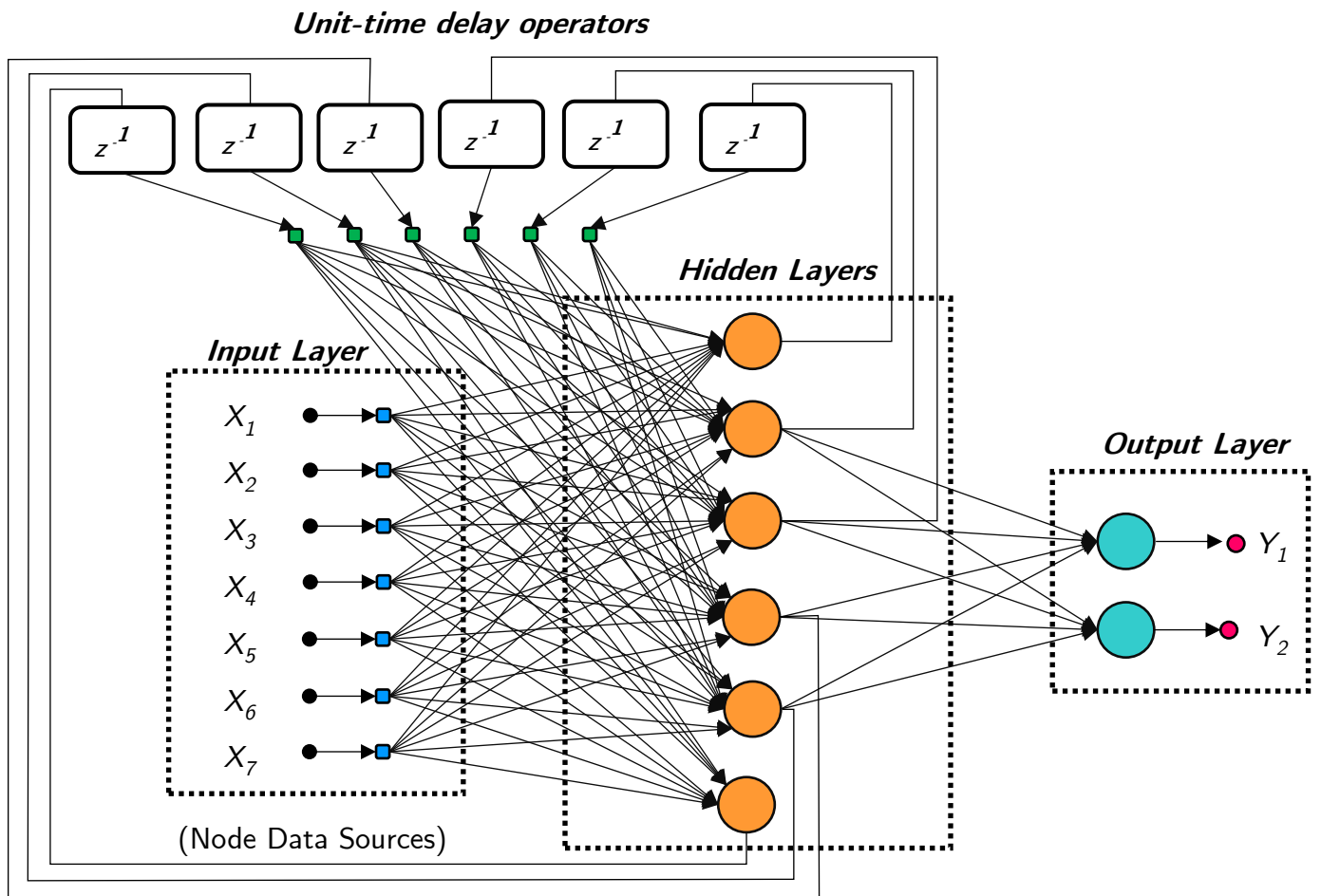


Figure 4.7 The structure of Recurrent Neural Network with hidden neurons

The filament architecture of the LSTM is shown in **Figure 4.7**. A cell serves as the basic core element of an LSTM, and the state of the algorithm is what allows it to function. A forget, input and output gate are the three types of gates that an LSTM uses to regulate the state of a cell. The amount of data that can enter through a gate is limited [190]. The following equations can be used to describe how information proceeds through the gates. The following equations explain the LSTM model [191].

$$f_t = \sigma(W_f h_{t-1} + U_f X^t + b_f) \quad \text{Forget gate's activation vector} \quad 4.24$$

$f_t = \sigma(W_f h_{t-1} + U_f X^t + b_f)$	Input/update gate's activation vector	4.25
$c_t^i = \sigma(W_c h_{t-1} + U_c X^t + b_c)$	Memory/cell candidate/input activation vector	4.26
$c_t = f_t \circ c_{t-1} + X^t \circ c_t^i$	Memory/cell state vector	4.27
$Y^t = \sigma(W_Y h_{t-1} + U_Y X^t + b_Y)$	Output gate's activation vector	4.28
$h_t = o_t \circ \tanh(c_t)$	Hidden state	4.29

Figure 4.8 shows the inputs and outputs of an LSTM for a number of timesteps. For the input, output, and an unrolled form of the equations across time for a timestep alone, the output of a typical ANN architect may be utilized as the input X_i^t for an LSTM. The inputs are h_{t-1} and c_{t-1} from a previous timestep of LSTM. For the current timestep, the LSTM's output is Y_i^t . The LSTM also generates the c_t and h_t for use by the following time step.

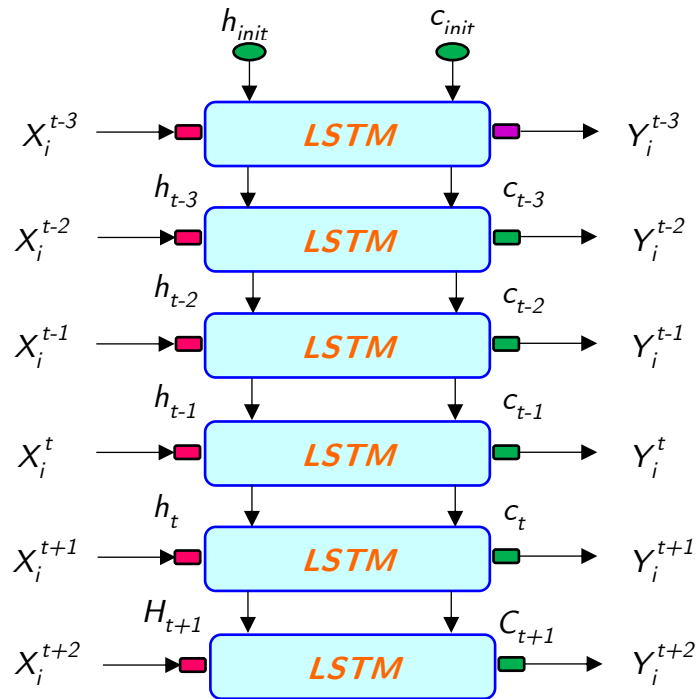


Figure 4.8 Single-layer LSTM network unrolled for many timesteps

Additionally, the LSTM algorithms provide f_t , X_t and c_t^i , which are used internally by the hidden layer to create $c(t)$ and $h. (t)$. Only one cycle is taken into consideration by the aforementioned groups formulas. This means that new calculations for these equations for the subsequent time step are required. Therefore, if our series has three timesteps, the previous equations will be solved three times. The value matrices ($W_f, W_f, W_X, W_Y, W_c, U_f, U_X, U_Y, U_c$) and biases (b_f, b_X, b_Y, b_c) are not time-dependent. This suggests that these weight matrices are time steady. Three steps are taken to implement the artificial neural network idea. To lower the error function, the model must initially be trained. The inaccuracy may be reduced by altering the weighting

coefficients based on comparisons between experimental and simulation results. Statistical criteria are used in the comparison. The goal of verification is to independently change a model's hyperparameters to fit the training data and evaluate it. The applicability of the model's results is then assessed. The determination coefficient (R^2), the root means square error (RMSE), and the mean squared error (MSE) are three performance metrics that are widely used to evaluate the efficacy of developed models. These indicators are given in equations 1.23 to 1.26.

4.4.5 Coupling method between physical models and deep learning

Couple of separated solvers are used in the computation of the combined Physical model and Deep learning. To perform dynamic simulation in real-world outside climatic conditions, a commercial Building Energy Simulation (BES) program (TRNSYS) [27] is used in the first step. Only the material's thermal properties are taken into account by TRNSYS software. However, this program does not take into consideration the material's hygroscopic qualities. In the second stage, commercial and open-source software is used to carry out the deep learning approach for converting the results of the TRNSYS thermal simulation into hygrothermal data. **Figure 4.10** depicts the coupling diagram and process. The ANN and LSTM models of deep learning are investigated. For the numerous coupling types, a number of couplings have been proposed [192].

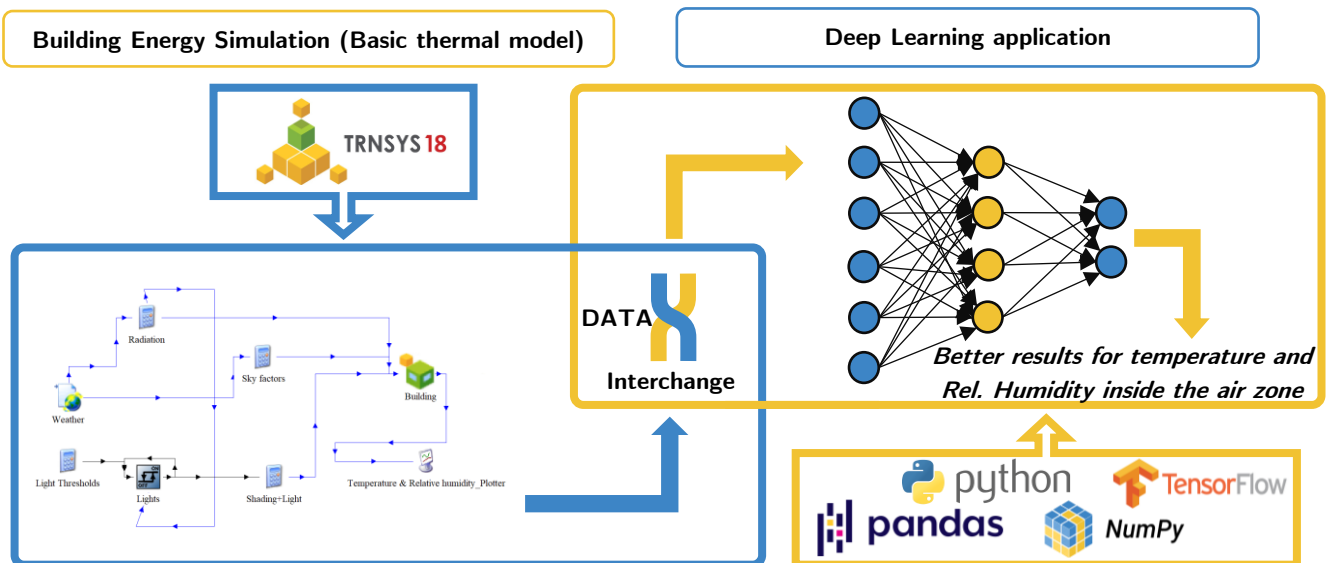


Figure 4.9 Co-simulation between BES (Building Energy Simulation) and AI (Artificial Intelligence)

In the framework of our job, using a one-step dynamic coupling is a promoting approach, deep learning only obtains the boundary conditions that thermal simulation provides. In this study, the primary data for deep learning computation is supplied as the air zone temperature and humidity simulated using TRNSYS. They are paired up until the convergence conditions are met (validation of the transformed outputs with the experimental results).

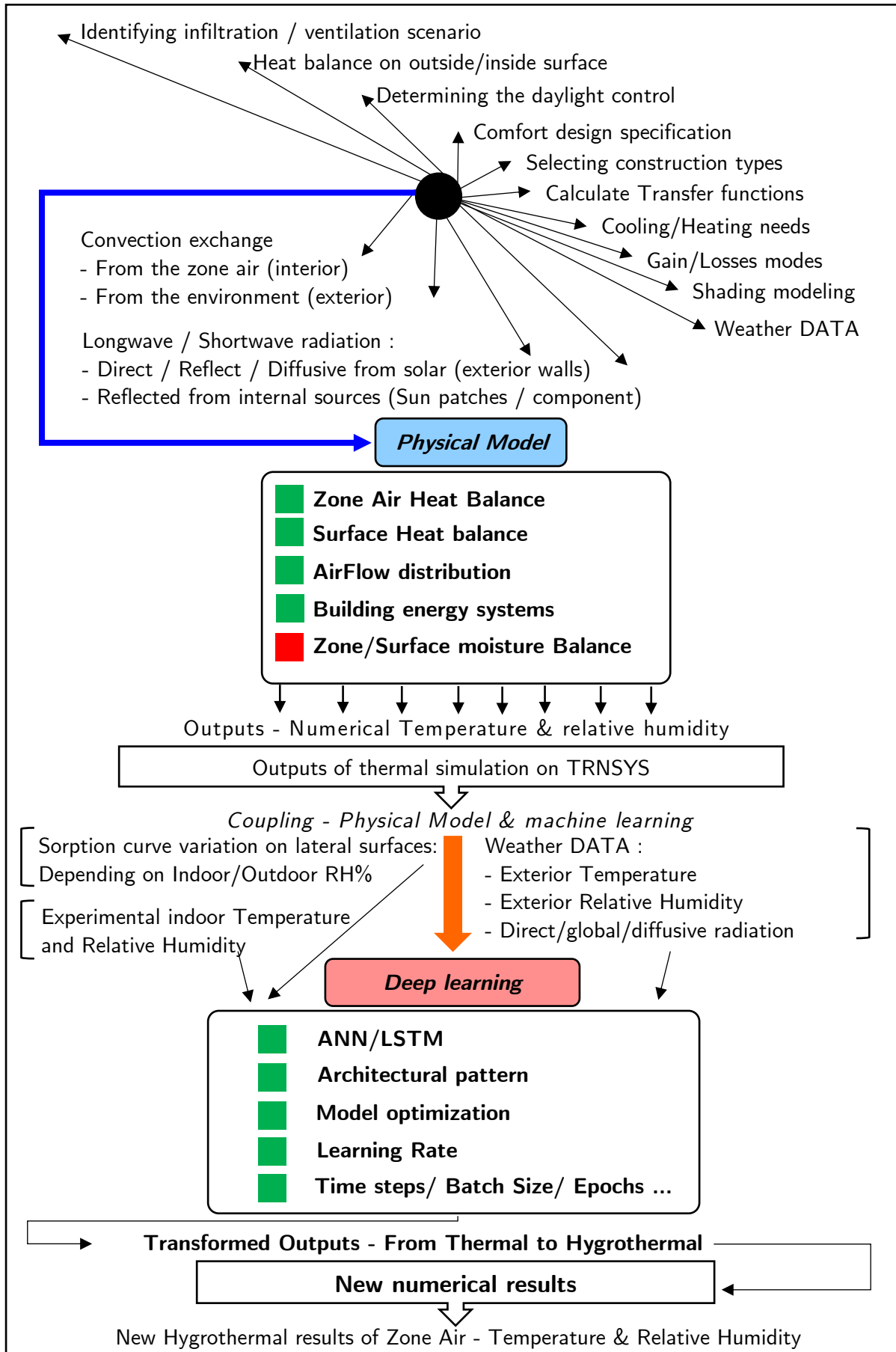


Figure 4.10 Flowchart for coupling thermal physical models with deep learning

The adoption of a direct dynamic connection occurs at the same time step (t). For the machine learning process to produce the best results, a certain number of iterations and data quantities must be provided from thermal simulation software. The physical modeling uses a 1-hour time step and there is no requirement for time step synchronization, but data values that depend on time must be compatible with the outputs of the BES program. **Figure 4.11** shows the boundary conditions used in TRNSYS.

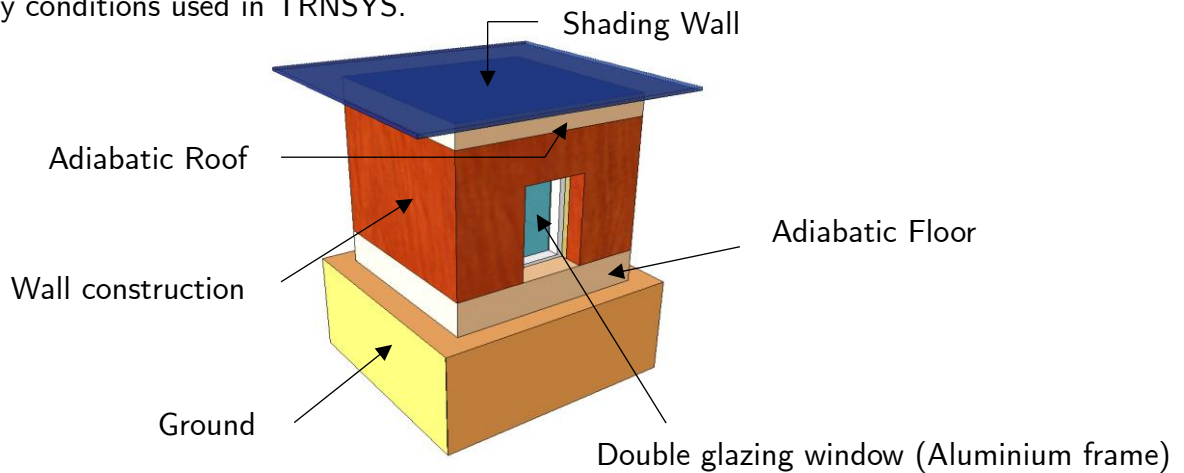


Figure 4.11 Boundary conditions of the simulated building

For earthen structures, it is sufficient to demonstrate the effectiveness of the model by conducting a straightforward analysis of the sorption curve of the walls, using this data as training examples for artificial intelligence, and adjusting the thermal performance that TRNSYS tools replicate to the hygrothermal behavior (**Figure 4.10**). This is being done to see if it can be utilized as a replacement for the entire comprehensive physical model of coupled heat and mass transport through a porous medium at the size of a building.



Figure 4.12 Lab-scale building location at the Builders engineer school

(Epron, Normandy, France) // (Google earth 3D satellite image)

The walls of the entire building were subjected to the local weather in the French region of Normandy. All starting and physical parameters that are employed in the computation are determined in accordance with experimental scenarios. From the Bouasria et al research [168], thermophysical data on earthen construction walls have been gathered and listed in **Table 4.2**.

4.5 Results and discussions of developed approach

The models presented in the current paper were verified by contrasting the results with experimental data using several approaches. The experimental evidence sets from the Bouasria et al. study [168] are shown in **Figure 4.3**, **Figure 4.11** and **Table 4.2**. It was used to test the model on structures made of earth. The sorption curve of building walls in our case is the only additional parameter that must be investigated in order to validate the model (**Figure 4.2**).

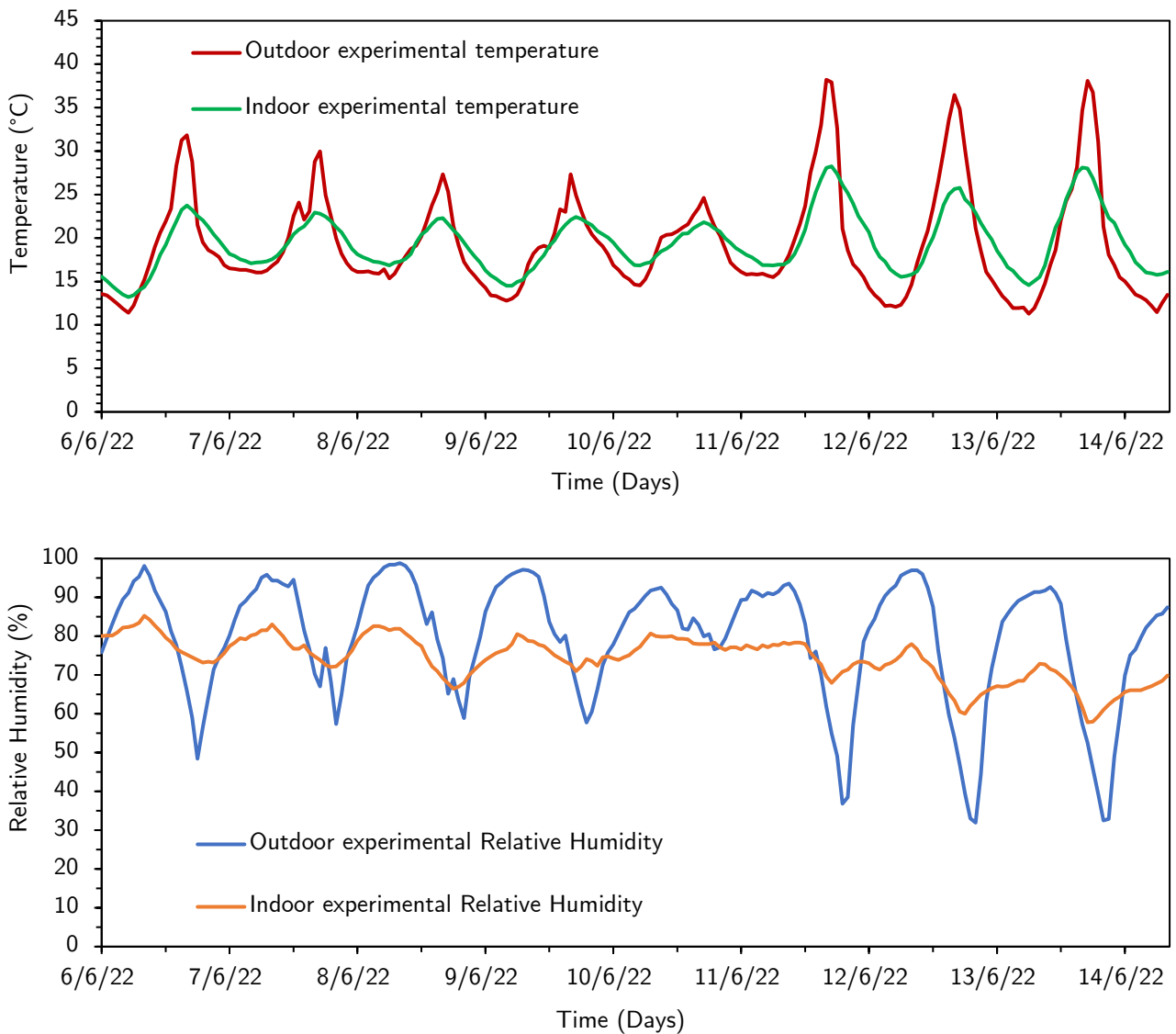


Figure 4.13 Indoor and outdoor real climate conditions of the building recorded in Caen town of the Normandy region (June 2022)

This parameter, along with other standard inputs, will later be used as training data by artificial intelligence in order to convert thermal behavior into hygrothermal behavior. This is being done to see whether it can be utilized as a replacement for the full detailed physical model of coupled heat and mass transport through a porous material at the size of a building.

The exterior walls of the entire building were exposed to the actual weather. They were suitably insulated and shielded from solar radiation in order to consider the upper and lower sides (Roof and Floor) as an isothermal boundary condition. First, it is assumed that the wall is 50 % dry and consistently reaches room temperature. All preliminary and physical parameters that are employed in the simulation are determined in accordance with experimental conditions. Calculations of the sorption isotherms were made using experimental data [168] for an ambient air temperature of 23°C and a relative humidity value of 0 % to 95 %.

The simulation's irradiation climate data (global and diffuse solar irradiations) were acquired from the open-source data of the "EU photovoltaic geographical information system," while the temperature and relative humidity were measured experimentally employing sensors.

Figure 4.13 shows the data that was captured during the first several weeks of June in 2022 with a time interval of 60 minutes.

We can properly deduce from the graphs that the inside climate replicates changes in the outside with a temperature differential brought on by thermal inertia. These indoor data are eventually used to value the simulation's outcomes. The findings indicate that given an external temperature range of 11.28 °C to 38.21 °C, the inside air temperature fluctuates between 13.43 °C and 28 °C. The temperature difference between the interior and outside environments was 10 degrees. Moreover, in comparison to an external humidity range of 33 % to 98 %, the interior humidity ranges from 58 % to 85 %.

4.5.1 Sensitivity analysis

Sensitivity analysis is the investigation of the relationship between the ambiguity in our codes' inputs and their output. The choice of these factors has the potential to be inaccurate, which might have a substantial effect or lead to limitations in the final solution of the outputs. Sensitivity analysis is used to define the model's optimum structure in order to effectively depict the thermal behavior of various measurement campaigns.

Consequently, by examining the hyper-parameters, such as the hidden layer and neuron synapses count. Depending on the number of neurons, the reliability of temperature and relative humidity estimations obviously varies. The computed hygrothermal output values are also less sensitive to training periods and learning ratios than the number of neurons within the hidden layer.

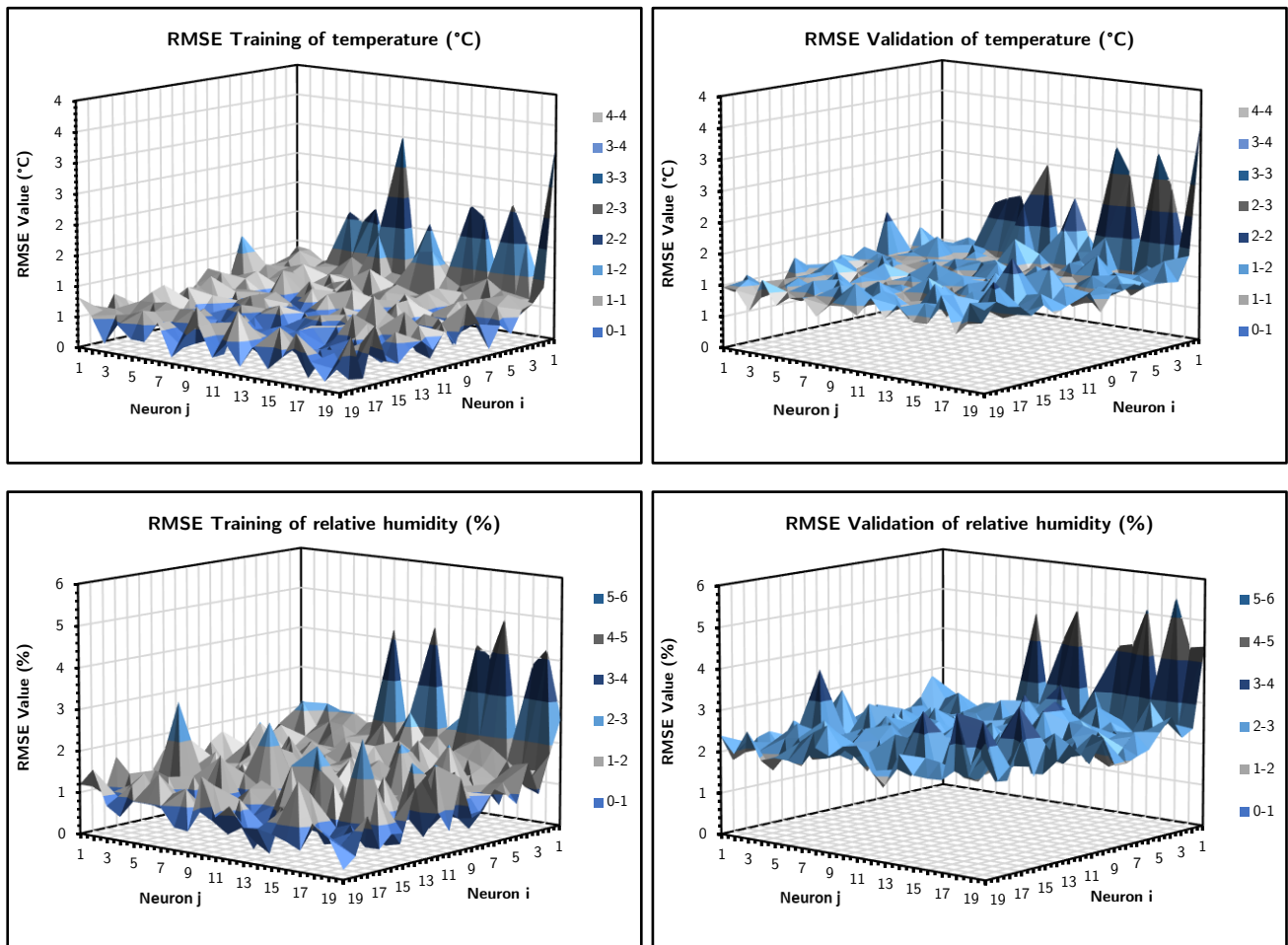


Figure 4.14 Influence of ANN architect on RMSE of outputs

Figure 4.14 illustrates the importance of selecting a suitable transfer function and an enough number of neurons for the hidden layer during parameter training and validation. In our artificial network, we selected a model with two hidden layers, each with 20 layers and 3 neurons. However, we must modify our technique for selecting architects to meet the criteria of the predicting simulation.

4.5.2 Outputs of the standard building energy simulation (BES)

The next section illustrates the determination of many factors that impact the thermal building performance. A low carbon and hygroscopic building envelope that is primarily made of recycled waste and soil has been modeled. As part of our current inquiry, we are particularly interested in the variations of the inner air temperature and relative humidity of the building. Determining the outputs of a basic thermal simulation of a hygroscopic building envelope is thus the main objective of our research. Then, we create a brand-new computing strategy that is more flexible, more efficient, and less complex than the complete hygrothermal full scale technique, making it suitable for use in academic research and engineering applications.

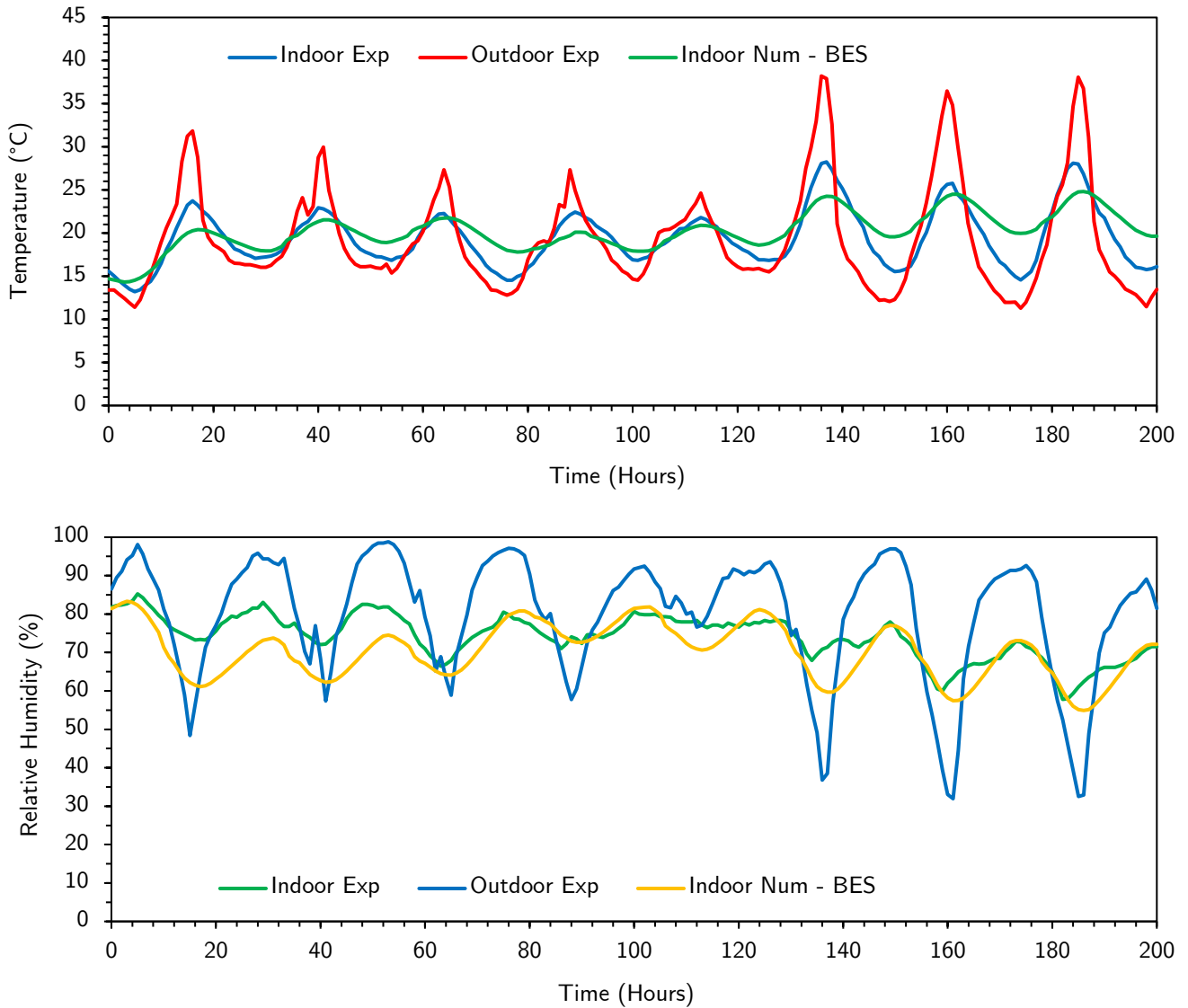


Figure 4.15 Numerical and experimental thermal simulation results of BES (TRNSYS) for temperature and relative humidity variations of inside air zone

Figure 4.15 displays experimental data on temperature and relative humidity fluctuations inside the building air zone together with predictions from the typical thermal simulation. When we evaluate the software outputs to the experiments using the conventional thermal simulation model, we can see that once we depend only on the pure thermal simulation and we do not take into account the buffer moisture of the building walls, the results are fairly appropriate. This remains insufficient for a credible comprehensive energy performance analysis.

When comparing numerical temperature simulation to experimental evidence, we can identify a short delay in results. But the results of the simulated temperature curve evolution follow the same pattern as the empirical one. Only a few outputs are underestimated in comparison to the real values on the numerical relative humidity curve.

Results and discussions of developed approach

Thermal physical model coupled with ANN (deep learning) to transform outputs into hygrothermal Data

This curve closely resembles the shape of the building's actual evolution. In the present simulated scenario, the highest deviations in temperature and relative humidity were 5 °C and 18.14 %, accordingly. The results of a typical thermal simulation are adequate for the creation of optimal and quantified solutions, but they are not enough, as we can reveal.

4.5.3 Thermal physical model coupled with ANN (deep learning) to transform outputs into hygrothermal Data

We anticipate being able to investigate the outcomes of a hygrothermal simulation of a very hygroscopic building envelope in this unique modeling approach by fusing the underlying physical model with artificial intelligence. We seek to create a revolutionary computing technique that is less involved, takes less inputs, and can be quickly computed using an algorithm with good usability, as compared to the whole hygrothermal research. In this section, we make an effort to identify the outcomes of actual hygroscopic building behavior by transforming the traditional thermal simulation outputs of the TRNSYS software into hygrothermal data utilizing machine learning (ANN) approach.

For the new method as well as the typical thermal simulation on TRNSYS, we continue to utilize the same operational scenario of a real building. To preserve a physical sense of modeling, especially when combining it later with the deep learning technique, the building envelope and physical parameters were undertaken using TRNSYS. On the basis of actual environmental conditions, computational analysis of the thermal behavior of buildings was initiated. When training the artificial intelligence model using numerical data, external real-world environmental conditions, and the data of the sorption curve on the walls, the outputs of the conventional simulation was coupled and incorporated into the program. With this method, the idea of the walls' hydric buffering behavior can be integrated while the numerical model is being trained.

Figure 4.16 displays the fluctuations in temperature and relative humidity inside the building air zone that were anticipated by the simulation technique. We can observe that the paired TRNSYS+ANN simulation values obtained produce more accurate findings than the normal thermal simulation when using a simple thermal simulation that ignores the interactions between heat and moisture flow in a building.

The evolutionary curves of both the experimental and numerical temperature values are the same. The same is true for relative humidity, where the numerical curve closely fits the profile of the building's actual evolution and there are very few underestimations of outcomes compared to experimental data. If we exclude the temperature response delay and the relative humidity response delay in the current simulation, the greatest temperature variations between numerical and experimental data are less than 2 °C.

Results and discussions of developed approach

Coupled thermal physical model with LSTM (deep learning) to transform outputs into hygrothermal Data

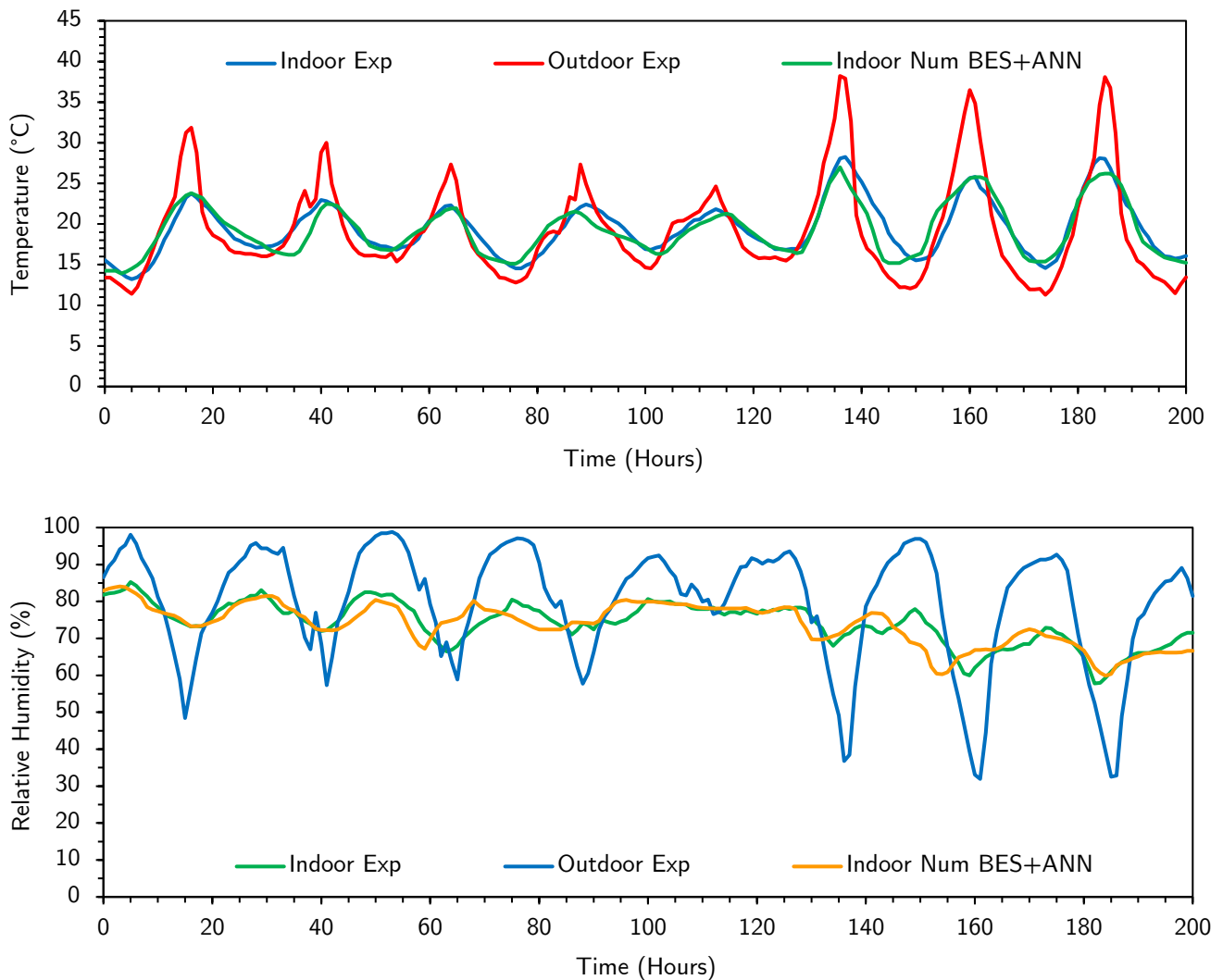


Figure 4.16 Results of numerical and experimental hygrothermal modeling using coupled BES and ANN for temperature and relative humidity variations of inside air zone (Earthen construction building)

We can reach the conclusion that the proposed hygrothermal simulation employing a coupled technique between the physical model and deep learning (ANN model) produces more trustworthy findings that are potentially more accurate than the conventional method, thus improvements are still required.

4.5.4 Coupled thermal physical model with LSTM (deep learning) to transform outputs into hygrothermal Data

This method relies on the integration of two software programs to create the fully coupled heat and humidity movement model at the whole building scale (LSTM model and TRNSYS tools). The same coupling method used in the ANN and LSTM models has been utilized in this section. The simulation's predictions for temperature and relative humidity fluctuations inside the building envelope are shown in **Figure 4.17** along with the experimental findings.

Results and discussions of developed approach

Coupled thermal physical model with LSTM (deep learning) to transform outputs into hygrothermal Data

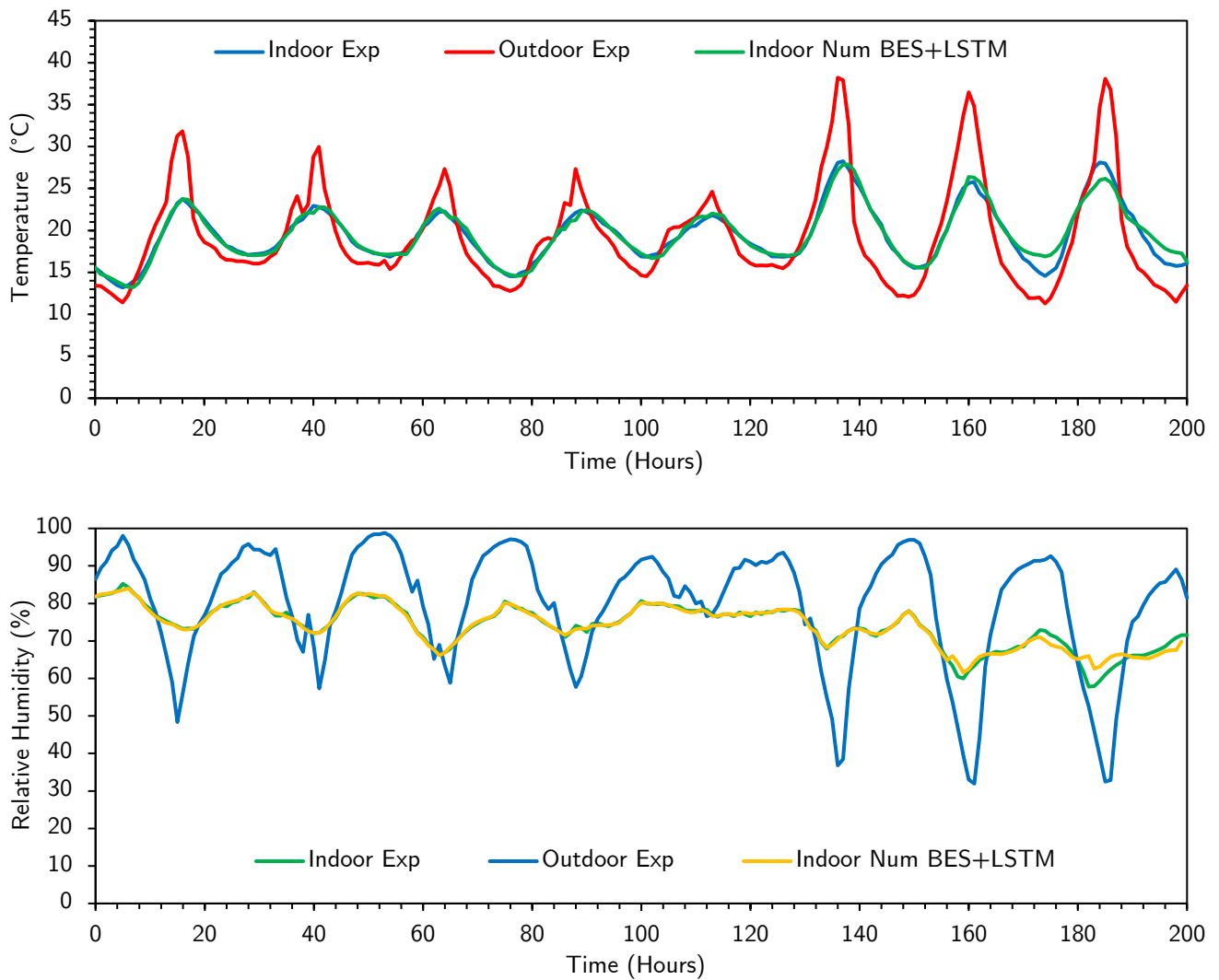


Figure 4.17 Results of numerical and experimental hygrothermal modeling using coupled BES and LSTM for temperature and relative humidity variations of inside air zone (Earthen construction building)

According to the outputs, TRNSYS+LSTM coupling provides more accuracy than TRNSYS+ANN. Better results are obtained while using LSTM as opposed to the ANN deep learning model. The LSTM model often performs better than the traditional ANN model. Due to the usual flood characteristics, ANN models are unable to create accurate simulations [193].

The statistical indicators for every model and the full building air zone are shown in **Table 4.5** for clarification. The basic TRNSYS simulation appears to have a higher temperature difference, with an RMSE of 2.31°C, since we used fewer experimental training data. The temperature RMSE of 0.57°C and relative humidity RMSE of 1.45 % are both highly encouraging results of the coupling approach TRNSYS+LSTM.

The deep learning LSTM model, which seems to perform better than the ANN model, is the foundation of the coupling strategy. To minimize the discrepancy between numerical and experimental data, we used straightforward physical models (just heat transport) with machine

learning to assess the accurate hygrothermal behavior of buildings.

Table 4.5 RMSE between the simulated and experimental values of temperature and relative humidity for different simulation approaches

Simulation approach	Air zone temperature		Air zone Relative Humidity	
	Data source compare	RMSE	Data source compare	RMSE
Thermal simulation with TRNSYS	Exp – num	2.31	Exp – num	6.37
Hygrothermal simulation [Coupling TRNSYS & ANN (AI)]	Exp – num	1.43	Exp – num	3.41
Hygrothermal simulation [Coupling TRNSYS & LSTM (AI)]	Exp – num	0.67	Exp – num	1.15

For the purpose of training deep learning models, we accomplished this by utilizing the sorption curve data as the only hygrothermal property (aside from the weather data and physical thermal properties of materials). The numerical outcomes for temperature and relative humidity are much improved than those obtained for the traditional thermal simulation, as shown in **Figure 4.16** and **Figure 4.17**.

4.6 Energy performance of studied earthen construction building

4.6.1 Needs for air conditioning

The basic treatments performed to the surrounding air are heating and cooling. The objective is to get an acceptable temperature in wintertime and a temperature reduction of barely relative to the outside environment in summertime. In this context, it is crucial to comprehend the energy performance of earthen construction buildings and their potential for decreasing the demand for energy. The summer air treatment provides a cooling sensation. Only the air temperature variation is considered. There is no control over the humidity. This might occasionally result in a sense of discomfort if it is neglected throughout the computations.

The energy efficiency of buildings made of earthen construction has been examined in this section, and the findings indicate that these structures provide a reasonable compromise in terms of energy consumption. Every sector (housing, educational institutions, and business) can employ heating and cooling systems. The comfort air conditioning or comfort heating aggregates all of the treatments used with ambient air to create an interior atmosphere which gives a feelings of comfortable in terms of humidity and temperature. Its goal is to create conditions that are

beneficial to the residents' quality of life, health, and wellness throughout the whole year. Therefore, energy performance is a principal factor in deciding the requirement for air conditioning.

- **Air conditioning processes**

The term "air conditioning" refers to any processes used on ambient air to produce specific temperature and humidity levels relevant to particular activities. Its purpose is to provide accurate, consistent, and dependable results throughout the year, ensuring optimum thermal and hydric comfort in the locale. It is crucial to understand the requirements for air conditioning. The factors considered to maintain excellent thermal comfort vary depending on the sort of activities, air quality (impurities, scents), humidity, significant inside loads (sensitive, latent), etc.

In general, maintaining these characteristics comes with more or less rigorous criteria for the accuracy of the result, the coherence of the performance in time and space, or the stability in the change of the dynamic outputs, as well as for its overall outcome quality.

4.6.2 Basic method for estimating the cooling loads

The cooling load estimation technique is widely used in many benchmark studies to rapidly estimate energy requirements. This approach is frequently used to calculate the amount of cooling required for a structure or an area, considering variables as outdoor temperatures. For the purpose of sizing HVAC equipment, the mentioned approach is recognized as a comparatively practical estimation of the total heat gains via a building envelope. However, it should be highlighted that the technique's accuracy can differ based on a number of variables, including the orientation of the structure and materials used for building. Determining cooling loads for a building in static mode can be done far more rapidly and effectively by using the last option. This technique is developed as a more straightforward computation alternative to complex and challenging calculation techniques such the transfer function approach.

When utilizing the upcoming calculation procedure, the following factors should be taken into account.

- Orientation of the studied zones or areas.
- The location of the place to be subjected in reference to.
 - Shades are provided by the nearby buildings.
 - Reflective surface, such as sky-scrapers, sandy lands or water lakes.
 - Locational information (latitude, longitude), directions and regional climate or weather.
- Building designs with specifics illustrating of the building's interior structure.
- Measurements of zones/spaces: size, depth, and height below the level of the roof.

- Building components: sort of material and the thickness of all partitions.
 - Panels colors, particularly the color of the roof and walls.
 - Building's outside factors include the temperature of the unconditioned areas, whether the floor is on the ground grade or a basement, and the amount of sunlight entering the space.
 - Windows' sizes and positions, metal or wood frames, glass type, and the sort and measurement of blinds.
 - Location, style, dimensions, and opening frequency of doors.
 - Amount of people using the space, their activities, and how long they have been using it.
 - Overall consumption of the various electrical equipment.
- **Heat gains by transmission through walls and windows**

The static heat transfer technique is a basic and well-known method for calculating the quantity of heat that traverses through a wall by estimating the heat transfer coefficient, denoted as "U coefficient," which allows one to quantify the heat loads of the various walls of the building under consideration. Due to its simplicity and dependability, despite its drawbacks, this technique is still frequently utilized in the engineering and construction sectors.

Table 4.6 Convective exchange coefficient considered for different situations [194]

Wall inclination	Convection coefficient	
	h_{in} (W m ⁻² K ⁻¹)	h_{out} (W m ⁻² K ⁻¹)
Vertical	8	25
Horizontal (up)	10	25
Horizontal (down)	6	25

More specifically, this coefficient represents the amount of heat that can move through a wall, or more particularly, the ability of the wall to allow heat to pass through. Designers and building engineers must appropriately size cooling/heating systems as well as develop energy-efficient insulating solutions.

$$Q_{tr} = U A \Delta T \tag{4.30}$$

$$U = \frac{1}{\frac{1}{h_{in}} + \sum_{i=0}^n \frac{e_i}{\lambda_i} + \frac{1}{h_{out}}} \tag{4.31}$$

Where U is the overall heat transfer coefficient (W m⁻² K⁻¹), A is the surface area (m²), ΔT is the cooling load temperature difference between the outdoor and the indoor climate (K), h_{in} and h_{out} are the indoor and outdoor convective exchange coefficient (W m⁻² K⁻¹), respectively, e is the thickness of the wall (m) and λ is the thermal conductivity of the wall (W m⁻¹ K⁻¹).

Table 4.7 Thermal load by transmission through walls and windows

Façade	U (W m ⁻² K ⁻¹)	S (m ²)	ΔT (K)	φ (W)
Wall (S-E)	1.23	0.27	18	5.9778
Wall (S-W)	1.23	0.26	18	5.7564
Wall (N-E)	1.23	0.26	18	5.7564
Wall (N-W)	1.23	0.27	18	5.9778
Roof	0.16	0.36	18	1.0368
Floor	0.08	0.36	0	0
Window (S-E)	2.7	0.06	18	2.916
Total (W)				27.4212

- **Solar heat gains through walls and windows**

A part of the solar radiation that hits a glass surface is transferred, part of it is absorbed, and some of it is reflected. Depending on the temperature differential, the received component raises the ambient temperature, and the heat is then gently transferred inside. As a result, a building's windows' glass selection is a significant factor in determining its overall building sustainability and level of energy efficiency. In comparison to the transmitted and reflected elements, the absorbed part of solar radiation is quite insignificant in comparison to thick and dense walls.

$$Q_{\text{rad_wall}} = \alpha F A R_s \quad 4.32$$

A is the surface area (m²), R_s is the amount of solar radiation absorbed on the wall surface (W m⁻²) and determined from **Table 4.12**, α is the absorption coefficient of the wall taking in the radiation. F is the solar radiation factor (**Table 4.8**), which shows the amount of heat captured by the surfaces and transmitted into the zone through the walls.

Table 4.8 Solar radiation factor "F" [195]

Thermal transmittance of the considered wall U (W m ⁻² K ⁻¹)	Solar radiation coefficient "F"
0	0
1	0.05
2	0.1
3	0.15
4	0.20

$$Q_{\text{rad_window}} = \alpha d_f A R_w \quad 4.33$$

Where α is the absorption coefficient of the wall receiving the radiation, d_f is the deduction factor ratio based on the nature of solar shading that covers the window, A is the surface area of window (m^2) and R_w is the solar radiation incident on the window surface in W m^{-2} and determined from **Table 4.12**.

Table 4.9 Absorption coefficient for walls, roofs and windows “ α ” [195]

	Colors and nature of the surface	“ α ”
Very light surfaces	White stone, white surface, clear or noticeably clear cement cream	0.4
Dark surfaces	Fibrocement, unpainted wood, brown stone, red brick, dark cement, red, green or grey staff	0.7
Very dark surfaces	Dark slate roofs - Very dark bitumen boards	0.9
	Single glazing	1
Glass (windows or skylights)	Double glazing	0.9
	Triple glazing	0.8

A key factor in assessing a building energy use is the absorption coefficient for construction elements such walls, roofs, and windows. Because the absorption coefficient impacts the amount that solar radiation is absorbed by the building envelope, knowing it and making a reasonable choice can assist architects and engineers in designing structures that are energy-efficient.

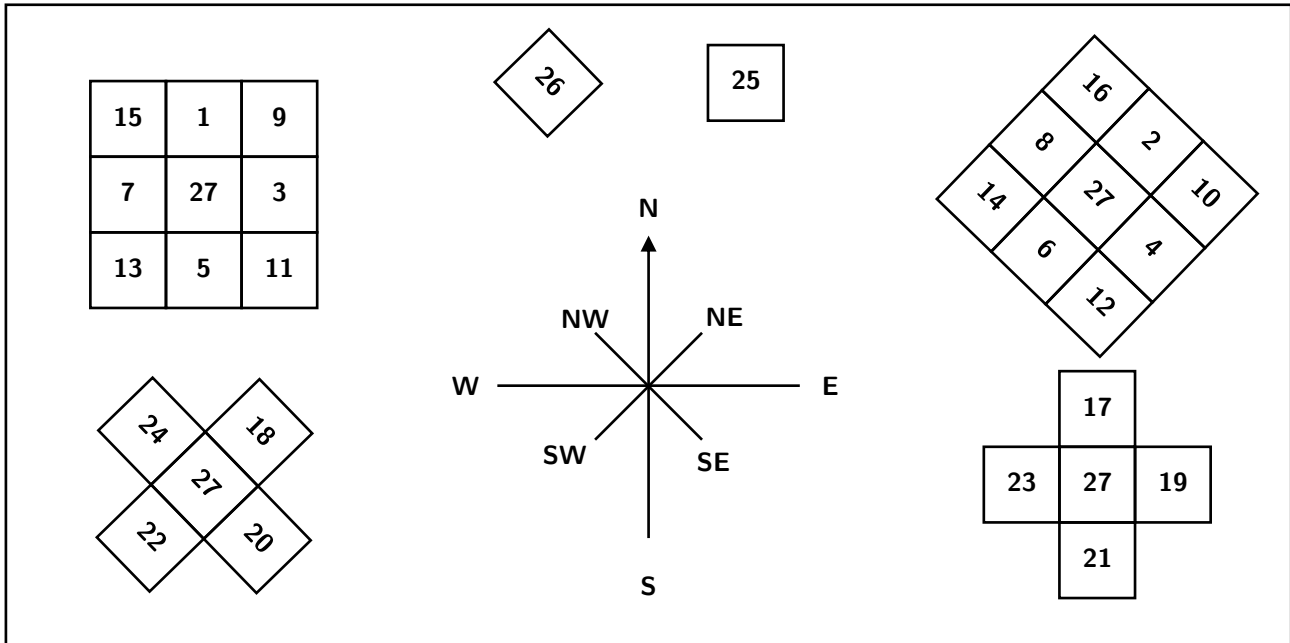
Table 4.10 Deduction factor for protected windows “ d_f ” [195]

Protected window	Colors	d_f
Exterior fabric blinds	Cream	0.28
Exterior fabric blinds	Aluminum	0.22
Interior blinds fully lowered	Aluminum	0.45
Interior blinds half lowered	White or Cream	0.63
Louvers fully lowered inside windows	Aluminum	0.58
Louvers fully lowered outside windows	Aluminum	0.22

The solar radiation absorbed deduction factor (**Table 4.10**) for covered windows refers to the decrease in solar energy that can pass through a window as a result of the existence of shade. This element is crucial for determining the solar heat intake via windows and making sure that building air conditioning systems are sized enough to control thermal comfort levels.

The solar radiation is influenced by the latitude at which the space is located, the exposure of the surfaces, the hour of the day during which the estimation is made, and other factors. The orientation data in **Table 4.11** are used to calculate the hour of highest solar gain. **Table 4.12** provides the amount of solar radiation absorbed by walls and windows, R_s & R_w ($W\ m^{-2}$), as function of latitude, orientation, and solar hour (already determined from **Table 4.11**).

Table 4.11 Hours of maximum cooling requirements in spaces with different orientations ([195] doc. AirWell)



Building orientation	Number of walls exposed	Exposed walls orientation	Hours			
			Protected window		Bare window	
			a	b	a	b
1		N	-	-	14	14
2		NE	-	-	14	14
3		E	12	12	9	9
4	1	SE	13	13	10	10
5		S	14	13	13	13
6		SW	15	14	16	15
7		W	15	15	16	16
8		NW	16	15	17	16
9	2	NE N and E	14	14	9	9
10		NE-SE	14	13	9	9

11		SE S and E	14	13	10	10
12		SE-SW	15	14	15	15
13	2	SW S and W	15	14	15	15
14		SW-NW	15	15	16	16
15		W-N	15	15	16	16
16		NW-NE	16	15	17	17
17		W-N-E	16	15	16	16
18		NW-NE-SE	15	15	16	16
19		N-E-S	14	14	10	10
20	3	NE-SE-SW	15	14	15	15
21		E-S-W	15	14	15	15
22		SE-SW-NW	15	15	16	16
23		S-W-N	15	15	16	16
24		SW-NW-NE	16	15	16	16
25	4	S-W-N-E	15	14	15	15
26		SW-NW-NE-SE	15	14	16	16
27	None	-	-	-	14	14

*a. Building with protected window

*b. Building with unprotected window

Table 4.12 Solar radiation for latitude 50 of Caen city ([195] doc. AirWell)

Latitude 50											
 	NE		E		SE		S		H		Hour
	Wall	Window									
6	280	240	315	280	175	135			95	50	18
7	405	340	555	485	375	315			255	185	17
8	370	285	640	550	525	445	110	35	440	360	16
9	230	120	575	480	580	485	250	150	590	500	15
10	35	6	430	330	570	470	370	265	720	620	14
11			225	110	475	370	440	335	790	685	13
12					330	225	470	365	810	710	12
Hour	Wall	Window	 								
	NW		W		SW		S		H		

Table 4.13 Thermal load from solar radiation on walls and windows

Façade	α	d_f "or" F	S (m ²)	Irr (W m ⁻²)	ϕ (W)
Wall (S-E)	0.7	0.064	0.163	525	3.83376
Wall (S-W)	0.7	0.064	0.154	525	3.62208
Wall (N-E)	0.7	0.064	0.154	0	0
Wall (N-W)	0.7	0.064	0.163	0	0
Roof	0.7	0.01	0.13	440	0.4004
Window (S-E)	0.9	1	0.06	445	24.03
Total (W)					31.88624

- **Thermal load by air ventilation**

Ventilation is the process of introducing air movement into a closed environment. It is used in areas where there is a chance that there will not be enough oxygen because of activity, people, or areas where unwelcome elements like moisture saturation might build up in the absence of air movement in the enclosure. Thus, the term "ventilation" is frequently used to describe the deliberate conveyance of outdoor air into a building's interior area. It serves as one of the most essential elements in maintaining buildings' appropriate levels of indoor air quality. Mechanical/forced and natural ventilation techniques can be used to ventilate a building.

However, it is crucial to consider the heat loads that are introduced into the space during the continuous exchange of air with the outdoor environment. The aforementioned indoor comfort conditions ($T_{indoor} = 20^{\circ}\text{C}$ and $RH_{indoor} = 60\%$), are considered as suitable parameters and are derived from the Givoni bioclimatic chart for adequate thermal comfort. These conditions are used for the pre-sizing of the ideal HVAC system, which will then be used to calculate the dynamic heat load based on the outputs of different calculation methods (BES, BES+AI...). The external climate conditions ($T_{outdoor} = 38^{\circ}\text{C}$ and $RH_{outdoor} = 85\%$), are selected based on the most unfavorable outdoor climate during the measurement period to ensure that the energy system can operate optimally.

$$\text{Sensible} \quad Q_{air_s} = 0.34 \quad Q_v \quad \Delta T \quad (\text{W}) \quad \mathbf{4.34}$$

$$\text{Latent} \quad Q_{air_L} = 0.84 \quad Q_v \quad \Delta T \quad (\text{W}) \quad \mathbf{4.35}$$

$$\text{Total} \quad Q_{air_total} = W_{air} \quad Q_v \quad \Delta H \quad (\text{W}) \quad \mathbf{4.36}$$

W_{air} is the mean specific volume of air (m³ kg_{da}⁻¹), Q_v is the air flow rate of renewal air (m³ h⁻¹), ΔT is the temperature difference between indoor and outdoor conditions (°C), and ΔH is the

air enthalpy difference between indoor and outdoor conditions ($\text{KJ Kg}_{\text{da}}^{-1}$).

Table 4.14 Thermal load due to air renewal

	Q_v ($\text{m}^3 \text{ h}^{-1}$)	Mean specific volume ($\text{m}^3 \text{ kg}_{\text{da}}^{-1}$)	ΔT (K)	Δrv ($\text{g}_{\text{water}}/\text{kg}_{\text{da}}$)	ϕ (W)
Sensible	0.0285	0.9	18	0	0.174
Latent	0.0285	0.9	0	24.9	0.596
*da refers to dry-air				Total (W)	0.770
	Q_v ($\text{m}^3 \text{ h}^{-1}$)	Specific volume ($\text{m}^3 \text{ kg}_{\text{as}}^{-1}$)	Moist air enthalpy h_{out} ($\text{KJ Kg}_{\text{da}}^{-1}$)	Moist air enthalpy h_{in} ($\text{KJ Kg}_{\text{da}}^{-1}$)	ϕ (W)
Or (total)	0.0285	0.9	125800	41800	0.739

- **Thermal load due to thermal bridges**

Thermal bridges are referred to as particular areas with increased thermal conductivity compared to the surrounding surface. A usual thermal bridge in a building enclosure would be where a material with significant conductivity, such as structural connection or steel studs that penetrates the insulation layer. A building assembly with a thermal bridge would have a higher heat transfer rate through the structure as well as a warmer surface temperature on the cold side of the wall. As a result, thermal bridges can be a significant source of energy loss in zones and buildings, which has a negative impact on their energy efficiency.

$$Q_{br} = \Psi L \Delta T \quad \mathbf{4.37}$$

Where Ψ is the coefficient of linear thermal loss ($\text{W m}^{-1} \text{ K}^{-1}$) and L is the length of the defined bridges (m) and ΔT is the temperature difference between indoor and outdoor conditions ($^{\circ}\text{C}$).

Table 4.15 Thermal load due to thermal bridges

Façade	Ψ ($\text{W m}^{-1} \text{ K}^{-1}$)	L (m)	ϕ (w)
Wall	0.15	1.76	4,752
Floor	0.33	1.44	8,5536
Roof	0.05	1.44	1,296
Total (W)			14,6016

4.6.3 Ideal Air-Conditioner system pre-sizing (basic simplified method)

- **Comfort temperature and relative humidity setpoints**

The relative humidity setpoint and comfort temperature parameters are crucial variables for

preserving a comfortable indoor climate. Relative humidity setpoints are the ideal ranges of moisture levels that help create a comfortable indoor environment. The comfort temperature is the range of temperatures at which most people feel comfortable without feeling dissatisfied due to their body temperature. These parameters were established based on research into the actual climate conducted during an experimental campaign of measures, as well as consideration of the Givoni bioclimatic chart [196] of hygrothermal comfort.

Table 4.16 Indoor hygrothermal comfort setpoint conditions

Givoni bioclimatic chart	Indoor relative humidity is set at.	65 %
	Indoor temperature is set at.	20°C

- **Ideal HVAC system pre-sizing**

Identifying the contributions of indoor and outdoor temperatures and humidity levels is essential for sizing an air-conditioning system. These values are influenced by the climate and location of the building that needs conditioning. We can define the temperatures and humidity levels in the current scenario using the meteorological data that has already been collected. The maximum amount of energy needed to condition our space can be determined using these data. The type of space affects the inside temperature and hygrometry. In our case, we have relied on Givoni's chart to determine the ideal level of comfort for our specific situation and to examine the energy efficiency more thoroughly for summertime temperatures. When investigating an air conditioning project, it becomes essential to look into the loads that the air conditioning unit will be subjected to over time in order to appropriately control it. The "sensitive" and "latent" loads must be considered in all cases.

Table 4.17 Air-conditioning air blowing characteristics

Supply air characteristics		
ΔT	$T_{\text{blowing}} (\text{°C})$	RH_{blowing}
6	14	60 %
Cooling coil characteristics	Efficiency	Power (w)
	Ideal system = 1	74.68
Air flow rate through cooling coil ($\text{kg}_{\text{as}} \text{s}^{-1}$)		$0.772285 \cdot 10^{-3}$

The mass flow of dry air at the outlet of air conditioning system and the temperature difference between the space and the outside must be known in order to identify the requirements for an air supply. These coordinates can be obtained by transferring them onto a psychometric diagram

or by using a set of equations to calculate values as enthalpy and water content, for example. To maintain the best possible interior air quality and comfort, this information is essential for planning and managing air conditioning systems in buildings. The energy balance that was already estimated in the previous section can be used for estimating the power of the coils and the volume of coolant that goes through them. Then, it allows us to make the assumption that this dry air flow is always constant and capable of delivering the full power required when necessary; as a consequence, this capacity can alter in response to variations in the interior temperature. It is simpler to estimate our energy needs if we assume that our air conditioning system is ideal.

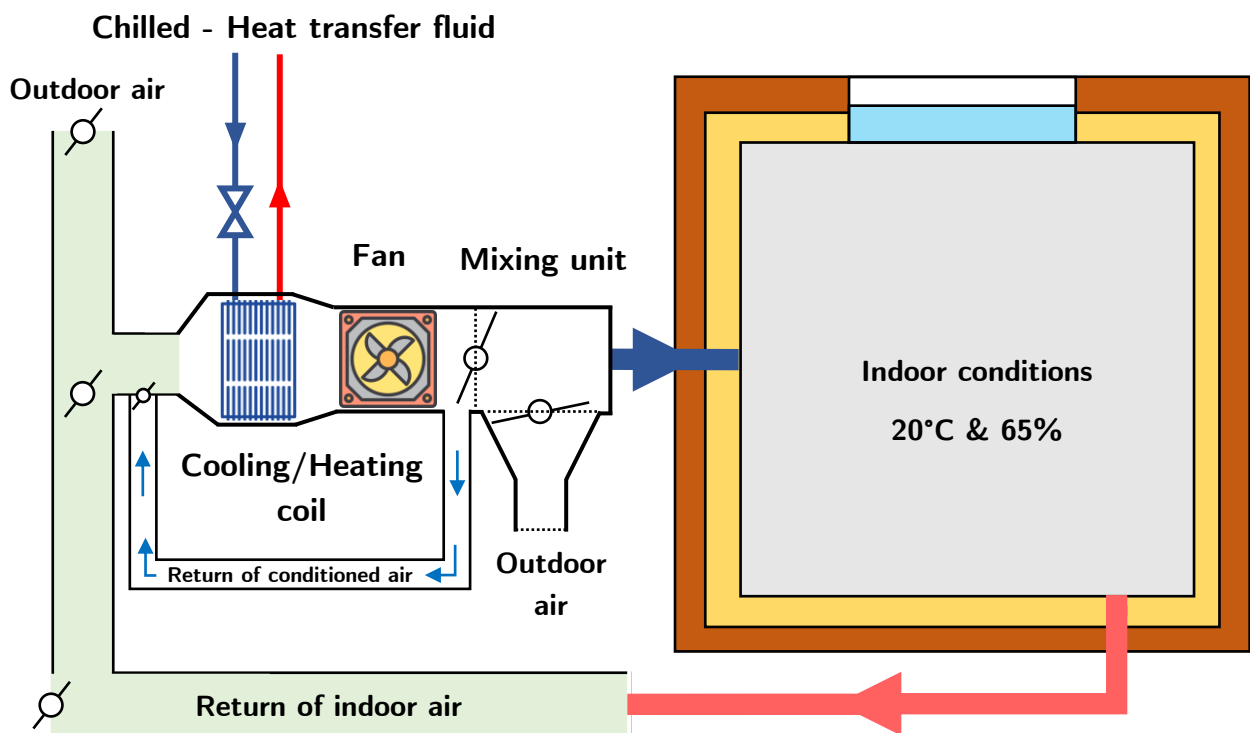


Figure 4.18 Schematic of an ideal air conditioning system simplified for our case study

4.6.4 Energy performance of our building based on the outputs of different dynamic simulation approaches

Utilizing computer-based simulation tools to conduct a thorough examination of a zones energy consumption and energy-using systems is a modern process of investigating the energy performance of a building. An approximate depiction of the building is presented by the simulation program through the use of a mathematical model. As part of the free evolution of internal conditions used in building energy simulation methods, detailed component analysis and whole-building modeling are conducted using specialized software tools that address issues like heat transfer through building materials, daylighting, indoor air quality, natural ventilation, and occupant comfort. An alternate strategy is provided by BES-AI, which promotes integrated,

adapted design solutions that provide greater cost reductions. It is strongly advised to examine the energy-efficiency possibilities of design choices before construction begins in order to maximize building energy performance or to investigate further retrofit prospects. Following the successful validation of our fundamental BES model coupled with AI, we expanded the scope of our investigation in this scenario. We had to improve upon our investigation in this instance. We want to determine the amount of energy required to maintain the proper level of comfort in the analyzed building following the validation of our fundamental BES model in conjunction with artificial intelligence. We intend to find out the amount of energy is required to keep the building under investigation comfortable. To do this, we'll use a set of assumptions and an independent calculation method to analyze the energy efficiency of different outcomes from various approaches, like the traditional thermal simulation on TRNSYS and a novel technique combined with artificial intelligence to convert the traditional outputs into hygrothermal data.

The equations used to calculate the air enthalpies at various locations in **Figure 4.18** are shown in the next section. In order to determine the hourly and daily energy requirements during the length of the measurement period, several dynamic outputs of various modeling methodologies have been employed.

- **Estimation of specific enthalpy of moist air**

We may express the specific enthalpy of moist air as.

$$h = h_a + w h_w \quad 4.38$$

Where, h is the specific enthalpy of moist air (kJ kg^{-1}), h_a is the specific enthalpy of dry air (kJ kg^{-1}), w is the humidity ratio ($\text{kg}_{\text{eau}} \text{kg}_{\text{as}}^{-1}$), h_w is the specific enthalpy of water vapor (kJ kg^{-1}).

$$h_w = c_{pw}T + h_{we} \quad 4.39$$

T is the water vapor temperature ($^{\circ}\text{C}$), c_{pw} is the specific heat of water vapor at constant pressure ($= 1.86 \text{ kJ kg}^{-1} \text{ K}^{-1}$), h_{we} is the evaporation heat of water at 0°C ($= 2501 \text{ kJ kg}^{-1}$)

The equation **4.38** can be written as follows.

$$h = c_{pa}T + w [c_{pw}T + h_{we}] = 1.006 T + w (1.86 T + 2501) \quad 4.40$$

- **Rankine formula**

In comparison to the thermodynamic tables, the Rankine formula, an improved version of the Dupré equation, provides values for the saturation vapor pressure of water with little varied coefficients (deviation of 0.5 % to 4 % throughout the range of the temperature of 5 to 140°C).

$$P_{sat} = e^{\left(13.7 - \frac{5120}{273.15 + T}\right)} \quad 4.41$$

Where, T is the air temperature in °C and P_{sat} expressed in bar.

- **Specific humidity w**

$$w = 0.6217 \frac{RH p_{sat}(T)}{p_{atm}(T) - 0.3783 RH p_{atm}(T)} \quad 4.42$$

RH is the relative humidity (0-1), p_{sat} is the saturation pressure of water vapor (Pa), p_{atm} is the atmospheric pressure (Pa) and w expressed in ($\text{kg}_{\text{water}} \text{kg}_{\text{dry-air}}^{-1}$).

The **Figure 4.19** and **Figure 4.20** are meant to provide a detailed examination of the diverse outcome results of energy demands obtained by various methodologies. Through the presentation of numerous graphs, the inquiry aims to give a thorough understanding of the energy requirements resulting from different approaches. The graphs also seek to improve comprehension of the relative performance levels of each strategy, which can assist in decision-making about energy production and distribution. The experimental data of temperature, relative humidity, and cooling energy needs can be used as a reference to compare other numerical results to those discussed in greater detail throughout this work. Information on peak load events, zone cooling, and system air flow sizing are all included in the air conditioning pre-sizing analysis findings. Additionally, academics and building engineers who are interested in learning more about energy-efficient methods and approaches will benefit from the offered data and analyses.

We computed the user-specified design load, airflow, and cooling energy values, which are displayed in the graphs (**Figure 4.19** and **Figure 4.20**) together with the peak temperature time and the sizing periods. The explanation of the experimental variation and the numerical outcomes offer pertinent data that can be used as a standard for evaluating different strategies for managing energy.

Additionally, the hourly energy consumption of the experimental variation and the numerical findings offer insightful information about the patterns of energy demands in building systems. Overall, these graphs are a useful tool for examining and contrasting the energy requirements generated by various methods. The solar radiation load and outside temperature, which are at their highest during this time period, could be potentially employed to clarify why the hourly energy demand in our case study occurs every day between 13 h and 20 h. The overall demand for energy can be minimized by employing this information to develop efficient energy management strategies and put in place energy-saving practices during these peak hours.

Energy performance of studied earthen construction building

Energy performance of our building based on the outputs of different dynamic simulation approaches

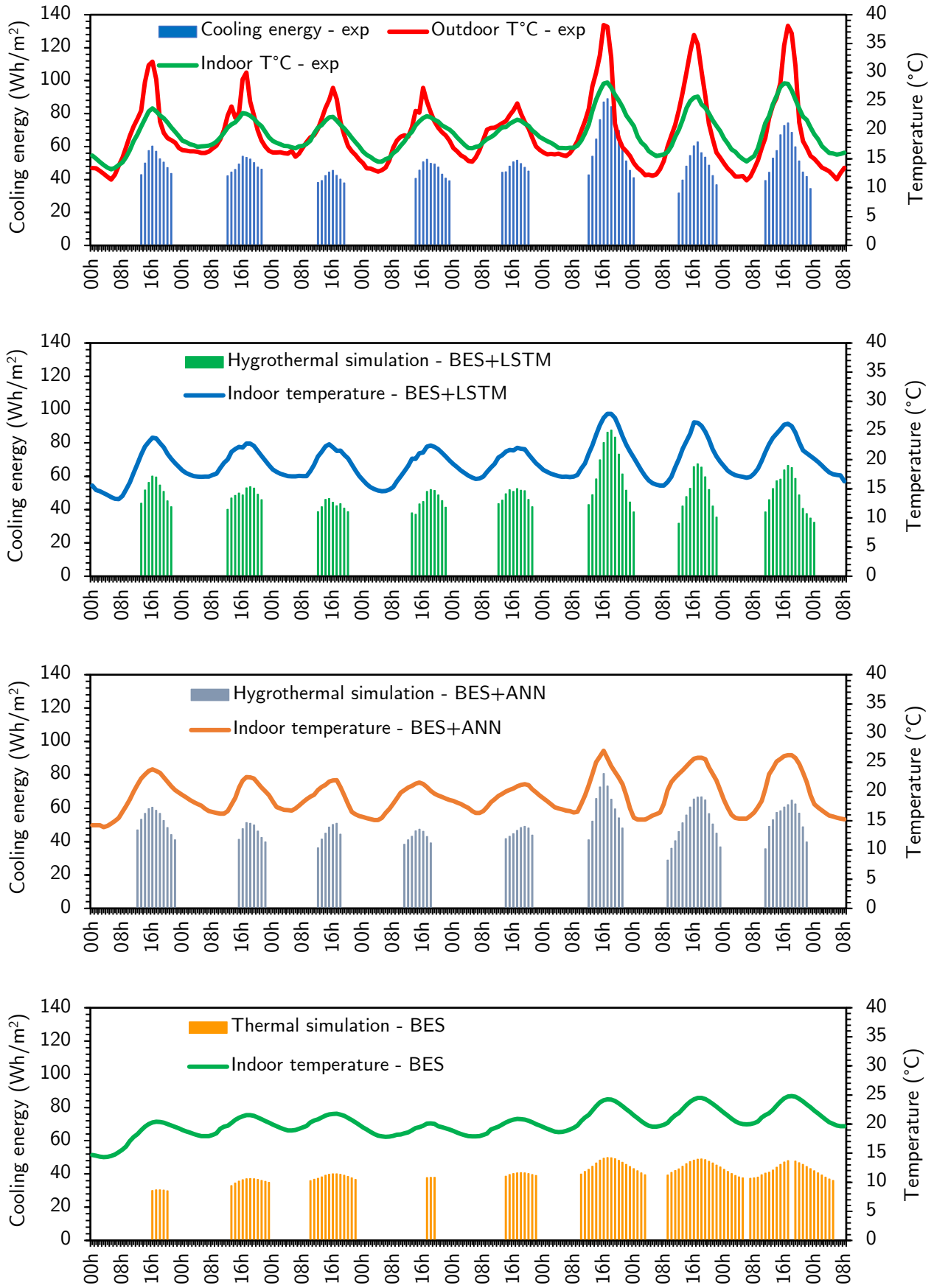


Figure 4.19 Hourly energy needs for cooling and dehumidification (06 - 13 June 2022)

According to European standards, we can presume that our earthen structure is categorized in class B for daily energy consumption (but only during the four months of the summer season). Therefore, we can conclude from the **Figure 4.20** that the new coupling method (BES-AI) provides better results for energy estimation than the conventional simulation method, which only considers thermal conduction through walls and ignores mass diffusion in porous media.

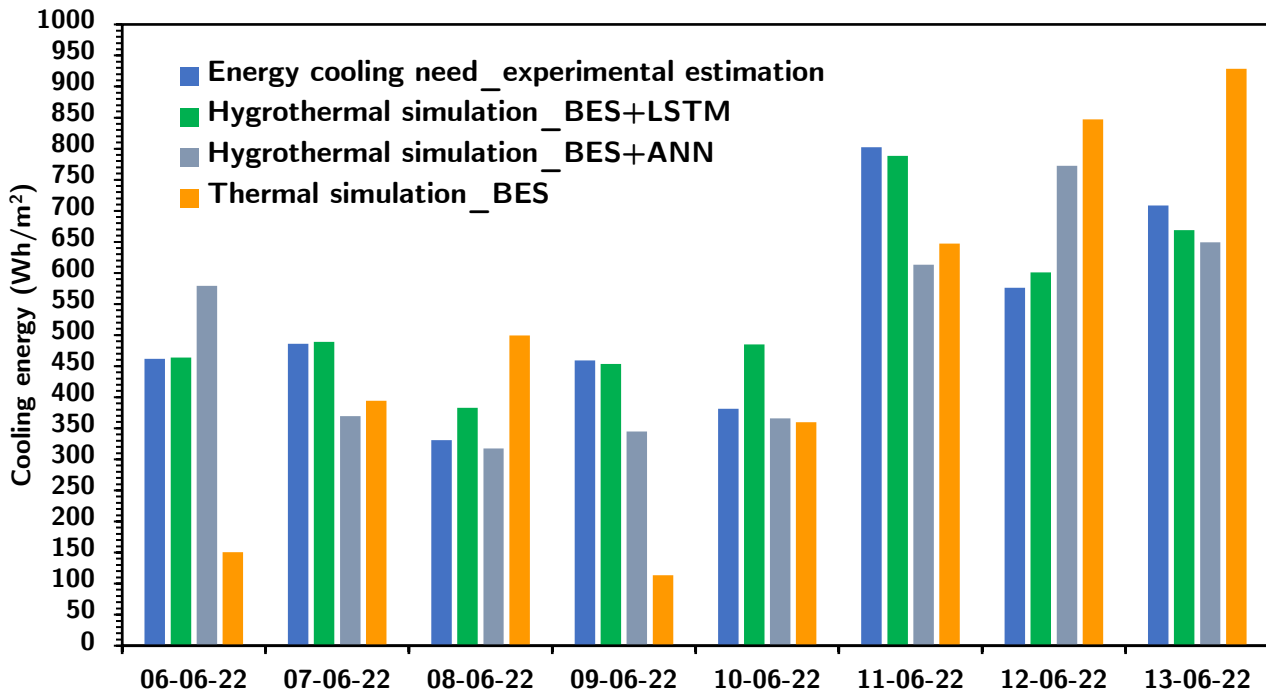


Figure 4.20 Daily energy needs for cooling and dehumidification (06 - 13 June 2022)

In terms of precisely forecasting building hygrothermal behavior and energy requirements, the AI-BES co-simulation approach has demonstrated encouraging results. The daily energy requirements for cooling were determined to have a mean relative error of less than 8 % (**Table 4.18**), which serves as proof of this. Compared to the conventional thermal simulation, which might over- or underestimate the daily energy need by 40 %. The assessment of the AI-BES co-simulation approach against numerical and experimental data demonstrated its accuracy in calculating the hygrothermal activity of buildings and their energy consumption.

Mean Relative Error of daily energy needs

Simulation approach	Data source compare	MRE %
Standard thermal simulation BES	Exp – num	39.45
Hygrothermal simulation [Coupling BES & ANN (AI)]	Exp – num	18.54
Hygrothermal simulation [Coupling BES & LSTM (AI)]	Exp – num	7.12

Table 4.18 Mean Relative Error of daily energy needs (06 – 13 June 2022)

4.7 Application of the novel co-simulation technique to a real building

4.7.1 Pre-processing and DATA gathering

Low-carbon construction materials are often produced using resources derived from bio-based sources or straw/rammed earth. The storage of carbon emissions and the sustainable use of natural resources are considerably aided by these mixes, which can be conceived of as massive volumes of low-carbon constituents and industrial organic material [32]. Industries and government organizations with appropriate responsibilities strongly recommend their use in newly built and renovated buildings and structures. As a result, a specific class of building materials that utilize natural fibers [33], and develop enormous porosities to significantly lower their heat conductivity have been developed for the construction sector in recent decades. A structural section and an upper layer of insulation make up the building's general structure. These walls' basic construction materials include soil, sand, straw, and date palm wood, each in a different proportion to satisfy requirements for construction. The following material qualities were evaluated and listed in **Table 4.19**.

Table 4.19 Thermal properties on dry materials of the Ouled Ammar earth-building structural walls

Properties	Structural Cob	Reference	Date palm wood	Reference
Density (kg m^{-3})	1384	65], [168]	254	[197]
Thermal conductivity ($\text{W m}^{-1} \text{k}^{-1}$)	0.45	[1]	0.046	[197]
Specific heat capacity ($\text{J kg}^{-1} \text{k}^{-1}$)	865	[165]	1442	[198]

The moisture adsorption profiles for the structural cob walls show type II isothermal behavior, which is typical of porous construction materials and is also seen in regular cob/clay construction application [153]. This specific curve is often used in full hygrothermal simulation study, shows how water content varies when hygroscopic materials are exposed to a strong humidity gradient. The porosity of walls, which has a big influence on how water molecules interact inside the micropores, is only one of several variables that may be utilized to interpret it.

Table 4.20 Properties of construction types of the earthen building at Ouled Ammar region

	Windows	Door	Wall
U-value ($\text{W m}^{-2} \text{K}^{-1}$)	1.1	0.79	0.63
Convective heat transfer coefficient (Inside) ($\text{W m}^{-2} \text{K}^{-1}$)	3	4	5
Convective heat transfer coefficient (Outside) ($\text{W m}^{-2} \text{K}^{-1}$)	18	16	17
Solar absorptance	0.6	0.5	0.5
Emissivity	0.9	0.9	0.9
Glazing Type	Simple	Opaque	Opaque

In our new computational method, these parameters are not anymore necessary to simulate the hygrothermal behavior. We would only need the sorption curve of earthen structural walls. We have counted on the study of Bouasria [1] to obtain the hygrothermal properties of walls made basically from earth and other building properties are illustrated in **Table 4.20**.

Subsequently is always advisable to rely on experimental studies to determine a wall's specific characteristics because it can be difficult to fully comprehend all the various physical phenomena. Furthermore, it is evident that the sorption behavior tends to gather more moisture close to the wall's border. This is made clear by the permeability of porous materials, which have a high capacity to absorb water.

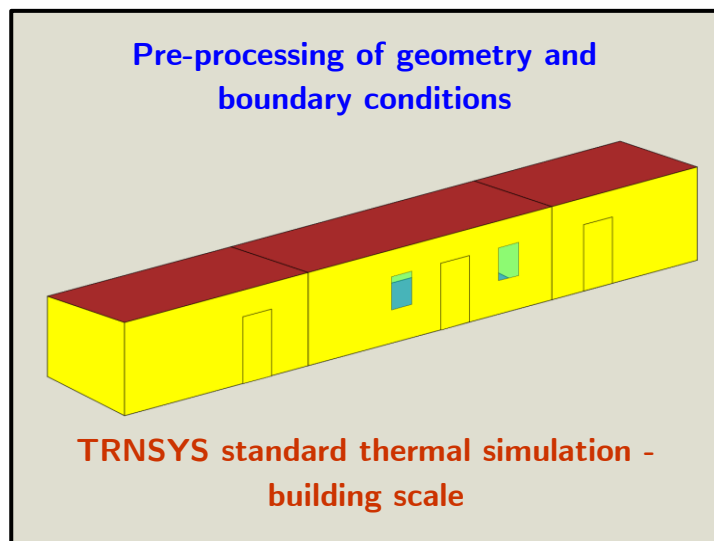
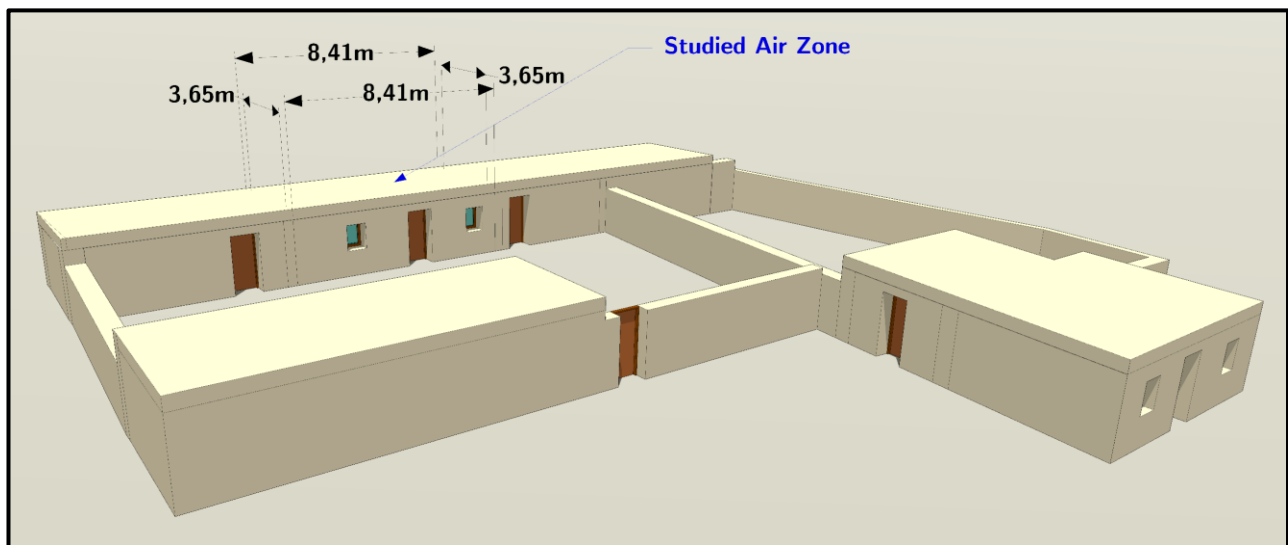


Figure 4.21 Basic structure of a real earth building and orientation of the spaces from different sights [199] (GPS - DMS 35°28'24.3"N 5°09'49.7"E || DD 35.4734028 , 5.1638)

We used a real-scaled earthen building from a Medjelekh PhD thesis [199] to imitate the hygrothermal behavior and to simulate the behavior of earthen construction more precisely. We relied on the real building structure that Medjelekh's [199] investigation study offered.

A 3D image satellite of the building's position, size of the conceptual design, orientation, and equipment has been generated using open access software **Figure 4.21**. Based on the gathered information, the weather conditions for the actual summertime scenario (**Figure 4.26**) were also taken from the same study [199].

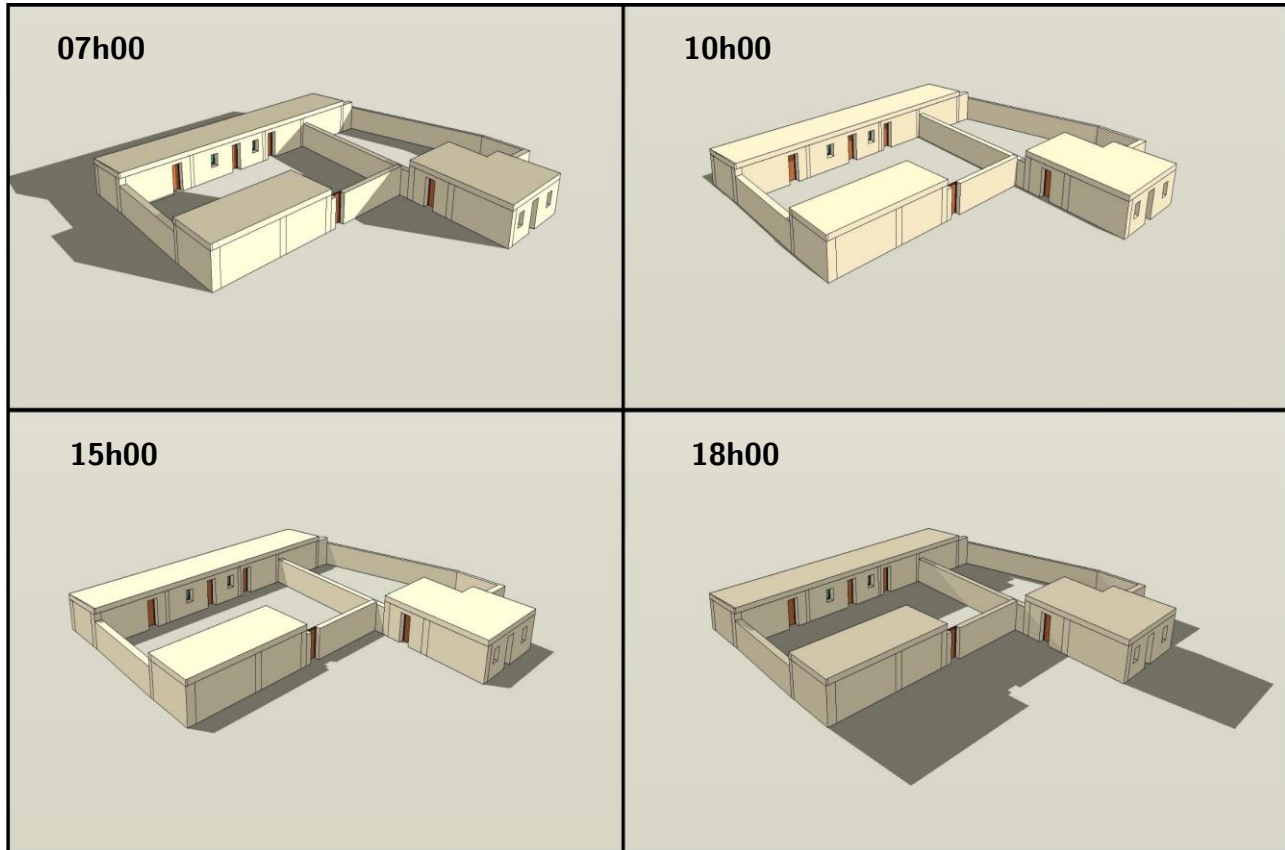


Figure 4.22 Shade profile during the whole day taking into account the actual conditions in relation to the building site [199] (Latitude 35.4734028 || Longitude 5.1638 || Time Zone UTC+01:00 || Altitude 451m || Month of July)

As a result, we were able to precisely simulate the hygrothermal behavior of the studied air zone using whole-building modeling software such as TRNSYS coupled with other co-simulation techniques. Our study aims to produce more realistic and trustworthy outputs about the hygrothermal responses of earthen buildings in real-world settings by using a real-case structure and proper meteorological data [199]. The results of this study have significant relevance for earthen structure design and construction, particularly in regions with a high prevalence of harsh climatic conditions. Additionally, this study emphasizes how crucial it is to take into account the different features and behaviors of clay materials in thermal models when developing sustainable structures. Furthermore, it has been shown that straw can improve the qualities of earthen building materials including thermal insulation and hygrothermal indoor comfort regulation.

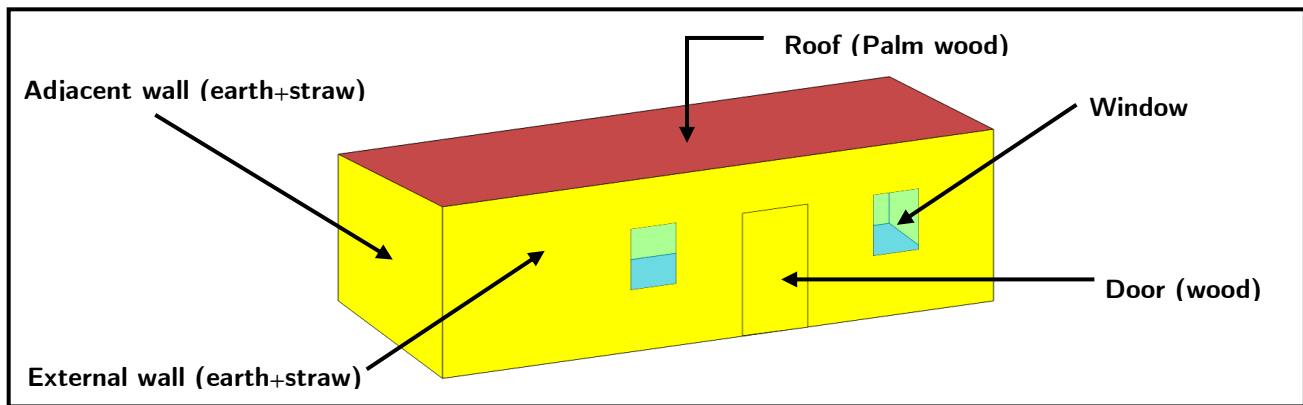


Figure 4.23 Boundary conditions of the simulated building [199]

In this research, the structure of experimental data [1], [165] serves as a testing and verification tool for the numerical technique. We will not get into specifics concerning the creation and description of the material properties. Another in-depth study is being conducted. This study's primary goal is to evaluate the effectiveness and dependability of the novel simulation technique by employing a real building assembly as a testing object. Through co-simulation, the study aims to show how well the numerical technique predicts the hygrothermal behavior of the building under varied loading circumstances.

4.7.2 Monitoring and analysis of building behavior

4.7.2.1 Instrumentation and locations

Instruments and sensor installations are placed in strategic positions to monitor and analyze the building's activities. For analyzing and getting accurate results, the sensor's placement is crucial. Time steps and duration are also significant. The warm and cold measurement periods for the building under investigation are shown in **Table 4.21**. It clearly identifies the start and finish of each measurement campaign interval while providing an excellent comprehensive overview.

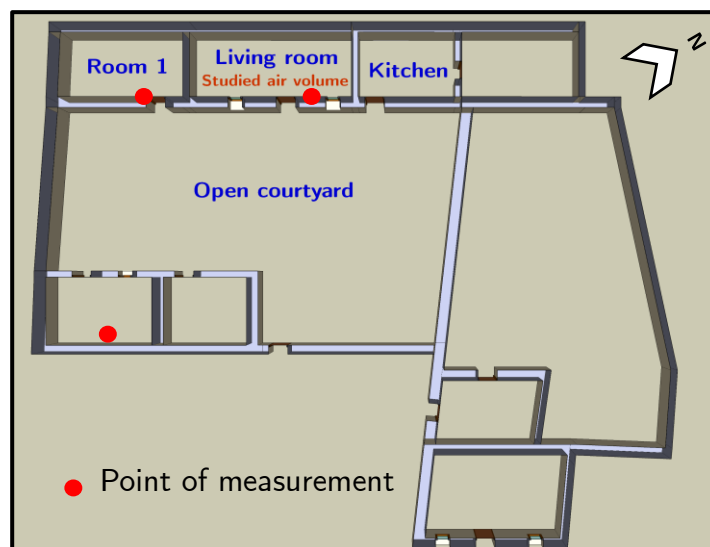
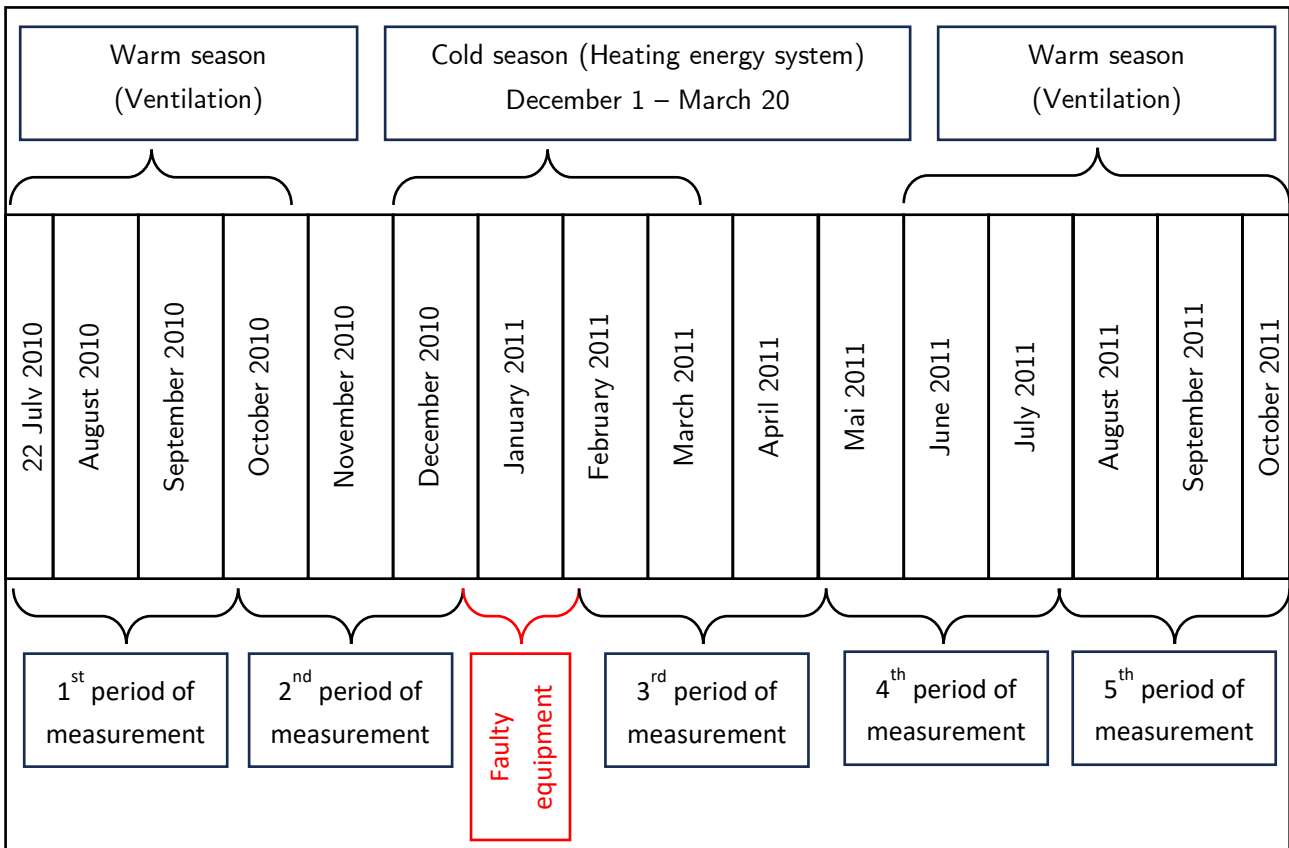


Figure 4.24 Measuring points of the building under investigation [199]

Over the course of 15 months, a number of monitoring tests were conducted in the domicile. Two "LogTags" devices of measurement were used to collect measurements of the temperature and relative humidity every 15 minutes in the living room and room 1, a pair of spaces that opened directly into the courtyard. To detect the external temperature and relative humidity, a third sensor was positioned underneath the south-east. façade's ceiling. **Figure 4.24** shows the study's data gathering setup as well as the monitoring sites.

Table 4.21 Experimental measurements of building behavior and temperature and relative humidity data acquisition [199]



4.7.2.2 Energy use and internal loads

Building behavior must be observed and analyzed to evaluate performance and make reasonable decisions about relative humidity and temperature regulation. It is essential to gather a significant quantity of data on the air zone under investigation before starting to analyze actual hygrothermal activity. As we can see from **Table 4.22**, which illustrates the type of air conditioning utilized to regulate indoor comfort throughout the cold and warm seasons.

Table 4.22 HVAC systems used for air conditioning [199]

Building type	Heating system	Cooling system
Earthen constuction	Fired heater (gas)	Natural ventilation

Table 4.23 displays the different equipment situated inside the investigated zone, which could have an impact on the energy balance within the building's space as well as the potential causes of moisture and temperature variations. Establishing decisions regarding the evolution of temperature and relative humidity need this kind of information to evaluate building performance.

Table 4.23 Various equipment located inside the studied zone of the building [199]

	Equipments	Number of items	Power (W)	Scenario
Living room	Television	2	130 W	4 h/day
	Decoder	1	20 W	4 h/day
	Hair dryer	1	2000 W	3 h/Week (Estimation)

The amount and sort of lights that have been placed in the studied air zone are shown in **Table 4.24**. They can affect the energy balance and temperature variations inside the structure, as well as contribute to heat gain during the colder months.

Table 4.24 Studied zone lighting scenario [199]

	Number and type of light bulbs used			
	Classic	Halogen	Economic	Fluorescent
Living room	3	0	0	0
Kitchen	0	0	0	1
Courtyard	1	0	0	0

In the air zone under consideration, the average number of residents and their daily routines are shown in **Table 4.25**. This data is critical for comprehending occupancy patterns and their effects on interior temperature and humidity levels. throughout a warm environment, the occupation is often active throughout the afternoon and overnight.

Table 4.25 Studied zone living scenario [199]

Building zone	Living room	
	Nombre of persons	Scenario
Earthern construction	4 persons	13h -> 16h 22h -> 7h

The airflow strategy to ventilate the home as shown in **Table 4.26** uses the opening of the windows. Understanding the situation is crucial. This knowledge sheds light on potential moisture and temperature sources, as well as how ventilation affects the temperature and humidity levels inside, which has a big influence on the interior climate.

Table 4.26 Windows opening and closing schedule - summer period [199]

Scenario	Windows	
	Opening time	Closing time
Earthern construction	18h -> 5h	5h -> 8h
	8h -> 10h	10h -> 18h

4.7.2.3 Experimental measurement data

The models presented in the current application of the novel co-simulation technique have been proven by contrasting the results with experimental data using several approaches. The experimental data evaluations from the Medjelekh [199] research were conducted. It was used to test the model on structures constructed with earth. In our case, the only additional parameter that needs to be investigated to validate the model is the sorption curve of the building walls. This parameter, along with other typical inputs, will be used later to provide training data to use artificial intelligence to convert the thermal behavior into hygrothermal data.

This is being done to see whether it can be utilized as a replacement for the meticulously developed physical model of coupled heat and mass transport across a porous material at the dimensions of a real building. The exterior walls of the entire building were subjected to the actual weather. First, it is assumed that the wall is 50% dry and consistently reaches room temperature. All initial and physical parameters employed in the computation are determined in accordance with experimental conditions established in Bouasria et al. [1] research. The sorption isotherms were determined for a temperature range of 23°C and an air relative humidity range of 0% to 95% using experimental data [168]. The simulation's radiation climate data (global and diffuse solar irradiations) were acquired from the free data source of the "EU photovoltaic geographical information system," while the temperature and relative humidity were measured through experimentation with sensors and extracted from Medjelekh's PhD study [199].

**Figure 4.25 Climatic environment of building location [199]**

Figure 4.26 shows the data that were captured during the last weeks of July in 2010, with an interval step of 60 minutes. We can properly infer from the graphs that the inside climate reflections cause alterations to the exterior with a temperature differential brought on by thermal inertia. These indoor data are eventually used to value the simulation's outcomes. The results show that the **Figure 4.25** accurately reflects the regional climate where the outside temperature fluctuates between 24 and 45 degrees Celsius.

The inside air temperature fluctuates between 27 °C and 35 °C. The temperature peak difference between the interior and exterior environments is 12 degrees. Moreover. In comparison to an external humidity range of 16 % to 50 %, the interior humidity varies from 32 % to 70 %.

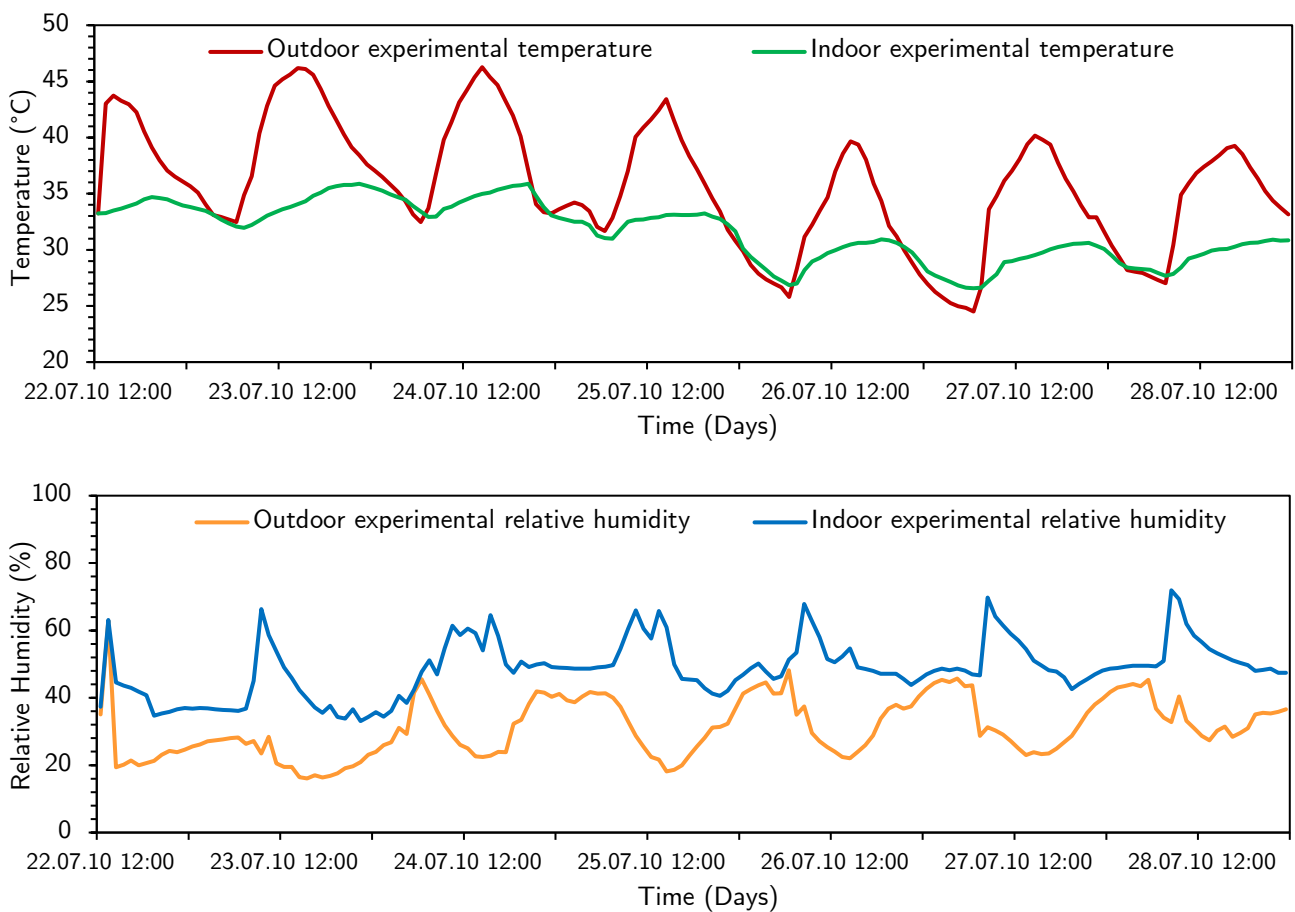


Figure 4.26 Indoor and outdoor real climate conditions of the building recorded in Ouled Ammar region of Algeria (July 2010) [199]

4.7.3 Outputs of the fundamental building energy simulation (BES)

The ability to identify a number of factors that affect a building's thermal performance is demonstrated in the preceding section. A low carbon and hygroscopic construction envelope that is primarily made of straw and soil has been modeled. For purposes of our current inquiry, we are particularly interested in the variations of the interior air temperature and relative humidity

of the building. Determining the outcomes of a conventional thermal simulation of a hygroscopic building envelope, then coupled with artificial intelligence, is thus the main objective of our research. Next, we created a unique computer technique that is very flexible, highly efficient, and requires fewer data inputs than the complete hygrothermal full scale method, making it suitable for use in academic research or engineering projects. **Figure 4.27** displays experimental data on temperature and relative humidity fluctuations inside the building air zone together with predictions from the typical thermal simulation. While we simply use the heat simulation and ignore the moisture buffering of the walls, the results are generally acceptable. However, it is insufficient for a trustworthy full energy performance study, as shown by a comparison of the software outputs to the experiments using the standard thermal simulation model.

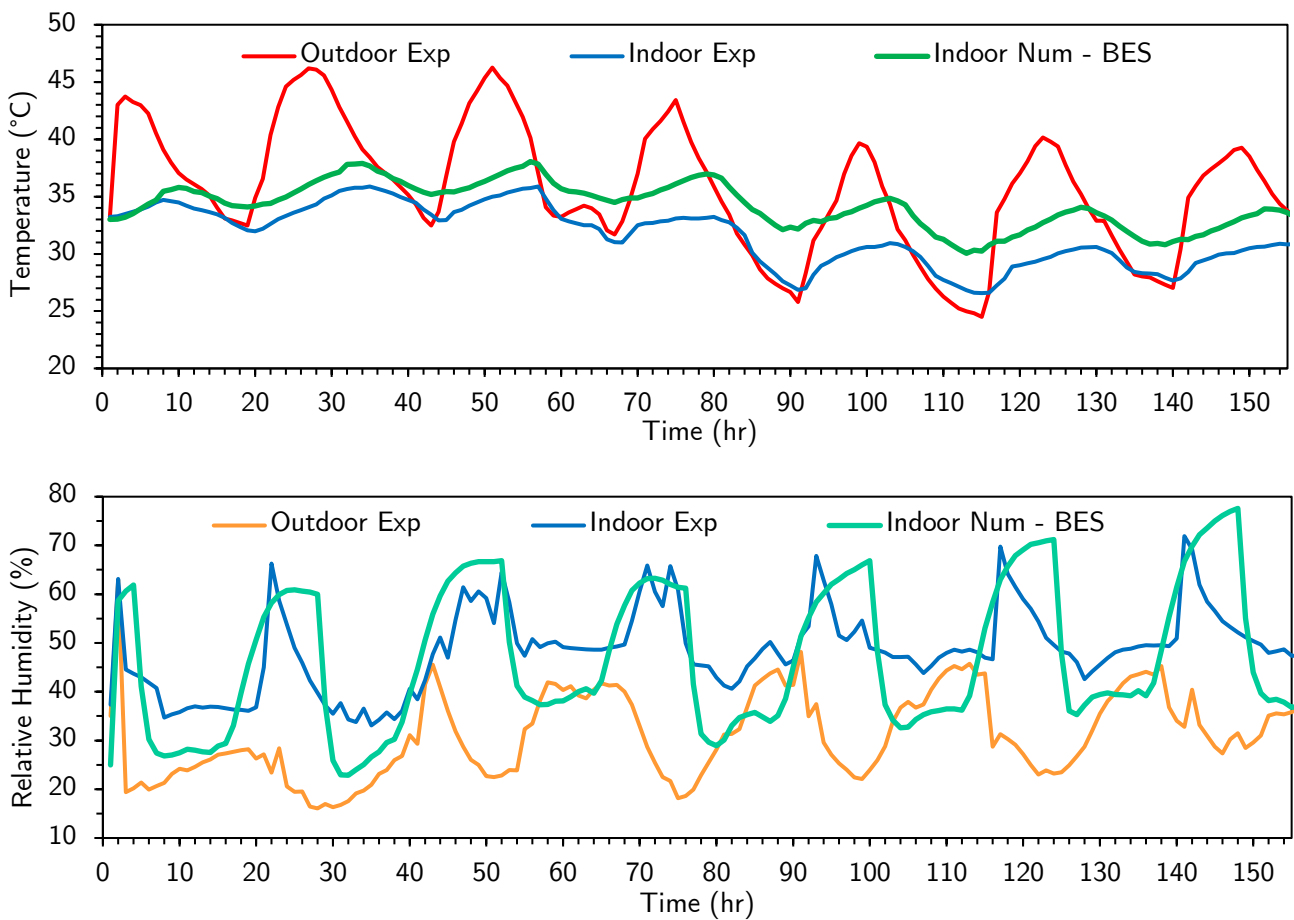


Figure 4.27 Numerical and experimental thermal simulation results of TRNSYS for temperature and relative humidity variations of the inside air zone (Earthen construction building) [199]

In comparison to experimental data, we can detect a similar pattern in the acquisition of the numerical temperature. However, the temperature curve progression simulation results exhibit the same characteristics as the experimental ones. Similar numerical curves exist for relative humidity, with some outputs underestimating or overestimating the actual outcomes. The genuine evolution of the building's curve is shown by this curve. In the current simulation scenario,

Application of the novel co-simulation technique to a real building

Transformed hygrothermal data resulting from the combination of ANN model and standard BES

the approximated biggest deviations between numerical and experimental results were 44.1 % and 5.7 °C, respectively, for relative humidity and temperature. We can say that even though the results of a typical thermal simulation are satisfactory, they are not enough to allow for the establishment of optimal and quantified solutions.

4.7.4 Transformed hygrothermal data resulting from the combination of ANN model and standard BES

We anticipate being able to investigate the outcomes of a hygrothermal simulation of a very hygroscopic building envelope in this unique modeling approach by fusing the underlying physical model with machine learning. We seek to create a unique computing technique that is simpler to implement, necessitates fewer inputs, and can be quickly computed using an algorithm with good usability, as opposed to the whole hygrothermal investigation. In this section, using a machine learning (ANN) approach, we try to deduce the outputs of actual hygroscopic building behavior from the standard thermal simulation results of the BES software.

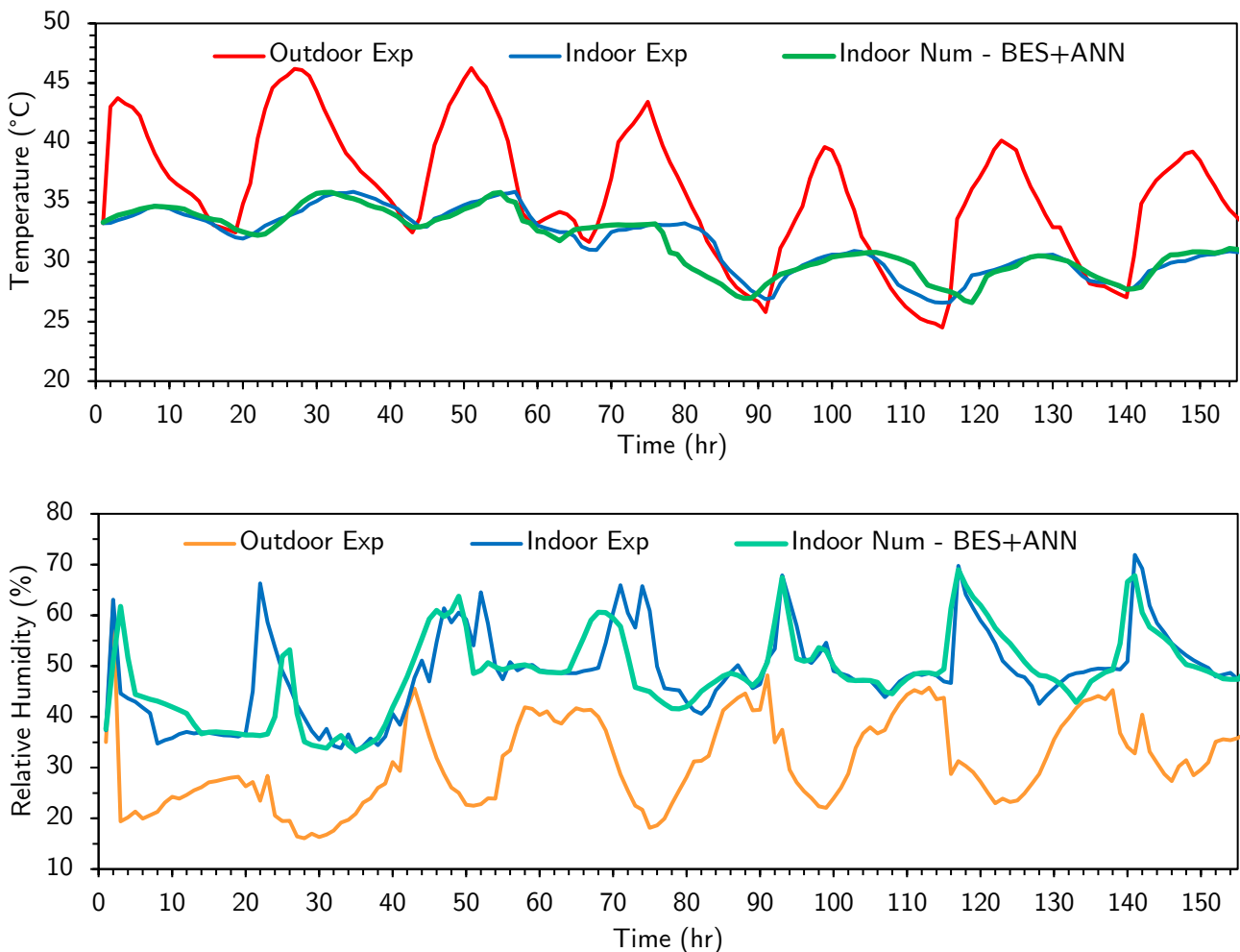


Figure 4.28 Results of numerical and experimental hygrothermal modeling using coupled BES and ANN for temperature and relative humidity variations of the inside air zone (Earthen construction building) [199]

Application of the novel co-simulation technique to a real building

Transformed hygrothermal data resulting from the combination of LSTM model and standard BES

For the new method as well as ordinary thermal simulation on TRNSYS, we continue to use the same thermo-hydric scenario of a real building. On TRNSYS, the physical parameters of the building envelope were completed to maintain the modeling's physical understanding, particularly when it was subsequently coupled with our deep learning method. Based on real-world climatic conditions, computational modeling of the thermal behavior of buildings has been initiated. When training the artificial intelligence model using numerical data, external real-world environmental conditions, and the data of the sorption curve on the walls, the outputs of the traditional simulation were integrated and incorporated into the program (Matlab). With this method, the idea of the walls' hydric buffering behavior can possibly be introduced while the numerical model is being trained. **Figure 4.28** displays the fluctuations in temperature and relative humidity inside the building air zone that were estimated using the novel co-simulation approach.

We can observe that the combined BES & ANN simulation model outputs produce more accurate findings than conventional heat modeling when using a basic thermal analysis that ignores the relationship between heat and moisture movement in buildings. The varying profiles of the temperature curves, whether experimental or numerical, are similar. Equivalent findings can be observed for relative humidity, as the numerical contour corresponds closely to the evolution profile of the building in real world, and reveals very few inaccurate estimates of outputs in comparison to the experimental one. If we consider the few response delays for temperature and relative humidity in our present simulation, the largest difference between numerical and experimental data is below 3.6 °C for temperature and 30% for relative humidity. We can draw the inference that the improved hygrothermal simulation employing a coupling technique between the physical model and deep learning (ANN model) produces more trustworthy findings that are potentially more accurate than the conventional method. Therefore, improvements are still required.

4.7.5 Transformed hygrothermal data resulting from the combination of LSTM model and standard BES

This method relies on the integration of two software programs for establishing a properly coupled heat and moisture transfer simulation over the building scale. In this section, the same coupling method has been used using TRNSYS tools and the LSTM model (Python) rather than the ANN. **Figure 4.29** exhibits the experimental data as well as the numerical simulation's estimates for changes in relative humidity and temperature inside the building shell. The outcomes demonstrate that BES&LSTM coupling provides greater accuracy than BES&ANN. Results are better when using LSTM rather than the ANN deep learning model. In general, the LSTM model performs better than the traditional ANN model. The common invader characteristics prevent the ANN models from producing accurate simulations.

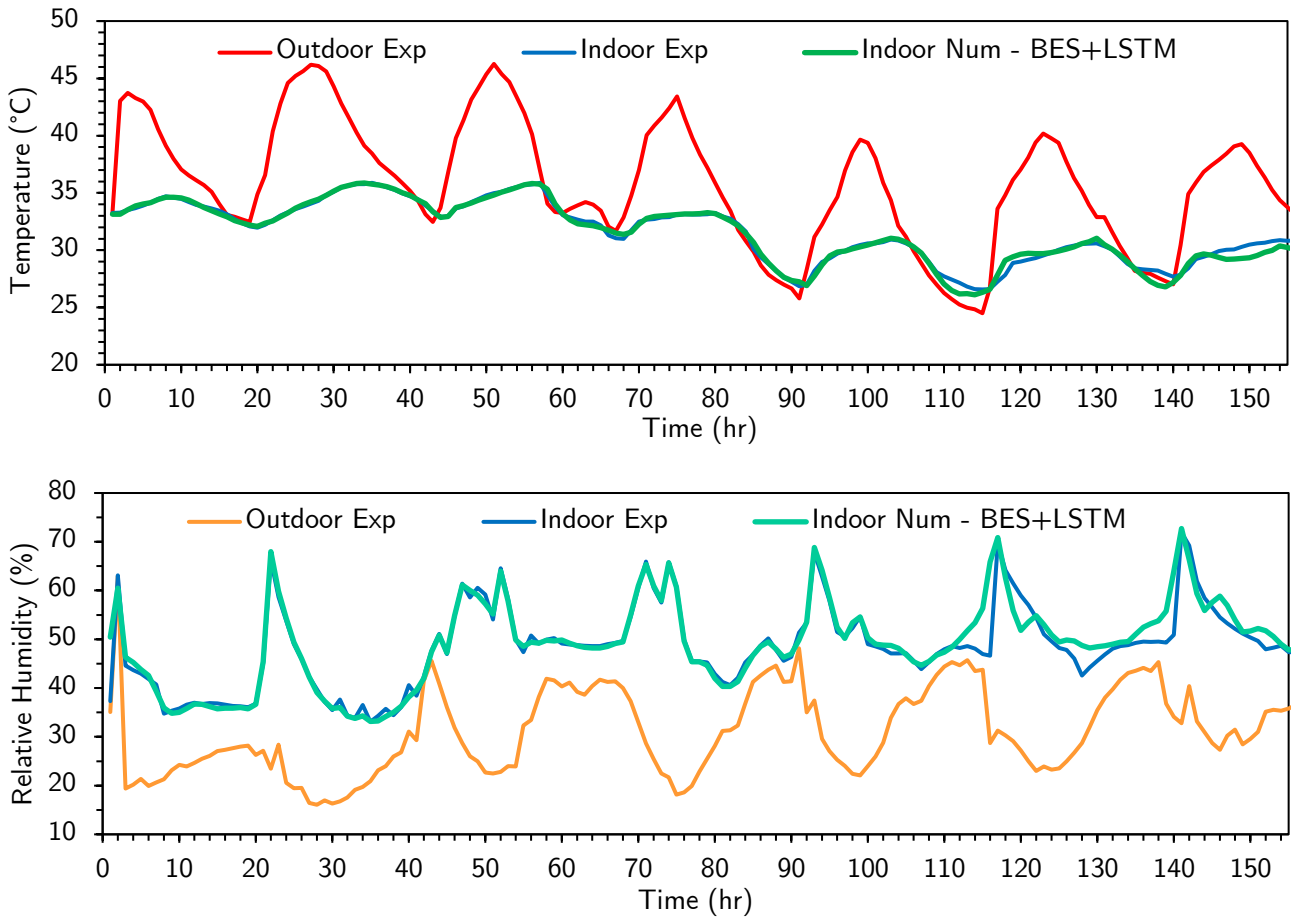


Figure 4.29 Results of numerical and experimental hygrothermal modeling using coupled BES and LSTM for temperature and relative humidity variations of the inside air zone (Earthen construction building) [199]

The statistical indicators for every model and for the whole building air zone are shown in **Table 4.27** providing clarity. The basic BES simulation appears to have a higher temperature difference because we used fewer experimentally collected data. The RMSE for this simulation is 2.83 °C. A remarkable temperature RMSE of 0.38 °C and a relative humidity RMSE of 2.87% are produced by the coupling approach BES+LSTM. The coupling method relies on the deep learning LSTM model, which seems to perform more effectively than the ANN model. To narrow the gap between numerical and experimental data, we used fundamental physical models (only heat transfer) alongside machine learning simulations to analyze the exact hygrothermal responses of full building envelopes and their effect on the comfort of the interior climate.

The only hygrothermal parameter we use for training deep learning models (apart from weather data, numerical outputs, and the physical thermal properties of materials) is the sorption curve data. The numerical outcomes for temperature and relative humidity are considerably better than those generated using the traditional thermal simulation, as shown in **Figure 4.27**, **Figure 4.28** and **Figure 4.29**.

Simulation approach	Air zone temperature		Air zone relative humidity	
	Data source compare	RMSE	Data source compare	RMS E
Thermal simulation with basic BES software (TRNSYS)	Exp – num	2.83	Exp – num	10.42
Hygrothermal simulation [Coupling BES & ANN (AI)]	Exp – num	1.01	Exp – num	5.93
Hygrothermal simulation [Coupling BES & LSTM (AI)]	Exp – num	0.38	Exp – num	2.87

Table 4.27 RMSE between the simulated and experimental values of temperature and relative humidity for different simulation approaches

4.7.6 Energy performance of earthen constructed buildings based on the outputs of different dynamic simulation approaches

To enhance building energy performance or to investigate additional retrofit opportunities, it is strongly encouraged to look into energy-efficiency options in design choices before starting construction. We broadened the scope of our inquiry in this case once our basic BES model and AI were successfully validated. In this case, our investigation needed to be strengthened. After our core BES model has been approved using artificial intelligence, we are interested in understanding how much energy is needed to maintain the right degree of comfort in the examined building. To achieve this, we are going to analyze the energy efficiency of various final results generated by different approaches, such as the conventional thermal simulation on TRNSYS and an innovative approach incorporating artificial intelligence (using Matlab or Python) to convert the conventional outputs into hygrothermal data.

The purpose of **Figure 4.31** and **Figure 4.32** is to offer a thorough analysis of the various outcomes of energy needs as estimated by different approaches. The investigation seeks to provide an exhaustive comprehension of the energy requirements arising from several techniques through the display of multiple graphs. The graphics also aim to make it easier to understand the relative performance degrees of each method, which can help with decisions about the distribution and production of energy. The experimental data for temperature, relative humidity, and cooling energy requirements can be compared to those addressed in more detail throughout this study for evaluating other numerical results. The provided data and analysis will also be helpful to academics and construction engineers who want to learn more about energy-saving techniques.

Application of the novel co-simulation technique to a real building

Energy performance of earthen constructed buildings based on the outputs of different dynamic simulation approaches

We calculated the user-specified design load, airflow, and cooling energy amounts, which are identical to those carried out on sections at p.185 and p.192, in addition to the peak temperature duration and the sizing periods. The hourly energy usage of the experimental variation and the numerical results also provide relevant data on the trends of energy demands in building systems. In our example study, the peaks of hourly energy demand occur every day between 10h00 and 19h00 hours. The solar radiation load and outdoor temperature, which are at their maximum during this time period, can help explain the reasons behind this peak. The overall demand for energy may be reduced by using this information to create effective energy management plans and implement energy-saving measures during these peak hours.

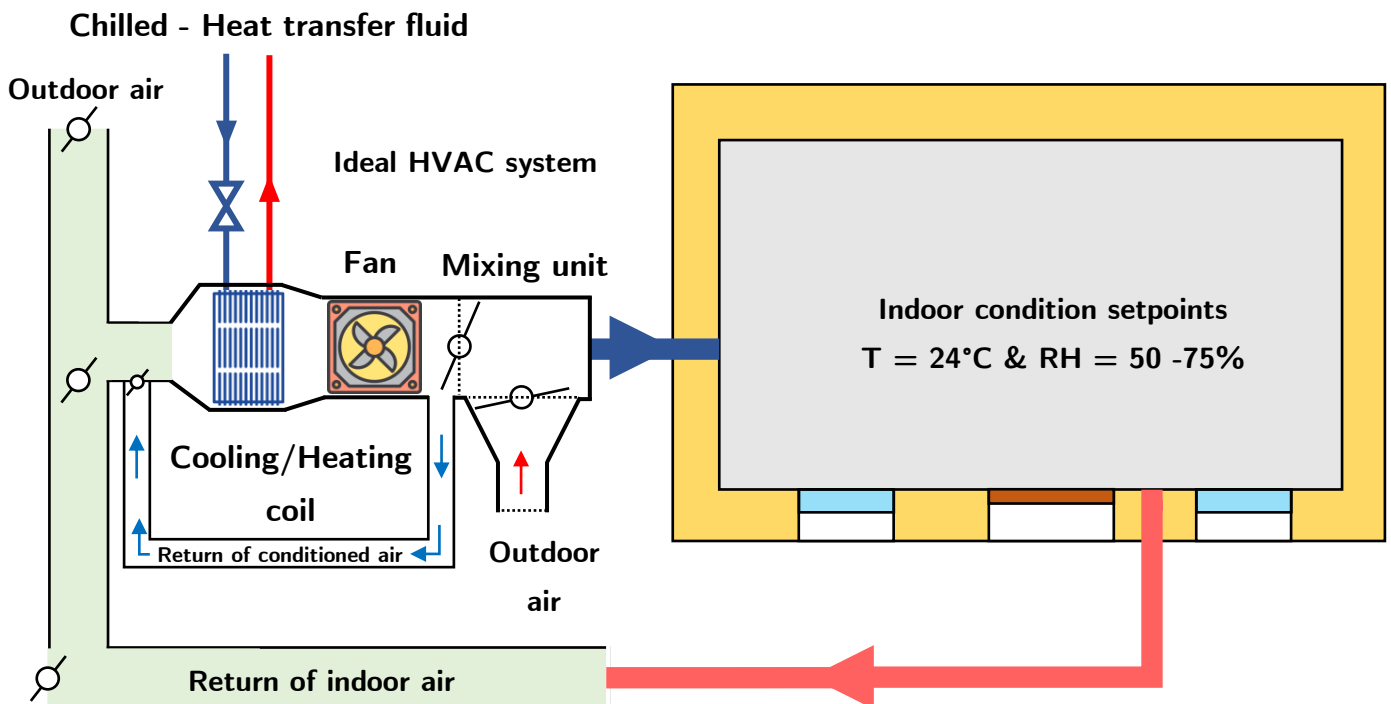


Figure 4.30 Schematic of an ideal air conditioning system simplified for our case study

It is important to note that the energy requirement values refer to our approximation of an ideal HVAC system and not the energy balance of the building (already considered by BES software for a free indoor parameter evolution). The objective is to facilitate the calculation and estimation of an ideal energy system. Our main goal in the current research is to improve the numerical outputs of temperature and relative humidity. Therefore, we would like to proceed further in studying an ideal energy system requirement, which is based on a simplified estimation that needs further investigation and validation with experimental measurements of real energy consumption. From **Figure 4.32**, it is clear that the novel coupling approach (BES-AI) yields more accurate energy estimation findings than the traditional simulation method, which only takes into account heat conduction via walls and neglects mass diffusion in porous materials.

Application of the novel co-simulation technique to a real building

Energy performance of earthen constructed buildings based on the outputs of different dynamic simulation approaches

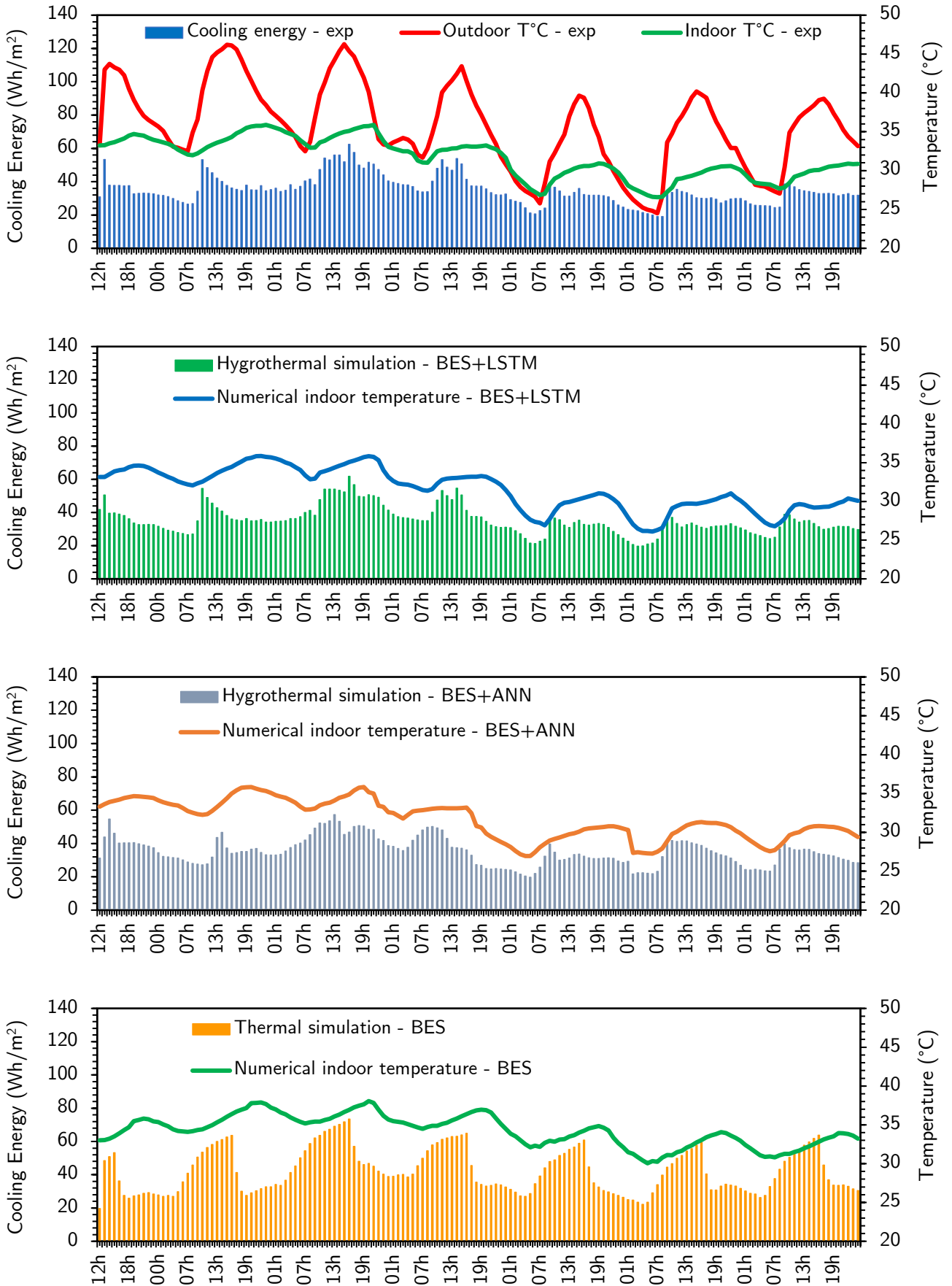


Figure 4.31 Hourly energy needs for cooling (22 July – 28 July 2010)

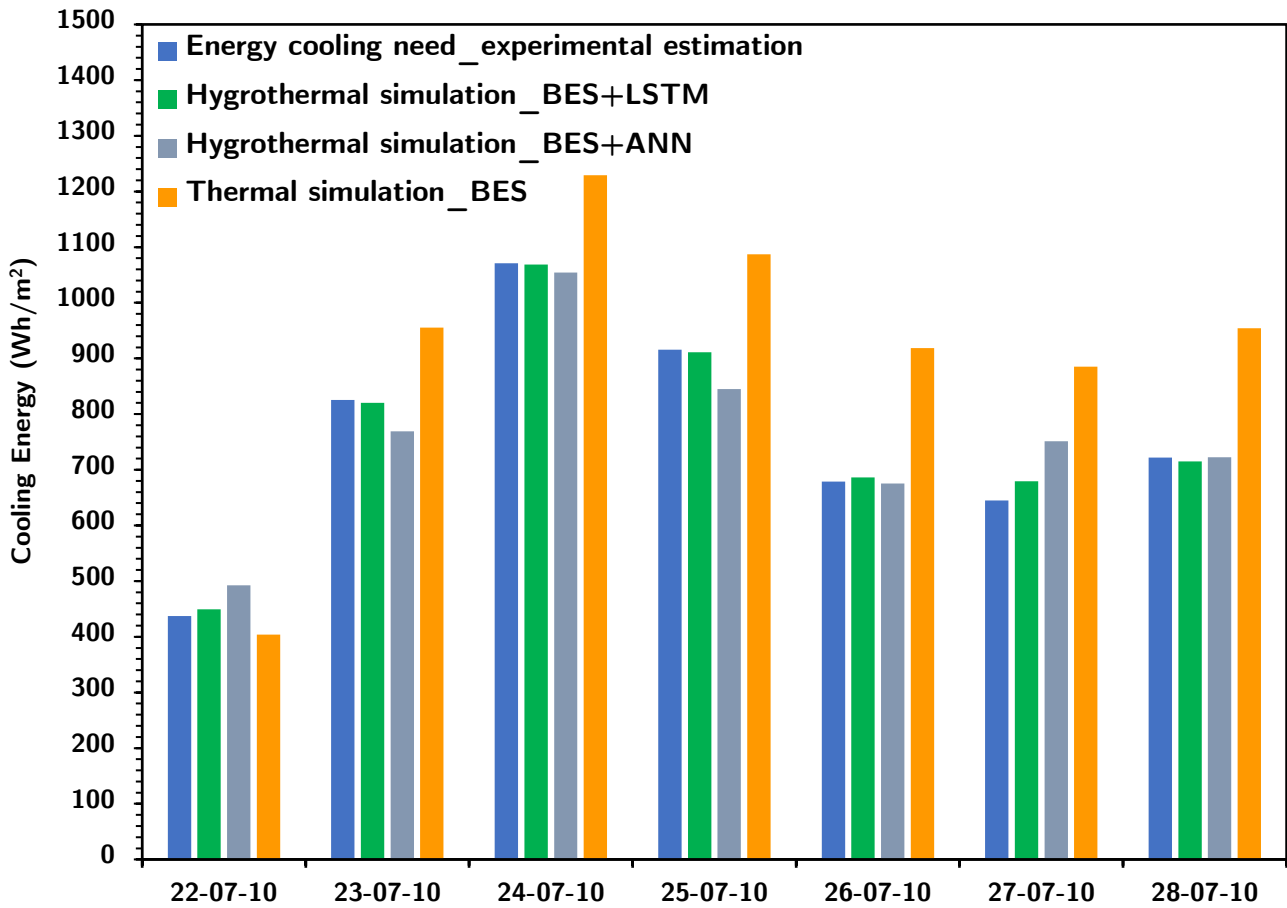


Figure 4.32 Daily energy needs for cooling (22 – 28 July 2010)

The AI-BES co-simulation technique has shown promising results in terms of correctly predicting building hygrothermal performance and energy demand. This is demonstrated by determining the mean relative error of the daily energy needs for cooling, which is less than 2%, compared to the traditional thermal simulation, which can have a mean relative error of up to 20% on the daily energy demand (see **Table 4.28**). The accuracy of the AI-BES co-simulation technique in estimating the hygrothermal requirements can be a promising solution to better estimate the energy needs in the future. Furthermore, it can help develop intelligent and self-monitored HVAC systems.

Table 4.28 Mean Relative Error of daily energy needs for cooling (22 – 28 July 2010)

Simulation approach	Mean Relative Error of daily energy needs	
	Data source compare	MRE %
Thermal simulation - BES (TRNSYS)	Exp – num	23.1
Hygrothermal simulation [Coupling BES & ANN (AI)]	Exp – num	6.53
Hygrothermal simulation [Coupling BES & LSTM (AI)]	Exp – num	1.63

4.8 Conclusion of the chapter and discussion

To investigate the behavior of whole hygroscopic construction enclosures in terms of humidity. A strategy for combining physical and deep learning models is presented in this study. As far as we are informed, the literature research on hygrothermal studies did not identify any studies that dealt with the coupling of deep learning with BES model (TRNSYS). We can conclude the followings:

- The sorption/desorption component of bio-based materials is ignored by the TRNSYS program because it lacks hygroscopic characteristic codes.
- This behavior must be integrated into TRNSYS using several physical tools, including COMSOL and MATLAB, which increase coupling complexity and demand significant computation time [16].
- It is difficult to include hysteresis effects in TRNSYS.
- The BES model requires a lot of inputs, including experimental data on the materials' thermo-hydric characteristics.

In order to overcome the identified issues, we presented in this study a co-simulation between two deep learning models (ANN and LSTM) and TRNSYS software. This method enables the addition of hygroscopic behavior to the TRNSYS "thermal" data. Comparisons to experimental data have demonstrated the effectiveness of this co-simulation strategy.

The numerical outputs highlight the significance of integrating moisture transport throughout the building walls into overall building model for the assessment of the building's hygrothermal behavior. In fact, considering more real climatic conditions, the deep learning and BES model coupling enables a hygrothermal simulation that is more accurate than standard calculations.

Additionally, we have demonstrated in this study how crucial it is to select the right deep learning model type in order to produce an efficient co-simulation. The outcomes demonstrate that the LSTM model outperforms the ANN model. Finally, we can sum up the significant challenges:

- Through fusing it with parametric physical models, the artificial intelligence model can be provided with a physical notion.
- Less experimental data sets are used to train AI algorithms.
- For building energy modeling, combine physical models with deep learning to convert thermal results into hygrothermal ones.

4.8.1 Summary of main results

Since it can give the building energy sector a clear means of combining the physical modeling and the AI algorithm in building energy simulations, the suggested technique is promising and

would improve with the development of other tools, such as model transformers. Data collection is necessary for the model to be trained, which is a significant disadvantage when using AI models in energy modeling.

This is due to the fact that AI models need a lot of data to be adequately trained, such as by gathering data from measured or simulated building elements, like temperature or humidity data, which is innovative in our application. For a comprehensive building model using TRNSYS, it is possible to acquire this sort of data. For the purpose of creating a full building model of hygrothermal behavior, the data from each simulated part must be examined and integrated. In order to test the effectiveness of the suggested co-simulation technique, we constructed a conventional BES model that is dynamically trained on an artificial neural network (ANN) using data from the TRNSYS thermal simulation. Eventually, the hygrothermal behavior of the entire building was examined by comparing the outcomes produced by the ANN&LSTM to those obtained by the conventional TRNSYS simulation.

4.8.2 Discussion on building energy modeling and Deep Learning co-simulation

The deep learning-based co-simulation has one benefit over parametric simulation: it does not require users to provide the input parameters for each construction component. There is no need to feed the model with input data because the models for each component are learnt from the data of the normal thermal simulation. Users may produce high-quality results without needing to be experts in physical and mathematical models, which is a plus. Users simply need to submit information about the components as well as the properties of their thermo-physical inputs, and the trained model will produce the appropriate hygrothermal outputs. The deep learning algorithm-trained model performs simulations significantly more quickly than the conventional ones. This makes it possible to simulate buildings with a high degree of efficiency.

In the same way that deep learning-based co-simulation with traditional building energy simulation minimizes the amount of data that users must provide, it also eliminates the necessity for them to develop and maintain in-depth information about the envelopes in the building simulation model.

As a result, it might speed up and simplify the creation of architectural models while also assisting in making physical models less complex. Another benefit of deep learning-based co-simulation over standard methods is that temperature, humidity, and other parameters are estimated based on experimental inputs and numerical outputs of conventional thermal simulation to the model, rather than being induced by the user to be determined by the model directly. As a result, users of the conventional building simulation tools are no longer required to acquire an in-depth understanding of the physical and mathematical models of the buildings energy behavior.

Conclusion of the chapter and discussion

Discussion on building energy modeling and Deep Learning co-simulation

The precision of the user's inputs into the model influences how well the predictions are made. This is one of the factors influencing the effectiveness of co-simulation tools based on deep learning. The training process produces more precise estimates of temperature and relative humidity (RH), which can dramatically decrease building energy consumption and expenses.

General conclusion and perspectives

Reflection and perspectives on building energy simulation of hygrothermal behavior

The goal of the thesis research is to provide a theoretical and experimental modeling framework for the coupled transfers of heat, air, and moisture at various scales, including materials, building walls, and envelopes. The major purpose of this study is to increase the prediction of the existence of heat and moisture transfer in new or renovated buildings and to better understand the influence of hydrothermal and aerulic transfers on the energy efficiency of buildings.

Originally, we put up a state-of-the-art, which became the first chapter, that relates an examination of the physical mechanisms involved in heat, air, and moisture flow in buildings. This included both the development of new models and enhancements to pre-existing ones in order to expand their capability and improve their accuracy. We have provided extensive bibliographic information on the characteristics of porous media, different physical methods incorporating coupled transfers of mass and heat. Also, we provided an idea of their modeling approach, as well as the main physical and deep learning computational techniques used in hygrothermal simulation of buildings. The major consideration for new low-carbon building designs is to incorporate the influence of hygrothermal exchanges at the envelope while doing an energy simulation analysis. This doctoral thesis has established a dynamic co-simulation technique combining a deep learning method (AI) and a building energy simulation model (BES). The dynamic co-simulation was made possible by combining two kinds of software, one of which can perform basic building thermal simulation and the other of which can perform deep learning calculations. The technique of connection between the two tools can be selected at will; it can be manual, automatically, or through a visual basic interface. The way chosen will rely on a number of simulation elements, programming skill, and modeling compatibility.

The importance of ensuring accurate predictions of hygrothermal transfers in structures has been underlined by this PhD thesis. The findings of this thesis have provided insight into the effectiveness of deep learning methods for simulating hygrothermal phenomena in buildings. The suggested deep learning solution enables building energy modeling with the user essentially giving standard inputs. Compared to current building energy simulation tools, the results demonstrate that the conceptual approach is precise and effective. The conceptual approach focuses on creating an appropriate prediction of the building's hygrothermal behavior by lowering the number of factors needed for precise prediction and decreasing the root mean square errors of the estimated temperature and relative humidity.

Optimization of energy performance for buildings with low carbon envelopes

The enhancement of an energy performance of building is a crucial step in achieving energy savings. The dynamic hygrothermal modeling technique is one of several strategies put out in the

literature to accomplish this aim. It is also one of the most well-known strategies.

This approach makes it possible to simulate how a building will behave in various weather scenarios and analyze how it will affect energy usage. The traditional technique has been primarily restricted by the complexity and sophistication of the simulation, and it is challenging to apply it to the actual design process. The following are the primary contributions to this thesis.

- Deep Learning (DL) techniques are used in the building energy simulation paradigm to simulate and estimate the hygrothermal behavior of buildings. This method is an effective tool for evaluating the building's thermal behavior based on its inputs and attributes. The suggested method can be applied throughout the design process to acquire early information on how the building will behave in various weather scenarios, enabling a more effective and superior design of the building enclosure.
- The creation of a novel algorithm to calculate the building's energy needs based on its hygrothermal behavior. The approach is based on an Artificial Neural Network (ANN&LSTM), which uses a small number of factors from a conventional thermal simulation output to approximate a performance of a building.

This model has undoubtedly shown reliable results through comparing its predictions to those found in the thesis of Bouasria [1] and Medjelekh [199] that used experimental data from actual buildings. Our results demonstrated that the suggested model could provide results with greater quality than those of a conventional building energy simulation while needing less processing labor and predicting building behavior with a better degree of precision as the other experimental works.

Benefits of the implementation of AI with the basic physical models of BES

The main benefits of implementing AI in the basic physical models of BES are:

- It enables a better degree of precision in the modeling of the building's thermal behavior by lowering the number of physical parameters needed as input for the hygrothermal simulation.
- The application of Deep Learning methods allows the building model to be trained and learned automatically, eliminating the requirement for input parameters to be defined manually for each case study.
- The outcomes of conventional building energy simulations and prediction models using ANN and LSTM deep learning techniques both contribute to an improvement in the ability of model to anticipate the future performance of buildings.
- It gives the building simulation process more comprehensive, appropriate results and estimations, permitting the designer to make better choices based on the information and prevent unintended changes in the building's final concept.

This can offer a solution that is flexible and can be adapted to the unique properties of the building as well as the required energy performance goals that need to be met for its development and use.

Limitations of the implementation of AI with the basic physical models of BES

The building physical modeling approach is very nonlinear, making it challenging to implement the development of the coupled models of heat and mass transfer, which is one of the key difficulties of incorporating AI in the fundamental BES physical models. The stated geometry and boundary conditions for each study case must be parameterized using a physical energy modeling program. The numerical simulation's results can then be utilized as training data for the deep learning model. The disadvantage of the co-simulation novel algorithm is that it is unable to save a record of the behavior of the trained models, and more research must be done on this subject to create AI-BES co-simulation snapshot models based on different types of building envelopes.

Bibliography

- [1] M. Bouasria, "Development and monitoring of the mechanical and hygrothermal performance of low-carbon materials by smart technology," PhD thesis, Normandie Université, 2022. [Online]. Available: <https://hal.science/tel-04008099>
- [2] United Nations and Department of Economic and Social Affairs, *Energy statistics pocketbook 2020*. 2020.
- [3] World Commission on Environment and Development, "Our common future," *Oxford: Oxford University Press*, 1987.
- [4] United Nations, "United Nations Framework Convention on Climate Change," *New York: United Nations, General Assembly*, 1992.
- [5] "Montreal Protocol on Substances that Deplete the Ozone Layer," Montreal, Sep. 16, 1987.
- [6] "Kyoto Protocol to the United Nations Framework Convention on Climate Change," Japon, Dec. 11, 1997. [Online]. Available: <http://unfccc.int/resource/docs/cop3/07a01.pdf>
- [7] "History of the Convention | UNFCCC." Accessed: Feb. 03, 2021. [Online]. Available: <https://unfccc.int/process/the-convention/history-of-the-convention#eq-2>
- [8] Eurostat, "Energy statistics - quantities," *Eur. Comm. Database*, 2020, [Online]. Available: <https://ec.europa.eu/eurostat/en/web/main/data/database>
- [9] Eurostat, "Energy consumption and use by households," *Eur. Comm. Database*, 2020, [Online]. Available: https://ec.europa.eu/eurostat/statistics-explained/index.php?title=Energy_consumption_in_households
- [10] J. Berger, W. Mazuroski, N. Mendes, S. Guernouti, and M. Woloszyn, "2D whole-building hygrothermal simulation analysis based on a PGD reduced order model," *Energy Build.*, vol. 112, pp. 49–61, Jan. 2016, doi: 10.1016/j.enbuild.2015.11.023.
- [11] H. J. Steeman, A. Janssens, J. Carmeliet, and M. D. Paepe, "Modelling indoor air and hygrothermal wall interaction in building simulation: Comparison between CFD and a well-mixed zonal model," *Build. Environ.*, p. 12, 2009.
- [12] M. Rahim, "Numerical investigation of the effect of non-isotherme sorption characteristics on hygrothermal behavior of two bio-based building walls," *J. Build. Eng.*, p. 10, 2016.
- [13] B. Seng, "Scale analysis of heat and moisture transfer through bio-based materials — Application to hemp concrete," *Energy Build.*, p. 13, 2017.
- [14] T. Colinart, "Temperature dependence of sorption isotherm of hygroscopic building materials. Part 2: Influence on hygrothermal behavior of hemp concrete," *Energy Build.*, p. 10, 2017.
- [15] B. Moujalled, Y. Aït Ouméziane, S. Moissette, M. Bart, C. Lanos, and D. Samri, "Experimental and numerical evaluation of the hygrothermal performance of a hemp lime concrete building: A long term case study," *Build. Environ.*, vol. 136, pp. 11–27, May 2018, doi: 10.1016/j.buildenv.2018.03.025.

Bibliography

- [16] G. Promis, O. Douzane, A. D. Tran Le, and T. Langlet, "Moisture hysteresis influence on mass transfer through bio-based building materials in dynamic state," *Energy Build.*, vol. 166, pp. 450–459, May 2018, doi: 10.1016/j.enbuild.2018.01.067.
- [17] T. Alioua, B. Agoudjil, N. Chennouf, A. Boudenne, and K. Benzarti, "Investigation on heat and moisture transfer in bio-based building wall with consideration of the hysteresis effect," *Build. Environ.*, vol. 163, p. 106333, Oct. 2019, doi: 10.1016/j.buildenv.2019.106333.
- [18] P. Huang *et al.*, "Heat and moisture transfer behaviour in *Phyllostachys edulis* (Moso bamboo) based panels," *Constr. Build. Mater.*, p. 15, 2018.
- [19] M. Khoukhi, "The combined effect of heat and moisture transfer dependent thermal conductivity of polystyrene insulation material: Impact on building energy performance," *Energy Build.*, vol. 169, pp. 228–235, Jun. 2018, doi: 10.1016/j.enbuild.2018.03.055.
- [20] J. M. P. Q. Delgado, E. Barreira, N. M. M. Ramos, and V. P. de Freitas, *Hygrothermal Numerical Simulation Tools Applied to Building Physics*. in SpringerBriefs in Applied Sciences and Technology. Berlin, Heidelberg: Springer Berlin Heidelberg, 2013. doi: 10.1007/978-3-642-35003-0.
- [21] J. R. Philip and D. A. De Vries, "Moisture movement in porous materials under temperature gradients," *Trans. Am. Geophys. Union*, vol. 38, no. 2, p. 222, 1957, doi: 10.1029/TR038i002p00222.
- [22] S. Whitaker, "Simultaneous Heat, Mass, and Momentum Transfer in Porous Media: A Theory of Drying," in *Advances in Heat Transfer*, vol. 13, Elsevier, 1977, pp. 119–203. doi: 10.1016/S0065-2717(08)70223-5.
- [23] A. V. Iuikov, "Application of irreversible thermodynamics methods to investigation of heat and mass transfer," *Int. J. Heat Mass Transf.*, vol. 9, pp. 139–152, 1966.
- [24] H. M. Künzle, *Simultaneous heat and moisture transport in building components: one- and two-dimensional calculation using simple parameters*. Stuttgart: IRB-Verl, 1995.
- [25] N. Mendes, I. Ridley, R. Lamberts, P. C. Philippi, and K. Budag, "UMIDUS: A PC program for the prediction of heat and moisture transfer in porous buildings elements," *Build. Simul.*, pp. 277–283, 1999.
- [26] M. H. Benzaama, L. H. Rajaoarisoa, B. Ajib, and S. Lecoeuche, "A data-driven methodology to predict thermal behavior of residential buildings using piecewise linear models," *J. Build. Eng.*, vol. 32, p. 101523, Nov. 2020, doi: 10.1016/j.job.2020.101523.
- [27] S. A. Klein *et al.*, "TRaNsient SYstem Simulation program 18: Programme's Guide." 2017. [Online]. Available: <https://sel.me.wisc.edu/trnsys/user18-resources/index.html>
- [28] P. LENORMAND *et al.*, "Manuel Comfie Pleiades Modeleur." Izuba énergies. [Online]. Available: https://docs.izuba.fr/v4/fr/index.php/Pleiades_et_ses_modules
- [29] H. KÜNZEL and K. KIESEL, "Calculation of heat and moisture transfer in exposed building components," *Int. J. Heat Mass Transf.*, vol. 40, no. 1, pp. 159–167, 1997.
- [30] N. Mendes and P. C. Philippi, "A method for predicting heat and moisture transfer through multilayered walls based on temperature and moisture content gradients," *Int. J. Heat Mass Transf.*, p. 15, 2005.

Bibliography

- [31] N. Mendes, P. C. Philippi, and R. Lamberts, "A new mathematical method to solve highly coupled equations of heat and mass transfer in porous media," *Int. J. Heat Mass Transf.*, vol. 45, no. 3, pp. 509–518, Jan. 2002, doi: 10.1016/S0017-9310(01)00172-7.
- [32] S.-H. Cho and C.-U. Chae, "A Study on Life Cycle CO₂ Emissions of Low-Carbon Building in South Korea," *Sustainability*, vol. 8, no. 6, Art. no. 6, Jun. 2016, doi: 10.3390/su8060579.
- [33] H. Dahy, "Biocomposite materials based on annual natural fibres and biopolymers – Design, fabrication and customized applications in architecture," *Constr. Build. Mater.*, vol. 147, pp. 212–220, Aug. 2017, doi: 10.1016/j.conbuildmat.2017.04.079.
- [34] G. Bumanis, L. Vitola, I. Pundiene, M. Sinka, and D. Bajare, "Gypsum, Geopolymers, and Starch—Alternative Binders for Bio-Based Building Materials: A Review and Life-Cycle Assessment," *Sustainability*, vol. 12, no. 14, Art. no. 14, Jul. 2020, doi: 10.3390/su12145666.
- [35] G. B. A. Coelho, H. E. Silva, and F. M. A. Henriques, "Calibrated hygrothermal simulation models for historical buildings," *Build. Environ.*, vol. 142, pp. 439–450, Sep. 2018, doi: 10.1016/j.buildenv.2018.06.034.
- [36] D. Gallipoli, A. W. Bruno, C. Perlot, and J. Mendes, "A geotechnical perspective of raw earth building," *Acta Geotech.*, vol. 12, no. 3, Art. no. 3, Jun. 2017, doi: 10.1007/s11440-016-0521-1.
- [37] N. N. Makhlof, D. Maskell, A. Marsh, S. Natarajan, M. Dabaieh, and M. M. Afify, "Hygrothermal performance of vernacular stone in a desert climate," *Constr. Build. Mater.*, vol. 216, pp. 687–696, Aug. 2019, doi: 10.1016/j.conbuildmat.2019.04.244.
- [38] L. Boukhattem, M. Boumhaout, H. Hamdi, B. Benhamou, and F. Ait Nouh, "Moisture content influence on the thermal conductivity of insulating building materials made from date palm fibers mesh," *Constr. Build. Mater.*, vol. 148, pp. 811–823, Sep. 2017, doi: 10.1016/j.conbuildmat.2017.05.020.
- [39] M. G. Gomes, I. Flores-Colen, L. M. Manga, A. Soares, and J. de Brito, "The influence of moisture content on the thermal conductivity of external thermal mortars," *Constr. Build. Mater.*, vol. 135, pp. 279–286, Mar. 2017, doi: 10.1016/j.conbuildmat.2016.12.166.
- [40] X. Zhang, M. Riaz Ahmad, and B. Chen, "Numerical and experimental investigation of the hygrothermal properties of corn stalk and magnesium phosphate cement (MPC) based bio-composites," *Constr. Build. Mater.*, vol. 244, p. 118358, May 2020, doi: 10.1016/j.conbuildmat.2020.118358.
- [41] N. Reuge, "Modeling of hygrothermal transfers through a bio-based multilayered wall tested in a bi-climatic room," *J. Build. Eng.*, p. 12, 2020.
- [42] M. Bagarić, I. Banjad Pečur, and B. Milovanović, "Hygrothermal performance of ventilated prefabricated sandwich wall panel from recycled construction and demolition waste – A case study," *Energy Build.*, vol. 206, p. 109573, Jan. 2020, doi: 10.1016/j.enbuild.2019.109573.
- [43] W. Dong, Y. Chen, Y. Bao, and A. Fang, "A validation of dynamic hygrothermal model with coupled heat and moisture transfer in porous building materials and envelopes," *J. Build. Eng.*, vol. 32, p. 101484, Nov. 2020, doi: 10.1016/j.job.2020.101484.
- [44] A. Tadeu, L. Škerget, N. Simões, and R. Fino, "Simulation of heat and moisture flow through walls covered with uncoated medium density expanded cork," *Build. Environ.*, vol. 142, pp. 195–210, Sep. 2018, doi: 10.1016/j.buildenv.2018.06.009.

Bibliography

- [45] S. Hou, F. Liu, S. Wang, and H. Bian, "Coupled heat and moisture transfer in hollow concrete block wall filled with compressed straw bricks," *Energy Build.*, vol. 135, pp. 74–84, Jan. 2017, doi: 10.1016/j.enbuild.2016.11.026.
- [46] P. M. Congedo, C. Baglivo, D. D'Agostino, G. Quarta, and P. Di Gloria, "Rising damp in building stones: Numerical and experimental comparison in lecce stone and carparo under controlled microclimatic conditions," *Constr. Build. Mater.*, vol. 296, p. 123713, Aug. 2021, doi: 10.1016/j.conbuildmat.2021.123713.
- [47] H. E. Huerto-Cardenas *et al.*, "Validation of dynamic hygrothermal simulation models for historical buildings: State of the art, research challenges and recommendations," *Build. Environ.*, vol. 180, p. 107081, Aug. 2020, doi: 10.1016/j.buildenv.2020.107081.
- [48] N. Cavalagli, A. Kita, V. L. Castaldo, A. L. Pisello, and F. Ubertini, "Hierarchical environmental risk mapping of material degradation in historic masonry buildings: An integrated approach considering climate change and structural damage," *Constr. Build. Mater.*, vol. 215, pp. 998–1014, Aug. 2019, doi: 10.1016/j.conbuildmat.2019.04.204.
- [49] C. Franzen and P. W. Mirwald, "Moisture sorption behaviour of salt mixtures in porous stone," *Geochemistry*, vol. 69, no. 1, pp. 91–98, Feb. 2009, doi: 10.1016/j.chemer.2008.02.001.
- [50] D. D'Agostino and P. M. Congedo, "CFD modeling and moisture dynamics implications of ventilation scenarios in historical buildings," *Build. Environ.*, vol. 79, pp. 181–193, Sep. 2014, doi: 10.1016/j.buildenv.2014.05.007.
- [51] D. D'Agostino, P. M. Congedo, and R. Cataldo, "Computational fluid dynamics (CFD) modeling of microclimate for salts crystallization control and artworks conservation," *J. Cult. Herit.*, vol. 15, no. 4, pp. 448–457, Jul. 2014, doi: 10.1016/j.culher.2013.10.002.
- [52] F. Corvo *et al.*, "Influence of Air Pollution and Humidity on Limestone Materials Degradation in Historical Buildings Located in Cities Under Tropical Coastal Climates," *Water. Air. Soil Pollut.*, vol. 205, no. 1, p. 359, May 2009, doi: 10.1007/s11270-009-0081-1.
- [53] M. Cellura, F. Guarino, S. Longo, and G. Tumminia, "Climate change and the building sector: Modelling and energy implications to an office building in southern Europe," *Energy Sustain. Dev.*, vol. 45, pp. 46–65, Aug. 2018, doi: 10.1016/j.esd.2018.05.001.
- [54] C. M. Grossi, P. Brimblecombe, and I. Harris, "Predicting long term freeze–thaw risks on Europe built heritage and archaeological sites in a changing climate," *Sci. Total Environ.*, vol. 377, no. 2, pp. 273–281, May 2007, doi: 10.1016/j.scitotenv.2007.02.014.
- [55] C. R. Pedersen, "Prediction of moisture transfer in building constructions," *Build. Environ.*, vol. 27, no. 3, pp. 387–397, Jul. 1992, doi: 10.1016/0360-1323(92)90038-Q.
- [56] H. D. Baehr and K. Stephan, "Mass transfer Theory," in *Heat and Mass Transfer*, Berlin, Heidelberg: Springer Berlin Heidelberg, 2011, pp. 87–102. doi: 10.1007/978-3-642-20021-2.
- [57] D. Lelievre, T. Colinart, and P. Glouannec, "Hygrothermal behavior of bio-based building materials including hysteresis effects: Experimental and numerical analyses," *Energy Build.*, vol. 84, pp. 617–627, Dec. 2014, doi: 10.1016/j.enbuild.2014.09.013.
- [58] J.-P. Hansen, *Theory of simple liquids with applications to soft matter*, 4th ed. Oxford, England: Academic Press, 2013.

Bibliography

- [59] H. Swenson and N. P. Stadie, "Langmuir's Theory of Adsorption: A Centennial Review," *Langmuir*, vol. 35, no. 16, Art. no. 16, Apr. 2019, doi: 10.1021/acs.langmuir.9b00154.
- [60] S. Brunauer, P. H. Emmett, and E. Teller, "Adsorption of Gases in Multimolecular Layers," *J. Am. Chem. Soc.*, vol. 60, no. 2, Art. no. 2, Feb. 1938, doi: 10.1021/ja01269a023.
- [61] M. Labat, M. Woloszyn, G. Garnier, and J. J. Roux, "Dynamic coupling between vapour and heat transfer in wall assemblies: Analysis of measurements achieved under real climate," *Build. Environ.*, vol. 87, pp. 129–141, May 2015, doi: 10.1016/j.buildenv.2015.01.022.
- [62] M. Van Belleghem, H.-J. Steeman, M. Steeman, A. Janssens, and M. De Paepe, "Sensitivity analysis of CFD coupled non-isothermal heat and moisture modelling," *Build. Environ.*, vol. 45, no. 11, pp. 2485–2496, Nov. 2010, doi: 10.1016/j.buildenv.2010.05.011.
- [63] M. Steeman, A. Janssens, H. J. Steeman, M. V. Belleghem, and M. D. Paepe, "On coupling 1D non-isothermal heat and mass transfer in porous materials with a multizone building energy simulation model," *Build. Environ.*, p. 13, 2010.
- [64] S. CHAPMAN and T. G. COWLING, "The Free Path, the collision-frequency and persistence of velocities," in *The mathematical theory of non-uniform gases: An account of the kinetic theory of viscosity, thermal conduction and diffusion in gases*, 1953, pp. 89–99.
- [65] M. G. Verbeek, "A Numerical Investigation of the Mean Free Path Distribution in the Knudsen Regime," *Transp. Porous Media*, vol. 123, no. 2, Art. no. 2, Jun. 2018, doi: 10.1007/s11242-018-1035-0.
- [66] H. D. Baehr and K. Stephan, "The different types of heat transfer," in *Heat and Mass Transfer*, Berlin, Heidelberg: Springer Berlin Heidelberg, 2011, pp. 1–27. doi: 10.1007/978-3-642-20021-2.
- [67] R. Karwa, "Mass Transfer," in *Heat and Mass Transfer*, Singapore: Springer Singapore, 2020, pp. 1041–1064. doi: 10.1007/978-981-15-3988-6.
- [68] C.-E. Hagentoft, A. S. Kalagasidis, and B. Adl-Zarrabi, "Benchmarks for One-dimensional Cases of Combined Heat, Air and Moisture Transfer in Building Components," p. 10.
- [69] D. Zirkelbach, T. Schmidt, M. Kehrer, and H. M. Künzel, "WUFI Pro 5 Manual." [Online]. Available: <https://wufi.de/en/service/downloads/>
- [70] A. D. Tran Le, J. S. Zhang, and Z. Liu, "Impact of humidity on formaldehyde and moisture buffering capacity of porous building material," *J. Build. Eng.*, vol. 36, p. 102114, Apr. 2021, doi: 10.1016/j.job.2020.102114.
- [71] R. Wang, "Moisture-safe attic design in extremely cold climate: Hygrothermal simulations," *Build. Environ.*, p. 12, 2020.
- [72] R. Djedjig, E. Bozonnet, and R. Belarbi, "Analysis of thermal effects of vegetated envelopes: Integration of a validated model in a building energy simulation program," *Energy Build.*, vol. 86, pp. 93–103, Jan. 2015, doi: 10.1016/j.enbuild.2014.09.057.
- [73] J. Preuss, "Moisture Balance," in *TRaNsient SYstem Simulation program 18: Multizone Building modeling with Type56 and TRNBuild*, TRNSYS, pp. 191–195.
- [74] "Effective Moisture Penetration Depth (EMPD) Model," in *EnergyPlus™ Version 9.4.0 Documentation: Engineering Reference*, US Department of Energy, 2020, pp. 80–83.
- [75] F. Antretter, M. Winkler, M. Fink, M. Pazold, J. Radon, and S. S. Stadler, "WUFI Plus 3.1 Manual." Jun. 01, 2017. [Online]. Available: <https://wufi.de/en/service/downloads/>

Bibliography

- [76] "EnergyPlus™ Version 9.4.0 Documentation: Engineering Reference," *US Department Energy*, p. 1758, Sep. 2020.
- [77] M. H. Benzaama, A. M. Mokhtari, M. Lachi, C. Maalouf, and S. Menhoudj, "Sunspot analysis under varying conditions climate: Distributed radiation on cooling floor and its effect on dynamic thermal behaviour," *Sol. Energy*, vol. 221, pp. 275–291, Jun. 2021, doi: 10.1016/j.solener.2021.03.082.
- [78] A. Kerestecioglu and A. Kamel, "Theoretical and computational investigation of simultaneous heat and moisture transfer in buildings: 'Effective penetration depth' theory.," in *AIVC*, 1989. Accessed: Apr. 05, 2021. [Online]. Available: <https://www.aivc.org/resource/theoretical-and-computational-investigation-simultaneous-heat-and-moisture-transfer>
- [79] J. Woods, J. Winkler, and D. Christensen, "Moisture Modeling: Effective Moisture Penetration Depth Versus Effective Capacitance," p. 13.
- [80] T. Yamamoto, A. Ozaki, M. Lee, and H. Kusumoto, "Fundamental study of coupling methods between energy simulation and CFD," *Energy Build.*, vol. 159, pp. 587–599, Jan. 2018, doi: 10.1016/j.enbuild.2017.11.059.
- [81] M. Simo-Tagne, M. C. Ndukwu, and Y. Rogaume, "Modelling and numerical simulation of hygrothermal transfer through a building wall for locations subjected to outdoor conditions in Sub-Saharan Africa," *J. Build. Eng.*, vol. 26, p. 100901, Nov. 2019, doi: 10.1016/j.jobbe.2019.100901.
- [82] "Comsol Multiphysics 5.6: Porous Media Flow Module User's Guide." [Online]. Available: <https://doc.comsol.com/5.6/docserver/#!/com.comsol.help.comsol/helpdesk/helpdesk.html>
- [83] "OpenFoam: User Guide version 8." [Online]. Available: <https://cfd.direct/openfoam/user-guide/>
- [84] ANSYS, Inc, "Heat Transfer," in *ANSYS Fluent Theory Guide: Release 15.0*, 2013, pp. 133–173.
- [85] Siemens PLM Software, "STAR-CCM+ Documentation Version 13.04." 2018.
- [86] Y. Kang, S. J. Chang, and S. Kim, "Hygrothermal behavior evaluation of walls improving heat and moisture performance on gypsum boards by adding porous materials," *Energy Build.*, vol. 165, pp. 431–439, Apr. 2018, doi: 10.1016/j.enbuild.2017.12.052.
- [87] M. Qin, R. Belarbi, A. Aït-Mokhtar, and L.-O. Nilsson, "Coupled heat and moisture transfer in multi-layer building materials," *Constr. Build. Mater.*, p. 9, 2009.
- [88] "Comsol Multiphysics 5.6: Heat and Moisture Transport in a Semi-Infinite Wall." [Online]. Available: <https://www.comsol.fr/model/heat-and-moisture-transport-in-a-semi-infinite-wall-39001>
- [89] Z. Zhai, Q. Chen, P. Haves, and J. H. Klems, "On approaches to couple energy simulation and computational uid dynamics programs," *Build. Environ.*, p. 8, 2002.
- [90] H. Zhang, "Investigating simultaneous transport of heat and moisture in hygroscopic materials by a semi-conjugate CFD-coupled approach," *Build. Environ.*, p. 11, 2015.
- [91] Q. Li, J. Rao, and P. Fazio, "Development of HAM tool for building envelope analysis," *Build. Environ.*, p. 9, 2009.

Bibliography

- [92] H.-J. Steeman, M. Van Belleghem, A. Janssens, and M. De Paepe, "Coupled simulation of heat and moisture transport in air and porous materials for the assessment of moisture related damage," *Build. Environ.*, vol. 44, no. 10, pp. 2176–2184, Oct. 2009, doi: 10.1016/j.buildenv.2009.03.016.
- [93] Q. Li, J. Rao, and P. Fazio, "Hygrothermal simulation of drying performance of typical north american building envelope," Montréal, Canada, 18/08 2005, p. 8.
- [94] L. Škerget, A. Tadeu, and C. A. Brebbia, "Transient simulation of coupled heat and moisture flow through a multi-layer porous solid exposed to solar heat flux," *Int. J. Heat Mass Transf.*, vol. 117, pp. 273–279, Feb. 2018, doi: 10.1016/j.ijheatmasstransfer.2017.10.010.
- [95] Guggenheim Edward Armand, *Applications of statistical mechanics / by E.A. Guggenheim*. Oxford: Clarendon Press, 1966.
- [96] R. B. Anderson, "Modifications of the Brunauer, Emmett and Teller Equation1," *J. Am. Chem. Soc.*, vol. 68, no. 4, Art. no. 4, Apr. 1946, doi: 10.1021/ja01208a049.
- [97] Boer Jan Hendrik de, *The dynamical character of adsorption / by J. H. de Boer*. Oxford: Clarendon Press, 1953.
- [98] I. Langmuir, "The adsorption of gases on plane surfaces of glass, mica and platinum.," *J. Am. Chem. Soc.*, vol. 40, no. 9, pp. 1361–1403, Sep. 1918, doi: 10.1021/ja02242a004.
- [99] M. T. van Genuchten, "A Closed-form Equation for Predicting the Hydraulic Conductivity of Unsaturated Soils," *Soil Sci. Soc. Am. J.*, vol. 44, no. 5, pp. 892–898, 1980, doi: <https://doi.org/10.2136/sssaj1980.03615995004400050002x>.
- [100] M. Maaroufi, "Experimental and numerical highlighting of water vapor sorption hysteresis in the coupled heat and moisture transfers," *J. Build. Eng.*, p. 10, 2021.
- [101] Y. Mualem, "A conceptual model of hysteresis," *Water Resour. Res.*, vol. 10, no. 3, pp. 514–520, 1974, doi: <https://doi.org/10.1029/WR010i003p00514>.
- [102] C. Rode, P. N. Hansen, and K. K. Hansen, "Combined heat and moisture transfer in building constructions," pp. 42–44, 1990.
- [103] H.-C. Huang, Y.-C. Tan, C.-W. Liu, and C.-H. Chen, "A novel hysteresis model in unsaturated soil," *Hydrol. Process.*, vol. 19, no. 8, pp. 1653–1665, 2005, doi: <https://doi.org/10.1002/hyp.5594>.
- [104] J. B. Kool and J. C. Parker, "Development and evaluation of closed-form expressions for hysteretic soil hydraulic properties," *Water Resour. Res.*, vol. 23, no. 1, pp. 105–114, 1987, doi: <https://doi.org/10.1029/WR023i001p00105>.
- [105] Y. A. Oumeziane, M. Bart, S. Moissette, and C. Lanos, "Hysteretic Behaviour and Moisture Buffering of Hemp Concrete," p. 19.
- [106] K.-T. Yang, "Artificial Neural Networks (ANNs): A New Paradigm for Thermal Science and Engineering," *J. Heat Transf.*, vol. 130, no. 093001, Jul. 2008, doi: 10.1115/1.2944238.
- [107] L. V. Kamble, D. R. Pangavhane, and T. P. Singh, "Heat Transfer Studies using Artificial Neural Network - a Review," p. 18, 2014.
- [108] A. K. Jain, Jianchang Mao, and K. M. Mohiuddin, "Artificial neural networks: a tutorial," *Computer*, vol. 29, no. 3, pp. 31–44, Mar. 1996, doi: 10.1109/2.485891.

Bibliography

- [109] I. Livshin, "Learning About Neural Networks," in *Artificial Neural Networks with Java: Tools for Building Neural Network Applications*, Apress, 2019, pp. 3–4. doi: 10.1007/978-1-4842-4421-0.
- [110] S. Haykin, "Learning Processes," in *Neural networks and learning machines*, 3. ed., New York: Pearson, 2009, pp. 34–44.
- [111] A. Tijskens, S. Roels, and H. Janssen, "Neural networks for metamodelling the hygrothermal behaviour of building components," *Build. Environ.*, vol. 162, p. 106282, Sep. 2019, doi: 10.1016/j.buildenv.2019.106282.
- [112] A. Tijskens, S. Roels, and H. Janssen, "Hygrothermal assessment of timber frame walls using a convolutional neural network," *Build. Environ.*, vol. 193, p. 107652, Apr. 2021, doi: 10.1016/j.buildenv.2021.107652.
- [113] O. May Tzuc *et al.*, "Modeling of hygrothermal behavior for green facade's concrete wall exposed to nordic climate using artificial intelligence and global sensitivity analysis," *J. Build. Eng.*, vol. 33, p. 101625, Jan. 2021, doi: 10.1016/j.job.2020.101625.
- [114] H. Sözer and S. S. Aldin, "Predicting the indoor thermal data for heating season based on short-term measurements to calibrate the simulation set-points," *Energy Build.*, vol. 202, p. 109422, Nov. 2019, doi: 10.1016/j.enbuild.2019.109422.
- [115] B. Chegari, M. Tabaa, E. Simeu, F. Moutaouakkil, and H. Medromi, "Multi-objective optimization of building energy performance and indoor thermal comfort by combining artificial neural networks and metaheuristic algorithms," *Energy Build.*, vol. 239, p. 110839, May 2021, doi: 10.1016/j.enbuild.2021.110839.
- [116] M. Van Belleghem, M. Steeman, H. Janssen, A. Janssens, and M. De Paepe, "Validation of a coupled heat, vapour and liquid moisture transport model for porous materials implemented in CFD," *Build. Environ.*, vol. 81, pp. 340–353, Nov. 2014, doi: 10.1016/j.buildenv.2014.06.024.
- [117] H. Rafidiarison, "Dataset for validating 1-D heat and mass transfer models within building walls with hygroscopic materials," *Build. Environ.*, p. 13, 2015.
- [118] P. von Böckh and T. Wetzel, *Heat Transfer*. Berlin, Heidelberg: Springer Berlin Heidelberg, 2012. doi: 10.1007/978-3-642-19183-1.
- [119] H. D. Baehr and K. Stephan, *Heat and Mass Transfer*. Berlin, Heidelberg: Springer Berlin Heidelberg, 2011. doi: 10.1007/978-3-642-20021-2.
- [120] D. Naouel and R. Mohamed-Sassi, *Exercices résolus de thermique: Rayonnement thermique*. Editions TECHNIP, 2013.
- [121] F. Kasten and A. T. Young, "Revised optical air mass tables and approximation formula," *Appl. Opt.*, vol. 28, no. 22, pp. 4735–4738, Nov. 1989, doi: 10.1364/AO.28.004735.
- [122] K. Bakirci, "Estimation of Solar Radiation by Using ASHRAE Clear-Sky Model in Erzurum, Turkey," *Energy Sources Part Recovery Util. Environ. Eff.*, vol. 31, no. 3, pp. 208–216, 2009, doi: 10.1080/15567030701522534.
- [123] M. Abouhashish, "Applicability of ASHRAE clear-sky model based on solar-radiation measurements in Saudi Arabia," *AIP Conf. Proc.*, vol. 1850, no. 1, p. 140001, Jun. 2017, doi: 10.1063/1.4984509.

Bibliography

- [124] E. American Society of Heating, Refrigerating and Air-Conditioning, *1997 ASHRAE Handbook - Fundamentals*. ASHRAE, 1997.
- [125] R. Karwa, *Heat and Mass Transfer*. Singapore: Springer, 2020. doi: 10.1007/978-981-15-3988-6.
- [126] D. Basmadjian, *Mass Transfer: Principles and Applications*. Boca Raton: CRC Press, 2003. doi: 10.1201/b12394.
- [127] I. Tosun, *Fundamental Mass Transfer Concepts in Engineering Applications*. CRC Press / Taylor & Francis Group, 2019.
- [128] G. A. Nagata, T. V. Costa, M. T. B. Perazzini, and H. Perazzini, "Coupled heat and mass transfer modelling in convective drying of biomass at particle-level: Model validation with experimental data," *Renew. Energy*, vol. 149, pp. 1290–1299, Apr. 2020, doi: 10.1016/j.renene.2019.10.123.
- [129] E. Esfanjary Kenari, *Persian Historic Urban Landscapes Interpreting and Managing Maibud over 6000 Years*. 2017.
- [130] M. Bouasria, Y. El Mendili, M.-H. Benzaama, V. Pralong, J.-F. Bardeau, and F. Hennequart, "Valorisation of stranded *Laminaria digitata* seaweed as an insulating earth material," *Constr. Build. Mater.*, vol. 308, p. 125068, Nov. 2021, doi: 10.1016/j.conbuildmat.2021.125068.
- [131] M. A. Riffat SB, "Building Energy Consumption and Carbon dioxide Emissions: Threat to Climate Change," *J. Earth Sci. Clim. Change*, vol. s3, 2015, doi: 10.4172/2157-7617.S3-001.
- [132] M. s. Lekshmi, S. Vishnudas, and D. G. Nair, "An investigation on the potential of mud as sustainable building material in the context of Kerala," *Int. J. Energy Technol. Policy*, vol. 13, no. 1–2, pp. 107–122, Jan. 2017, doi: 10.1504/IJETP.2017.080621.
- [133] Y. El Mendili *et al.*, "Mud-Based Construction Material: Promising Properties of French Gravel Wash Mud Mixed with Byproducts, Seashells and Fly Ash as a Binder," *Materials*, vol. 14, no. 20, Art. no. 20, Jan. 2021, doi: 10.3390/ma14206216.
- [134] L. Miccoli, U. Müller, and P. Fontana, "Mechanical behaviour of earthen materials: A comparison between earth block masonry, rammed earth and cob," *Constr. Build. Mater.*, vol. 61, pp. 327–339, Jun. 2014, doi: 10.1016/j.conbuildmat.2014.03.009.
- [135] K. ABAHRI, R. BELARBI, N. Oudjehani, N. Issaadi, and M. Ferroukhi, "Total Pressure Gradient Incidence on Hygrothermal Transfer in Highly Porous Building Materials," *Adv. Mater. Res.*, vol. 772, pp. 124–129, Sep. 2013, doi: 10.4028/www.scientific.net/AMR.772.124.
- [136] M. Y. Ferroukhi, R. Djedjig, K. Limam, and R. Belarbi, "Hygrothermal behavior modeling of the hygroscopic envelopes of buildings: A dynamic co-simulation approach," *Build. Simul.*, vol. 9, no. 5, pp. 501–512, Oct. 2016, doi: 10.1007/s12273-016-0292-5.
- [137] Z. Slimani, A. Trabelsi, J. Virgone, and R. Zanetti Freire, "Study of the Hygrothermal Behavior of Wood Fiber Insulation Subjected to Non-Isothermal Loading," *Appl. Sci.*, vol. 9, no. 11, Art. no. 11, Jan. 2019, doi: 10.3390/app9112359.

Bibliography

- [138] M.-A. Hamdaoui, M.-H. Benzaama, Y. El Mendili, and D. Chateigner, "A review on physical and data-driven modeling of buildings hygrothermal behavior: Models, approaches and simulation tools," *Energy Build.*, vol. 251, p. 111343, Nov. 2021, doi: 10.1016/j.enbuild.2021.111343.
- [139] Y. Mualem, "Modified approach to capillary hysteresis based on a similarity hypothesis," *Water Resour. Res.*, vol. 9, no. 5, pp. 1324–1331, 1973, doi: 10.1029/WR009i005p01324.
- [140] Y. Mualem, "A conceptual model of hysteresis," *Water Resour. Res.*, vol. 10, no. 3, Art. no. 3, 1974, doi: <https://doi.org/10.1029/WR010i003p00514>.
- [141] G. Promis, O. Douzane, A. D. Tran Le, and T. Langlet, "Moisture hysteresis influence on mass transfer through bio-based building materials in dynamic state," *Energy Build.*, vol. 166, pp. 450–459, May 2018, doi: 10.1016/j.enbuild.2018.01.067.
- [142] D. Lelievre, T. Colinart, and P. Glouannec, "Hygrothermal behavior of bio-based building materials including hysteresis effects: Experimental and numerical analyses," *Energy Build.*, vol. 84, pp. 617–627, Dec. 2014, doi: 10.1016/j.enbuild.2014.09.013.
- [143] Z. Zhang, M. Thiery, and V. Baroghel-Bouny, "A review and statistical study of existing hysteresis models for cementitious materials," *Cem. Concr. Res.*, vol. 57, p. 44, Mar. 2014, doi: 10.1016/j.cemconres.2013.12.008.
- [144] X. Zhang, B. Chen, and M. Riaz Ahmad, "Characterization of a novel bio-insulation material for multilayer wall and research on hysteresis effect," *Constr. Build. Mater.*, vol. 290, p. 123162, Jul. 2021, doi: 10.1016/j.conbuildmat.2021.123162.
- [145] A. Patera, H. Derluyn, D. Derome, and J. Carmeliet, "Influence of sorption hysteresis on moisture transport in wood," *Wood Sci. Technol.*, vol. 50, no. 2, pp. 259–283, Mar. 2016, doi: 10.1007/s00226-015-0786-9.
- [146] F. Volhard, *Light Earth Building: A Handbook for Building with Wood and Earth*. Walter de Gruyter GmbH, 2016.
- [147] J. Köbbing, N. Thevs, S. Zerbe, W. Wichtmann, and J. Couwenberg, "The utilisation of reed (*Phragmites australis*): a review," *undefined*, 2013, Accessed: Feb. 15, 2022. [Online]. Available: [https://www.semanticscholar.org/paper/The-utilisation-of-reed-\(Phragmites-australis\)%3A-a-K%C3%B6bbing-Thevs/307c5503de54c11cddb325f1f28491b561cc75eb](https://www.semanticscholar.org/paper/The-utilisation-of-reed-(Phragmites-australis)%3A-a-K%C3%B6bbing-Thevs/307c5503de54c11cddb325f1f28491b561cc75eb)
- [148] J. C. Miranda-Trevino and C. A. Coles, "Kaolinite properties, structure and influence of metal retention on pH," *Appl. Clay Sci.*, vol. 23, no. 1, pp. 133–139, Aug. 2003, doi: 10.1016/S0169-1317(03)00095-4.
- [149] "NF EN ISO 12572," Afnor EDITIONS. Accessed: Jul. 27, 2022. [Online]. Available: <https://www.boutique.afnor.org/fr-fr/norme/nf-en-iso-12572/performance-hygrothermique-des-materiaux-et-produits-pour-le-batiment-deter/fa184538/57928>
- [150] "NF ISO 5017," Afnor EDITIONS. Accessed: Jul. 27, 2022. [Online]. Available: <https://www.boutique.afnor.org/fr-fr/norme/nf-iso-5017/produits-refractaires-faconnes-denses-determination-de-la-masse-volumique-a/fa169530/41164>
- [151] "NF EN ISO 11357-4," Afnor EDITIONS. Accessed: Jul. 27, 2022. [Online]. Available: <https://www.boutique.afnor.org/fr-fr/norme/nf-en-iso-113574/plastiques-analyse-calorimetrique-differentielle-dsc-partie-4-determination/fa199556/238238>

Bibliography

- [152] "NF EN ISO 12571," Afnor EDITIONS. Accessed: Jul. 27, 2022. [Online]. Available: <https://m.boutique.afnor.org/fr-fr/norme/nf-en-iso-12571/performance-hygrothermique-des-materiaux-et-produits-pour-le-batiment-deter/fa177734/42249>
- [153] R. Andrade and C. Pérez, "Models of sorption isotherms for food: Uses and limitations," *Vitae Rev. Fac. Quimica Farm.*, vol. 18, pp. 325–334, Sep. 2011.
- [154] P. Moodley and C. Trois, "2 - Lignocellulosic biorefineries: the path forward," in *Sustainable Biofuels*, R. C. Ray, Ed., in Applied Biotechnology Reviews. , Academic Press, 2021, pp. 21–42. doi: 10.1016/B978-0-12-820297-5.00010-4.
- [155] W. G. Glasser, C. A. Barnett, and Y. Sano, "Classification of lignins with different genetic and industrial origins," *J Appl Polym Sci Appl Polym Symp U. S.*, Art. no. CONF-8205234-Vol.1, Jan. 1983, Accessed: Feb. 27, 2022. [Online]. Available: <https://www.osti.gov/biblio/7146700-classification-lignins-different-genetic-industrial-origins>
- [156] B. Sena da Fonseca, A. Vilão, C. Galhano, and J. A. R. Simão, "Reusing coffee waste in manufacture of ceramics for construction," *Adv. Appl. Ceram.*, vol. 113, no. 3, pp. 159–166, Apr. 2014, doi: 10.1179/1743676113Y.0000000131.
- [157] D. Eliche-Quesada *et al.*, "The use of different forms of waste in the manufacture of ceramic bricks," *Appl. Clay Sci. - APPL CLAY SCI*, vol. 52, pp. 270–276, May 2011, doi: 10.1016/j.clay.2011.03.003.
- [158] M. Ben-Hur, M. M. L. J., and M. U., "Adsorption of polymers on clays as affected by clay charge and structure, polymer properties, and water quality.," *Soil Sci.*, 1992.
- [159] H. M. Künzle, *Simultaneous heat and moisture transport in building components: one- and two-dimensional calculation using simple parameters*. Stuttgart: IRB-Verl, 1995.
- [160] R. Rémond, G. Almeida, and P. Perré, "The gripped-box model: A simple and robust formulation of sorption hysteresis for lignocellulosic materials," *Constr. Build. Mater.*, vol. 170, pp. 716–724, May 2018, doi: 10.1016/j.conbuildmat.2018.02.116.
- [161] Z. Zhang, "Modelling of sorption hysteresis and its effect on moisture transport within cementitious materials," p. 237.
- [162] B. Haba, B. Agoudjil, A. Boudenne, and K. Benzarti, "Hygric properties and thermal conductivity of a new insulation material for building based on date palm concrete," *Constr. Build. Mater.*, vol. 154, pp. 963–971, Nov. 2017, doi: 10.1016/j.conbuildmat.2017.08.025.
- [163] N. Chennouf, B. Agoudjil, T. Alioua, A. Boudenne, and K. Benzarti, "Experimental investigation on hygrothermal performance of a bio-based wall made of cement mortar filled with date palm fibers," *Energy Build.*, vol. 202, p. 109413, 2019, doi: 10.1016/j.enbuild.2019.109413.
- [164] N. Benmansour, B. Agoudjil, A. Gherabli, A. Kareche, and A. Boudenne, "Thermal and mechanical performance of natural mortar reinforced with date palm fibers for use as insulating materials in building," *Energy Build.*, vol. 81, pp. 98–104, Oct. 2014, doi: 10.1016/j.enbuild.2014.05.032.
- [165] M. A. Hamdaoui, M.-H. Benzaama, Y. El Mendili, D. Chateigner, and S. Gascoin, "Investigation of the mechanical and hygrothermal behavior of coffee ground wastes

Bibliography

- valorized as a building material: analysis of mix designs performance and sorption curve linearization effect," *Arch. Civ. Mech. Eng.*, vol. 23, no. 1, p. 57, Jan. 2023, doi: 10.1007/s43452-022-00579-2.
- [166] T. Alioua, B. Agoudjil, N. Chennouf, A. Boudenne, and K. Benzarti, "Investigation on heat and moisture transfer in bio-based building wall with consideration of the hysteresis effect," *Build. Environ.*, vol. 163, p. 106333, Oct. 2019, doi: 10.1016/j.buildenv.2019.106333.
- [167] U. N. Environment, "2021 Global Status Report for Buildings and Construction," UNEP - UN Environment Programme. Accessed: Nov. 09, 2022. [Online]. Available: <http://www.unep.org/resources/report/2021-global-status-report-buildings-and-construction>
- [168] M. Bouasria, Pr. Y. El Mendili, M.-H. Benzaama, V. Pralong, J.-F. Bardeau, and F. Hennequart, "Valorisation of stranded *Laminaria digitata* seaweed as an insulating earth material," *Constr. Build. Mater.*, vol. 308, p. 125068, Nov. 2021, doi: 10.1016/j.conbuildmat.2021.125068.
- [169] S. O. Bamaga, "A Review on the Utilization of Date Palm Fibers as Inclusion in Concrete and Mortar," *Fibers*, vol. 10, no. 4, Art. no. 4, Apr. 2022, doi: 10.3390/fib10040035.
- [170] Y. Shang and F. Tariku, "Hempcrete building performance in mild and cold climates: Integrated analysis of carbon footprint, energy, and indoor thermal and moisture buffering," *Build. Environ.*, vol. 206, p. 108377, Dec. 2021, doi: 10.1016/j.buildenv.2021.108377.
- [171] F. Bennai, M. Y. Ferroukhi, F. Benmahiddine, R. Belarbi, and A. Nouviaire, "Assessment of hygrothermal performance of hemp concrete compared to conventional building materials at overall building scale," *Constr. Build. Mater.*, vol. 316, p. 126007, Jan. 2022, doi: 10.1016/j.conbuildmat.2021.126007.
- [172] M. S. Abbas, E. Gourdon, P. Glé, F. McGregor, M. Y. Ferroukhi, and A. Fabbri, "Relationship between hygrothermal and acoustical behavior of hemp and sunflower composites," *Build. Environ.*, vol. 188, p. 107462, Jan. 2021, doi: 10.1016/j.buildenv.2020.107462.
- [173] G. Costantine, C. Maalouf, T. Moussa, and G. Polidori, "Experimental and numerical investigations of thermal performance of a Hemp Lime external building insulation," *Build. Environ.*, vol. 131, pp. 140–153, Mar. 2018, doi: 10.1016/j.buildenv.2017.12.037.
- [174] M. Labat, C. Magniont, N. Oudhof, and J.-E. Aubert, "From the experimental characterization of the hygrothermal properties of straw-clay mixtures to the numerical assessment of their buffering potential," *Build. Environ.*, vol. 97, pp. 69–81, Feb. 2016, doi: 10.1016/j.buildenv.2015.12.004.
- [175] R. Gallegos-Ortega, T. Magaña-Guzmán, J. A. Reyes-López, and M. S. Romero-Hernández, "Thermal behavior of a straw bale building from data obtained in situ. A case in Northwestern México," *Build. Environ.*, vol. 124, pp. 336–341, Nov. 2017, doi: 10.1016/j.buildenv.2017.08.015.
- [176] L. Shi *et al.*, "Analysis of moisture buffering effect of straw-based board in civil defence shelters by field measurements and numerical simulations," *Build. Environ.*, vol. 143, pp. 366–377, Oct. 2018, doi: 10.1016/j.buildenv.2018.07.018.

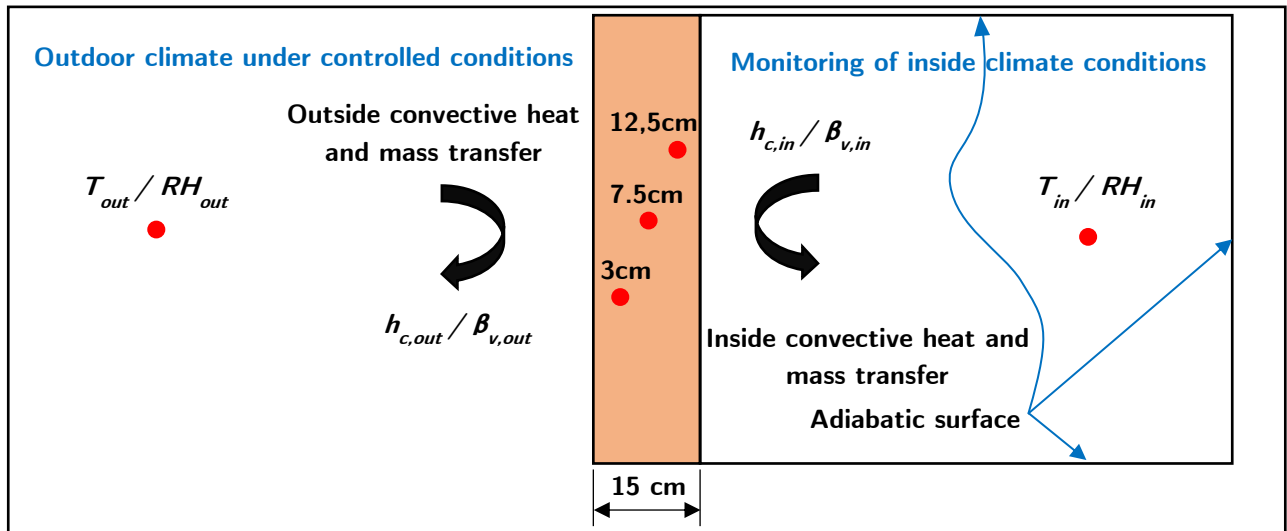
Bibliography

- [177] B. Marques, A. Tadeu, J. Almeida, J. António, and J. de Brito, "Characterisation of sustainable building walls made from rice straw bales," *J. Build. Eng.*, vol. 28, p. 101041, Mar. 2020, doi: 10.1016/j.job.2019.101041.
- [178] R. Belloum, B. Agoudjil, N. Chennouf, and A. Boudenne, "Hygrothermal performance assessment of a bio-based building made with date palm concrete walls," *Build. Environ.*, vol. 223, p. 109467, Sep. 2022, doi: 10.1016/j.buildenv.2022.109467.
- [179] B. Delcroix, M. Kummert, A. Daoud, and M. Hiller, "Conduction transfer functions in TRNSYS multizone building model: Current implementation, limitations and possible improvements," Aug. 2012, pp. 219–226.
- [180] M. Y. Ferroukhi, R. Djedjig, K. Limam, and R. Belarbi, "Hygrothermal behavior modeling of the hygroscopic envelopes of buildings: A dynamic co-simulation approach," *Build. Simul.*, vol. 9, no. 5, pp. 501–512, Oct. 2016, doi: 10.1007/s12273-016-0292-5.
- [181] R. Djedjig, E. Bozonnet, and R. Belarbi, "Analysis of thermal effects of vegetated envelopes: Integration of a validated model in a building energy simulation program," *Energy Build.*, vol. 86, pp. 93–103, Jan. 2015, doi: 10.1016/j.enbuild.2014.09.057.
- [182] M.-H. Benzaama, L. Rajaoarisoa, F. Boukhelf, and Y. El Mendili, "Hygrothermal transfer modelling through a bio-based building material: Validation of a switching-linear model," *J. Build. Eng.*, vol. 55, p. 104691, Sep. 2022, doi: 10.1016/j.job.2022.104691.
- [183] X. Q. Li, Y. Chen, J. D. Spitler, and D. Fisher, "Applicability of calculation methods for conduction transfer function of building constructions," *Int. J. Therm. Sci.*, vol. 48, no. 7, pp. 1441–1451, Jul. 2009, doi: 10.1016/j.ijthermalsci.2008.11.006.
- [184] S. Wang and Y. Chen, "A simple procedure for calculating thermal response factors and conduction transfer functions of multilayer walls," *Appl. Therm. Eng.*, vol. 22, no. 3, pp. 333–338, Mar. 2002, doi: 10.1016/S1359-4311(01)00086-2.
- [185] H. T. Ceylan and G. E. Myers, "Long-Time Solutions to Heat-Conduction Transients with Time-Dependent Inputs," *J. Heat Transf.*, vol. 102, no. 1, pp. 115–120, Feb. 1980, doi: 10.1115/1.3244221.
- [186] J. E. Seem, "Modeling of Heat Transfer in Buildings," 1987, Accessed: Nov. 14, 2022. [Online]. Available: <https://minds.wisconsin.edu/handle/1793/7916>
- [187] K. Ouyang and F. Haghighat, "A procedure for calculating thermal response factors of multi-layer walls—State space method," *Build. Environ.*, vol. 26, no. 2, pp. 173–177, Jan. 1991, doi: 10.1016/0360-1323(91)90024-6.
- [188] US Department of Energy, "Chapter 3. Surface Heat Balance Manager / Processes," in *EnergyPlus™ Version 9.4.0 Documentation: Engineering Reference*, 2020, pp. 62-69 (1785).
- [189] S. S. Haykin, *Neural networks and learning machines*, 3. ed. New York Munich: Prentice-Hall, 2009.
- [190] L. Ni *et al.*, "Streamflow and rainfall forecasting by two long short-term memory-based models," *J. Hydrol.*, vol. 583, p. 124296, Apr. 2020, doi: 10.1016/j.jhydrol.2019.124296.
- [191] A. Chatterjee, M. W. Gerdes, and S. G. Martinez, "Statistical Explorations and Univariate Timeseries Analysis on COVID-19 Datasets to Understand the Trend of Disease Spreading and Death," *Sensors*, vol. 20, no. 11, Art. no. 11, Jan. 2020, doi: 10.3390/s20113089.

Bibliography

- [192] B. L. Gowreesunker, S. A. Tassou, and M. Kolokotroni, "Coupled TRNSYS-CFD simulations evaluating the performance of PCM plate heat exchangers in an airport terminal building displacement conditioning system," *Build. Environ.*, vol. 65, pp. 132–145, Jul. 2013, doi: 10.1016/j.buildenv.2013.04.003.
- [193] G. Kan *et al.*, "Improving event-based rainfall-runoff simulation using an ensemble artificial neural network based hybrid data-driven model," *Stoch. Environ. Res. Risk Assess.*, 2015, Accessed: Nov. 14, 2022. [Online]. Available: <https://doi.org/10.1007/s00477-015-1040-6>
- [194] P. Dal Zotto, J.-M. Larre, A. Merlet, and L. Picau, *Mémotech - Génie énergétique*, 3e édition. Casteilla, 2003.
- [195] P. Dal Zotto, J.-M. Larre, A. Merlet, and L. Picau, *Mémotech - Génie énergétique*, 4e édition. Casteilla, 2009.
- [196] B. Givoni, "Comfort, climate analysis and building design guidelines," *Energy Build.*, vol. 18, no. 1, pp. 11–23, Jan. 1992, doi: 10.1016/0378-7788(92)90047-K.
- [197] B. Agoudjil, A. Benchabane, A. Boudenne, L. Ibos, and M. Fois, "Renewable materials to reduce building heat loss: Characterization of date palm wood," *Energy Build.*, vol. 43, no. 2–3, pp. 491–497, Feb. 2011, doi: 10.1016/j.enbuild.2010.10.014.
- [198] M. Raza, H. A. Abdallah, A. Abdullah, and B. Abu-Jdayil, "Date Palm Surface Fibers for Green Thermal Insulation," *Buildings*, vol. 12, no. 6, p. 866, Jun. 2022, doi: 10.3390/buildings12060866.
- [199] D. Medjelekh, "Caractérisation multi-échelle du comportement thermo hybride des enveloppes hygroscopiques," Theses, Université de Limoges; Université Mentouri (Constantine, Algérie), 2015. Accessed: Jan. 05, 2023. [Online]. Available: <https://theses.hal.science/tel-01286901>

Appendix



Annex 1. Scheme of geometry and boundary conditions for numerical simulation of Chapter 3

Acknowledgement

I would like to express my appreciation to the University of Caen Normandy for the warm welcome I received at the beginning of my PhD and for the opportunity to start my doctoral project with them.

My gratitude extends to the excellent academic management of the doctoral school PSIME 591, and in particular to the administrative managers, Mrs Esther Camus, Marie Meleux, and Sandrine Maviel , for their availability and facilitating the proceedings of the doctoral program.

I thank the state department of Calvados (14) for the benefits granted to researchers and the arrangements made to facilitate their activities.

I would also like to extend my sincere thanks to my professors, especially Nassim Sebaibi, for trusting me and agreeing to supervise my doctoral project, as well as for the time they devoted to monitoring the progress of my doctoral project.

I sincerely would like to thank Manal Bouasria who provided us with her thesis data to be used in my PhD project [1], Dalel Medjelekh, who granted us permission to utilize its data for academic purposes [199]. Faraj who helped me with the experimental part, Hichem Benzaama for the good quality of the collaborative work and finally Pr. Daniel Chateigner for his advices and remarks.

I also thank Bechara, Manon, Benjamin, Ilyes, Samira, Walid, Aurélie, Karim, Fatima, Malo, AbdelAziz, Mohamed, Hamza, Ferhat, Badreddine, Mariem, Abdel, Houssam, Imane, Athmane, Lally for the good atmosphere created, and the shared nice moments. My thanks also go to the members of the Builders école d'ingénieurs administrative division, Johann, Fabrice, Jean-Baptiste, Aurélie, Mathieu, Dylann, Gabin. Likewise, I thank Clara, Sophie and Marie-Laure for their administrative help and Eric Guillot for providing us with diverse research data.

I would like to thank the Tunisian Ministry of Higher Education & Scientific Research and the National School of Engineers of Monastir (ENIM) for granting me a scholarship of excellence to study abroad.

In memory of my grandfather Ali Hamdaoui, I would like to thank him for financing a few years of my higher education. Also, in memory of my grandmother Zina Bent Rahal Al Waredy.

My first and last thanks go to my parents and brothers, Ammar, Hayet and Manelle, Melek. My family and cousins for their encouragement and their permanent support. I take the opportunity to mention most of them.

Acknowledgement

حمد ال حمداوي (القيرواني - قریش) ، علي بن حمد
ال حمداوي ، مصطفى بن حمد ال حمداوي ، عمر بن حمد
ال حمداوي ، محمد بن حمد ال حمداوي ، قاسم بن حمد
ال حمداوي ، عمار بن حمد ال حمداوي ، منصور بن علي
ال حمداوي ، مسعود بن علي ال حمداوي ، عبدالله بن
علي ال حمداوي ، صالح بن علي ال حمداوي ، هادي بن
علي ال حمداوي ، عمار بن علي ال حمداوي ، خديجة
بنت علي ال حمداوي ، مختار بن منصور ال حمداوي ،
علي بن منصور ال حمداوي ، هادي بن منصور ال
حمداوي ، محسن بن منصور ال حمداوي ، محمد بن
منصور ال حمداوي ، مريم بنت منصور ال حمداوي ،
زينة بنت منصور الحمداوي ، حمد بن مسعود ال
حمداوي ، عمر بن مسعود ال حمداوي ، محمد بن مسعود
ال حمداوي ، عدي بن مسعود ال حمداوي ، فتيحي بن
مسعود ال حمداوي ، نبيهة بنت مسعود ال حمداوي ،
هنية بنت مسعود ال حمداوي ، عمار بن عبدالله ال
حمداوي ، طاهر بن عبدالله ال حمداوي ، صالح بن
عبدالله ال حمداوي ، عمر بن عبدالله ال حمداوي ، محمد
بن عبدالله ال حمداوي ، ربيع بنت عبدالله ال حمداوي ،
زينة بنت عبدالله ال حمداوي ، داود بن صالح ال
حمداوي ، هادي بن صالح ال حمداوي ، نائل بن صالح
ال حمداوي ، محمد بن بوبكر ال حمداوي ، علي بن
بوبكر ال حمداوي ، عمر بن بوبكر ال حمداوي ، هادي
بن بوبكر ال حمداوي ، مريم بنت بوبكر ال حمداوي ،
حنات بنت بوبكر ال حمداوي ، محبوبة بنت بوبكر ال
حمداوي ، عائشة بنت بوبكر ال حمداوي ، فاطمة بنت
بوبكر ال حمداوي.

Hamad Al Hamdawi (Al Qayrawani), Ali ben Hamad
Al Hamdawi, Mustafa ben Hamad Al Hamdawi,
Omar ben Hamad Al Hamdawi, Mohamed ben
Hamad Al Hamdawi, Qasem ben Hamad Al
Hamdawi, Ammar ben Hamad Al Hamdawi, Mansour
ben Ali Al Hamdawi, Masoud ben Ali Al Hamdawi,
Abdullah ben Ali Al Hamdawi, Saleh ben Ali Al
Hamdawi, Hedy ben Ali Al Hamdawi, Ammar ben Ali
Al Hamdawi, Khadyja bent Ali Al Hamdawi, Mukhtar
ben Mansour Al Hamdawi, Ali ben Mansour Al
Hamdawi, Hedy ben Mansour Al Hamdawi, Mohsen
ben Mansour Al Hamdawi, Mohamed ben Mansour
Al Hamdawi, Maryem bent Mansour Al Hamdawi,
Zina bent Mansour Al Hamdawi, Hamad ben Masoud
Al Hamdawi, Omar ben Masoud Al Hamdawi,
Mohamed ben Masoud Al Hamdawi, Uday ben
Masoud Al Hamdawi, Fethi ben Masoud Al
Hamdawi, Nabiha bent Masoud Al Hamdawi,
Haniyeh bent Masoud Al Hamdawi, Ammar ben
Abdullah Al Hamdawi, Taher ben Abdullah Al
Hamdawi, Saleh ben Abdullah Al Hamdawi, Omar
ben Abdullah Al Hamdawi, Mohamed ben Abdullah
Al Hamdawi, Rebah bent Abdullah Al Hamdawi, Zina
bent Abdullah Al Hamdawi. Dawood ben Saleh Al
Hamdawi, Hedy ben Saleh Al Hamdawi, Neil ben
Saleh Al Hamdawi, Mohamed ben Boubaker Al
Hamdawi, Ali ben Boubaker Al Hamdawi, Omar ben
Boubaker Al Hamdawi, Hedy ben Boubaker Al
Hamdawi, Maryem bent Boubaker Al Hamdawi,
Jannette bent Boubaker Al Hamdawi, Mahbouba
bent Boubaker Al Hamdawi, Aisha bent Boubaker Al
Hamdawi, Fatima bent Boubaker Al Hamdaoui

I extended my sincere gratitude to other members of my family, My grandparents, Salah and Faiza and also my uncle Mohamed Ben Salah. My aunts, Bochra, Houda, Amel, Basma, Olfa

Acknowledgement

and Saida. My cousins Amir, Mustapaha, Oussema, Achref, Marwen, Iheb, Mohamed, Ahmed, Mohamed, Anas, Rania, Khouloud, Marwa, Asma, Mariem, Chaima, Imen, Ines. And the rest of my family member as Habib, Ayoub, Mahmoud, Abdelwaheb, Mohsen, Faysal.

I am sincerely very thankful to my family members Al-Shafi'i, like uncle Nouredine, Mohamed, as well as Lalla Atira, Fatima and Amel, as well as my cousins, Mohamed Ayachi, Nour, Ichraq, Farah, Maram, Emna.

Finally, my thanks to all those who have contributed in any way to the achievement of my academic career.